ANNUAL REPORT 2021

Institute of Ion Beam Physics and Materials Research

HZDR-118

Annual Report 2021

Institute of Ion Beam Physics and Materials Research

Editors

J. Fassbender, M. Helm,
M. Zahn, P. Zahn

HZDR

HELMHOLTZ ZENTRUM
DRESDEN ROSSENDORF

Cover Picture - Trapping spins with sound: Acoustic manipulation of electron spins could lead to new methods of quantum control

Color centers – defects in the crystal lattice of solids containing one or more trapped electrons – are often paramagnetic, making them promising systems for applications in quantum technologies, e.g. as quantum memories (qubits) or quantum sensors. Here, the challenge is to develop efficient methods to manipulate their spin states, the magnetic quantum property of electrons. This is usually realized by applying electromagnetic fields. A laser excitation is used for the initialization and optical readout of the spin states, while the coherent spin control is performed with microwaves. An alternative method for coherent control is the use of mechanical vibrations like surface acoustic waves (SAWs), which are elastic vibrations confined at the surface of a solid. Due to their short wavelengths, they are commonly integrated in microchips as radio frequency filters, oscillators, and transformers in current electronic devices like mobile phones and tablets.

The illustration on the cover page schematically shows the electron spin precession in silicon carbide (SiC) induced by SAWs. Due to a giant interaction between the periodic vibrations of the crystal lattice and the electrons trapped in the color centers, simultaneous manipulation of the electron spin in the ground and excited state is realized. Under this condition, the quantum information stored in the electron spin can be decoupled from the external perturbation caused by the laser. This allows the efficient spin manipulation by the SAW when the center is in the excited state and simultaneous preservation of the long coherence time intrinsic to the ground state. SiC is a robust material for nano-electromechanical applications that also hosts highly-coherent spin color centers. Therefore, their acoustic manipulation provides new opportunities for the development of quantum information protocols to be implemented in quantum devices with dimensions similar to those of current microchips.

Image: © HZDR / Blaurock

URN: urn:nbn:de:bsz:d120-qucosa2-799198
URL: www.hzdr.de/publications/Publ-34008

This report is also available at https://www.hzdr.de/FWI.

Helmholtz-Zentrum Dresden - Rossendorf e.V.
Institute of Ion Beam Physics and Materials Research

Bautzner Landstraße 400
01328 Dresden
Germany

Directors	Prof. Dr. M. Helm	Prof. Dr. J. Fassbender
Phone	+49 351 260 2260	+49 351 260 3096
Fax	+49 351 260 3285	+49 351 260 3285
Email	m.helm@hzdr.de	j.fassbender@hzdr.de

www.hzdr.de/FWI

Preface by the directors

The year 2021 was still overshadowed by waves of the COVID-19 pandemic, although the arrival of efficient vaccinations together with the experience of the preceding year gave us a certain routine in handling the situation. By now the execution of meetings in an online mode using zoom and similar video conference systems has been recognized as actually being useful in certain situations, e.g. instead of flying across Europe to attend a three-hours meeting, but also to be able to attend seminars of distinguished scientists which otherwise would not be easily accessible.

The scientific productivity of the institute has remained on a very high level, counting 190 publications with an unprecedented average impact factor of 8.0. Six outstanding and representative publications are reprinted in this Annual Report. 16 new third-party projects were granted, among them 7 DFG projects, but very remarkably also an EU funded project on nonlinear magnons for reservoir computing with industrial participation of Infineon Technologies Dresden and GlobalFoundries Dresden coordinated by Kathrin Schultheiß of our Institute.

The scientific success was also reflected in two HZDR prizes awarded to the members of the Institute: Dr. Katrin Schultheiß received the HZDR Forschungspreis for her work on "Nonlinear magnonics as basis for a spin based neuromorphic computing architecture", and Dr. Toni Hache was awarded the Doktorandenpreis for his thesis entitled "Frequency control of auto-oscillations of the magnetization in spin Hall nano-oscillators". Our highly successful theoretician Dr. Arkady Krasheninnikov was quoted as Highly Cited Researcher 2021 by Clarivate.

The new 1-MV facility for accelerator mass spectrometry (AMS) has been ordered from NEC (National Electrostatics Corporation). Design of a dedicated building to house the accelerator, the SIMS and including additional chemistry laboratories for enhanced sample preparation capabilities has started and construction is planned to be finished by mid 2023, when the majority of the AMS components are scheduled for delivery.

In the course of developing a strategy for the HZDR - **HZDR 2030+** Moving Research to the NEXT Level for the NEXT Gens - six research focus areas for our institute were identified.

Concerning personalia, it should be mentioned that the long-time head of the spectroscopy department PD Dr. Harald Schneider went into retirement. His successor is Dr. Stephan Winnerl, who has been a key scientist in this department already for two decades. In addition, PD Dr. Sebastian Fähler was hired in the magnetism department who transferred several third-party projects with the associated PhD students to the Institute and strengthens our ties to the High Magnetic Field Laboratory, but also to the Institute of Fluid Dynamics.

Finally, we would like to cordially thank all partners, friends, and organizations who supported our progress in 2021. First and foremost we thank the Executive Board of the Helmholtz-Zentrum Dresden-Rossendorf, the Minister of Science and Arts of the Free State of Saxony, and the Ministers of Education and Research, and of Economic Affairs and Climate Action of the Federal Government of Germany. Many partners from universities, industry and research institutes all around the world contributed essentially, and play a crucial role for the further development of the institute. Last but not least, the directors would like to thank all members of our institute for their efforts in these very special times and excellent contributions in 2021.

Prof. Manfred Helm   Prof. Jürgen Fassbender

Contents

Selected Publications

Statistics

Selected Publications

Copyright remarks

The following journal articles and abstracts are reprinted with kind permission from:

ARTICLE

High electron mobility in strained GaAs nanowires

Leila Balaghi[1,2], Si Shan[1], Ivan Fotev[1,2], Finn Moebus[1], Rakesh Rana[1], Tommaso Venanzi[1,2], René Hübner[1], Thomas Mikolajick[2,3], Harald Schneider [1], Manfred Helm[1,2], Alexej Pashkin[1] & Emmanouil Dimakis[1✉]

Transistor concepts based on semiconductor nanowires promise high performance, lower energy consumption and better integrability in various platforms in nanoscale dimensions. Concerning the intrinsic transport properties of electrons in nanowires, relatively high mobility values that approach those in bulk crystals have been obtained only in core/shell heterostructures, where electrons are spatially confined inside the core. Here, it is demonstrated that the strain in lattice-mismatched core/shell nanowires can affect the effective mass of electrons in a way that boosts their mobility to distinct levels. Specifically, electrons inside the hydrostatically tensile-strained gallium arsenide core of nanowires with a thick indium aluminium arsenide shell exhibit mobility values 30–50 % higher than in equivalent unstrained nanowires or bulk crystals, as measured at room temperature. With such an enhancement of electron mobility, strained gallium arsenide nanowires emerge as a unique means for the advancement of transistor technology.

[1] Institute of Ion Beam Physics and Materials Research, Helmholtz-Zentrum Dresden-Rossendorf, 01328 Dresden, Germany. [2] Center for Advancing Electronics Dresden (cfaed), Technische Universität Dresden, 01062 Dresden, Germany. [3] NaMLab gGmbH, Dresden, Germany. ✉email: e.dimakis@hzdr.de

ARTICLE

Many transistor concepts that aim at further miniaturisation, faster switching, lower power consumption or quantum transport applications rely on the nanowire or nanosheet geometry. Nanowires or nanosheets are inherently suitable for the realisation of gate-all-around field-effect transistors (FETs) that allow for the best possible electrostatic control of the channel potential. Various FET concepts like conventional inversion channel metal-oxide-semiconductor FETs[1,2], junctionless FETs[3], reconfigurable Schottky-barrier FETs[4], band-to-band tunnel FETs (for steep current–gate-voltage subthreshold transfer characteristics below 60 mV/dec)[5] or modulation-doped FETs[6] can benefit from the gate-all-around architecture. Furthermore, very thin or core/shell heterostructured nanowires provide charge carrier confinement that leads to one-dimensional ballistic transport[7–10], with the possibility to host multiple conduction channels within the same nanowire[11]. All the aforementioned devices also have the potential for monolithic integration in heterogeneous platforms like the mainstream Si CMOS[12] or future platforms that may be based on emerging 2D materials[13].

Owing to the high mobility of electrons in III–V semiconductors, this class of materials is the ideal candidate for high-speed low-power logic and radio-frequency applications. However, the mobility of charge carriers in nanowires made of III–V semiconductors is negatively affected by scattering at the interface of the nanowire to the surrounding isolation layers of the nanowires. Consequently, nanowires with smaller diameters, i.e. larger surface-to-volume ratios, exhibit lower mobility values[14,15]. To reduce interface scattering, the charge carriers are kept away from the nanowire surface by overgrowing the nanowires with a thick enough and usually lattice-matched shell of a semiconductor with a larger bandgap. With such an approach, electron mobility values of up to 3000 $cm^2\,V^{-1}\,s^{-1}$ at room temperature for electron concentrations of 10^{17}– $10^{18}\,cm^{-3}$ have been reported for the core of GaAs/Al$_x$Ga$_{1-x}$As core/shell nanowires, approaching values, which are typical for bulk GaAs[16]. Recently, we demonstrated that in GaAs/In$_x$Al$_{1-x}$As core/shell nanowires with large lattice mismatch between the core and the shell (the larger the In-content x in the shell, the larger the core/shell lattice mismatch), the few-µm-long core can be hydrostatically strained with remarkable effects on its electronic properties[17]. Specifically, hydrostatic tensile strain (expansion in all three dimensions) in the GaAs core of up to 7% was obtained, narrowing the bandgap of GaAs from its unstrained value of 1.42 eV at 300 K down to 0.87 eV (i.e. a reduction of 40%). Band structure calculations for hydrostatically tensile-strained GaAs predict that the effective mass of electrons in the Γ-valley of the conduction band should also undergo a significant reduction[17,18]. This implies higher electron mobility, which would be beneficial for high-speed low-power transistors. It should be noted that unlike biaxially strained thin films or small-sized asymmetrically shaped quantum dots, only nanowires offer the possibility for large hydrostatic strain in a transistor-relevant geometry. Improved mobility has been reported for holes in the core of [110]-oriented Ge/Si core/shell nanowires[19], but that was attributed more to the high structural quality of the coherent heterostructure rather than the built-in strain (which was not hydrostatic in this case). A relative improvement of mobility due to strain has only been reported for electrons in the shell of Si$_x$Ge$_{1-x}$/Si core/shell nanowires[20], but the actual mobility values were significantly lower than those in bulk Si.

Here, the transport properties of electrons inside the strained core of GaAs/In$_{0.37}$Al$_{0.63}$As core/shell nanowires are investigated to verify the aforementioned expectations and to assess the potential of this type of nanowires for transistor applications. First, the strain in the core and its effect on band structure are determined by a combination of spectroscopic methods and

theoretical simulations. Then, the main study uses optical-pump THz-probe spectroscopy (OPTPS), which is a contactless method for probing the charge carrier transport and dynamics, circumventing challenges in the fabrication of electrical contacts on nanowires and the analysis of the corresponding electrical measurements[21]. Particular attention is paid to the role in OPTPS analysis of the spatial arrangement of the nanowires in the probed sample and the presence of an optional oxidation-protective In$_y$Ga$_{1-y}$As capping shell. The results of electron scattering rate and mobility are compared with those of unstrained GaAs/Al$_{0.35}$Ga$_{0.65}$As nanowires and bulk GaAs, revealing the beneficial effect of tensile strain. Electron mobility values higher than those in bulk crystals are demonstrated, raising the promises of mismatched core/shell nanowires for high-speed low-power transistor applications.

Results

Nanowire samples: general description and simulations. This work was based on the study of two samples with free-standing GaAs/In$_x$Al$_{1-x}$As core/shell nanowires of zinc blende crystal structure, which were grown on Si(111) substrates by solid-source molecular beam epitaxy (MBE). The GaAs core was 2 µm long and 22 nm thick, whereas the In$_x$Al$_{1-x}$As shell was 80 nm thick. The main difference between the two samples is that for one of them, the In$_x$Al$_{1-x}$As shell was overgrown with a 5-nm-thick lattice-matched In$_y$Ga$_{1-y}$As capping shell ($y \approx x + 0.01$) to protect the Al-containing shell from oxidation in air. The In-content x in the In$_x$Al$_{1-x}$As shell was in the range of 0.4 for both samples, i.e. 0.37 for the uncapped and 0.43 for the capped nanowires. More details about the growth and the structural properties of the nanowires can be found in ref. [17]. A representative side-view scanning electron microscopy (SEM) image of the as-grown capped nanowires is shown in Fig. 1a. Chemical composition analysis was performed along and normal to the axis of single nanowires by energy-dispersive X-ray spectroscopy (EDXS) in a transmission electron microscope (TEM). Figure 1b, c shows representative EDXS-based element maps from capped nanowires. It can be seen that the core and the two shells are well defined and have uniform chemical compositions (except for the six In-poor corner lines along the $\langle 11\bar{2} \rangle$ crystallographic directions, which have been attributed to the combination of different growth rates, surface energies and possibly strain relaxation mechanisms on $\{1\bar{1}0\}$ and $\{11\bar{2}\}$ facets, as well as to the different diffusivities of In, Al and Ga adatoms[22]). The uncapped nanowires show the same morphological and compositional characteristics like the capped ones (see Supplementary Note 1). The measured core radius and In-content x in the shell are found to vary as little as ±2 nm (in agreement to previous SEM measurements on bare GaAs nanowires[23]) and ±0.02, respectively, within single nanowires or in different nanowires from the same sample (see Supplementary Note 1).

The strain distribution in the nanowires was simulated using three-dimensional finite-element continuum elasticity theory (nextnano[24] software). Figure 1d shows selected results close to the core (at the middle of the nanowire length) for a nanowire with $x = 0.37$. The presence of a thin capping shell does not have any measurable influence on the strain. As it can be seen, both the axial (ε_{zz}) and the radial (ε_{xx}, ε_{yy}) strain components inside the core are positive and quite uniform, with the axial one being the dominant one and practically equal to the lattice misfit (i.e. the relative difference between the lattice constants of the core and the shell). This means that the core is tensile-strained in all three dimensions and mostly along the nanowire axis. The large positive value of hydrostatic strain ($\varepsilon_h = \varepsilon_{zz} + \varepsilon_{xx} + \varepsilon_{yy}$) expresses the significant volumetric increase of the crystal lattice.
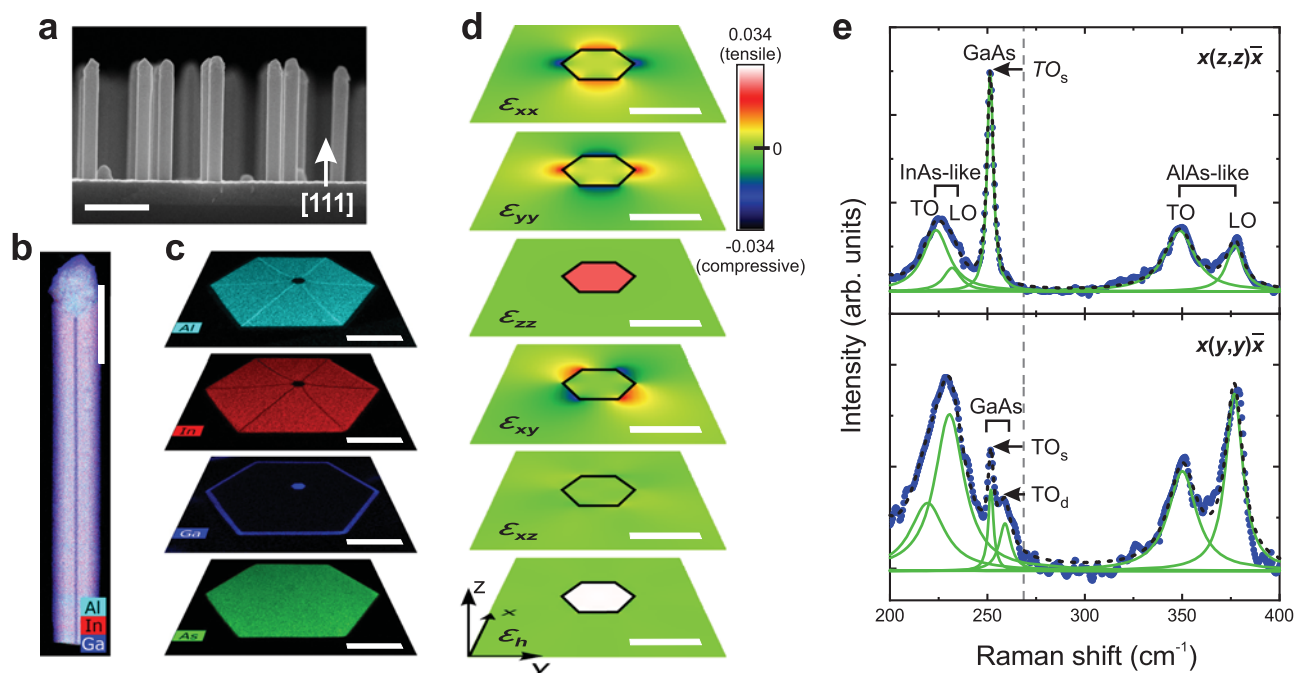
ARTICLE

Fig. 1 Morphology, chemical composition and strain of the investigated GaAs/In$_{0.37}$Al$_{0.63}$As core/shell (uncapped) and GaAs/In$_{0.43}$Al$_{0.57}$As/In$_{0.44}$Ga$_{0.56}$As core/shell/capping-shell (capped) nanowires. a Side-view scanning electron microscopy (SEM) image of as-grown capped nanowires on a Si(111) substrate. **b** Energy-dispersive X-ray spectroscopy (EDXS)-based compositional map from the side of one capped nanowire. The signal from Al, In and Ga is illustrated in cyan, red and blue, respectively. **c** Individual EDXS-based compositional maps for each constituent element perpendicular to the axis of a capped nanowire. Here, a TEM lamella from the middle of a nanowire was analysed. The signal from As is illustrated in green. **d** Simulated strain components close to the core of an uncapped nanowire using continuum elasticity theory. The core is outlined with a black line. **e** Raman scattering spectra at room temperature from a single uncapped nanowire in two different polarisation configurations: $x(z,z)\overline{x}$ at the top, and $x(y,y)\overline{x}$ at the bottom. The measured data were plotted with blue points and the fitted curves with lines: green for the individual peaks and dashed black for the cumulative curve. The scale bars correspond to 1 μm in (**a**), 400 nm in (**b**), 60 nm in (**c**) and 20 nm in (**d**).

Table 1 Simulated and measured strain components in the core of two types of GaAs/In$_x$Al$_{1-x}$As core/shell nanowires.

	Nanowire type	
	uncapped	capped
In-content x	0.37	0.43
Core/shell misfit	0.027	0.032
Simulated ε_{zz}	0.025	0.029
Simulated ε_{xx}, ε_{yy}	0.004	0.005
Simulated ε_h	0.033	0.038
Measured ε_{zz}	0.027 (2)	0.031 (2)
Measured ε_{xx}, ε_{yy}	0.004 (1)	0.005 (1)
Measured ε_h	0.035 (2)	0.041 (2)

The simulations employed continuum elasticity theory and the listed values correspond to the centre of the core. The measured values resulted from Eqs. 2 and 3. The x, y and z directions are defined in Fig. 1d. The positive values of all strain components indicate that the core is tensile-strained in all three dimensions. The small value of $\varepsilon_{xx}/\varepsilon_{zz}$ ratio indicates that the core is predominantly strained along the [111] nanowire axis. The In-content x (as measured by energy-dispersive x-ray spectroscopy) and the corresponding core/shell misfit are also listed.

On the other hand, the strain components ε_{xy} and ε_{xz} (as well as ε_{yz}, which is similar to ε_{xz}) are equal to zero in the core. The values of all non-zero strain components at the centre of the core of the nanowires with $x = 0.37$, as well as for $x = 0.43$ (like the capped nanowires), are listed in Table 1. Concerning the strain in the shell, ε_{zz}, ε_h and ε_{xz} are equal to zero. Only ε_{xx}, ε_{yy} and ε_{xy} have complex non-zero patterns close to the interface with the core, but they all become equal to zero within ~10–20 nm away from it. This means that the shell can mainly be considered unstrained, which is understood as the result of its larger volume compared to that of the core[17]. The corresponding simulated distribution of

stress in the core and the shell, together with simulations for the capped nanowires with $x = 0.43$, can be found in Supplementary Note 2.

Experimentally, the strain can be probed by the shift that it causes to the phonon lines of the core and the shell in micro-Raman scattering spectroscopy. Room temperature measurements were performed in the back-scattering configuration on single nanowires, which had been previously transferred on an Au-coated Si wafer, lying on their $\{1\bar{1}0\}$ side. Excitation ($\lambda = 532$ nm, beam spot size ≈1 μm) and measurements were performed normal to the Si wafer, thus normal to one of the $\{1\bar{1}0\}$ sidewalls of the nanowires (along x-axis), using a confocal microscope. The excitation light was linearly polarised with an orientation that could be arbitrarily rotated with respect to the nanowire axis (z-axis) in the (y, z) plane using a half-wavelength plate. For polarisation-resolved measurements, a rotatable analyser was placed in front of the detector. Figure 1e shows an example of Raman spectra from one uncapped nanowire in two polarisation configurations. The plot at the top shows measurement in $x(z,z)\overline{x}$ configuration, i.e. with excitation and measurement polarisation along the nanowire axis (z-axis). The peak at 252 cm^{-1} (249 cm^{-1} for the capped ones) corresponds to transverse optical (TO) phonons with atomic displacement along the nanowire axis (TO$_s$) in the GaAs core. The downshift of the peak position with respect to $\omega_{TO} = 268.6$ cm^{-1} (indicated with a vertical dashed line) of bulk GaAs is attributed to tensile strain in the core. Transverse and longitudinal optical (LO) phonons from the shell are seen in the ranges of 220–230 cm^{-1} (InAs-like) and 350–375 cm^{-1} (AlAs-like). Their positions are close to those for bulk In$_{0.37}$Al$_{0.63}$As[25], which is indicative of an almost strain-free shell. According to the selection rules for the specific polarisation
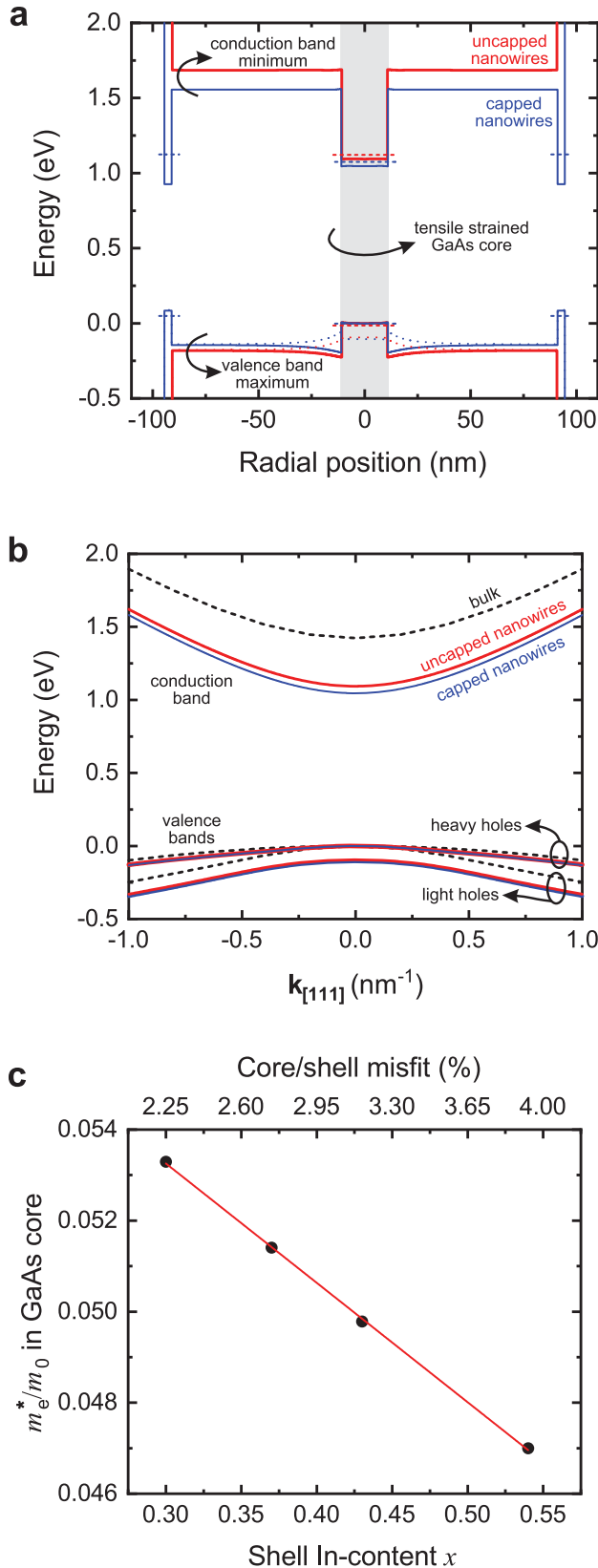
Fig. 2 Simulated electronic structure of the investigated GaAs/In$_{0.37}$Al$_{0.63}$As core/shell (uncapped) and GaAs/In$_{0.43}$Al$_{0.57}$As/In$_{0.44}$Ga$_{0.56}$As core/shell/capping-shell (capped) nanowires at 300 K using 8-band k·p theory. a Band-edge profile at the Γ-point of the Brillouin zone, along the [1̄10] crystallographic direction (from the middle of one side-facet, through the centre of the core at zero position, to the middle of the opposite side-facet). The valence bands for heavy and light holes are shown with continuous and dotted lines, respectively. The lowest confined energy levels in the core and the capping shell are indicated with horizontal dashed lines. **b** Γ-valley energy dispersion in the GaAs core, simulated along the [111] crystallographic orientation. One conduction and two valence bands (heavy and light holes) are shown. Results for unstrained bulk are also shown (black dashed lines) for comparison. The valence band maximum at $\mathbf{k_{[111]}} = 0$ has been set to zero energy. **c** Simulated dependence of the electron effective mass in the GaAs core on the In-content x of the In$_x$Al$_{1-x}$As shell (bottom x-axis) and the corresponding core/shell misfit (top x-axis). The data points are calculated values, which have been linearly fitted.

and measurement polarisation orthogonal to the nanowire axis (along the y-axis). Besides TO$_s$, though, GaAs TO phonons with atomic displacement along the y-axis (TO$_d$) are visible at 259 cm^{-1}. TO$_s$ and TO$_d$ are degenerate in bulk GaAs, whereas their splitting in the nanowire core stems from the strain anisotropy (shear strain)[26,28,29].

In a previous study on the same type of nanowires, we considered only the role of volumetric strain in phonon shifts, neglecting the contribution of shear strain. Nevertheless, the deduced strain values from Raman scattering measurements could sufficiently explain the observed changes in the bandgap of the GaAs core in good agreement with theory[17]. Here, both volumetric and shear contributions are taken into account for a more precise analysis. Assuming uniform strain around the [111] axis, the strain tensor in Cartesian coordinates gets the form[30]

$$\boldsymbol{\varepsilon} = \frac{1}{3}\begin{pmatrix} 2\varepsilon_{xx} + \varepsilon_{zz} & \varepsilon_{zz} - \varepsilon_{xx} & \varepsilon_{zz} - \varepsilon_{xx} \\ \varepsilon_{zz} - \varepsilon_{xx} & 2\varepsilon_{xx} + \varepsilon_{zz} & \varepsilon_{zz} - \varepsilon_{xx} \\ \varepsilon_{zz} - \varepsilon_{xx} & \varepsilon_{zz} - \varepsilon_{xx} & 2\varepsilon_{xx} + \varepsilon_{zz} \end{pmatrix} \quad (1)$$

where the diagonal (off-diagonal) elements represent the hydrostatic (shear) components. The frequencies of TO$_s$ (ω_{TO_s}) and TO$_d$ (ω_{TO_d}) in the presence of strain can be found by solving the corresponding secular equation as described in ref. [31]. In this way, one gets[30,31]

$$\omega_{TO_s}^2 = \omega_{TO}^2\left[1 - 2\gamma_T\left(2\varepsilon_{xx} + \varepsilon_{zz}\right) + \frac{4}{3}\widetilde{K}_{44}^T\left(\varepsilon_{zz} - \varepsilon_{xx}\right)\right], \quad (2)$$

$$\omega_{TO_d}^2 = \omega_{TO}^2\left[1 - 2\gamma_T\left(2\varepsilon_{xx} + \varepsilon_{zz}\right) - \frac{2}{3}\widetilde{K}_{44}^T\left(\varepsilon_{zz} - \varepsilon_{xx}\right)\right], \quad (3)$$

where $\omega_{TO} = 268.6$ cm^{-1} is the TO phonon frequency for strain-free GaAs, $\gamma_T = 1.35$ is the hydrostatic deformation potential (mode Grüneisen parameter), and $\widetilde{K}_{44}^T = -0.88$ is the shear deformation potential for GaAs TO phonons[29]. The second (third) term inside the square bracket represents the contribution of hydrostatic (shear) strain to the total phonon shift. One can see that the hydrostatic strain causes the same shift for both ω_{TO_s} and ω_{TO_d}, whereas the shear strain is responsible for the splitting between the two frequencies. From the measured values of $\omega_{TO_s} = 251(1)$ cm^{-1} and $\omega_{TO_d} = 258(1)$ cm^{-1} on five uncapped nanowires, the strain components in the GaAs core were calculated from Eqs. 2 and 3 to be $\varepsilon_{zz} = 0.030(6)$, $\varepsilon_{xx} = 0.002(2)$ and $\varepsilon_h = 0.034(8)$. Despite of a slight overestimation

configuration, only the TO phonons should be visible[26,27]. Nevertheless, the presence of LO modes can be attributed to possible geometric deviations (e.g. not completely planar nanowires), the finite detection angle, as well as the possible roughness of the shell surface. The Raman spectrum is similar in $x(y,y)\bar{x}$ configuration (bottom plot in Fig. 1e), i.e. with excitation

                                                                                                                          ARTICLE

(underestimation) of ε_{zz} (ε_{xx}), the values are in reasonable agreement with the results from elasticity theory in Table 1. Because of the low intensity of the TO_d peak, though, it was difficult to repeat the measurement of ω_{TO_d} on many nanowires. For this reason, the statistical sampling relied exclusively on measurements of ω_{TO_s} and the use of Eq. 2, knowing from elasticity theory that $\varepsilon_{xx} \approx 0.15\,\varepsilon_{zz}$. The results for both uncapped and capped nanowires are listed in Table 1. It is worthwhile to mention that owing to the three-dimensional stress in the core, the ratio of $-\varepsilon_{xx}/\varepsilon_{zz}$ is negative, in contrast to the positive Poisson's ratio of 0.16 for uniaxially stressed GaAs nanowires[26].

It is well known that the hydrostatic strain in GaAs changes the bandgap, whereas the shear strain separates the valence bands of heavy and light holes at the Γ-point of the Brillouin zone, lifting the degeneracy that characterises the unstrained GaAs[17,18,26,32]. Here, the optical bandgap of the tensile-strained core for both uncapped and capped nanowires was measured by photoluminescence (PL) spectroscopy to be in the range of 1.1 eV at room temperature (to be discussed in more detail in the following), i.e. ~0.3 eV lower than the expected value for unstrained GaAs (1.453 eV) assuming the same radial confinement. These values are in good agreement with our 8-band $\mathbf{k \cdot p}$ calculations (using nextnano) shown in Fig. 2a, where the simulated band-edge profiles at the Γ-point of the Brillouin zone across the core/shell heterostructure at 300 K for both samples are plotted. The core of the uncapped (capped) nanowires has an optical bandgap of 1.136 eV (1.071 eV) and is surrounded by the shell of 1.862 (1.695) eV. The capping shell has been considered to have an effective thickness of 3 nm after oxidation of the outer 2 nm, which results in an optical bandgap of 1.075 eV. The calculations were performed along the [1$\bar{1}$0] crystallographic direction, i.e. normal to the nanowire sidewalls and through the core centre (zero position).

Besides bandgap narrowing, a reduction of the electron effective mass in the tensile-strained core is also expected[18]. Our calculations shown in Fig. 2b (energy dispersion around the Γ-point) predict a reduction of the effective mass of electrons from 0.067 m_0 for unstrained GaAs to 0.0514 m_0 (0.0498 m_0) for the strained GaAs core in the uncapped (capped) nanowires. The general dependence of the electron effective mass in the GaAs core on the In-content of the $In_xAl_{1-x}As$ shell and the corresponding core/shell misfit is plotted in Fig. 2c. In the following, we will show that electrons in the strained core exhibit high mobility values, well above the previously reported ones for unstrained GaAs nanowires, as well as for bulk GaAs.

Electron transport properties. The transport properties of electrons in the core/shell nanowires were probed at room temperature by OPTPS. The particular method has been established in recent years as a reliable way to measure electron transport and dynamics in nanowires[21,33–35]. The basic principle is schematically described in Fig. 3a. Nanowires were transferred from their Si substrate onto z-cut quartz, which is transparent for the THz radiation in the range of 0–3.8 THz[14]. The transfer method (rubbing of quartz against the as-grown sample) aimed at obtaining lying nanowires on quartz, with their axes oriented along the same direction. As it is shown in the dark-field optical microscopy image in Fig. 3a, this was roughly the case for the majority of the nanowires, but not for all of them (see Supplementary Note 3). Nevertheless, we will be referring to the average orientation of the majority of the nanowires in the following for the description of our measurements and analyses. An optical-pump pulse with an average photon energy of 1.55 eV, pump fluence of 70 μJ cm^{-2}, pulse duration of 60 fs and polarisation parallel to the nanowire axes generates electrons and holes only

inside the GaAs core and the $In_{0.44}Ga_{0.56}As$ capping shell (multi-photon generation of charge carriers in the $In_xAl_{1-x}As$ shell for $x = 0.37$ or 0.43 is negligible). After a delay time τ, THz pulses in the frequency range of $\omega/2\pi = 0.2$–2.7 THz, with polarisation that can be set either parallel or perpendicular to the nanowire axes, are transmitted through the sample, driving plasmon oscillations of the photo-generated carriers. Time-domain THz spectroscopy allows for measuring the complex conductivity spectrum $\Delta\sigma(\omega,\tau)$, which carries information about the dynamics of the average density $n(\tau)$ and the average mobility $\mu_e(\tau)$ of the photo-generated electrons in the probed ensemble of nanowires (the contribution from the much heavier holes is neglected). Comparative measurements on uncapped and capped nanowires allowed us to distinguish between the contributions from electrons in the core and the capping shell. More details about the OPTPS setup are given in Methods.

Figure 3b shows the complex photoconductivity spectra $\Delta\sigma(\omega)$ for two selected time delays (0 and 100 ps) and for two polarisation directions of the THz pulse (parallel and perpendicular to the nanowire axes). The characteristic peak in the real part of $\Delta\sigma(\omega)$ is the signature of localised surface plasmons (LSP) in the nanowires. For both delay times, the conductivity signal for the parallel THz polarisation is almost one order of magnitude higher than that for the perpendicular one. This result manifests that only the lowest-order longitudinal LSP mode along the [111] nanowire axis is excited by the THz probe, in agreement with previous reports[14,33,35,36]. This is true independent of the presence of a capping shell or the actual value of x (here, an auxiliary sample with capped nanowires with $x = 0.49$ was measured). The sensitivity only to the longitudinal LSP mode means that the nanowires that are not exactly parallel to the THz polarisation will just contribute less to the conductivity signal[35].

The conductivity spectra $\Delta\sigma(\omega)$ at a given τ can be fitted with an LSP model (the contribution of unintentional dopants is neglected) using a Lorentzian function of the form[33]

$$\Delta\sigma(\omega) = \frac{ine^2\omega}{m_e^*\left(\omega^2 - \omega_0^2 + i\omega\gamma\right)},\qquad(4)$$

where the electron density n is equal to

$$n = \frac{m_e^*\varepsilon_r\varepsilon_0}{ge^2}\omega_0^2.\qquad(5)$$

In these equations, ω_0 is the surface plasmon resonance frequency (i.e. the peak position of Re $\Delta\sigma(\omega)$), γ is the momentum scattering rate of electrons (which is associated with the peak width of Re $\Delta\sigma(\omega)$), m_e^* is the electron effective mass, e is the electronic charge, g is the geometrical factor and $\varepsilon_r = 14.16$ and ε_0 is the electric permittivity of the strained nanowire core and the free space in the THz range, respectively[37–39]. The fitted conductivity spectra are shown with continuous curves in Fig. 3b, where ω_0 and γ are the only fitting parameters. Finally, the electron mobility μ_e is calculated from ref. [33]

$$\mu_e = \frac{e}{m_e^*\gamma}.\qquad(6)$$

The model assumes that the peak width of Re $\Delta\sigma(\omega)$ is dictated only by the value of γ. In practice though, we have observed that the peak can be additionally broadened when ensembles of nanowires with a higher number density are measured (for a higher signal-to-noise ratio), where inevitably some of the nanowires are in close proximity or even in contact with others. An example is shown in Fig. 3c (capped nanowires with $x = 0.43$), where measurements performed on two locations with different number density of nanowires on the same sample are compared (for the same carrier concentration; $\tau = 70$ ps). The peak width of
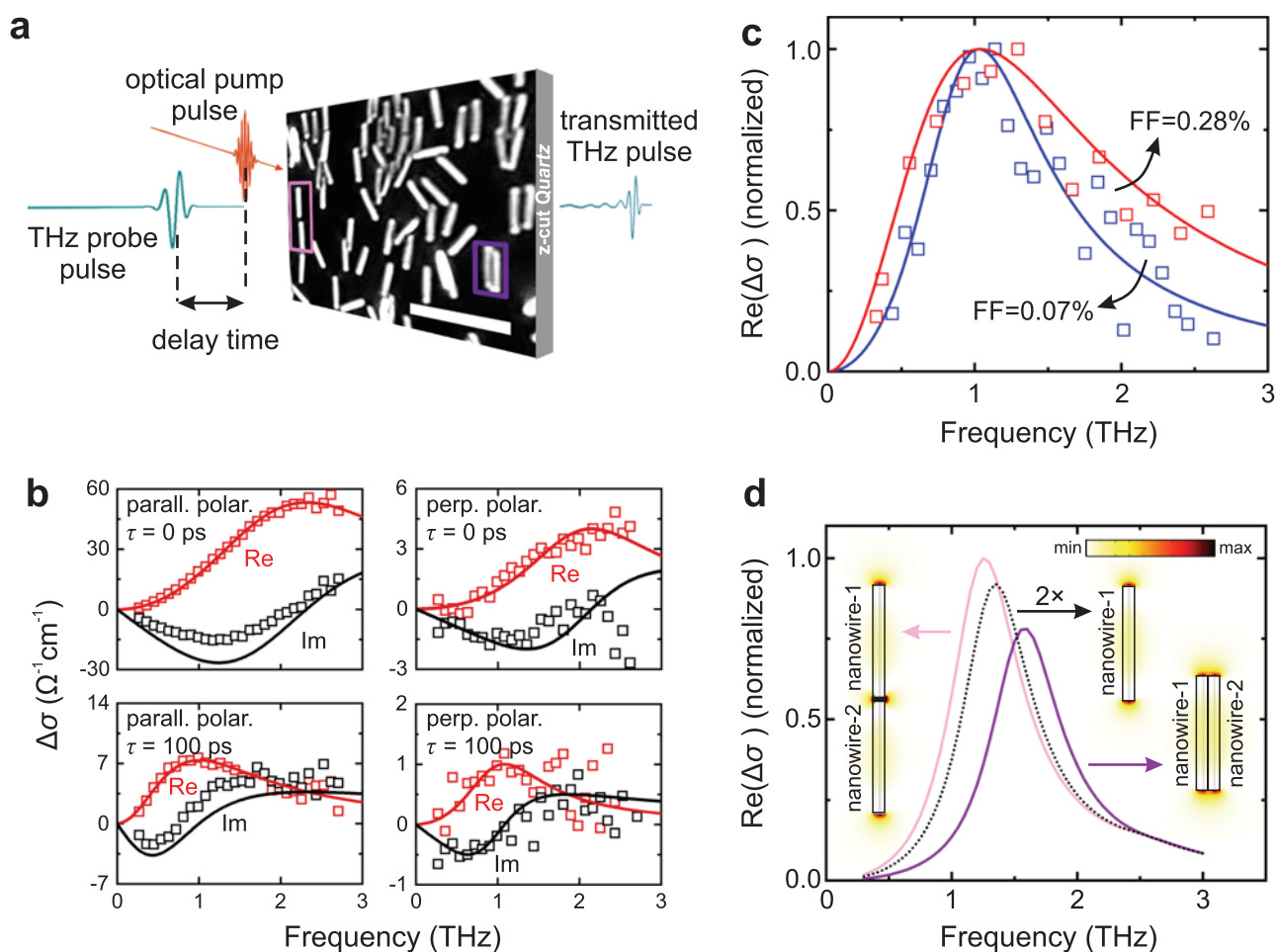
Fig. 3 Basic description and characteristics of optical-pump THz-probe spectroscopy measurements on core/shell nanowires. a Schematic description of the basic principle of the method. All measurements were performed at room temperature. The optical microscopy image shows transferred nanowires on z-cut quartz and was acquired with 100× magnification in dark-field mode. Two examples of nanowires in close proximity are indicated with pink (nanowires in a row) and purple (nanowires side-by-side) frames. The scale bar corresponds to 5 μm. **b** Photoconductivity spectra from capped GaAs/ In$_{0.49}$Al$_{0.51}$As nanowires at selected pump-probe delays (0 and 100 ps) and different polarisations of the THz-probe pulse (parallel and perpendicular to the nanowires). The real part is shown in red symbols and the imaginary part in black symbols. The lines are fits to the data using the localised surface plasmon (LSP) model described in Eqs. 4 and 5. **c** Real part of the photoconductivity spectra ($\tau = 70$ ps) from two areas with the different number density of capped GaAs/In$_{0.43}$Al$_{0.57}$As nanowires on the same sample. The corresponding filling factor (FF) was 0.28% (red symbols) and 0.07% (blue symbols). The lines are LSP model fits. **d** Calculated (by COMSOL) real part of the photoconductivity spectra of two distant (black curve) or two grouped photo-doped GaAs/In$_{0.44}$Al$_{0.56}$As nanowires in two different configurations (pink and purple curves), as shown in the insets. The spectra are normalised to the highest value. The two configurations of grouped nanowires resemble those of the framed nanowires in (**a**). The simulated component of the THz-probe electric field (modulus) along the nanowire axis is also shown in the insets as a colour plot. The colour scale ranges from 0 to 10 V m^{-1} (the probe field was set to be 1 V m^{-1} far away from the nanowires).

Re $\Delta\sigma(\omega)$ is 70% larger for measurements on the dense area (filling factor FF = 0.28%, 1.84 THz) compared to those on the sparse one (FF = 0.07%, 1.08 THz). Consequently, the deduced mobility from Eq. 6 appears to be 41% lower in the dense area. This means that the extracted electron mobility from OPTPS can generally be regarded as a lower limit for the real value of an isolated nanowire. The accuracy of the method improves for samples with lower number densities of nanowires, where the probability to have nanowires in close proximity or in contact with each other is lower.

If two or more nanowires are very close or even touch each other, they form different geometries that generally have different plasmon resonances. To analyse the effect of the nanowire proximity on the conductivity spectra, we numerically modelled the plasmonic response of two photo-doped GaAs/In$_{0.44}$Al$_{0.56}$As NWs in an external electric field (which plays the role of a THz-probe) using COMSOL. The two nanowires were positioned in

three simple configurations (shown as insets in Fig. 3d): in a row along their axes, side-by-side, or in large distance (isolated) from each other. As shown in Fig. 3d, if the two nanowires are positioned in a row, the simulated peak position is shifted to lower frequencies (pink curve) compared to the isolated nanowires (black dotted curve). In contrast, if the nanowires are positioned side-by-side, the peak position is shifted to higher frequencies (purple curve). In Fig. 3a, examples of grouped nanowires that are similar to the simulated configurations are framed with the corresponding colours. Considering that OPTPS measurements are performed on large ensembles of randomly positioned nanowires, where isolated and grouped nanowires coexist, the Re $\Delta\sigma(\omega)$ spectrum is expected to be inhomogeneously broadened owing to the superposition of peaks from both isolated and grouped nanowires. The arrangement and number density of nanowires cannot be measured at the exact location of OPTPS measurements. However, the number density can be

ARTICLE
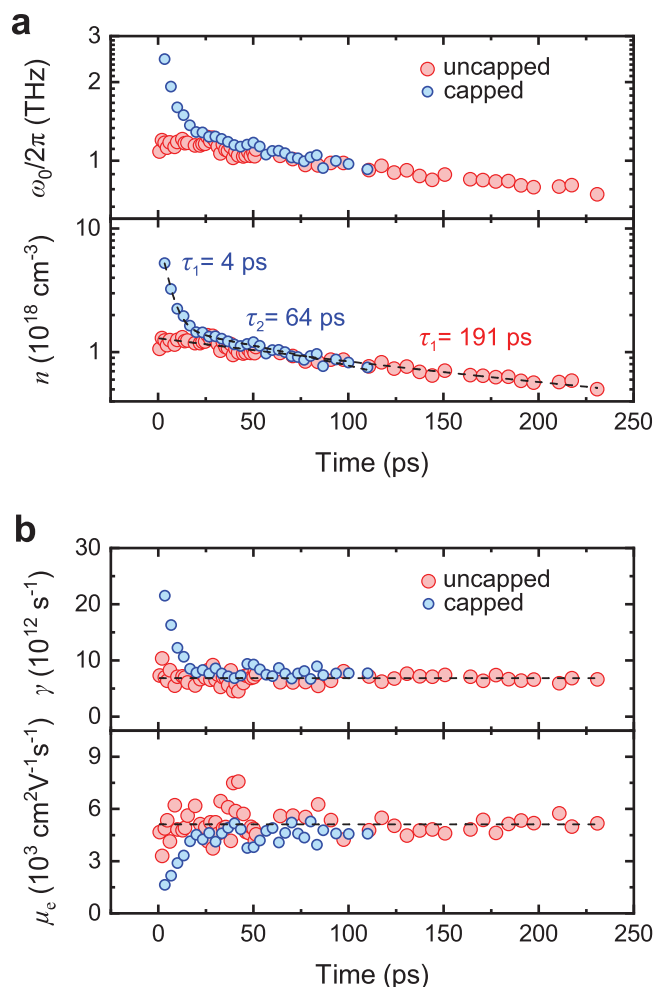
Fig. 4 Analysis of electron transport dynamics inside GaAs/In$_{0.37}$Al$_{0.63}$As (uncapped) and GaAs/In$_{0.43}$Al$_{0.57}$As/In$_{0.44}$Ga$_{0.56}$As (capped) nanowires based on optical-pump THz-probe spectroscopy measurements at room temperature. a Temporal evolution of plasmon frequency ω_0 (top) and the associated electron density n (bottom). The dashed lines are mono-exponential and bi-exponential fits for the uncapped and capped nanowires, respectively. **b** Temporal evolution of momentum scattering rate γ (top) and the associated mobility μ_e (bottom) of electrons. The dashed lines are linear fits for the uncapped nanowires.

Fig. 5 Study of charge carrier dynamics in the core of GaAs/In$_{0.37}$Al$_{0.63}$As (uncapped) and GaAs/In$_{0.43}$Al$_{0.57}$As/In$_{0.44}$Ga$_{0.56}$As (capped) core/shell nanowires at room temperature. a Time-resolved photoluminescence spectroscopy scan from uncapped nanowires. **b** Integrated photoluminescence intensity (normalised) as a function of time for uncapped (red curve) and capped (blue curve) nanowires. The data have been fitted with mono-exponential (uncapped nanowires) and bi-exponential (capped nanowires) decay functions (black curves), and the resulting lifetimes are indicated.

estimated from the $\Delta\sigma(\omega)$ intensity and the fitted FF or by using optical microscopy on the same area of the sample after the OPTPS measurements. Although the number density of nano-wires alone does not strictly reflect the level of nanowire grouping, a larger inhomogeneous broadening can generally be expected for denser ensembles, in agreement with the results in Fig. 3c. Furthermore, the inhomogeneous broadening in Fig. 3c is more pronounced on the high-frequency wing of the LSP peak, suggesting a stronger contribution from nanowires that are grouped side by side.

The analysis of the conductivity spectra was repeated for different delay times and the results are shown in Fig. 4 for uncapped (red data points) and capped (blue data points) core/shell nanowires. The measurements were performed on relatively sparse ensembles of nanowires to minimise the inhomogeneous plasmon broadening effect. Unavoidably, the resulting signal-to-noise ratio was quite low even for the relatively high pump fluence of 70 μJ cm^{-2} that was used. Thus, a reliable analysis was possible only within the first few hundreds of ps of delay time. Figure 4a shows the monotonic decrease of ω_0 and the

corresponding n as a function of time, which is the result of the recombination of photo-generated electrons in the core of the uncapped nanowires or in both the core and the capping shell of the capped nanowires. An apparent difference between the two types of nanowires is the higher n at zero delay time and its faster decay within the first 40 ps in capped nanowires. This is attributed to the photo-generation of electrons in the capping shell and, subsequently, their fast recombination at the free-surface states, similar to reports for GaAs/Al$_{0.4}$Ga$_{0.6}$As/GaAs core/shell/capping-shell nanowires[16]. After the first few tens of ps, the decay rate of n in capped nanowires becomes slower, i.e. more representative of electrons in the core.

The experimental data for the uncapped nanowires are best fitted with a mono-exponential decay function, considering only monomolecular recombination, i.e. $dn/dt \propto n$. The electron lifetime is deduced to be 191 ps. In any case, bimolecular and Auger recombination in GaAs are negligible in the range of $n = 10^{17}$–10^{18} cm^{-3} [40]. Similar carrier dynamics were observed in time-resolved PL measurements. Figure 5a shows the measured

spectra at room temperature with excitation energy of 1.55 eV. As shown in Fig. 5b (red curve), the integrated PL signal is also fitted as a mono-exponential decay with a lifetime of 147 ps.

According to previous reports[41,42], electron dynamics in such thin nanowires is governed by recombination at the core/shell interface. The corresponding interface recombination velocity S for electrons in the core can be deduced from[43]

$$\frac{1}{\tau_{\text{core}}} = \frac{1}{\tau_{\text{volume}}} + \frac{2S}{R}, \qquad (7)$$

where R is the core radius, τ_{core} is the measured lifetime (191 ps by OPTPS or 147 ps by PL), and τ_{volume} is the time constant for recombination in the core excluding the effect of the core/shell interface. Using $\tau_{\text{volume}} = 1.6 - 2.5$ ns according to reports on passivated unstrained GaAs nanowires[16,41], S is estimated to be in the range of $2.8 - 4.0 \times 10^3$ cm s^{-1}. The fact that similar values have been reported for lattice-matched core/shell nanowires with GaAs core[41,44] points to the high quality of the GaAs/In$_{0.37}$Al$_{0.63}$As interface despite of the large lattice mismatch. It should not be excluded though that the low value of S may also be a result of the saturation of interface traps under the particular pump fluence used here[42].

The dynamics of electrons in the capped nanowires is more complex. OPTPS in Fig. 4a (blue points) combined with time-resolved PL in Fig. 5b (blue curve; see the full scan in Supplementary Note 4) reveal the existence of three distinct lifetimes of 4, 62–64 and 151 ps. It should be mentioned that the longest lifetime of 151 ps is not seen in OPTPS because of the restricted time range of 0–100 ps (the signal-to-noise ratio becomes too low after that because of the low density of the nanowire ensemble), whereas the shortest lifetime of 4 ps is not resolved in PL owing to the limited temporal resolution of the experimental setup. Concerning their origin, the lifetime of 151 ps is similar to that in uncapped nanowires and, thus, it is attributed to electrons in the strained GaAs core. On the other hand, the shorter lifetimes of 4 and 62–64 ps, which were not observed in uncapped nanowires, probably correspond to the capture of electrons in the In$_{0.44}$Ga$_{0.56}$As capping shell via saturable surface traps and non-saturable recombination channels, respectively[14,33].

Figure 4b shows the dynamics of the scattering rate of electrons γ, as extracted from OPTPS measurements at different delay times, and the corresponding mobility μ_e from Eq. 6, where the previously calculated value of m_e^* (0.0514 m_0 for uncapped and 0.0498 m_0 for capped nanowires) was used for the strained core. As it is observed, electrons in the core of the uncapped nanowires exhibit quite stable values in the range of $\gamma = 6.8 \times 10^{12}$ s^{-1} and $\mu_e = 5100$ cm^2 V^{-1} s^{-1}. On the other hand, a temporal variation is observed for the capped nanowires as a result of the combined contribution of electrons in the strained core and the capping shell. Owing to the strong electron scattering at the free surface of the capping shell, higher γ and, consequently, lower μ_e values are measured just after the pump pulse, i.e. for $\tau \approx 0$ (electrons with the same value of m_e^* in both the strained GaAs core and the unstrained In$_{0.44}$Ga$_{0.56}$As shell[45] have been assumed). Within the first 40 ps, though, the population of electrons in the capping shell decreases fast (recall the short lifetimes) and the contribution of electrons in the core dominates, exhibiting γ and μ_e values similar to those in uncapped nanowires.

Combining the data in Fig. 4a, b, the dependence of γ and the corresponding μ_e on n is deduced, as shown in Fig. 6 (red symbols). Here, only the results for uncapped nanowires, thus for electrons in the core, are shown. For comparison, OPTPS measurements were also performed on GaAs/Al$_{0.35}$Ga$_{0.65}$As/GaAs core/shell/capping-shell nanowires of similar dimensions
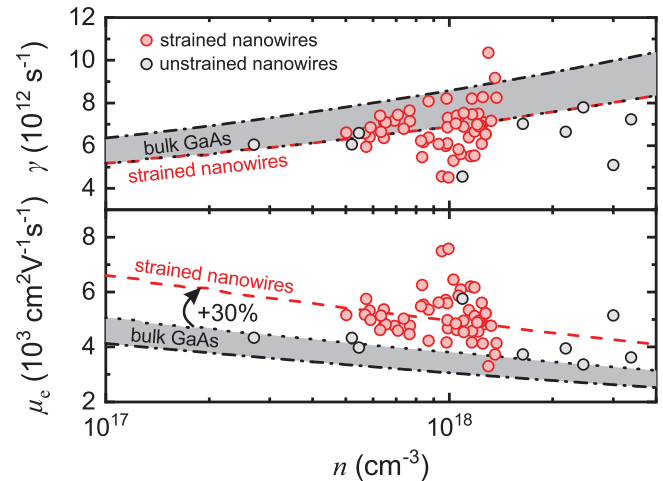
Fig. 6 Momentum scattering rate γ (top) and the associated mobility μ_e (bottom) of electrons as a function of electron density n inside the strained core of uncapped GaAs/In$_{0.37}$Al$_{0.63}$As core/shell nanowires (red symbols) and the unstrained core of GaAs/Al$_{0.35}$Ga$_{0.65}$As/GaAs core/shell/capping-shell nanowires (grey symbols). All data originate from optical-pump THz-probe spectroscopy (OPTPS) measurements at room temperature. For comparison, OPTPS data (fitted by the Caughey-Thomas relation) for undoped bulk GaAs from refs. [46] (black dotted curve) and [48] (black dash-dotted curve) are also shown. The grey-shaded area covers all values between the two reference curves. The red dashed curves describe the results for strained nanowires.

(22 nm thick core, 80 nm thick shell, 5 nm thick capping shell). In this case, the core is unstrained and the results for the electrons therein are also shown in Fig. 6 (grey symbols). Furthermore, OPTPS data for bulk GaAs from the literature[46–48] are also plotted (black dotted and dash-dotted lines; the data were either directly copied or calculated using Eq. 6). The shadowed area in the plot covers all values between those in ref. [46] (black dotted line) and ref. [48] (black dash-dotted line).

Concerning γ (top plot in Fig. 6), both strained and unstrained nanowires exhibit average values close to the lowest reported ones for bulk GaAs. This means that neither the decrease of electron effective mass in strained nanowires nor the thin diameter (large surface-to-volume ratio) of the core affect significantly, if at all, the total scattering rate of electrons. Let us now discuss what this means for the individual scattering mechanisms that are relevant here. Typically, the scattering of electrons by LO phonons (Fröhlich interaction) is the dominant scattering mechanism in undoped bulk GaAs at room temperature. Scattering rates of ~3×10^{12} s^{-1}, which correspond to mobility values of ~8700 cm^2 V^{-1} s^{-1}, have been reported[49]. In OPTPS measurements, though, also the scattering of electrons by holes becomes important because equal densities of electrons and holes are photo-generated. This explains the relatively higher (lower) values of scattering rate (mobility), as well as their increase (decrease) with n, shown in Fig. 6 for bulk GaAs[16,47,48]. Furthermore, the scattering of electrons at the core/shell interface (by crystal defects, interface roughness, and other imperfections) may also come into play for nanowires with a thin core. In the end, the total scattering rate γ can be approximated by Matthiessen's rule as[50]

$$\gamma = \gamma_{\text{p}} + \gamma_{\text{h}} + \gamma_{\text{i}}, \qquad (8)$$

where γ_{p}, γ_{h} and γ_{i} are the individual scattering rates of electrons by bulk LO phonons, photo-generated holes and the core/shell interface, respectively. Using the data for bulk GaAs ($\gamma = 7$–8 $\times 10^{12}$ s^{-1} and $\gamma_{\text{p}} \approx 3 \times 10^{12}$ s^{-1})[46,48,49] in Eq. 8, we obtain

      ARTICLE

$\gamma_h = 4$–$5 \times 10^{12}\,\text{s}^{-1}$, i.e. comparable scattering rates by holes and LO phonons. Assuming that the same γ_p and γ_h values also exist in unstrained nanowires (confined or interface phonons are neglected for the particular core radius[51,52]), the similar total scattering rates found for unstrained nanowires and bulk GaAs suggest that the interface scattering is negligible: $\gamma_i \ll \gamma_p + \gamma_h$. This result is reasonable for a longitudinal LSP mode because the transport of electrons is parallel to the core/shell interface. In tensile-strained nanowires, γ_p and γ_h should be affected as follows: the decrease of m_e^* from 0.067 to 0.0514 should result in a 12% decrease of γ_p compared to unstrained nanowires and bulk GaAs because γ_p is proportional to $m_e^{*1/2}$[49,53,54]. On the other hand, γ_h is expected to increase by a similar percentage because it is inversely proportional to the reduced mass of electrons and holes: $\gamma_h \propto \left(m_e^{*-1} + m_h^{*-1} \right)^{1/2}$ (as described by the equation for scattering by ionised impurities[47,54–56]). A further increase of γ_h could result from the higher concentration of heavy holes compared to light holes in strained nanowires because of the valence band splitting. After all, the effect of strain on the total scattering rate γ must be limited because of the counterbalancing of the decreased γ_p by the increased γ_h. Indeed, although the scattering of OPTPS data in Fig. 6 obscures any small changes in γ, no obvious dependence on strain can be resolved.

The corresponding mobility values μ_e are shown in the bottom plot of Fig. 6. The values for unstrained GaAs nanowires are the highest reported so far, which we consider a consequence of both the high structural quality of the nanowires and the minimisation of the inhomogeneous plasmon broadening in sparse nanowire ensembles, and agree well with the highest reported ones for bulk GaAs[46]. Most important though, the strained nanowires exhibit even higher values by a factor of 1.3 (this is equal to the effective mass ratio 0.067/0.0514). This is because they have similar γ but lower m_e^* compared to unstrained nanowires and bulk GaAs. It is remarkable that high average values in the range of 5500–4800 cm^2 V^{-1} s^{-1} for electron densities of 5–14×10^{17} cm^{-3} are obtained for a core diameter as small as 22 nm, i.e. approximately only twice the exciton Bohr radius in GaAs. This implies a high structural quality of the core/shell interface and its minor influence on the electron transport along the nanowire axis. Furthermore, the electron mobility without the scattering of electrons by holes, which is an inherent effect of the photoexcitation in OPTPS, can be estimated from Eq. 6 after setting $\gamma = (0.0514/0.067)^{1/2} \cdot \gamma_p$ (where $\gamma_p \approx 3 \times 10^{12}$ s^{-1} is the value for bulk GaAs[49]). This results in μ_e in the range of 13,000 cm^2/Vs, i.e. an increase of 50% with respect to bulk GaAs.

Discussion

Our results demonstrate that the reduction of the electron effective mass inside the hydrostatically tensile-strained core of GaAs/In$_{0.37}$Al$_{0.63}$As core/shell nanowires causes a significant enhancement of mobility. The relative increase of mobility with respect to unstrained nanowires and bulk GaAs was measured by OPTPS equal to 30%. A larger increase of 50% is predicted, if the scattering of electrons by photo-generated holes (which is an inherent effect in OPTPS) is excluded, as it would also be the case for high-electron-mobility transistors. It is anticipated that even larger mobility values can be achieved in nanowires with larger lattice mismatch (higher In-content in the shell). The epitaxial growth of In$_x$Ga$_{1-x}$As nanowires with high x would be a more direct approach to obtain high electron mobility with III-arsenides on Si, but this is challenging (excluding Au-catalysed methods as incompatible with Si CMOS) because of either the limited incorporation of In into the nanowire crystal in Ga-catalysed growth[57,58] or the high density of stacking faults in

selective area growth[59]. The distinct enhancement of charge carrier mobility shown here is of major importance for the realisation of transistors with high speed and low-power consumption, having the potential to trigger major advancements in high-performance nanowire electronic devices. It is also important that GaAs is anyway among the semiconductors with the highest electron mobilities and that GaAs nanowires can be monolithically integrated in heterogeneous platforms like Si CMOS. Nevertheless, the findings from this work are not only relevant for GaAs, but can also give important guidelines for strained core/shell nanowires made from other semiconductor systems.

Methods

Optical-pump THz-probe spectroscopy. The setup is based on a Ti:sapphire femtosecond amplifier (Coherent RegA) operating at a repetition rate of 250 kHz. The pulse duration is ~60 fs and the central wavelength is 800 nm (photon energy of 1.55 eV). The broadband THz-probe pulses are generated using a large-area photoconductive GaAs emitter biased by a modulated voltage and focused onto the sample by an off-axis parabolic mirror with a focal length of 10 cm. The FWHM THz spot size is estimated to be 0.7–0.8 mm. The probe pulses transmitted through the sample are detected via electro-optic sampling in a (110) ZnTe crystal. The optical-pump beam is modulated by an optical chopper and focused by a lens at a point located far behind the sample. The resulting pump spot FWHM size at the sample is 1.7 mm—more than the doubled THz spot size. In this way, we ensure homogeneous photoexcitation conditions. The photo-induced change in the transmitted THz field is measured using a double demodulation technique by two lock-in amplifiers.

Time-resolved photoluminescence spectroscopy. The excitation source is a Ti:sapphire laser at 1.55 eV photon energy. The fluence is ~8 μJ cm^{-2} with a spot diameter of 20 μm. The pulse length is 2 ps. The photoluminescence is collected with a 100× objective and dispersed in a spectrometer (100 grooves mm^{-1}). The photoluminescence is measured with a streak camera with a time resolution of 9 ps.

Reporting Summary. Further information on research design is available in the Nature Research Reporting Summary linked to this article.

Data availability

The data that support the findings of this study are available from the corresponding author upon reasonable request.

References

1. Gu, J. J. et al. 20–80nm Channel length InGaAs gate-all-around nanowire MOSFETs with EOT=1.2nm and lowest SS=63mV/dec. *International Electron Devices Meeting*; 2012 Dec 10–13; San Francisco, CA, USA. IEEE; 2012.
2. Egard, M. et al. Vertical InAs nanowire wrap gate transistors with f(t) > 7 GHz and f(Max) > 20 GHz. *Nano Lett.* **10**, 809–812 (2010).
3. Colinge, J. P. et al. Nanowire transistors without junctions. *Nat. Nanotechnol.* **5**, 225–229 (2010).
4. Heinzig, A., Slesazeck, S., Kreupl, F., Mikolajick, T. & Weber, W. M. Reconfigurable silicon nanowire transistors. *Nano Lett.* **12**, 119–124 (2012).
5. Riel, H., Wernersson, L. E., Hong, M. W. & del Alamo, J. A. III-V compound semiconductor transistors-from planar to nanowire structures. *MRS Bull.* **39**, 668–677 (2014).
6. Morkötter, S. et al. Demonstration of confined electron gas and steep-slope behavior in delta-doped GaAs-AlGaAs core-shell nanowire transistors. *Nano Lett.* **15**, 3295–3302 (2015).
7. Chuang, S. et al. Ballistic InAs nanowire transistors. *Nano Lett.* **13**, 555–558 (2013).
8. Gooth, J. et al. Ballistic one-dimensional InAs nanowire cross-junction interconnects. *Nano Lett.* **17**, 2596–2602 (2017).
9. Heedt, S., Prost, W., Schubert, J., Grützmacher, D. & Schäpers, T. Ballistic transport and exchange interaction in InAs nanowire quantum point contacts. *Nano Lett.* **16**, 3116–3123 (2016).
10. van Weperen, I., Plissard, S. R., Bakkers, E. P. A. M., Frolov, S. M. & Kouwenhoven, L. P. Quantized conductance in an InSb nanowire. *Nano Lett.* **13**, 387–391 (2013).

11. Irber, D. M. et al. Quantum transport and sub-band structure of modulation-doped GaAs/AlAs core-superlattice nanowires. *Nano Lett.* **17**, 4886–4893 (2017).
12. Tomioka, K., Yoshimura, M. & Fukui, T. A III–V nanowire channel on silicon for high-performance vertical transistors. *Nature* **488**, 189 (2012).
13. Hong, Y. J. et al. Van der Waals epitaxial double heterostructure: InAs/single-layer graphene/InAs. *Adv. Mater.* **25**, 6847–6853 (2013).
14. Joyce, H. J. et al. The influence of surfaces on the transient terahertz conductivity and electron mobility of GaAs nanowires. *J. Phys. D. Appl. Phys.* **50**, 224001 (2017).
15. Joyce, H. J. et al. Electronic properties of GaAs, InAs and InP nanowires studied by terahertz spectroscopy. *Nanotechnology* **24**, 214006 (2013).
16. Joyce, H. J. et al. Electron mobilities approaching bulk limits in "surface-free" GaAs nanowires. *Nano Lett.* **14**, 5989–5994 (2014).
17. Balaghi, L. et al. Widely tunable GaAs bandgap via strain engineering in core/shell nanowires with large lattice mismatch. *Nat. Commun.* **10**, 2793 (2019).
18. Christensen, N. E. Electronic-structure of GaAs under strain. *Phys. Rev. B* **30**, 5753–5765 (1984).
19. Conesa-Boj, S. et al. Boosting hole mobility in coherently strained [110]-oriented Ge-Si core-shell nanowires. *Nano Lett.* **17**, 2259–2264 (2017).
20. Wen, F. & Tutuc, E. Enhanced electron mobility in nonplanar tensile strained Si epitaxially grown on SixGe1-x nanowires. *Nano Lett.* **18**, 94–100 (2018).
21. Joyce, H. J., Boland, J. L., Davies, C. L., Baig, S. A. & Johnston, M. B. A review of the electrical properties of semiconductor nanowires: insights gained from terahertz conductivity spectroscopy. *Semicond. Sci. Tech.* **31**, 103003 (2016).
22. Bergamaschini, R., Montalenti, F. & Miglio, L. Sunburst pattern by kinetic segregation in core-shell nanowires: a phase-field study. *Appl. Surf. Sci.* **517**, 146056 (2020).
23. Tauchnitz, T. et al. Decoupling the two roles of Ga droplets in the self-catalyzed growth of GaAs nanowires on SiOx/Si(111) substrates. *Cryst. Growth Des.* **17**, 5276–5282 (2017).
24. Birner, S. et al. nextnano: general purpose 3-D simulations. *IEEE Trans. Electron Dev.* **54**, 2137–2142 (2007).
25. Milekhin, A. G. et al. Vibrational spectroscopy of InAlAs epitaxial layers. *J. Appl. Phys.* **104**, 073516 (2008).
26. Signorello, G., Karg, S., Björk, M. T., Gotsmann, B. & Riel, H. Tuning the light emission from GaAs nanowires over 290 meV with uniaxial strain. *Nano Lett.* **13**, 917–924 (2013).
27. Zardo, I. et al. Raman spectroscopy of wurtzite and zinc-blende GaAs nanowires: polarization dependence, selection rules, and strain effects. *Phys. Rev. B* **80**, 245324 (2009).
28. Montazeri, M. et al. Direct measure of strain and electronic structure in GaAs/GaP core-shell nanowires. *Nano Lett.* **10**, 880–886 (2010).
29. Wickboldt, P., Anastassakis, E., Sauer, R. & Cardona, M. Raman phonon piezospectroscopy in GaAs: infrared measurements. *Phys. Rev. B* **35**, 1362–1368 (1987).
30. Menéndez, J., Singh, R. & Drucker, J. Theory of strain effects on the Raman spectrum of Si-Ge core-shell nanowires. *Ann. Phys.* **523**, 145–156 (2011).
31. Cerdeira, F., Buchenauer, C. J., Cardona, M. & Pollak, F. H. Stress-induced shifts of first-order Raman frequencies of diamond and zinc-blende-type semiconductors. *Phys. Rev. B-Solid St.* **5**, 580 (1972).
32. Van de Walle, C. G. Band lineups and deformation potentials in the model-solid theory. *Phys. Rev. B* **39**, 1871–1883 (1989).
33. Fotev, I. et al. Electron dynamics in InxGa1-xAs shells around GaAs nanowires probed by terahertz spectroscopy. *Nanotechnology* **30**, 244004 (2019).
34. Lang, D. et al. Nonlinear plasmonic response of doped nanowires observed by infrared nanospectroscopy. *Nanotechnology* **30**, 084003 (2019).
35. Rana, R. et al. Nonlinear charge transport in InGaAs nanowires at terahertz frequencies. *Nano Lett.* **20**, 3225–3231 (2020).
36. Strait, J. H. et al. Measurements of the carrier dynamics and terahertz response of oriented germanium nanowires using optical-pump terahertz-probe spectroscopy. *Nano Lett.* **9**, 2967–2972 (2009).
37. Goni, A. R., Syassen, K., Strössner, K. & Cardona, M. Pressure-dependence of the direct optical gap and refractive-index of Ge and GaAs. *Semicond. Sci. Tech.* **4**, 246–247 (1989).
38. Samara, G. A. Temperature and pressure dependences of the dielectric-constants of semiconductors. *Phys. Rev. B* **27**, 3494–3505 (1983).
39. Vurgaftman, I., Meyer, J. R. & Ram-Mohan, L. R. Band parameters for III-V compound semiconductors and their alloys. *J. Appl. Phys.* **89**, 5815–5875 (2001).
40. Strauss, U., Rühle, W. W. & Köhler, K. Auger recombination in intrinsic GaAs. *Appl. Phys. Lett.* **62**, 55–57 (1993).
41. Demichel, O., Heiss, M., Bleuse, J., Mariette, H. & Fontcuberta i Morral, A. Impact of surfaces on the optical properties of GaAs nanowires. *Appl. Phys. Lett.* **97**, 201907 (2010).
42. Parkinson, P. et al. Carrier lifetime and mobility enhancement in nearly defect-free core-shell nanowires measured using time-resolved terahertz spectroscopy. *Nano Lett.* **9**, 3349–3353 (2009).
43. Demichel, O. Surface recombination velocity measurements of efficiently passivated gold-catalyzed silicon nanowires by a new optical method. *Nano Lett.* **10**, 2323–2329 (2010).
44. Chia, A. C. E. et al. Electrical transport and optical model of GaAs-AlInP core-shell nanowires. *J. Appl. Phys.* **111**, 094319 (2012).
45. Adachi, S. I. I. I.-V. ternary and quaternary compounds. In: Kasap S, Capper P, editors. Springer handbook of electronic and photonic materials. Cham: Springer; 2017.
46. Mics, Z., D'Angio, A., Jensen, S. A., Bonn, M. & Turchinovich, D. Density-dependent electron scattering in photoexcited GaAs in strongly diffusive regime. *Appl. Phys. Lett.* **102**, 231120 (2013).
47. Nuss, M. C., Auston, D. H. & Capasso, F. Direct subpicosecond measurement of carrier mobility of photoexcited electrons in gallium-arsenide. *Phys. Rev. Lett.* **58**, 2355–2358 (1987).
48. Sharma, G. et al. Carrier density dependence of the nonlinear absorption of intense THz radiation in GaAs. *Opt. Express* **20**, 18016–18024 (2012).
49. Liu, T. H., Zhou, J. W., Liao, B. L., Singh, D. J. & Chen, G. First-principles mode-by-mode analysis for electron-phonon scattering channels and mean free path spectra in GaAs. *Phys. Rev. B* **95**, 075206 (2017).
50. Saxena, A. K. & Mudares, M. A. L. Validity of Matthiessen's-rule for calculating electron-mobility in Ga1-xAlxAs alloys. *J. Appl. Phys.* **58**, 2795–2797 (1985).
51. Požela, J., Požela, K. & Jucienė, V. Scattering of electrons by confined interface polar optical phonons in a double-barrier heterostructure. *Semiconductors* **41**, 1074–1079 (2007).
52. Ferreira, R. & Bastard, G. Evaluation of some scattering times for electrons in unbiased and biased single-quantum-well and multiple-quantum-well structures. *Phys. Rev. B* **40**, 1074–1086 (1989).
53. Levi AFJ. Essential electron transport for device physics. New York: AIP Publishing; 2020.
54. Ridley, B. K. Quantum processes in semiconductors. (Oxford: Oxford Univ. Press; 2013).
55. Yu, P. & Cardona, M. Fundamentals of semiconductors. Berlin Heidelberg: Springer-Verlag; 2010.
56. Höpfel, R. A., Shah, J., Block, D. & Gossard, A. C. Picosecond time-of-flight measurements of minority electrons in GaAs/AlGaAs quantum-well structures. *Appl. Phys. Lett.* **48**, 148–150 (1986).
57. Dubrovskii, V. G. Understanding the vapor-liquid-solid growth and composition of ternary III-V nanowires and nanowire heterostructures. *J. Phys. D. Appl. Phys.* **50**, 453001 (2017).
58. Heiss, M. et al. In(Ga)As quantum dot formation on group-III assisted catalyst-free InGaAs nanowires. *Nanotechnology* **22**, 195601 (2011).
59. Treu, J. et al. Widely tunable alloy composition and crystal structure in catalyst-free InGaAs nanowire arrays grown by selective area molecular beam epitaxy. *Appl. Phys. Lett.* **108**, 053110 (2016).

Author contributions
L.B., F.M. and E.D. performed the Raman scattering and PL studies. T.V. performed the time-resolved PL. A.P. directed the OPTPS studies, which were carried out by I.F., S.S., R.R., F.M. and L.B. R.H. performed the TEM and EDXS measurements and analyses. E.D. directed the work, performed the growth experiments, and wrote the manuscript. All authors, together with T.M., H.S. and M.H. discussed the results and contributed to the manuscript preparation.

Competing interests
The authors declare no competing interests.

Additional information
Supplementary information The online version contains supplementary material available at https://doi.org/10.1038/s41467-021-27006-z.

Correspondence and requests for materials should be addressed to Emmanouil Dimakis.

Peer review information *Nature Communications* thanks the anonymous reviewer(s) for their contribution to the peer review of this work.

Reprints and permission information is available at http://www.nature.com/reprints

ARTICLE

RESEARCH ARTICLE

Enhanced Trion Emission in Monolayer MoSe₂ by Constructing a Type-I Van Der Waals Heterostructure

Juanmei Duan,* Phanish Chava, Mahdi Ghorbani-Asl, Denise Erb, Liang Hu, Arkady V. Krasheninnikov, Harald Schneider, Lars Rebohle, Artur Erbe, Manfred Helm, Yu-Jia Zeng, Shengqiang Zhou,* and Slawomir Prucnal*

Trions, quasi-particles consisting of two electrons combined with one hole or of two holes with one electron, have recently been observed in transition metal dichalcogenides (TMDCs) and drawn increasing attention due to potential applications of these materials in light-emitting diodes, valleytronic devices as well as for being a testbed for understanding many-body phenomena. Therefore, it is important to enhance the trion emission and its stability. In this study, a $MoSe_2/FePS_3$ van der Waals heterostructure (vdWH) with type-I band alignment is constructed, which allows for carriers injection from $FePS_3$ to $MoSe_2$. At low temperatures, the neutral exciton (X^0) emission in this vdWH is almost completely suppressed. The I_{Trion}/I_{x0} intensity ratio increases from 0.44 in a single $MoSe_2$ monolayer to 20 in this heterostructure with the trion charging state changing from negative in the monolayer to positive in the heterostructure. The optical pumping with circularly polarized light shows a 14% polarization for the trion emission in $MoSe_2/FePS_3$. Moreover, forming such type-I vdWH also gives rise to a 20-fold enhancement of the room temperature photoluminescence from monolayer $MoSe_2$. These results demonstrate a novel approach to convert excitons to trions in monolayer 2D TMDCs via interlayer doping effect using type-I band alignment in vdWH.

1. Introduction

2D transition metal dichalcogenides (TMDCs), MX_2 (M = Mo, W; X = S, Se, Te) with a hexagonal crystal structure are an exciting class of materials.[1–3] Monolayer TMDs feature a direct bandgap, a large binding energy of neutral exciton (X^0) of up to several hundred meV because of the reduced dielectric screening,

valley-selective optical coupling due to the lack of inversion symmetry, and a strong spin–orbit coupling.[4] Excitons in TMDCs can often trap an electron (X^-) or a hole (X^+) to form so-called trions.[4–7] With these exotic features and tunable bandgaps from visible to near-infrared regions, TMDCs are considered as a highly desired material class for the next-generation optoelectronic and valley-based electronic applications.[8]

Stacking 2D layered materials with pre-selected properties will give rise to the formation of van der Waals heterostructures (vdWHs) with atomically sharp and near-defect-free interfaces, which may exhibit novel physics and possess versatile properties.[9–11] So far, the most extensively studied TMDC vdWHs include $MoS_2–MoSe_2$,[12] $MoS_2–WS_2$,[13,14] $MoS_2–WSe_2$,[15,16] $MoSe_2–WSe_2$,[17] $MoSe_2–WS_2$,[18] and $WS_2–WSe_2$.[19] Their band alignment is found to be staggered type-II, where the conduction band minimum (CBM) and valence band maximum (VBM) are located in the wider-bandgap (WBG) and narrower-bandgap (NBG) materials, respectively. Electrons and holes can be spatially separated, which results in the formation of the interlayer excitons and consequently in quenching of the photoluminescence (PL) in their component layers.[13]

However, the type-I band alignment, which is common in conventional semiconductor heterostructures like GaAs-AlGaAs,

J. M. Duan, P. Chava, Dr. M. Ghorbani-Asl, Dr. D. Erb,
Dr. A. V. Krasheninnikov, Dr. H. Schneider, Dr. L. Rebohle,
Dr. A. Erbe, Prof. M. Helm, Dr. S. Q. Zhou, Dr. S. Prucnal
Helmholtz-Zentrum Dresden-Rossendorf
Institute of Ion Beam Physics and Materials Research
Bautzner Landstrasse 400, D-01328 Dresden, Germany
E-mail: juanmei.duan@hzdr.de; s.zhou@hzdr.de; s.prucnal@hzdr.de
J. M. Duan, Prof. M. Helm
Institute of Applied Physics
Technische Universität Dresden
D-01062 Dresden, Germany

P. Chava
Faculty of Electrical and Computer Engineering
Technische Universität Dresden
D-01062 Dresden, Germany
Dr. L. Hu
Key Laboratory of Novel Materials for Sensor of Zhejiang Province
Institute of Advanced Magnetic Materials
Hangzhou Dianzi University
Hangzhou 310018, P. R. China
Dr. A. V. Krasheninnikov
Department of Applied Physics
Aalto University School of Science
Aalto FI- 00076, Finland
Prof. Y. J. Zeng
College of Physics and Optoelectronic Engineering
Shenzhen University
Shenzhen 518060, P. R. China

is very rarely reported in vdWHs. The CBM and VBM of type-I band alignment are both located in the NBG layer.[20] Therefore, in the heterojunction with type-I band alignment, carriers will flow only from the WBG to the NBG material. Consequently, in the NBG layer, the carrier concentration increases and its PL intensity is enhanced.[21–23] Nevertheless, besides the use of hexagonal boron nitride (h-BN) for passivation, up to now only a few implementations of the type-I band alignment in 2D materials, like PbI$_2$/WS$_2$[23] and MoS$_2$/ReS$_2$,[20] MoS$_2$/ZnO-QDs,[24] have been reported. Those papers focus on the charge transfer process at the interface, which leads to a PL enhancement of the NBG layer. However, trion and exciton emission behavior in type-I vdWH with TMCDs has not yet been investigated. The conversion from excitons to trions controlled by charge density can influence the exciton lifetime and leads to a large valley polarization via valley-selective optical pumping.[25] Since in straddling bands carriers flow only in one direction, by proper selection of WBG materials (n-type or p-type) the charging state of trion can be controlled. Moreover, positively charged trions, X$^+$, have a much longer dephasing time than negatively charged trions, X$^-$ and thus a smaller linewidth, which makes them attractive for quantum technology.[26]

In this work, we demonstrate the manipulation of the trion charging state and population in monolayer MoSe$_2$ by constructing a vdWH MoSe$_2$/FePS$_3$ with type-I band alignment. FePS$_3$ with an indirect bandgap is chosen as the WBG semiconductor. The type-I band alignment is supported by density-functional theory (DFT) calculation, such that MoSe$_2$ with the narrower bandgap acts as the carrier extraction layer and p-type FePS$_3$ is a source of holes. We have achieved an enhancement

of the trion emission with the I_T/I_{X0} ratio increasing from 0.44 to 20, and a 20-fold enhancement of PL emission from the MoSe$_2$ monolayer due to carrier injection from FePS$_3$. Moreover, both the exciton emission in a single MoSe$_2$ monolayer and the trion emission in MoSe$_2$/FePS$_3$ depend on the chirality of the excitation light, indicating the valley polarization selectivity. Our study provides essential insight into the underlying carrier transport mechanism and points to potential device application based on type-I band alignment vdWH.

2. Results and Discussion

2.1. Raman Results

Figure 1a shows the schematic configuration of MoSe$_2$/FePS$_3$ vdWH covered with a few layers of h-BN. Except protecting samples from air, the h-BN encapsulation also reduces the linewidth of the trion and exciton emission from the MoSe$_2$ monolayer.[26] The MoSe$_2$ monolayer was fully laying on the top of FePS$_3$ and the heterostructure area is around 100 μm^2 which is much larger than the laser spot size (about 7 μm^2). Therefore, all the optical signals (including micro-Raman and micro-PL) are coming from the heterojunction. For the reference, individual MoSe$_2$ monolayers and FePS$_3$ flakes covered with h-BN were prepared as well. Figure 1b shows the optical microscope image of MoSe$_2$/FePS$_3$ vdWH, where regions with magenta and orange outlines represent FePS$_3$ and MoSe$_2$, respectively.

Figure 1c,d shows the Raman spectra of monolayer MoSe$_2$ combined with 22 nm (corresponding to 31 layers) FePS$_3$,
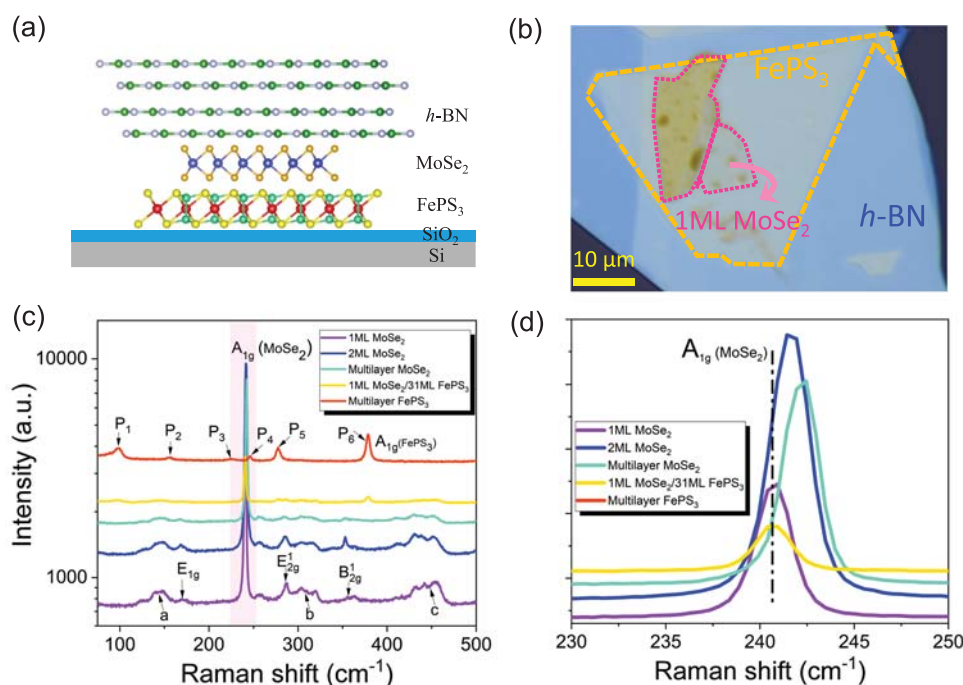
Figure 1. a) Schematic diagram of a fully h-BN-covered MoSe$_2$/FePS$_3$ vdWH on a SiO$_2$/Si substrate. b) Optical image of the 1ML MoSe$_2$ placed on the 31ML FePS$_3$ in vdWH. c) Raman spectra from the 1ML MoSe$_2$, 2ML MoSe$_2$, multilayer MoSe$_2$, 1ML MoSe$_2$/31ML FePS$_3$ vdWH, and multilayer FePS$_3$. d) Zoomed-in Raman spectra for the marked region in panel (c) in the range of 230–250 cm^{-1} under a 532 nm laser excitation. All spectra were shifted vertically for clarity.

defined as 1ML $MoSe_2$/31ML $FePS_3$, multilayer $FePS_3$, and individual $MoSe_2$ flakes with different thicknesses (1ML, 2ML, and multilayer). For $MoSe_2$, the A_{1g} mode is an out-of-plane vibration modes in which Se atoms in all layers oscillate in phase with reference to the corresponding central Mo atom.[27] Figure 1d shows the micro-Raman spectra taken from the $MoSe_2$ layer with different thicknesses. The peak positions of the A_{1g} mode at 240.6 cm^{-1} for 1ML $MoSe_2$, 241.7 cm^{-1} for 2ML, and 242.3 cm^{-1} for multilayer $MoSe_2$ are in good agreement with previous reports,[27] confirming the thickness of $MoSe_2$ in our study. Besides the A_{1g} phonon mode, the $MoSe_2$ flake has other Raman active phonon modes like E^1_{2g} and B^1_{2g} visible at about 286.9 and 355.7 cm^{-1}, as well as E_{1g} at 169.7 cm^{-1} for 1ML $MoSe_2$ (see Figure 1c). Their peak positions shift to lower wavenumbers as the number of layers increases and the highest peak intensities are observed for the $MoSe_2$ bilayer. The other peaks labeled in Figure 1c with a, b, and c showing much broader features especially pronounced in monolayer and bilayer $MoSe_2$ are assigned to second-order Raman processes.[28] Interestingly, the A_{1g} phonon mode from 1ML $MoSe_2$ in vdWH has the same peak position as that from individual 1ML $MoSe_2$, but the peak intensity is significantly reduced, probably due to the softening of the phonons by phonon–carrier interaction.

The Raman spectrum from $FePS_3$ is also presented in Figure 1c. $FePS_3$ shows six distinguishable peaks labeled with P_1–P_6. The observed phonon modes are in agreement with previously reported ones.[29] The P_3–P_6 phonon modes are assigned

to the $(P_2S_6)^{4-}$ bipyramid structures and P_1–P_2 are related to the Fe atoms and are sensitive to the magnetic coupling between Fe atoms.[30] According to the temperature-dependent micro-Raman spectra, the evolution of the P_1 and P_2 phonon modes in $FePS_3$ is very similar both in the individual flake and in the vdWH. We found that the Néel temperature of $FePS_3$ is at around 120 K (see Figure S1, Supporting Information), which is in good agreement with the data reported in the literature.[29]

2.2. Band Alignment from DFT Calculations

We used DFT calculations to investigate the band alignment for monolayer $MoSe_2$/$FePS_3$. For the calculations, we have considered a monolayer heterojunction 1ML $MoSe_2$/1ML $FePS_3$ and a heterojunction prepared of 3ML $MoSe_2$ on monolayer $FePS_3$, as shown in **Figure 2**a. After structural optimization, an average interlayer distance of d = 3.63 Å was found between $FePS_3$ and $MoSe_2$. The binding energy between $FePS_3$ and $MoSe_2$ was calculated to be 16 meV $Å^{-2}$ which is close to the values in other 2D vdWH interfaces.[31] Our electronic structure calculations indicate that the $MoSe_2$ monolayer has a direct band gap of 1.33 eV at the K point (Figure S2, Supporting Information). The $FePS_3$ monolayer shows a quasi-direct bandgap of 2.27 eV where VBM and CBM are both located at the Σ point (midpoint of Γ and K points). Although DFT band gap cannot directly be compared with the optical gap measured in the experiment, our
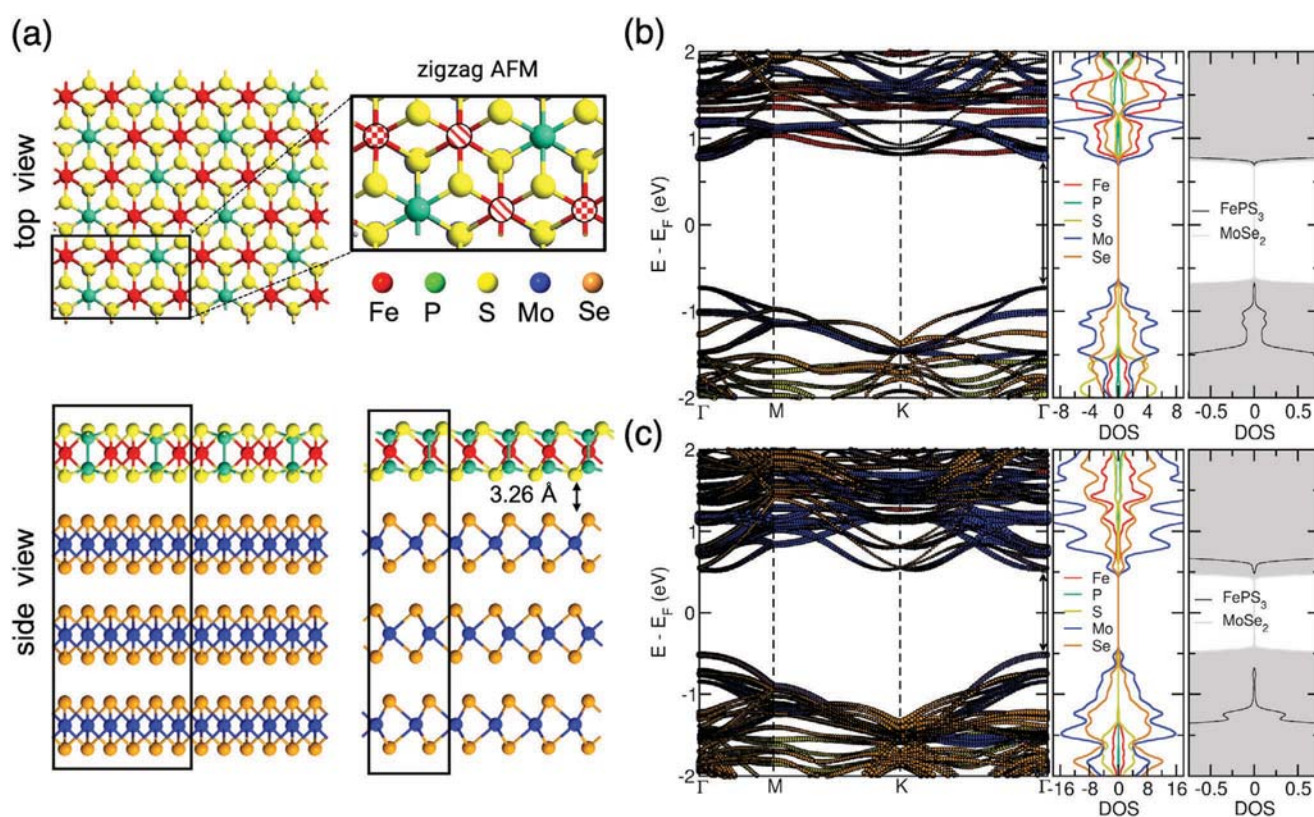
Figure 2. a) Atomic structure of $FePS_3$/$MoSe_2$, the top and side views. The rectangular unit cell of $FePS_3$ is indicated by black lines. The hatched red markers illustrate the directions of local spins (up and down, checkerboard and striped circles) of zigzag antiferromagnetic order in the unit cell. b) Calculated electronic band structure and density of states (DOS) of 1ML $MoSe_2$/1ML $FePS_3$ and c) 3ML $MoSe_2$/1ML $FePS_3$ by DFT.

Annual Report IIM 2021, HZDR-118   25

**ADVANCED
SCIENCE NEWS**
www.advancedsciencenews.com

**ADVANCED
FUNCTIONAL
MATERIALS**
www.afm-journal.de

results are in line with the experimental band gap (2.2 eV)[32] and the theoretical band gap (2.5 eV)[33] for FePS$_3$ monolayer. The slight difference of band gap values for FePS$_3$ monolayer between our calculation and the previous theoretical report[33] is due to different calculation methods. Based on the electronic structure calculations, the CBM of the MoSe$_2$ is lower than that of the FePS$_3$ while the VBM is higher than that of the FePS$_3$, forming type-I band alignment, as schematically illustrated in Figure 2b,c. Both heterostructures with 1ML-MoSe$_2$ and 3ML-MoSe$_2$ show direct band gaps of 1.51 and 1.07 eV, situated at the Γ point in Figure 2b,c. The projected densities of states suggest that the VBM mainly consists of Mo d and Se p orbitals, whereas the CBM is mainly composed of the Mo d orbitals and slight contributions from Fe d states. To further analyze the effect of coupling between FePS$_3$ and MoSe$_2$, the average potential profile across the heterostructure and the charge difference between the combined system and isolated parts are shown in Figure S3 in the Supporting Information. Owing to the higher potential energy of MoSe$_2$, the charge is redistributed in the system with predominant accumulation at the side of MoSe$_2$ layer facing FePS$_3$.

2.3. Photoluminescence Results

Figure 3a shows the room temperature PL (RTPL) spectra of 1ML MoSe$_2$/31ML FePS$_3$ and individual MoSe$_2$ monolayer. The RTPL spectra obtained from 2ML individual MoSe$_2$ and its heterostructure are presented in Figure 3b. Note that the RTPL measurement was performed in air under ambient conditions. Insets show optical images of investigated samples. 1ML and 2ML MoSe$_2$ are specially chosen here since MoSe$_2$ possesses thickness-dependent bandgap features,[2,34] i.e., a direct bandgap for monolayer MoSe$_2$ and an indirect bandgap for thicker MoSe$_2$. Similar to Raman spectra, the PL measurements can be used to determine the thickness of investigated MoSe$_2$ flakes. All the samples for PL measurement were covered with h-BN in order to prevent oxygen/moisture contaminations and obtain a high quality of optical emission spectra.[35] Since FePS$_3$ is an indirect band gap semiconductor[33] and its photogenerated carriers can quickly relax to MoSe$_2$ due to their type-I band alignment, all the PL peaks presented here originate only from MoSe$_2$ flakes. The single MoSe$_2$ monolayer flake shows the RT excitonic PL emission at 1.573 eV while the PL
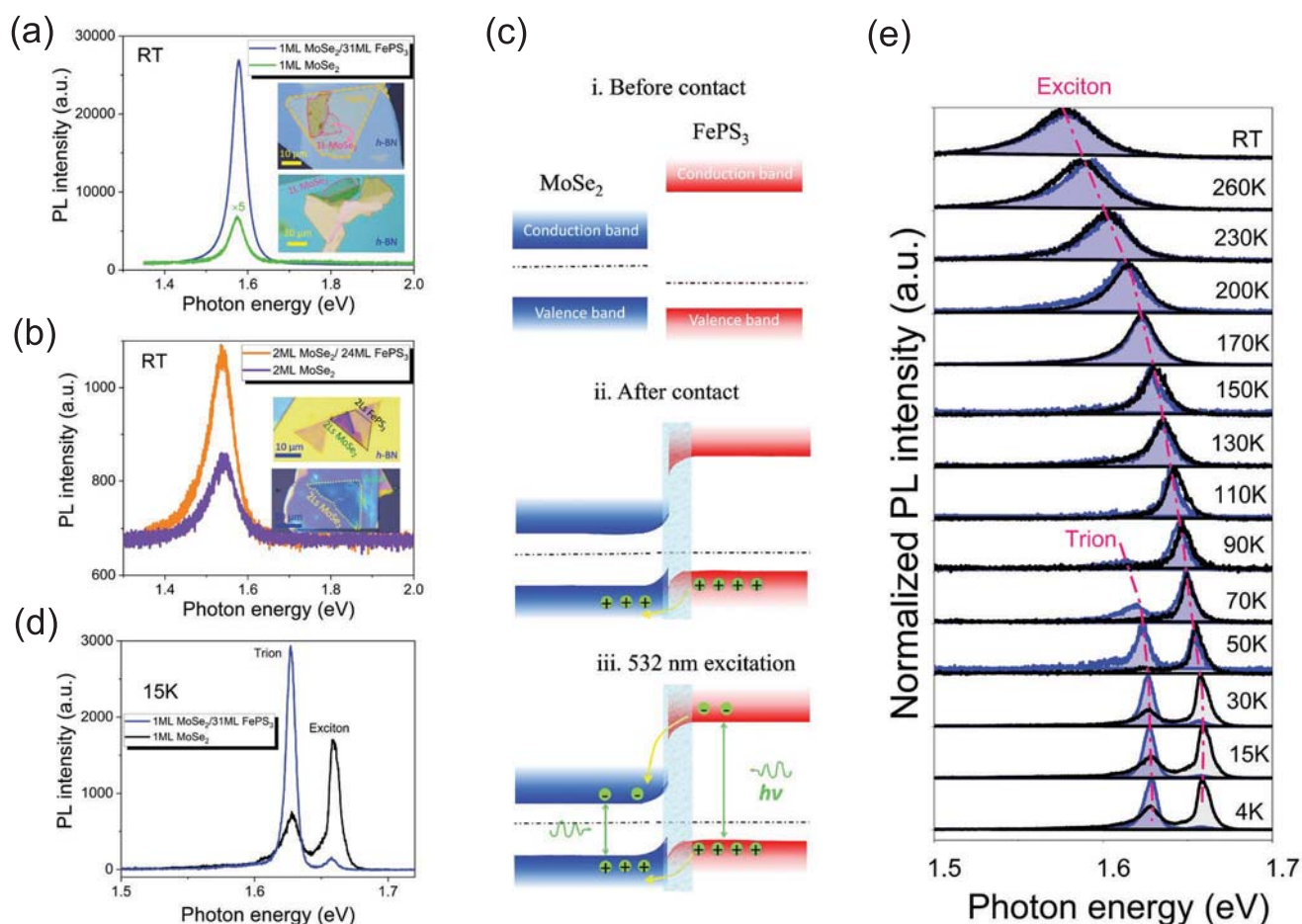
Figure 3. a) RTPL spectra of 1ML MoSe$_2$/31ML FePS$_3$ and 1ML MoSe$_2$-single layer. b) RTPL spectra of 2ML MoSe$_2$/24ML FePS$_3$ and 2ML MoSe$_2$-single layer. Insets are optical images of samples. c) Band alignment of MoSe$_2$/FePS$_3$: before contact of constituent layers, after contact of constituent layers, and under laser excitation. The shadowed areas visualize the band alignment for 1ML MoSe$_2$/multilayer FePS$_3$. d) PL spectra of 1ML MoSe$_2$/31ML FePS$_3$ and single 1ML MoSe$_2$ at 15 K. e) Normalized TDPL spectra for 1ML MoSe$_2$/31ML FePS$_3$ (blue-shaded areas) and 1ML MoSe$_2$ (black-shaded areas).

emission from 1ML $MoSe_2/FePS_3$ is slightly blue-shifted to 1.579 eV. More importantly, the heterostructure shows 20-fold enhancement of PL emission. Since the exciton lifetime in indirect semiconductors is generally much longer than in direct ones, the photogenerated carriers in $FePS_3$ can quickly diffuse into $MoSe_2$ and radiatively recombine there, which accounts for this giant PL enhancement in 1ML $MoSe_2/31ML$ $FePS_3$. The PL emission from bilayer $MoSe_2$ on $FePS_3$ observed at 1.543 eV is enhanced by a factor of 1.3 in comparison to the individual flake. Zhang et al. have shown strong enhancement of the exciton emission from the WS_2 monolayer covered with WO_3 due to the reduction of nonradiative recombination and the charge transfer within the heterostructure.[36]

As concluded from DFT calculation, 1ML $MoSe_2/FePS_3$ shows a straddling type-I band alignment between $MoSe_2$ (NBG) and $FePS_3$ (WBG). In addition, the conductivity type of single $MoSe_2$ and $FePS_3$ flakes is confirmed by electrical measurements presented in Figure S4 in the Supporting Information. $MoSe_2$ and $FePS_3$ possess n-type and p-type conductivity, respectively, which is consistent with other reports.[37,38] After forming a heterojunction with type-I band alignment, holes will flow from $FePS_3$ to $MoSe_2$ to achieve an equilibrium state (see the middle panel in Figure 3c). In our case, the thickness of the $MoSe_2$ is limited to one monolayer (about 0.7 nm), which can be completely converted to p-type when combining with 31 ML $FePS_3$. The shallowed areas in Figure 3c indicate the band alignment for 1ML $MoSe_2$/multilayer $FePS_3$. Under excitation, both electrons and holes generated in $FePS_3$ can diffuse to $MoSe_2$ with a result of its PL enhancement due to type-I band alignment (see the right panel in Figure 3c).

The smaller enhancement in 2ML $MoSe_2/24ML$ $FePS_3$ is due to the fact that 2ML $MoSe_2$ is an indirect bandgap semiconductor with much lower radiative recombination rate.[34] Since the $MoSe_2$ layer is placed fully on the $FePS_3$ flake, we can exclude the possibility that surface charges in the SiO_2 substrate can donate carriers into $MoSe_2$, as it was previously reported.[35,39] Therefore, in our case only $FePS_3$ can be the extra source of photogenerated carriers in $MoSe_2$. A PL emission enhancement for the narrower bandgap material in type-I van der Waals heterojunctions has been reported before, e.g., for $MoTe_2$–WSe_2,[21] PbI_2–WS_2,[40] WSe_2–black phosphorus,[41] MoS_2–ReS_2,[20] GaSe–GaTe,[22] etc. This distinct feature is substantially different from that of the widespread type-II band alignment for TMDCs heterostructures, like MoS_2–WSe_2,[15] MoS_2–$MoSe_2$,[12] MoS_2–WS_2, and WSe_2–MoS_2,[13,42] where the PL emissions of two constituent layers are both quenched along with the appearance of an additional interlayer exciton peak with low energy.[17,43]

To shine more light on the interaction and charge transfer between $FePS_3$ and $MoSe_2$, temperature-dependent PL (TDPL) measurements were performed. In this measurement, we focus on the sample 1ML $MoSe_2/31ML$ $FePS_3$. As the reference sample, an individual $MoSe_2$ monolayer was also investigated. Figure 3d shows the PL spectra of 1ML $MoSe_2/31ML$ $FePS_3$ and individual $MoSe_2$ monolayer at 15 K. The peaks at 1.66 and 1.63 eV in both spectra correspond to neutral exciton (X) and charged trion (T) emission from the $MoSe_2$ monolayer, respectively. The appearance of the trion emission in the individual $MoSe_2$ monolayer is due to the unintentional n-type doping as

a consequence of impurities attached to reactive chalcogenide vacancies or defects in the SiO_2 substrate.[44–46] In Figure 3d, we observe a giant enhancement of the trion emission and a dramatic suppression of the exciton emission (the PL intensity ratio $\frac{I_{Trion}}{I_X} = \approx 20$) for $MoSe_2$ in the heterojunction in comparison with $\frac{I_{Trion}}{I_X} = \approx 0.44$ for individual 1ML $MoSe_2$. The strong enhancement of the trion emission implies a strong doping of $MoSe_2$ in vdWH. Again, this agrees well with the definition of type-I band alignment where carriers can flow only in one direction from WBG to NBG. In heavily doped semiconductors, excitons can trap free electrons or holes to form trions. This phenomenon also can be explained by a model based on the law of mass action[47,48]

$$\frac{N_X n_e}{N_T} = \left(\frac{4 m_X m_e}{\pi \hbar^2 m_T} \right) k_B T \exp\left(-\frac{E_B}{k_B T} \right) \tag{1}$$

here N_T, N_X, and n_e are trion, exciton, and charge carrier concentrations, $\hbar$ is the reduced Planck's constant, k_B is the Boltzmann constant, T is the temperature, E_B is the trion binding energy, m_e is effective mass of electrons, m_X and m_T are exciton and trion effective masses, respectively. According to this model, there is a positive correlation between $\frac{N_T}{N_X}$ and n_e, i.e., $\frac{N_T}{N_X}$ increases with increasing carrier concentration n_e. Since the concentrations of trions and excitons are proportional to their PL intensities $\left(\frac{N_T}{N_X} \propto \frac{I_T}{I_X} \right)$, it means that doping (higher n_e or n_p) can lead to a higher PL intensity ratio $\frac{I_T}{I_X}$. Besides, the increased trion binding energy, which can be modified by the dielectric environment, could also lead to a higher $\frac{I_T}{I_X}$. Specifically, a lower dielectric constant of the environment can reduce the total screening effect on 1ML TMDCs, which can result in a higher trion binding energy and further can contribute to a higher $\frac{I_T}{I_X}$.[35] Due to $\varepsilon_{FePS_3} < \varepsilon_{SiO_2}$, it means that $FePS_3$ in vdWHs may provide an environment that is more energetically favorable for trion formation in $MoSe_2/FePS_3$ than in individual $MoSe_2$ being directly contacted with a SiO_2 substrate.

Figure 3e shows the normalized TDPL spectra for vdWHs (blue-shaded areas) and individual 1ML $MoSe_2$ (black-shaded areas). The red shift of exciton and trion peaks for both samples is observed with increasing temperature, which is due to temperature-induced bandgap shrinkage. Below 50 K, the trion emission gives a pronounced peak and dominates the spectra of vdWH, while in individual 1ML $MoSe_2$ the exciton emission dominates the PL spectra because of the lower carrier concentration and thus lower trion concentration. At 50 K, the trion and exciton emissions from the heterojunction have comparable intensity, but with increasing temperature the trion emission vanishes. This is due to thermal fluctuations resulting in the conversion from trions to excitons. In individual 1ML $MoSe_2$, the trion emission is already negligible as compared with the exciton peak at 50 K as a consequence of lower carrier concentration. In the temperature range of 90–300 K, only the exciton emission peak is observed for both
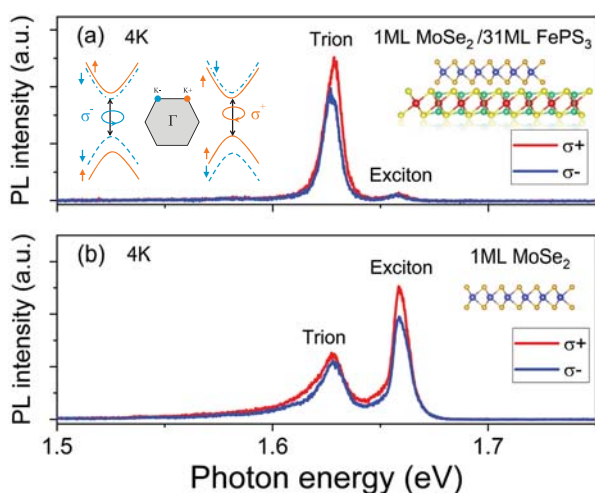
Figure 4. Low-temperature PL emission after excitation with left- or right-handed circularly polarized light obtained a) from the heterojunction and b) from the individual MoSe$_2$ monolayer. The inset shows the chiral optical selection rules for interband optical transitions in nonequivalent valleys K+ and K− in monolayer MoSe$_2$.

vdWHs and individual MoSe$_2$. Note that we assume FePS$_3$ has no effect on the exciton peak position of MoSe$_2$ in vdWHs. In addition, the thermal stability of the trion also depends on its charge state. Positively charged trions, X$^+$, have localized holes that are less prone to scattering, leading to the reduced line width.[26]

In order to clarify the charge sign of trions in both systems and to explore their potential impacts on valleytronics, we have employed PL excitation with circularly polarized light (see **Figure 4**). Using left-(σ^-) or right-handed (σ^+) excitation in both systems, we have seen differences in the PL emission. Here, the degree of circular polarization is evaluated as $P_c = [I(\sigma+) - I(\sigma-)]/[I(\sigma+) + I(\sigma-)]$, where $I(\sigma+)$ and $I(\sigma-)$ correspond to the PL intensities under left-(σ^-) or right-handed (σ^+) excitation. In the individual monolayer MoSe$_2$, the exciton emission is enhanced by 13% for σ^+ excitation while the trion emission is almost not affected with a small broadening. The exciton emission polarization is resulted from the broken inversion symmetry and the strong SOC in monolayer TMDCs,[49] which gives rise to two inequivalent K+ and K− valleys with different population. Due to the spin-valley locking effect, the right-handed (σ^+) circular polarized photon initializes a carrier in the K+ valley and the left-handed (σ^-) initializes a carrier in the K− valley, i.e., valley-dependent optical selection rules.[50,51] Zeng et al. reported that 30% valley polarization can be achieved in pristine monolayer MoS$_2$ with circularly polarized light pump.[51] For the PbI$_2$/WS$_2$ heterostructure with type-I band alignment, Zhang and co-workers have shown near unity spin polarization in PbI$_2$ due to the modification of the carrier lifetime.[52] In the heterostructure MoSe$_2$/FePS$_3$, the exciton emission is the same for both excitations, while the trion emission exhibits a polarization of about 14%. It suggests that no carrier spin polarization is introduced from Ising-type antiferromagnetic FePS$_3$ to MoSe$_2$. Moreover, the trion emission from the heterostructure is narrower than from the individual MoSe$_2$ monolayer and the peak position is blue shifted for the

heterostructure by about 2 meV. Since holes are more localized than electrons in MoSe$_2$, X$^+$ are immobile and less prone to scattering, leading to a narrow linewidth of X$^+$ than X$^-$.[26] A similar energy difference for the X$^+$ and X$^-$ emission and narrowing of the PL emission for X$^+$ in MoSe$_2$ were observed by Shepard et al.[26] Therefore, we can conclude that in our case negatively charged trions X$^-$ form at low temperature in the individual MoSe$_2$ monolayer, while in the heterostructures the trions are positively charged due to hole injection from p-type FePS$_3$ into the MoSe$_2$ monolayer.

3. Conclusion

In conclusion, we have performed a systematic study of optical properties for a novel semiconductor-antiferromagnetic MoSe$_2$/FePS$_3$ vdWH. DFT calculations show the type-I band alignment in ultrathin MoSe$_2$/FePS$_3$, which is verified by the PL results. The room temperature PL shows 20-fold enhancement of the emission from 1ML MoSe$_2$ in MoSe$_2$/FePS$_3$ vdWH, which is due to carrier injection from WBG FePS$_3$ to NBG MoSe$_2$. At low temperatures, the intensity ratio between trion and exciton emission increases from 0.44 to about 20. Moreover, the heterojunction exhibits trion emission polarization, which makes it attractive for valleytronics. Our results present a novel approach to modify the population of trions and excitons as well as the trion charge state by forming a heterostructure with type-I band alignment. This approach is transferable to many other 2D materials and is opening a broad playground for fundamental physics and for valleytronic applications.

4. Experimental Section

Sample Preparation: The 2D material flakes were mechanically exfoliated through blue tape and then transferred onto SiO$_2$/Si substrates (90 nm thick SiO$_2$ on heavily doped Si) by using a polymer stamp transfer technique within a nitrogen atmosphere in a glove box environment. This technique provided good crystalline quality, intact atomic interfaces, and less contamination of the flake in comparison with other transfer techniques.[53] Also, prepatterned electrodes with Ti/Au (5/45 nm) on SiO$_2$/Si substrates were fabricated by standard photolithography and electron-beam evaporation processes. To fabricate the MoSe$_2$/FePS$_3$ vdWH, FePS$_3$ was first transferred onto the SiO$_2$/Si substrate, and then the monolayer MoSe$_2$ was transferred onto the top of the FePS$_3$ flake. For reference, the single MoSe$_2$ monolayer flakes were prepared in the same way. Finally, both the vdWH and single MoSe$_2$ flakes were covered with h-BN in order to reduce flake contamination and degradation resulting from contact with air.

Characterization: For the micro-PL and micro-Raman measurements, a cw frequency-doubled Nd:YAG laser was used for excitation at a wavelength of λ = 532 nm. The laser power was controlled by introducing neutral density filters. The maximum laser power used here was 3.2 mW to avoid heating of the flake. The spot diameter of the laser on the sample was ≈3 µm, i.e., smaller than the size of the target flakes. Both PL and micro-Raman investigations were performed in the temperature range from 4 to 300 K using a liquid-He cooled chamber and temperature controller. A liquid nitrogen-cooled Si-CCD camera was used to detect the PL emission, which was dispersed in a spectrometer. To check the PL polarization of trion and exciton in MoSe$_2$, the excitation with circular left-(right-) handed polarized light was performed. The measurement was done at 4 K. The thickness of FePS$_3$ was measured with atomic force microscopy (AFM) with a Bruker Multimode 8 system,

and the thicknesses of $MoSe_2$ were estimated by optical contrast and confirmed by micro-Raman, PL results.

Calculation Details: Spin-polarized DFT calculations were performed in the framework of the projector augmented wave method using the VASP code.[54] The generalized gradient approximation with the Perdew–Burke–Ernzerhof parametrization was used for the exchange–correlation functional.[55] To account for the strong correlation effects among d-orbital electrons of iron atoms, the DFT + U method with an effective Hubbard value (U) of 4.5 eV for Fe atoms was employed. The plane-wave basis set with a kinetic energy cutoff of 600 eV was used. The Brillouin zone of the system was sampled using $8 \times 8 \times 1$ k-mesh for primitive cells and $5 \times 5 \times 1$ k-mesh for supercells. London dispersion interactions were included in the total energy as proposed by Grimme in the DFT-D2 method.[56] The geometry optimization was carried out until the atomic forces were less than 0.01 eV Å^{-1}. A vacuum layer of 20 Å perpendicular to the basal plane was introduced to implement the isolated slab condition. In order to adopt zigzag antiferromagnetic ordering in $FePS_3$, a unit cell of tetragonal shape with 20 atoms was considered, as shown in Figure 2a. The heterostructures were constructed by using an interface consisting of 1×1 unit cell of $FePS_3$ and 1×3 unit cells of monolayer $MoSe_2$ corresponding to a lattice mismatch of only 0.6%. The supercells contained 38 atoms in two layers and 74 atoms in four layers ($MoSe_2$ triple layers + $FePS_3$ monolayer) configurations.

Supporting Information

Supporting Information is available from the Wiley Online Library or from the author.

Acknowledgements

Conflict of Interest

The authors declare no conflict of interest.

Data Availability Statement

Research data are not shared.

Keywords

[1] A. Splendiani, L. Sun, Y. Zhang, T. Li, J. Kim, C.-Y. Chim, G. Galli, F. Wang, *Nano Lett.* **2010**, *10*, 1271.

[2] K. F. Mak, C. Lee, J. Hone, J. Shan, T. F. Heinz, *Phys. Rev. Lett.* **2010**, *105*, 136805.

[3] W. Zhao, Z. Ghorannevis, L. Chu, M. Toh, C. Kloc, P.-H. Tan, G. Eda, *ACS Nano* **2013**, *7*, 791.

[4] K. F. Mak, K. He, C. Lee, G. H. Lee, J. Hone, T. F. Heinz, J. Shan, *Nat. Mater.* **2013**, *12*, 207.

[5] A. M. Jones, H. Yu, N. J. Ghimire, S. Wu, G. Aivazian, J. S. Ross, B. Zhao, J. Yan, D. G. Mandrus, D. Xiao, *Nat. Nanotechnol.* **2013**, *8*, 634.

[6] J. S. Ross, S. Wu, H. Yu, N. J. Ghimire, A. M. Jones, G. Aivazian, J. Yan, D. G. Mandrus, D. Xiao, W. Yao, *Nat. Commun.* **2013**, *4*, 1474.

[7] A. Singh, G. Moody, K. Tran, M. E. Scott, V. Overbeck, G. Berghäuser, J. Schaibley, E. J. Seifert, D. Pleskot, N. M. Gabor, *Phys. Rev. B* **2016**, *93*, 041401.

[8] K. F. Mak, K. He, J. Shan, T. F. Heinz, *Nat. Nanotechnol.* **2012**, *7*, 494.

[9] Y. Liu, N. O. Weiss, X. Duan, H.-C. Cheng, Y. Huang, X. Duan, *Nat. Rev. Mater.* **2016**, *1*, 16042.

[10] F. Xia, H. Wang, D. Xiao, M. Dubey, A. Ramasubramaniam, *Nat. Photonics* **2014**, *8*, 899.

[11] K. Novoselov, o. A. Mishchenko, o. A. Carvalho, A. C. Neto, *Science* **2016**, *353*, aac9439.

[12] F. Ceballos, M. Z. Bellus, H.-Y. Chiu, H. Zhao, *ACS Nano* **2014**, *8*, 12717.

[13] X. Hong, J. Kim, S.-F. Shi, Y. Zhang, C. Jin, Y. Sun, S. Tongay, J. Wu, Y. Zhang, F. Wang, *Nat. Nanotechnol.* **2014**, *9*, 682.

[14] Y. Yu, S. Hu, L. Su, L. Huang, Y. Liu, Z. Jin, A. A. Purezky, D. B. Geohegan, K. W. Kim, Y. Zhang, *Nano Lett.* **2015**, *15*, 486.

[15] M.-H. Chiu, M.-Y. Li, W. Zhang, W.-T. Hsu, W.-H. Chang, M. Terrones, H. Terrones, L.-J. Li, *ACS Nano* **2014**, *8*, 9649.

[16] T. Roy, M. Tosun, X. Cao, H. Fang, D.-H. Lien, P. Zhao, Y.-Z. Chen, Y.-L. Chueh, J. Guo, A. Javey, *ACS Nano* **2015**, *9*, 2071.

[17] P. Rivera, J. R. Schaibley, A. M. Jones, J. S. Ross, S. Wu, G. Aivazian, P. Klement, K. Seyler, G. Clark, N. J. Ghimire, *Nat. Commun.* **2015**, *6*, 6242.

[18] F. Ceballos, M. Z. Bellus, H.-Y. Chiu, H. Zhao, *Nanoscale* **2015**, *7*, 17523.

[19] W.-T. Hsu, Z.-A. Zhao, L.-J. Li, C.-H. Chen, M.-H. Chiu, P.-S. Chang, Y.-C. Chou, W.-H. Chang, *ACS Nano* **2014**, *8*, 2951.

[20] M. Z. Bellus, M. Li, S. D. Lane, F. Ceballos, Q. Cui, X. C. Zeng, H. Zhao, *Nanoscale Horiz.* **2017**, *2*, 31.

[21] T. Yamaoka, H. E. Lim, S. Koirala, X. Wang, K. Shinokita, M. Maruyama, S. Okada, Y. Miyauchi, K. Matsuda, *Adv. Funct. Mater.* **2018**, *28*, 1801021.

[22] H. Cai, J. Kang, H. Sahin, B. Chen, A. Suslu, K. Wu, F. Peeters, X. Meng, S. Tongay, *Nanotechnology* **2016**, *27*, 065203.

[23] W. Zheng, B. Zheng, Y. Jiang, C. Yan, S. Chen, Y. Liu, X. Sun, C. Zhu, Z. Qi, T. Yang, *Nano Lett.* **2019**, *19*, 7217.

[24] Y. H. Zhou, Z. B. Zhang, P. Xu, H. Zhang, B. Wang, *Nanoscale Res. Lett.* **2019**, *14*, 364.

[25] J. J. Carmiggelt, M. Borst, T. van der Sar, *Sci. Rep.* **2020**, *10*, 17389.

[26] G. D. Shepard, J. V. Ardelean, O. A. Ajayi, D. Rhodes, X. Zhu, J. C. Hone, S. Strauf, *ACS Nano* **2017**, *11*, 11550.

[27] P. Tonndorf, R. Schmidt, P. Böttger, X. Zhang, J. Börner, A. Liebig, M. Albrecht, C. Kloc, O. Gordan, D. R. Zahn, *Opt. Express* **2013**, *21*, 4908.

[28] D. Nam, J.-U. Lee, H. Cheong, *Sci. Rep.* **2015**, *5*, 17113.

[29] J.-U. Lee, S. Lee, J. H. Ryoo, S. Kang, T. Y. Kim, P. Kim, C.-H. Park, J.-G. Park, H. Cheong, *Nano Lett.* **2016**, *16*, 7433.

[30] X. Wang, K. Du, Y. Y. F. Liu, P. Hu, J. Zhang, Q. Zhang, M. H. S. Owen, X. Lu, C. K. Gan, P. Sengupta, *2D Mater.* **2016**, *3*, 031009.

[31] T. Björkman, A. Gulans, A. V. Krasheninnikov, R. M. Nieminen, *Phys. Rev. Lett.* **2012**, *108*, 235502.

[32] Z. Cheng, T. A. Shifa, F. Wang, Y. Gao, P. He, K. Zhang, C. Jiang, Q. Liu, J. He, *Adv. Mater.* **2018**, *30*, 1707433.

[33] X. Zhang, X. Zhao, D. Wu, Y. Jing, Z. Zhou, *Adv. Sci.* **2016**, *3*, 1600062.

[34] F. Bussolotti, H. Kawai, Z. E. Ooi, V. Chellappan, D. Thian, A. L. C. Pang, K. E. J. Goh, *Nano Futures* **2018**, *2*, 032001.

[35] J. Wierzbowski, J. Klein, F. Sigger, C. Straubinger, M. Kremser, T. Taniguchi, K. Watanabe, U. Wurstbauer, A. W. Holleitner, M. Kaniber, *Sci. Rep.* **2017**, *7*, 12383.

[36] B. Zheng, W. Zheng, Y. Jiang, S. Chen, D. Li, C. Ma, X. Wang, W. Huang, X. Zhang, H. Liu, *J. Am. Chem. Soc.* **2019**, *141*, 11754.

[37] Y. Gao, S. Lei, T. Kang, L. Fei, C.-L. Mak, J. Yuan, M. Zhang, S. Li, Q. Bao, Z. Zeng, *Nanotechnology* **2018**, *29*, 244001.

[38] X. Wang, Y. Gong, G. Shi, W. L. Chow, K. Keyshar, G. Ye, R. Vajtai, J. Lou, Z. Liu, E. Ringe, *ACS Nano* **2014**, *8*, 5125.

[39] D. Sercombe, S. Schwarz, O. Del Pozo-Zamudio, F. Liu, B. Robinson, E. Chekhovich, I. Tartakovskii, O. Kolosov, A. Tartakovskii, *Sci. Rep.* **2013**, *3*, 3489.

[40] W. Zheng, B. Zheng, C. Yan, Y. Liu, X. Sun, Z. Qi, T. Yang, Y. Jiang, W. Huang, P. Fan, *Adv. Sci.* **2019**, *6*, 1802204.

[41] X. Zong, H. Hu, G. Ouyang, J. Wang, R. Shi, L. Zhang, Q. Zeng, C. Zhu, S. Chen, C. Cheng, *Light: Sci. Appl.* **2020**, *9*, 114.

[42] R. Cheng, D. Li, H. Zhou, C. Wang, A. Yin, S. Jiang, Y. Liu, Y. Chen, Y. Huang, X. Duan, *Nano Lett.* **2014**, *14*, 5590.

[43] M. Van der Donck, F. Peeters, *Phys. Rev. B* **2018**, *98*, 115104.

[44] K. Dolui, I. Rungger, S. Sanvito, *Phys. Rev. B* **2013**, *87*, 165402.

[45] A. Singh, A. K. Singh, *Phys. Rev. B* **2019**, *99*, 121201.

[46] H.-P. Komsa, J. Kotakoski, S. Kurasch, O. Lehtinen, U. Kaiser, A. V. Krasheninnikov, *Phys. Rev. Lett.* **2012**, *109*, 035503.

[47] J. Siviniant, D. Scalbert, A. Kavokin, D. Coquillat, J. Lascaray, *Phys. Rev. B* **1999**, *59*, 1602.

[48] N. Peimyoo, W. Yang, J. Shang, X. Shen, Y. Wang, T. Yu, *ACS Nano* **2014**, *8*, 11320.

[49] R. Suzuki, M. Sakano, Y. Zhang, R. Akashi, D. Morikawa, A. Harasawa, K. Yaji, K. Kuroda, K. Miyamoto, T. Okuda, *Nat. Nanotechnol.* **2014**, *9*, 611.

[50] T. Cao, G. Wang, W. Han, H. Ye, C. Zhu, J. Shi, Q. Niu, P. Tan, E. Wang, B. Liu, *Nat. Commun.* **2012**, *3*, 887.

[51] H. Zeng, J. Dai, W. Yao, D. Xiao, X. Cui, *Nat. Nanotechnol.* **2012**, *7*, 490.

[52] D. Zhang, Y. Liu, M. He, A. Zhang, S. Chen, Q. Tong, L. Huang, Z. Zhou, W. Zheng, M. Chen, *Nat. Commun.* **2020**, *11*, 4442.

[53] M. Velický, P. S. Toth, *Appl. Mater. Today* **2017**, *8*, 68.

[54] G. Kresse, J. Hafner, *Phys. Rev. B* **1993**, *47*, 558.

[55] J. P. Perdew, K. Burke, M. Ernzerhof, *Phys. Rev. Lett.* **1996**, *77*, 3865.

[56] S. Grimme, *J. Comput. Chem.* **2006**, *27*, 1787.

FULL PAPER

Phase Selection in Mn–Si Alloys by Fast Solid-State Reaction with Enhanced Skyrmion Stability

Zichao Li,* Yufang Xie, Ye Yuan,* Yanda Ji, Viktor Begeza, Lei Cao, René Hübner, Lars Rebohle, Manfred Helm, Kornelius Nielsch, Slawomir Prucnal, and Shengqiang Zhou*

B20-type transition-metal silicides or germanides are noncentrosymmetric materials hosting magnetic skyrmions, which are promising information carriers in spintronic devices. The prerequisite is to prepare thin films on technology-relevant substrates with magnetic skyrmions stabilized at a broad temperature and magnetic-field working window. A canonical example is the B20-MnSi film grown on Si substrates. However, the as-yet unavoidable contamination with $MnSi_{1.7}$ occurs due to the lower nucleation temperature of this phase. In this work, a simple and efficient method to overcome this problem and prepare single-phase MnSi films on Si substrates is reported. It is based on the millisecond reaction between metallic Mn and Si using flash-lamp annealing (FLA). By controlling the FLA energy density, single-phase MnSi or $MnSi_{1.7}$ or their mixture can be grown at will. Compared with bulk MnSi, the prepared MnSi films show an increased Curie temperature of up to 41 K. In particular, the magnetic skyrmions are stable over a much wider temperature and magnetic-field range than reported previously. The results constitute a novel phase selection approach for alloys and can help to enhance specific functional properties, such as the stability of magnetic skyrmions.

1. Introduction

Magnetic skyrmions are topologically protected spin configurations[1,2] and have been experimentally discovered in a series of magnetic compounds with noncentrosymmetric crystal structure, such as B20-type transition-metal silicides or germanides.[3–5] In those materials, the Dzyaloshinskii Moriya (DM) interaction and Heisenberg exchange interaction compete with each other, resulting in the formation of a whirling spin structure. The size of skyrmions or the associated magnetic modulation period is determined by the ratio between the magnitudes of the DM interaction and the ferromagnetic exchange interaction, and typically ranges from 1 to 100 nm.[4–8] To drive skyrmions, a much smaller current is needed in comparison to those used to generate spin transfer torques in ferromagnetic metals, which results in lower power consumption and decreases the Joule heat.[9–11] Magnetic skyrmions are proposed for applications in new-generation data storage.[12,13]

B20-type MnSi is regarded as the canonical example, in which magnetic skyrmions were first observed.[3] Up to now, though bulk B20-MnSi compounds are relatively easy to fabricate by rod-casting furnace or Czochralski method,[14,15] skyrmions are only stable in very narrow temperature and magnetic-field ranges.[3] Thin films of B20-MnSi exhibit a much broader temperature range for the existence of skyrmions.[16] Moreover, the preparation of thin film materials on technology-relevant substrates (such as Si) is a prerequisite for today's information technology. B20-type

Z. C. Li, Y. F. Xie, Dr. Y. Yuan, V. Begeza, Dr. L. Cao, Dr. R. Hübner,
Dr. L. Rebohle, Prof. M. Helm, Dr. S. Prucnal, Dr. S. Q. Zhou
Helmholtz-Zentrum Dresden-Rossendorf
Institute of Ion Beam Physics and Materials Research
Bautzner Landstrasse 400, D-01328 Dresden, Germany
E-mail: zichao.li@hzdr.de; yuanye@sslab.org.cn; s.zhou@hzdr.de
Z. C. Li, Prof. K. Nielsch
Institute of Materials Science
Technische Universität Dresden
01069 Dresden, Germany

Y. F. Xie, V. Begeza, Prof. M. Helm, Prof. K. Nielsch
Institute of Applied Physics
Technische Universität Dresden
01062 Dresden, Germany
Dr. Y. Yuan
Songshan Lake Materials Laboratory
Dongguan, Guangdong 523808, People's Republic of China
Dr. Y. D. Ji
Department of Applied Physics
College of Science
Nanjing University of Aeronautics and Astronautics
Nanjing, Jiangsu 211106, People's Republic of China
Prof. K. Nielsch
Institute for Metallic Materials
IFW-Dresden
01069 Dresden, Germany

The ORCID identification number(s) for the author(s) of this article can be found under https://doi.org/10.1002/adfm.202009723.

MnSi films have been prepared by molecular beam epitaxy and solid-phase epitaxy.[17–20] However, several scientific issues remain challenging for the MnSi thin-film growth. The most important one is the coexistence of the $MnSi_{1.7}$ impurity phase always with MnSi.[19] Another one is that the film can only be grown to a limited thickness of around 30 nm; for larger film thicknesses the stability of skyrmions is deteriorated.[15] From the equilibrium Mn–Si phase diagram, it is found that the B20-MnSi phase is very sensitive to the ratio of the Mn and Si composition.[21] Diffusion induced ingredient fluctuations will result in the formation of $MnSi_{1.7}$. Moreover, $MnSi_{1.7}$ has a lower crystallization temperature than MnSi,[19,22,23] and grows naturally as a parasitic phase in the heating or cooling process during the solid-state reaction. $MnSi_{1.7}$ is a weak itinerant magnet and exhibits excellent thermoelectric properties.[24,25] Recently, it was suggested that $MnSi_{1.7}$ can apply strain to MnSi and increase its Curie temperature.[26] Therefore, separating the MnSi and $MnSi_{1.7}$ phases and/or controlling their mixture ratio is challenging, but is necessary in order to optimize the functionality and to design the topological magnetic properties of MnSi films on demand. This is exactly the question to be tackled in this article.

The relationship between the nucleation activation energy Q, the heating rate Φ, and the crystallization temperature T_p can be expressed by the Kissinger equation[27]

$$\ln\left(\frac{\Phi}{T_p^2}\right) = -\frac{Q}{RT_p} + C \tag{1}$$

where R is the gas constant, and C is a constant ($C = \frac{AR}{Q}$, A is pre-exponential factor also known as the frequency factor). For a particular crystalline phase, when increasing the heating rate Φ, the crystallization temperature will be shifted to higher temperatures. The interval of the crystallization temperatures for different phases will be enlarged. So, different phases can be separated and the microstructure can be selected. Moreover, in the situation of ultrafast heating, the temperature increases so fast that the phase with lower crystallization temperature cannot nucleate within such a short time. This has been demonstrated for CuZr-based metallic glasses in ref. [28]. In particular, by increasing the heating rate above 250 Ks^{-1}, the ductile B2 phase has been selectively formed and the formation of the low-temperature brittle phases $CuZr_2$ and $Cu_{10}Zr_7$ is suppressed. The fast heating and cooling rates make the system-temperature cross the crystallization temperature of brittle phases in a very short time. There is no nucleation time for the brittle phases due to the transient heating and cooling processes. This approach also works well for amorphous Au-based and Pt-based alloys.[29,30] Therefore, we anticipate that a fast annealing method, such as flash-lamp annealing (FLA),[31] provides an effective way to separate B20-MnSi and $MnSi_{1.7}$ and to control the ratio between both phases. During FLA, the sample is exposed to xenon flash lamps, such that the total energy budget is low, leading to a fast heating and cooling rate. The details can be found in the Supporting Information.

In this manuscript, we report the fabrication of phase-controlled $MnSi_x$ films by the solid-state reaction of metallic Mn layers with Si during millisecond flash-lamp annealing. By controlling the energy density deposited to the sample surface by the flash lamps, single-phase B20-MnSi, $MnSi_{1.7}$ or their controlled mixture can be fabricated. The obtained B20-MnSi

thin film has a high Curie temperature of 41 K and exhibits characteristic signatures of magnetic skyrmions. The formation window of skyrmions in our film is significantly enlarged with respect to the magnetic field (2–10 kOe) or temperature (up to 41 K) range compared to previously published results.[3,15,17]

2. Results

2.1. MnSi and $MnSi_{1.7}$ Phase Reaction

As shown in **Figure 1**a, depending on different annealing temperatures, two reactions are possible. Due to the ultrafast FLA process, diffusion and nucleation happen at the same time. The diffusion of Si dominates this phase formation process.[32] The reaction at low-temperature is the reaction between Mn and Si, leading to $MnSi_{1.7}$ directly. The reaction at high temperature can form B20-MnSi at the beginning. However, since the Si wafer can provide endless Si atoms, MnSi can further react with extra Si, forming the Si-rich phase, namely $MnSi_{1.7}$. In the conventional solid-state reaction process, $MnSi_{1.7}$ is more easily formed as an inevitable secondary phase in MnSi films. According to our anticipation, a fast or transient reaction between Mn and Si by flash-lamp annealing can inhibit the formation of $MnSi_{1.7}$ by controlling different annealing temperatures with ultrafast heating/cooling rates. In the following, we focus on 3 samples: 4.2R, 4.3R, and 4.3F, which were annealed using flash lamps from the rear-side (R) or from the front-side (F) with the capacitor charged up to 4.2 or 4.3 kV corresponding to the energy density of 134.6 or 139.5 J cm^{-2}, respectively. Therefore, sample 4.2R experienced a lower reaction temperature than sample 4.3R. Sample 4.3F was processed at an intermediate temperature due to the large reflectance of the metallic Mn front side compared to the rough rear side of the Si wafer. In particular, the larger reflectance of the Mn film leads to lower absorbance and therefore lower energy annealing temperature.

Figure 1b displays the XRD patterns obtained from the samples prepared at different annealing parameters. The (111) and (222) diffraction peaks of the Si substrate are at 28.4° and 58.9°, respectively. For sample 4.3R (red, bottom trace) annealed at high temperature, the MnSi-(111) and (222) Bragg peaks are present at 34.2° and 72.4°, respectively. MnSi (210) is also observed at 45° with a much weaker intensity. According to the powder PDF card (01-081-0484),[33] the MnSi (210) peak should be the strongest. Taking into account the intensity ratios between the different diffraction peaks, the majority of the MnSi phase in sample 4.3R is (111)-textured. In comparison to sample 4.3R, sample 4.2R (blue, top trace) shows only the Bragg peaks of $MnSi_{1.7}$. The lower annealing temperature for sample 4.2R promotes the formation of the $MnSi_{1.7}$ single phase. Sample 4.3F (black, middle trace) was processed at an intermediate temperature and shows a mixture of MnSi and $MnSi_{1.7}$. The MnSi phase is also highly (111)-textured. Thus, by tuning the FLA parameters, we have full control over the Mn-silicide phase formation: single-phase B20-MnSi and $MnSi_{1.7}$ are obtained for the highest and lowest annealing temperatures, respectively, which is in accordance with the Kissinger equation.

The in-plane field-dependent magnetizations of these three samples are shown in Figure 1c. Sample 4.3R with single B20-MnSi phase displays multihysteresis, which originates from the transition of different magnetic structures, a typical
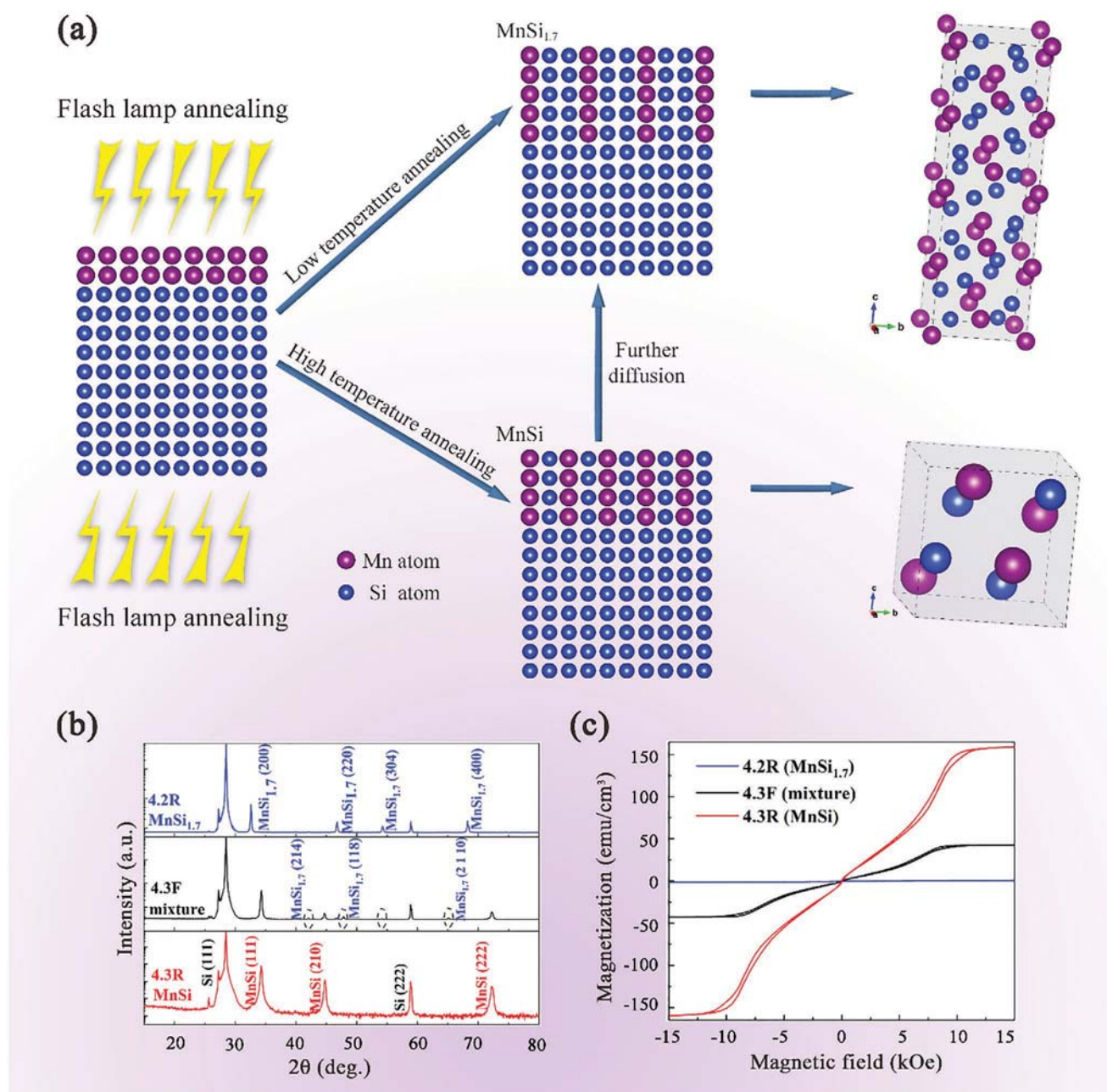
Figure 1. The separation of MnSi and MnSi$_{1.7}$ phases. a) Schematic representation of atom diffusion and solid-state reaction between metal Mn and Si. The blue and purple balls stand for Si and Mn atoms, respectively. MnSi$_{1.7}$ can be formed at low-temperature. B20-MnSi is formed at high temperature. MnSi can further react with Si forming MnSi$_{1.7}$ during cooling down. b) XRD patterns of Mn/Si samples after FLA at different annealing parameters. Single-phase MnSi (bottom, red trace) or MnSi$_{1.7}$ (top, blue trace) was formed in sample 4.3 or 4.2 R, respectively. Sample 4.3F (an enlarged XRD pattern is shown in the Supporting Information) is a mixture of MnSi and MnSi$_{1.7}$. c) In-plane magnetic hysteresis curves recorded at 5 K for the same set of samples. As expected, the magnetization is the highest for the sample containing only B20-type MnSi. The sample containing only MnSi$_{1.7}$ shows negligible magnetization. By the transient reaction between Mn and Si via millisecond flash-lamp annealing, we can synthesize single-phase MnSi or MnSi$_{1.7}$, as well as their mixture at will.

magnetic feature of B20-MnSi.[16,17] The sample 4.3F reveals much reduced magnetization due to the fact that it also contains MnSi$_{1.7}$. As is well known, MnSi$_{1.7}$ is a weak itinerant magnet with a saturation magnetization of 0.012 μB Mn^{-1}.[34] As expected, sample 4.2R containing only MnSi$_{1.7}$ shows negligible magnetization in comparison with the other two samples.

Figure 2a–d shows cross-sectional bright-field transmission electron microscopy (TEM) images a,c) and energy-dispersive

X-ray spectroscopy (EDXS)-based element distributions obtained in scanning TEM mode b,d) for the samples 4.2R and 4.3R, respectively. According to Figure 2a,b, sample 4.2R is characterized by a continuous MnSi$_{1.7}$ film with a thickness of around 90 nm and a sharp interface to the Si substrate. Besides an amorphous Mn–Si oxide capping layer and isolated crystalline Si inclusions between this oxide and the MnSi$_{1.7}$ film, there is no other Mn–Si compound. In contrast, for sample
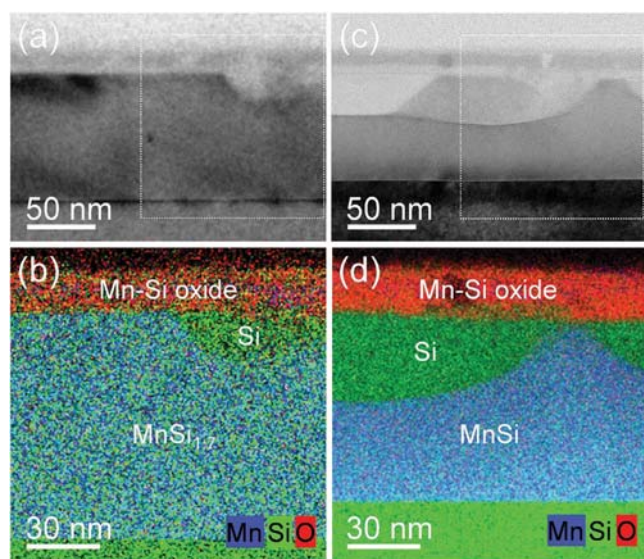
Figure 2. Cross-sectional bright-field TEM images a,c) and EDXS-based element distributions b,d) (Mn: blue, Si: green, O: red) for the samples 4.2 (left) and 4.3R (right) confirming the presence of a continuous single-phase $MnSi_{1.7}$ and MnSi film, respectively, each characterized by a sharp interface to the Si substrate. Thus $MnSi_{1.7}$ and MnSi thin films can be synthesized at will by controlling the flash energy density.

4.3R, an up to 75 nm thick continuous single-phase B20-type MnSi film is obtained (Figure 2c,d). Moreover, extra Si from the substrate can diffuse through the MnSi layer, and an amorphous Mn–Si oxide capping layer protects the sample from further oxidation. The TEM analyses, which are described in more detail in Figures S5 and S6 (Supporting Information), well corroborate the XRD and magnetization measurements. By controlling the reaction temperature during millisecond flash-lamp annealing, we can obtain films of pure tetragonal $MnSi_{1.7}$, of pure cubic B20-type MnSi or of their mixture.

2.2. Magnetic Skyrmions

Lorentz transmission electron microscopy (LTEM), magnetic force microscopy and neutron scattering can give direct confirmation of magnetic skyrmions in real or reciprocal space.[3,4,7,15,16,26,35] For MnSi thin films, both LTEM and magnetization measurements were performed on the same sample and provided consistent results.[16] Therefore, magnetization and magneto-transport measurements are also accepted as methods to characterize magnetic skyrmions.[16,17,36] In this section, we present a detailed magnetic and electrical investigation of sample 4.3R, which contains only the B20-MnSi phase. The MnSi film prepared by our method exhibits nontrivial magnetic properties as known from samples prepared by other methods.[15,16,37]

Figure 3a shows the temperature-dependent saturation magnetization for the B20-MnSi film. The derivative dM/dT of the
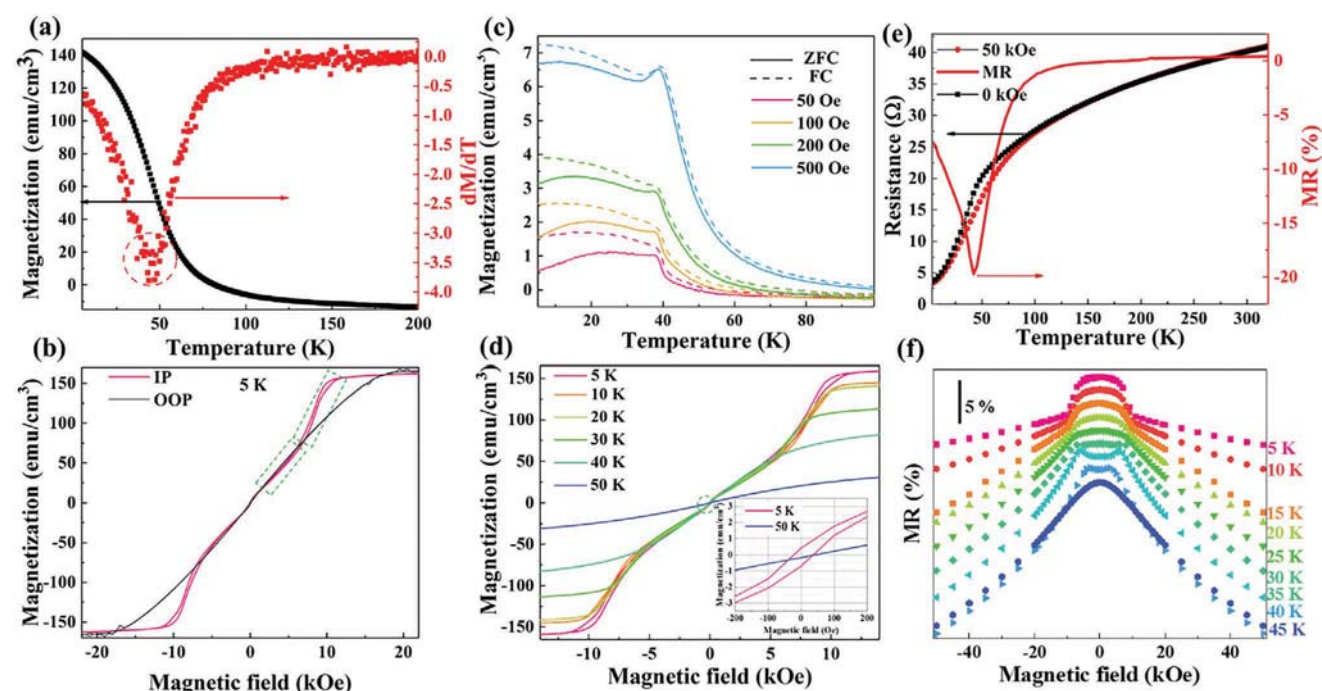
Figure 3. a) In-plane saturation magnetization and the calculated dM/dT. The valley of dM/dT at around 41 K indicates the Curie temperature or the transition from ferromagnetic to paramagnetic. b) In-plane and out-of-plane MH curves recorded at 5 K. The easy axis and multihysteresis are stabilized in-plane. The areas of green dotted rectangles show multihysteresis. c) In-plane field cooling (FC) and zero field cooling (ZFC) magnetization measured under different magnetic fields. There is also a kink around 41 K, which is the transition from helical to paramagnetic. d) In-plane MH curves measured at different temperatures. The inset shows the data around the origin. e) Temperature-dependent resistance under 0 (black square) and 50 kOe (red circle) fields. The red solid line is the calculated MR at 50 kOe. f) Magnetic field-dependent magnetoresistance at various temperatures. The anomalous behaviour disappears at 45 K (above the Curie temperature).

MT curve has a minimum at 41 K, indicating the Curie temperature, which is higher than for bulk MnSi (29.5 K[3]) due to the tensile strain in the MnSi film[16,19,38] (see also the Raman analysis in Section 4 in the Supporting Information[39,40]). The ZFC/FC magnetization under different magnetic fields is shown in Figure 3c. Near 41 K, a cusp feature is observed. It is the transition from the ground helimagnetic to paramagnetic state above 41 K. When increasing the magnetic field, the cusp becomes more pronounced. The shift and disappearance of this cusp are shown in the Supporting Information, which prove the transformations of different magnetic structures again.

Magnetic hysteresis loops at 5 K of the up to 75 nm thick MnSi film with in-plane and out-of-plane magnetic fields reveal the in-plane easy axis favored by the shape anisotropy,[19,41] as shown in Figure 3b. Moreover, both hysteresis loops show almost zero remanence, indicating the formation of a multidomain state at zero field. The saturation field is about 13 and 19 kOe for the in-plane and out-of-plane direction, respectively. In addition, the multihysteresis feature is observed only in-plane, indicating Bloch-type skyrmions.[42] Figure 3d shows in-plane MH curves at various temperatures, where the MH curves have multihysteresis below the Curie temperature. This suggests the transformation between different spin structures. For better visualization, enlarged MH curves from −200 to 200 Oe are shown in the inset of Figure 3d. Magnetic hysteresis disappears above the Curie temperature, where the material becomes paramagnetic.

The electrical resistances of the MnSi film under a magnetic field of 0 and 50 kOe are shown as a function of temperature in Figure 3e. The resistance increases with increasing temperature, which means that the MnSi film behaves like a metal.[43] The calculated magnetoresistance (MR), $MR = \frac{R_H - R_0}{R_0} \times 100\%$ (R_H: resistance at 50 kOe, R_0: resistance at zero field), is shown as a red solid line in Figure 3e. The negative magnetoresistance in MnSi can be understood as follows: the magnetic field increases the effective field acting on the localized spins and suppresses the fluctuation of spins in space and time, which leads to a decrease of the resistivity.[43] The peak of (negative) MR at around 41 K implies that the largest resistance change occurs near the Curie temperature.

The magnetoresistance of the MnSi film at various temperatures is shown in Figure 3f. Below the Curie temperature, it shows an anomalous phenomenon at low magnetic field. More MR data around the Curie temperature is presented in the Supporting Information. Above the Curie temperature, the MR becomes normal without any specific features, which is consistent with bulk MnSi.[43]

In **Figure 4**a,c, the derivatives of the static magnetization dM/dH show four critical transition fields, termed as H_β, $H_{\alpha 1}$, $H_{\alpha 2}$, and H_{sat}. The dashed lines show their shift depending on temperature. H_{sat} is the critical field, above which the material changes into field-polarized ferromagnetism. Below H_β, the system is at its ground helicoid state. At 40 K, there is no clear
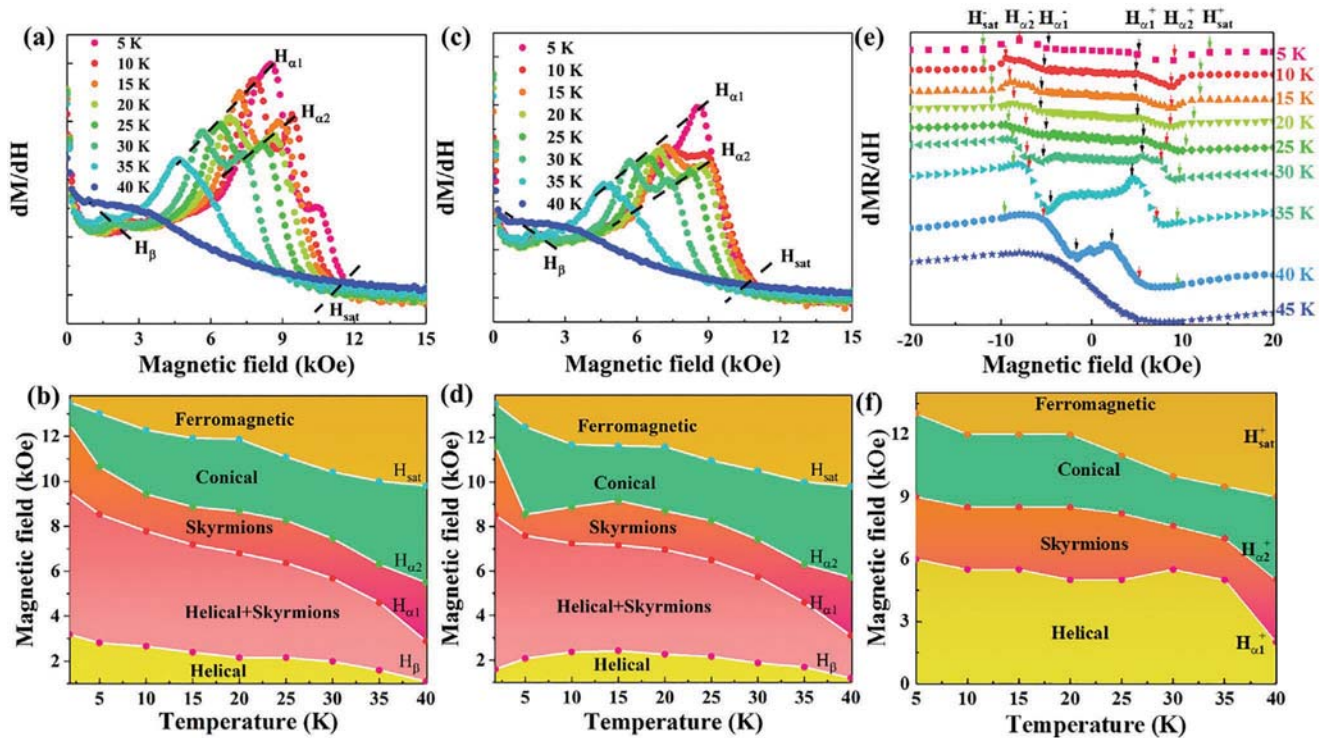
Figure 4. Static susceptibility in increasing a) and decreasing c) field sweeps for the MnSi film at various temperatures. Black dashed lines in (a) and (c) show the shift of transition fields at each temperature. Four critical fields are identified and labeled as H_β, $H_{\alpha 1}$, $H_{\alpha 2}$, and H_{sat}. $H_{\alpha 1}$ and $H_{\alpha 2}$ bound the region of stable elliptic skyrmions. The dashed lines define the boundary for metastable helicoids H_β and ferromagnetic H_{sat}. Magnetic phase diagram in increasing b) and decreasing d) field. With increasing temperature, these magnetic phases (Helical, Helical + Skyrmions, Skyrmions, Conical, and Ferromagnetic) can be formed at lower fields. e) Calculated dMR/dH from data in Figure 3 . The black, red, and green arrows stand the position of $H_{\alpha 1}$, $H_{\alpha 2}$, and H_{sat}, respectively. f) Magnetic phase diagram of the MnSi film with respect to temperatures and magnetic fields.

peak resolvable, but only a plateau, meaning the smearing out of phase boundary near the Curie temperature. With decreasing temperature, we observe two apparent peaks at $H_{\alpha 1}$ and $H_{\alpha 2}$, indicating the appearance of another phase. The first-order transitions in and out of this phase bounded by $H_{\alpha 1}$ and $H_{\alpha 2}$ indicate a difference in topology between this state and the neighbouring ferromagnetic (above $H_{\alpha 2}$) and helicoid (below $H_{\alpha 1}$) states. The phase between $H_{\alpha 1}$ and $H_{\alpha 2}$ is the so-called skyrmion phase.[15,16] Above $H_{\alpha 2}$, the skyrmion phase nearly vanishes and the system evolves via a first-order phase transition into a conical state. With increasing field from H_{β} to $H_{\alpha 1}$, the system changes into a meta-stable helicoid state. Compared with field-increase and decrease processes, these transition fields show a small difference below 15 K due to the hysteresis. However, above 15 K these transition fields do not change significantly with respect to field increase or decrease due to the coinciding of MH curves.

The temperature-dependent transition fields are plotted in Figure 4b,d. With increasing the magnetic field, the magnetic structure transforms into the Helical, Helical + Skyrmions, Skyrmions, Conical, and Ferromagnetic phase. Compared with other B20-MnSi, skyrmions in our MnSi film can be stabilized over the whole temperature range below the Curie temperature and a wider magnetic field range of around 10 kOe.[15,16] It is known that the temperature and magnetic field intervals of skyrmions become narrower with increasing the thickness of the MnSi film.[4,15] However, our MnSi film has a thickness of up to 75 nm and is thicker than other reported MnSi films.[17] This enlarged skyrmion stability in wider temperature and magnetic field ranges offers more flexibility in spintronic applications.[9,10,44] It is speculated that the reaction by flash-lamp annealing stabilizes the strain above the critical thickness, therefore increasing both the Curie temperature and the stability of skyrmions.

Indeed, by analyzing the magnetoresistance one also can investigate the field-driven evolution of the spin textures in MnSi.[41,45] As shown in Figure 4e, we examine more closely the derivative dMR/dH for the same data displayed in Figure 3f. We defined the transition fields $H_{\alpha 1}$, $H_{\alpha 2}$, and H_{sat}, as marked by the arrows. Values for positive and negative magnetic fields are denoted by the superscripts "+" and "−", respectively. However, the transition from Helical to Helical + Skyrmions is not resolved probably due to the negligible MR variation, being consistent with previous reports.[5,41,45] With increasing magnetic field, the helimagnetic phase transforms into skyrmions via a first order phase transition, manifested as peaks at $H_{\alpha 1}$ due to the completely different topological properties between helimagnetic and skyrmions. Above the critical field $H_{\alpha 2}$, the system transforms into the conical phase. Skyrmions can be stabilized at the range between $H_{\alpha 1}$ and $H_{\alpha 2}$. H_{sat} is the critical magnetic field, above which MnSi changes into the ferromagnetic state. Figure 4f shows the magnetic phase diagram of MnSi. Compared with Figure 4b,d, this magnetic phase diagram obtained from MR shows qualitatively the same temperature and magnetic-field range for skyrmions.

2.3. Discussion and Outlook

There are 4 stable Mn–Si compounds. With increasing Si concentration, Mn_3Si, Mn_5Si_3, B20-MnSi, and higher manganese silicides can form at thermal equilibrium. Characterized by tetragonal crystal structures with different c-axis lengths, higher manganese silicides have many chemical formulas such as: Mn_4Si_7, $Mn_{11}Si_{19}$, $Mn_{15}Si_{26}$, and $Mn_{27}Si_{47}$ and are generally written as $MnSi_{1.7}$.[34,46] The single B20-MnSi phase can only form at 50 at% Si and $MnSi_{1.7}$ exists from 55 to 95 at% Si. In a Mn–Si thin film grown on Si substrates, the richness of Si makes the Mn_3Si and Mn_5Si_3 phase hard to form due to the limited amount of Mn. However, $MnSi_{1.7}$ is much easier to form in these thin films. Moreover, the crystallization temperature for B20-MnSi is 1276 °C, which is higher than 1150 °C for $MnSi_{1.7}$. This means that $MnSi_{1.7}$ can nucleate prior to B20-MnSi in thermal equilibrium condition. Therefore, $MnSi_{1.7}$ often coexists with B20-MnSi in thin films grown by solid-phase epitaxy.[19] The equilibrium phase diagram of the Mn–Si system is shown in Figure S2a in the Supporting Information.

During flash-lamp annealing, the heating and cooling rates are much higher compared to conventional rapid thermal annealing and can be adjusted by controlling the energy budget, i.e., the flash energy density delivered to the sample surface. However, we cannot measure the temperature in situ. Presumably, by increasing the heating rate above a threshold (see Figure S2b, Supporting Information), the high-temperature phase can be selectively formed and the formation of low-temperature phases will be suppressed, as schematically shown in Figure S2b (Supporting Information). Therefore, this fast annealing method leads to a transient reaction between Mn and Si, serving as an effective way to separate B20-MnSi and $MnSi_{1.7}$ and to control the ratio between MnSi and $MnSi_{1.7}$ in the presence of both phases. Note that for this purpose the fast reaction and the high heating/cooling rate are important. This approach is not only limited to flash lamps. Millisecond lasers are expected to lead to similar effects and have been widely used in semiconductor industry.[47]

Both magnetron sputtering and flash-lamp annealing are ready to be scaled up to whole Si wafers. Therefore, this approach can be integrated with the existing and well-developed Si microelectronic technology. As shown in Figure 2a, our $MnSi_{1.7}$ film has a reasonable flat interface and surface. The surface oxide can be selectively etched by acids (e.g., HF). By applying lithography to pattern the Mn film and therefore the $MnSi_{1.7}$ film, one can integrate a stand-along, thermoelectric power source to Si-based devices on a single chip.[48] The top surface of B20-MnSi layer is still not smooth enough. This might be due to the slight oxidation of the Mn metal film right before annealing. However, the surface can be processed by well-developed chemical-mechanical planarization.[49] Nevertheless, the much higher Curie temperature and the broader magnetic-field and temperature window for stabilizing skyrmions in our MnSi film are profound advantages. They might be exclusively related with the ultrafast thermal processing.

3. Conclusion

In summary, by controlling the reaction parameters using strongly nonequilibrium flash-lamp annealing, we have full control over the phase formation of Mn–silicides in thin films from single-phase B20-MnSi or $MnSi_{1.7}$ to mixed phases. The

obtained films are highly textured and reveal sharp interfaces to the Si substrate. The obtained B20-MnSi films exhibit a high Curie temperature at 41 K. The skyrmion phase can be stabilized in broad temperature and magnetic-field ranges. We propose millisecond intense pulse light annealing as a general approach for phase separation in transition-metal silicides and germanides and for the growth of B20-type films with enhanced topological stability.

4. Experimental Section

Sample Preparation: In order to fabricate the MnSi films, a 30 nm thick Mn film was first deposited on a Si (111) wafer by DC magnetron sputtering. Afterward, FLA was employed to anneal the samples at different annealing parameters, rendering the reaction between Mn and Si. The FLA device is made by Rovak GmbH, and illustrated in Figure S1 (Supporting Information). During annealing, the samples were heated up by 12 Xe 30 cm long lamps in a continuous N_2 flow.[31] The annealing temperature was controlled by varying the power density. 4.2R, 4.3R, and 4.3F represent the samples with annealing parameters of 4.2 kV (Voltage applied to the capacitor of the flash lamps, to produce an intense flash pulse) from the rear side (4.2R), 4.3 kV from the rear side (4.3R) and 4.3 kV from the front side (4.3F), respectively. For all samples, the flash duration was 20 ms. 4.2 or 4.3 kV is the high voltage to charge the flash lamps, which corresponds to an energy density of 134.6 and 139.5 J cm^{-2}. Generally, a higher voltage generates a higher temperature on the surface if the absorbance of the materials are the same. The annealing from the front side (4.3F) is supposed to generate a slightly lower temperature than 4.3R due to the large reflectivity of the Mn metal film than the Si wafer. With a 20 ms pulse duration, the heating and cooling rates are estimated to be 80 000 and 160 Ks^{-1}, respectively. When the sample was annealed by flash-lamp from the rear side, the Si wafer absorbed the light and was heated-up to high temperature, then transferred the energy to the Mn layer. At high temperature, Si atoms diffused into the Mn layer. After the reaction between Mn and Si, extra Si can further diffuse to the sample surface and form crystalline Si (see Figure 2). Its formation can be minimized or eliminated by further optimizing the Mn thickness and the annealing parameters. Being different from ref. [28], in which the electrical current was used to induce heating in bulk materials and the heating rate was in the range of 250–700 Ks^{-1}, a light pulse was used. The approach is better suitable for thin-film materials and can reach much higher heating rates, which are crucial for the phase selection of synthesized silicides and germanides.

Structure Characterization: X-ray diffraction (XRD) and transmission electron microscopy (TEM) were employed to analyze the microstructure of the obtained films. XRD was performed at room temperature on a Bruker D8 Advance diffractometer with a Cu-target source. The measurements were done in Bragg–Brentano-geometry with a graphite secondary monochromator and a scintillator detector. Bright-field and high-resolution TEM imaging were performed on an image-C$_s$-corrected Titan 80–300 microscope (FEI) operated at an accelerating voltage of 300 kV. High-angle annular dark-field scanning transmission electron microscopy (HAADF-STEM) imaging and spectrum imaging analysis based on energy-dispersive X-ray spectroscopy (EDXS) were done at 200 kV with a Talos F200X microscope equipped with an X-FEG electron source and a Super-X detector system (FEI).

Magnetic and Transport Property Measurements: The magnetization of the films was measured by a superconducting quantum interference device equipped with a vibrating sample magnetometer (SQUID-VSM) with the field parallel (in-plane) or perpendicular (out-of-plane) to the films. For the zero field cooling (ZFC) measurements, the samples were cooled down to 5 K under a zero field, then different fields were applied and magnetization data were collected during the warming-up process. When reaching 100 K, the samples were recooled to 5 K at the same field while the data recording was continued. This process was

called field cooling (FC). The transport properties of the MnSi film were investigated by a Lake Shore Hall measurement system. Magnetic-field dependent resistance was measured between 5 and 300 K using the van der Pauw geometry. In the resistivity measurement the magnetic field was applied along the sample surface plane (in-plane).

Supporting Information

Supporting Information is available from the Wiley Online Library or from the author.

Conflict of Interest

The authors declare no conflict of interest.

Data Availability Statement

Research data are not shared.

[1] A. N. Bogdanov, D. A. Yablonskii, *Sov. Phys. JETP* **1989**, *68*, 101.
[2] U. K. Rößler, A. N. Bogdanov, C. Pfleiderer, *Nature* **2006**, *442*, 797.
[3] S. Mühlbauer, B. Binz, F. Jonietz, C. Pfleiderer, A. Rosch, A. Neubauer, R. Georgii, P. Böni, *Science* **2009**, *323*, 915.
[4] X. Z. Yu, Y. Onose, N. Kanazawa, J. H. Park, J. H. Han, Y. Matsui, N. Nagaosa, Y. Tokura, *Nat. Mater.* **2011**, *10*, 106.
[5] M. J. Stolt, S. Schneider, N. Mathur, M. J. Shearer, B. Rellinghaus, K. Nielsch, S. Jin, *Adv. Funct. Mater.* **2019**, *29*, 1805418.
[6] M. Yang, Q. Li, R. V. Chopdekar, R. Dhall, J. Turner, J. D. Carlström, C. Ophus, C. Klewe, P. Shafer, A. T. N'Diaye, J. W. Choi, G. Chen, Y. Z. Wu, C. Hwang, F. Wang, Z. Q. Qiu, *Sci. Adv.* **2020**, *6*, eabb5157.
[7] M. Raju, A. Yagil, A. Soumyanarayanan, A. K. Tan, A. Almoalem, F. Ma, O. Auslaender, C. Panagopoulos, *Nat. Commun.* **2019**, *10*, 696.

[8] W. Legrand, D. Maccariello, N. Reyren, K. Garcia, C. Moutafis, C. Moreau-Luchaire, S. Collin, K. Bouzehouane, V. Cros, A. Fert, *Nano Lett.* **2017**, *17*, 2703.

[9] F. Jonietz, S. Mühlbauer, C. Pfleiderer, A. Neubauer, W. Münzer, A. Bauer, T. Adams, R. Georgii, P. Böni, R. A. Duine, K. Everschor, M. Garst, A. Rosch, *Science* **2010**, *330*, 1648.

[10] A. Fert, V. Cros, J. Sampaio, *Nat. Nanotechnol.* **2013**, *8*, 152.

[11] Y. Luo, S. Z. Lin, M. Leroux, N. Wakeham, D. M. Fobes, E. D. Bauer, J. B. Betts, J. D. Thompson, A. Migliori, B. Maiorov, *Commun. Mater.* **2020**, *1*, 83.

[12] D. Maccariello, W. Legrand, N. Reyren, K. Garcia, K. Bouzehouane, S. Collin, V. Cros, A. Fert, *Nat. Nanotechol.* **2018**, *13*, 233.

[13] E. Ruff, S. Widmann, P. Lunkenheimer, V. Tsurkan, S. Bordács, I. Kézsmárki, A. Loidl, *Sci. Adv.* **2015**, *1*, e1500916.

[14] A. Neubauer, C. Pfleiderer, B. Binz, A. Rosch, R. Ritz, P. G. Niklowitz, P. Böni, *Phys. Rev. Lett.* **2009**, *102*, 186602.

[15] X. Yu, A. Kikkawa, D. Morikawa, K. Shibata, Y. Tokunaga, Y. Taguchi, Y. Tokura, *Phys. Rev. B* **2015**, *91*, 054411.

[16] Y. Li, N. Kanazawa, X. Z. Yu, A. Tsukazaki, M. Kawasaki, M. Ichikawa, X. F. Jin, F. Kagawa, Y. Tokura, *Phys. Rev. Lett.* **2013**, *110*, 117202.

[17] M. N. Wilson, E. A. Karhu, A. S. Quigley, U. K. Rößler, A. B. Butenko, A. N. Bogdanov, M. D. Robertson, T. L. Monchesky, *Phys. Rev. B* **2012**, *86*, 144420.

[18] E. A. Karhu, S. Kahwaji, M. D. Robertson, H. Fritzsche, B. J. Kirby, C. F. Majkrzak, T. L. Monchesky, *Phys. Rev. B* **2011**, *84*, 060404(R).

[19] E. A. Karhu, S. Kahwaji, T. L. Monchesky, C. Parsons, M. D. Robertson, C. Maunders, *Phys. Rev. B* **2010**, *82*, 184417.

[20] S. Higashi, Y. Ikedo, P. Kocan, H. Tochihara, *Appl. Phys. Lett.* **2008**, *93*, 013104.

[21] P. Villars, *Springer Science Materials*, Springer, Heidelberg **2016**.

[22] S. Tang, I. Kravchenko, J. Yi, G. Cao, J. Howe, D. Mandrus, N. Materials, O. Ridge, *Nano Res.* **2014**, *7*, 1788.

[23] N. L. Okamoto, T. Koyama, K. Kishida, K. Tanaka, H. Inui, *Acta Mater.* **2009**, *57*, 5036.

[24] Z. Li, J. F. Dong, F. H. Sun, Asfandiyar, Y. Pan, S. F. Wang, Q. Wang, D. Zhang, L. Zhao, J. F. Li, *Adv. Sci.* **2018**, *5*, 1800626.

[25] G. Kim, H. Kim, H. Lee, J. Kim, K. Lee, J. W. Roh, W. Lee, *Nano Energy* **2020**, *72*, 104698.

[26] A. S. Sukhanov, P. Vir, A. Heinemann, S. E. Nikitin, D. Kriegner, H. Borrmann, C. Shekhar, C. Felser, D. S. Inosov, *Phys. Rev. B* **2019**, *100*, 180403(R).

[27] H. E. Kissinger, *Anal. Chem.* **1957**, *29*, 1702.

[28] I. V. Okulov, I. V. Soldatov, M. F. Sarmanova, I. Kaban, T. Gemming, K. Edström, J. Eckert, *Nat. Commun.* **2015**, *6*, 7932.

[29] X. Monnier, D. Cangialosi, B. Ruta, R. Busch, S. Gallino, *Sci. Adv.* **2020**, *6*, eaay1454.

[30] S. Sohn, Y. Xie, Y. Jung, J. Schroers, J. J. Cha, *Nat. Commun.* **2017**, *8*, 1980.

[31] L. Rebohle, S. Prucnal, W. Skorupa, *Semicond. Sci. Technol.* **2016**, *31*, 103001.

[32] L. Zhang, D. G. Ivey, *J. Mater. Res.* **1991**, *6*, 1518.

[33] M. Salvo, F. Smeacetto, F. D'Isanto, G. Viola, P. Demitri, F. Gucci, M. J. Reece, *J. Eur. Ceram. Soc.* **2019**, *39*, 66.

[34] U. Gottlieb, A. Sulpice, B. Lambert-Andron, O. Laborde, *J. Alloys Compd.* **2003**, *361*, 13.

[35] Z. Hou, W. Ren, B. Ding, G. Xu, Y. Wang, B. Yang, Q. Zhang, Y. Zhang, E. Liu, F. Xu, W. Wang, G. Wu, X. Zhang, B. Shen, Z. Zhang, *Adv. Mater.* **2017**, *29*, 1701144.

[36] S. X. Huang, C. L. Chien, *Phys. Rev. Lett.* **2012**, *108*, 267201.

[37] N. Kanazawa, S. Seki, Y. Tokura, *Adv. Mater.* **2017**, *29*, 1603227.

[38] A. I. Figueroa, S. L. Zhang, A. A. Baker, R. Chalasani, A. Kohn, S. C. Speller, D. Gianolio, C. Pfleiderer, G. van der Laan, T. Hesjedal, *Phys. Rev. B* **2016**, *94*, 174107.

[39] H. M. Eiter, P. Jaschke, R. Hackl, A. Bauer, M. Gangl, C. Pfleiderer, *Phys. Rev. B* **2014**, *90*, 024411.

[40] T. Tite, G. J. Shu, F. C. Chou, Y. M. Chang, *Appl. Phys. Lett.* **2010**, *97*, 031909.

[41] H. F. Du, J. P. DeGrave, F. Xue, D. Liang, W. Ning, J. Y. Yang, M. L. Tian, Y. H. Zhang, S. Jin, *Nano Lett.* **2014**, *14*, 2026.

[42] D. Okuyama, M. Bleuel, J. S. White, Q. Ye, J. Krzywon, G. Nagy, Z. Q. Im, I. Živkovi'c, M. Bartkowiak, H. M. Rønnow, S. Hoshino, J. Iwasaki, N. Nagaosa, A. Kikkawa, Y. Taguchi, Y. Tokura, D. Higashi, J. D. Reim, Y. Nambu, T. J. Sato, *Commun. Phys.* **2019**, *2*, 79.

[43] K. Kadowaki, K. Okuda, M. Date, *J. Phys. Soc. Jpn.* **1982**, *51*, 2433 .

[44] A. Fert, N. Reyren, V. Cros, *Nat. Rev. Mater.* **2017**, *2*, 17031.

[45] H. Du, D. Liang, C. Jin, L. Kong, M. J. Stolt, W. Ning, J. Yang, Y. Xing, J. Wang, R. Che, J. Zang, S. Jin, Y. Zhang, M. Tian, *Nat. Commun.* **2015**, *6*, 7637.

[46] S. Zhou, K. Potzger, G. Zhang, A. Mücklich, F. Eichhorn, N. Schell, R. Grötzschel, B. Schmidt, W. Skorupa, M. Helm, J. Fassbender, *Phys. Rev. B* **2007**, *75*, 0852032007.

[47] O. Gluschenkov, H. Jagannathan, *ECS Trans.* **2018**, *85*, 11.

[48] T. Taniguchi, T. Ishibe, N. Naruse, Y. Mera, Md. M. Alam, K. Sawano, Y. Nakamura, *ACS Appl. Mater. Interfaces* **2020**, *12*, 25428.

[49] P. Zantye, A. Kumar, A. Sikder, *Mater. Sci. Eng. R* **2004**, *45*, 89.

2009723 (8 of 8)

RESEARCH ARTICLE

Flexible Magnetoreceptor with Tunable Intrinsic Logic for On-Skin Touchless Human-Machine Interfaces

Pavlo Makushko, Eduardo Sergio Oliveros Mata, Gilbert Santiago Cañón Bermúdez, Mariam Hassan, Sara Laureti, Christian Rinaldi, Federico Fagiani, Gianni Barucca, Nataliia Schmidt, Yevhen Zabila, Tobias Kosub, Rico Illing, Oleksii Volkov, Igor Vladymyrskyi, Jürgen Fassbender, Manfred Albrecht, Gaspare Varvaro,* and Denys Makarov*

Artificial magnetoception is a new and yet to be explored path for humans to interact with the surroundings. This technology is enabled by thin film magnetic field sensors embedded in a soft and flexible format to constitute magneto-sensitive electronic skins (e-skins). Being limited by the sensitivity to in-plane magnetic fields, magnetosensitive e-skins are restricted to basic proximity and angle sensing and are not used as switches or logic elements of interactive wearable electronics. Here, a novel magnetoreceptive platform for on-skin touchless interactive electronics based on flexible spin valve switches with sensitivity to out-of-plane magnetic fields is demonstrated. The technology relies on all-metal Co/Pd-based spin valves with a synthetic antiferromagnet possessing perpendicular magnetic anisotropy. The flexible magnetoreceptors act as logic elements, namely momentary and permanent (latching) switches. The switches maintain their performance even upon bending to a radius of less than 3.5 mm and withstand repetitive bending for hundreds of cycles. Here, flexible switches are integrated in on-skin interactive electronics and their performance as touchless human-machine interfaces is demonstrated, which are intuitive to use, energy efficient, and insensitive to external magnetic disturbances. This technology offers qualitatively new functionalities for electronic skins and paves the way towards full-fledged on-skin touchless interactive electronics.

1. Introduction

Flexible electronics is a game changer for prospective personal appliances and human-machine interfaces.[1–4] There are already numerous demonstrations of mechanically imperceptible, wearable, and even on-skin interactive systems exploiting tactile,[5–8] optical,[9] electrical,[10–12] and magnetic[13–16] stimuli. Mechanically compliant magnetoresistive sensors were used as touchless human-machine interfaces enabling the interaction with magnetic objects by means of proximity sensing, motion, and orientation tracking features.[13,15,17,18] Although basic interactive functionality has been demonstrated, the current on-skin magnetoreceptors are not employed as advanced spintronics-enabled switches and logic elements for skin compliant electronics. The major limitation remains on the material science side, primarily due to the use of

P. Makushko, E. S. Oliveros Mata, Dr. G. S. Cañón Bermúdez,
Dr. Y. Zabila, Dr. T. Kosub, Dr. R. Illing, Dr. O. Volkov, Prof. J. Fassbender,
Dr. D. Makarov
Helmholtz-Zentrum Dresden-Rossendorf e.V.
Institute of Ion Beam Physics and Materials Research
Dresden, Germany
E-mail: d.makarov@hzdr.de
P. Makushko, Dr. I. Vladymyrskyi
Paton Institute of material Science and Electric Welding
National Technical University of Ukraine "Igor Sikorsky Kyiv Polytechnic
Institute"
Prospect Peremogy 37, Kyiv 03056, Ukraine
M. Hassan, Dr. S. Laureti, Dr. G. Varvaro
Consiglio Nazionale delle Ricerche
Istituto di Struttura della Materia
nM2-Lab, Via Salaria km 29, 300 Monterotondo Scalo, Roma 00015, Italy
E-mail: gaspare.varvaro@ism.cnr.it

M. Hassan, Prof. G. Barucca
Università Politecnica delle Marche
Dipartimento SIMAU
Via Brecce Bianche 12, Ancona 60131, Italy
Prof. C. Rinaldi, Dr. F. Fagiani
Department of Physics
Politecnico di Milano
c/o via G. Colombo 81, Milano 20133, Italy
Dr. N. Schmidt, Prof. M. Albrecht
Institute of Physics
University of Augsburg
Universitätsstraße 1 Nord, D-86159 Augsburg, Germany
Dr. Y. Zabila
The H. Niewodniczanski Institute of Nuclear Physics
Polish Academy of Sciences
Krakow 31-342, Poland

Annual Report IIM 2021, HZDR-118   39

**ADVANCED
SCIENCE NEWS**
www.advancedsciencenews.com

**ADVANCED
FUNCTIONAL
MATERIALS**
www.afm-journal.de

magnetic layer stacks, which are in-plane magnetized and, hence, are mainly sensitive to magnetic fields oriented in the sensor plane.[13,15,16,19–35] The use of proximity sensors with in-plane sensitivity encumbers the readout of touchless on-skin switches, as magnetic objects approaching from directions other than the out-of-plane axis can falsely trigger switching. Introducing flexible Hall effect sensors[36–39] could provide a solution to this conundrum, however, they cannot be intrinsically tuned to be bistable as needed for switches, and thus require additional flexible electronic modules. Considering the lower performance of flexible electronics compared to their rigid counterparts in terms of integration density and speed,[16,40,41] full-fledged interactive systems should be built based on smart sensors with intrinsic logic functionality, which can be tailored by the material properties rather than by the circuit design.

In rigid electronics, including hard disk drives and magnetic random access memory elements, magnetic switches are typically built on spin valve (SV) layer stacks with out-of-plane easy axis of magnetization.[42] The switching between two logical states "1" and "0" is uniquely encoded in the orientation of magnetization being pointing either up or down. This lifts any ambiguity in the interpretation of the logic state of the switch and makes SV switches an indispensable component of any spintronic circuit. These advanced sensing elements are substantially more demanding in the accuracy of the layer thickness and the interface quality. By now, reports are focused on the realization of flexible spin valve sensors with in-plane sensitivity only.[33,43–45] The demonstration of mechanically flexible SVs with out-of-plane easy axis remains a major material science challenge in the community of flexible magnetoelectronics.

Here, we realize the first mechanically flexible SV switch sensitive to out-of-plane magnetic fields. The device consists of a Co/Pd-based spin valve stack with a synthetic antiferromagnetic reference layer possessing perpendicular magnetic anisotropy deposited onto a flexible polyethylene naphthalate (PEN) foil. By tuning the magnetic coupling in the SV layer stack via the choice of the thickness of the Cu spacer layer, we can tailor the flexible device to act as a momentary as well as permanent (latching) switch. The magnetoresistive performance of the SV switches does not degrade upon mechanical bending up to 3.5 mm. Furthermore, the devices withstand more than 600 bending cycles without sacrificing their performance. We demonstrate the advantages of the tunable logic functionality offered by our flexible SV switches by integrating them in an on-skin interactive system. The latching switches enable the realization of magnetic interfaces to permanently switch ON/OFF an electronic circuit in a touchless way. Due to the intrinsic memory function, the magnetic latching switches can reliably operate in an environment with strong magnetic disturbances. Momentary switches respond exclusively to one polarity of the magnetic field and can be used to temporarily switch on a virtual display when the SV switch is in proximity to a magnetic ON button. This operation mode is very useful for energy saving while interacting with displays, which is highly relevant for portable and wearable electronics. In this respect, the developed technology platform offers qualitatively new functionalities for on-skin touchless interactive systems, namely dedicated out-of-plane sensitivity and high tunability of the logic characteristics.

2. Results and Discussions

2.1. Flexible Magnetoreceptors

To realize flexible spin valves sensitive to out-of-plane magnetic fields, we deposited a layer stack consisting of a compensated synthetic antiferromagnet (SAF) $[Co(0.4)/Pd(0.9)]_4/Ru(0.4)/[Co(0.4)/Pd(0.9)]_3/Co(0.4)$ and a magnetic sensing layer $[Co(0.4)/Pd(0.9)]_2$ (numbers in brackets are thicknesses in nm) on PEN flexible foils with a thickness of 125 μm (**Figure 1**a). The thickness of the Cu spacer layer between the SAF and the magnetic sensing layer was changed between 2 and 5 nm to tailor the strength of the coupling between the two magnetic layers. Cross sectional transmission electron microscopy (TEM) images of the layer stack deposited on a PEN foil reveal firm adhesion of the metal layer stack to the foil and sharp interfaces in the SV stack (Figure 1b and Figure S1, Supporting Information) as needed for high magnetoresistive performance. A photograph of the flexible SV on a polymeric foil is shown in Figure 1c. Due to the thinness of the layer stack (about 30 nm), the samples are partly transparent (Figure S2, Supporting Information). Even when deposited on a PEN foil, the flexible SV switches maintain the magnetic properties of their rigid counterparts prepared on reference Si/SiO_x wafers (compare Figures S3 and S4, Supporting Information, for samples with different Cu spacer thickness). A typical three-step magnetization reversal behavior of the spin valve is observed in the magnetic hysteresis loops (Figure 1d,e (top panels) and Figure S5, Supporting Information). The corresponding magnetoresistive curves in Figure 1d,e (bottom panels) illustrate a sharp resistance switching as the magnetization of the magnetic sensing layer is reversed. The magnetoresistive (MR) ratio is defined as $MR = (R_{\uparrow\downarrow} - R_{\uparrow\uparrow})/R_{\uparrow\uparrow}$ where $R_{\uparrow\downarrow}$ and $R_{\uparrow\uparrow}$ are the values of the electrical resistance corresponding to the antiparallel and parallel alignment of the magnetization of the ferromagnetic layers at the top and bottom interfaces of the Cu spacer layer. An MR ratio of about 2.5% is obtained for the samples with a Cu spacer thickness of 2 and 3 nm prepared on flexible PEN foils.

The switching fields of the sensing layer define the operation mode of the SV switch (momentary or latching). Tailoring the thickness of the Cu spacer layer allows adjusting the switching fields of the sensing layer in a wide range. We note that a qualitative change in the behavior of the SV is observed when the thickness of the Cu spacer layer changed from 2 to 3 nm (Figures S3 and S5, Supporting Information). Further increase in the Cu spacer thickness does not change the qualitative behavior of the SVs, but slightly decreases the magnitude of the MR effect due to the enhanced current shunting and scattering effects with the increase of Cu spacer layer thickness.[46] The SV switch with a 2 nm thick Cu spacer layer reveals a shifted minor loop with both switching fields of the ascending and descending branches of the magnetoresistive curves positioned in the range of negative fields (Figure 1f, red line). In this case, the magnetoresistive switching can be actuated only by the application of a magnetic field oriented opposite to the magnetization of the SAF reference layer. This SV operates as a momentary switch, which responds to a magnetic field of a certain direction and will not be affected by a field of opposite polarity.

Increasing the Cu spacer thickness to 3 nm reduces the strength of the magnetic bias in the stack associated to
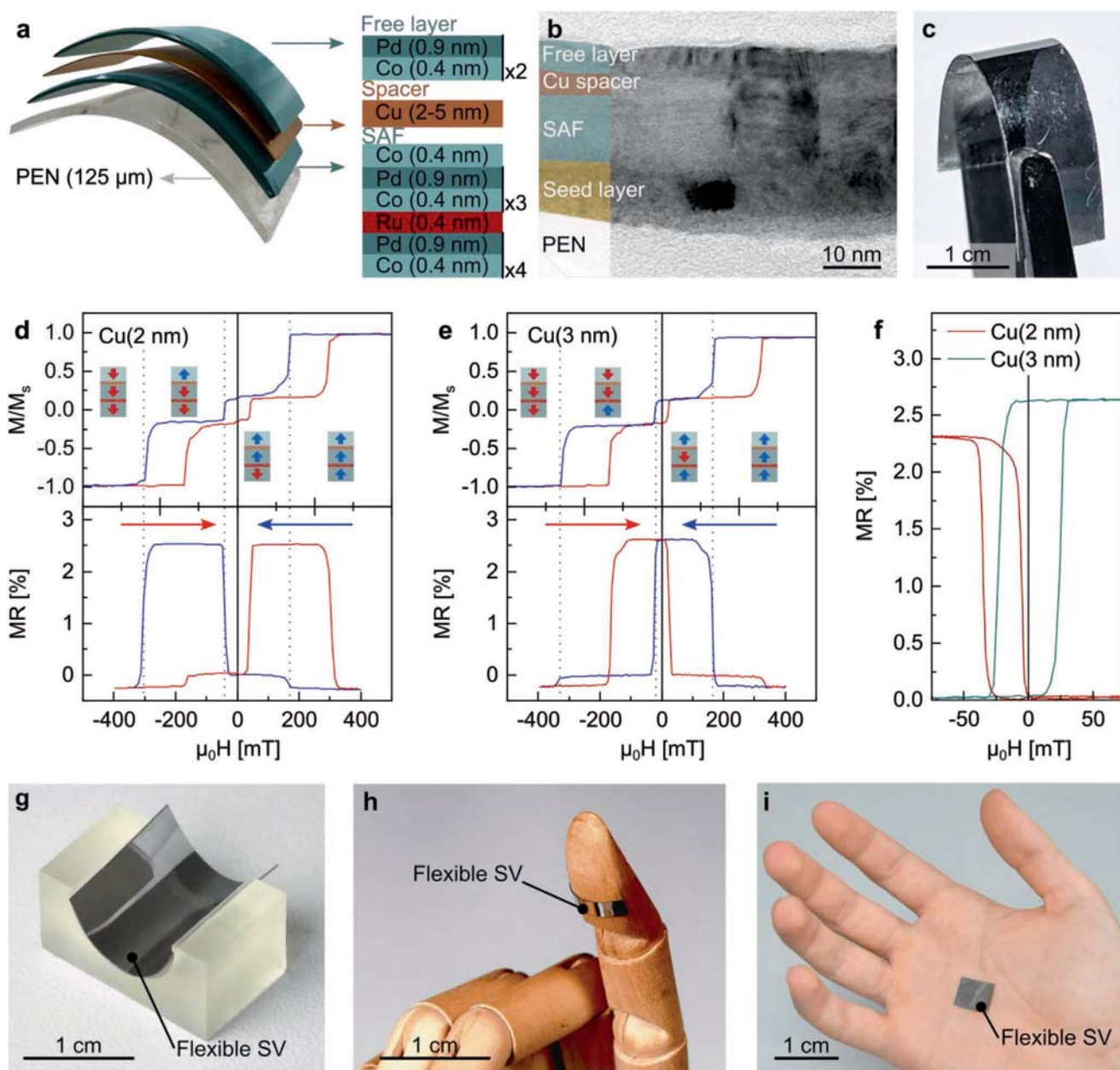
Figure 1. Flexible spin valves with out-of-plane sensitivity. a) Schematic representation of the Co/Pd-based spin valve stack. b) Cross-sectional TEM image of the spin valve deposited on a PEN flexible substrate. c) Optical micrograph of a flexible SV switch. Magnetic hysteresis loops (top panels) and corresponding magnetoresistive curves (bottom panels) measured of SV switches with a Cu spacer layer thickness of d) 2 and e) 3 nm. Magnetic field was applied perpendicular to the sample plane. Arrows indicate the direction of the magnetic field sweeping for ascending (red) and descending (blue) branches of the measured curves. Inset schematics in panels (d) and (e) represent a 3-step magnetization reversal process corresponding to blue branch of the hysteresis loops (further details are provided in Figure S5, Supporting Information). f) Magnetoresistive (MR) performance of the SV switches measured in a limited magnetic field range up to 150 mT after saturation of SAF in a positive field of +0.5 T. The samples with 2-nm and 3-nm-thick Cu spacer layer act as momentary and latching switches, respectively. Mechanical flexibility allows the spin valves to be integrated in g) processing tools, h) robotics, and i) on-skin interactive systems.

the magnetic coupling between the SAF reference layer and the free layer. The magnetoresistance curves become symmetric with respect to zero field. In this case, the initially programmed resistance state of the device is retained even after the magnetic field is removed. This SV operates as a latching switch, a key element of electronic circuits, typically used to maintain a state with lower current consumption and circuit complexity compared to momentary switches. These elements are especially needed for flexible electronics to minimize the number of active elements for sensor conditioning. One of the major advantages given by the magnetic latching switch is that it becomes insensitive to magnetic disturbances, provided they do not exceed the switching field of the SV. Our samples are designed to have their switching fields in the range of 20 mT, which is substantially

larger than regular magnetic disturbances stemming from, e.g. power lines, electric transport, wireless communication systems.

We note that the latching functionality of the SV switch remains unchanged even when the sample is exposed to a magnetic field oriented under an angle to the easy axis (out-of-plane). The width of the magnetoresistive hysteresis of the magnetic sensing layer (minor loop) favorably increases up to about 40 mT when the magnetic field is applied at 80° with respect to the sample normal (Figures S6 and S7, Supporting Information). This makes the switch even more resilient against magnetic disturbances under realistic settings when the device is exposed to complex three-dimensional magnetic fields.

Due to their mechanical flexibility, these SV switches can find applications in various fields where conformal coating of a curved surface is needed, e.g. for processing tools (Figure 1g), robotics (Figure 1h), and on-skin electronics (Figure 1i).

2.2. Mechanical Performance of Flexible SV Switches

To assess their mechanical performance, the flexible SV switches were bent by moving two ends of the foil closer together from their initial flat state until a maximum bending radius of 3.5 mm was reached. Representative photographs showing a side view of the sample in a bent state are shown in **Figure 2**a. The photograph is color coded with respect to the change of the curvature radius along the sample. The corresponding strain in the metal stack for different curvature radii is shown in Figure 2b (see also Figure S8, Supporting Information). Scanning electron microscopy (SEM) images of the sample bent to 4 mm radius reveal no appearance of cracks or delamination (Figure 2c). The metal stack remains firmly attached to the polymeric foil. At a bending radius of 4 mm, the metal layer stack experiences a tensile strain of about 1.5%. When the sample is further bent to a 3.5 mm radius, the metal layer fractures (Figure 2d).

The MR ratio was measured in the bent state and after flattening the sample (Figure 2e). The MR ratio remains constant at the level of 2.5% independent of the bending radius. At the same time, the electrical resistance of the sample slightly increases in the bent state but fully recovers when the SV is flattened (Figure 2f). At the critical bending radius of 3.5 mm the electrical resistance of the SV sharply increases and is not fully recovered to its initial value upon flattening (Figure 2f, shaded region). However, functionality of the device is not affected and the MR ratio remains on the same level even when the sample is bent to 3.5 mm (Figure 2e). The increase of the sample resistance when approaching a 3.5 mm bending radius is caused by the appearance of a periodic fracture pattern in the metal films (Figure 2d and Figure S9, Supporting Information). Still, after the sample is flattened, the cracks close, which leads to the partial recovery of the sample resistance.

The impact of the cyclic bending on the MR performance of the SV switches was investigated by repeatedly bending the sample between radii of 28 mm and 14 mm for more than 600 cycles. The electrical resistance of the sample was continuously monitored revealing the stable device operation with a resistance change of 0.8% only (Figure 2g). Even after 600 bending cycles, the 2.5% MR effect remains and does not change compared to the flat samples.
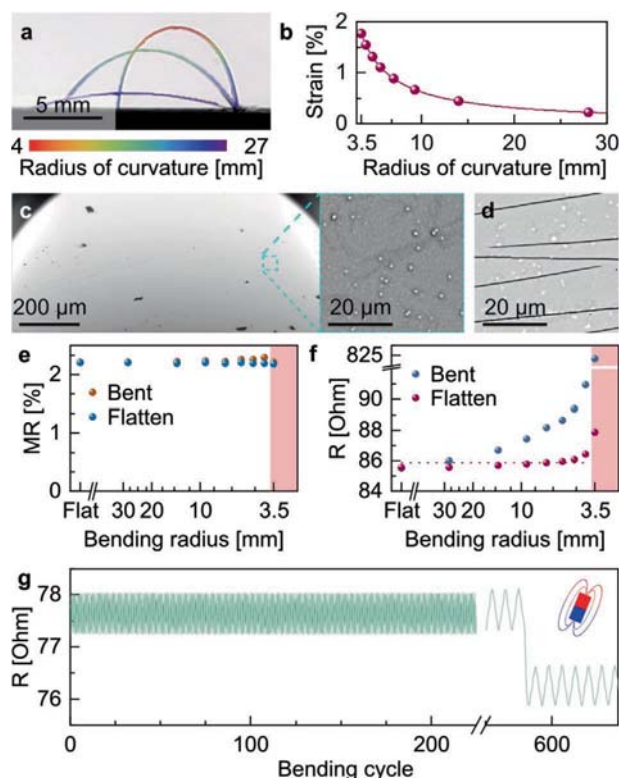
Figure 2. Mechanical and magnetoresistive performance of flexible spin valves upon bending. a) Optical photographs showing the sample at different bending radii. The photographs are color coded with the distribution of the radius of curvature along the SV. b) Tensile strain in the metal film as a function of radius of curvature. c) Overview SEM micrograph of the bent surface of the spin valve. The sample is bent to a radius of 4 mm. Inset shows a top view SEM micrograph focused on the most curved region of the sample. d) SEM micrograph of the fracture pattern on the sample bent to a radius of 3.5 mm. e) MR ratio and f) electrical resistance measured of the SV switch bent to the indicated radius. The measurement was carried out in the bent state (red symbols) and after the sample was flattened out (blue symbols). g) Cyclic bending test showing the change of the electrical resistance of the SV during more than 600 bending cycles between radii 28 and 14 mm. The zoom around the 600th bending cycle indicates the change of the SV resistance when the device is exposed to the field of a permanent magnet with a strength of about 100 mT at the device location.

2.3. Interactive Smart Skin Demonstration

We explore the application potential of these SV switches with different thickness of the Cu spacer layer as functional elements of interactive on-skin electronics. In contrast to regular proximity sensors based on giant magnetoresisitive (GMR) multilayers (Figure S10, Supporting Information), SV switches act as logic elements of the electronic circuit without the need of additional electronic components. For instance, momentary switches will respond to one user-defined polarity of the magnetic field. However, latching switches will enable the realization of magnetic ON/OFF interfaces, which are not sensitive to the magnetic noise stemming from the surroundings. The reliable operation of magnetosensitive smart skins in complex environments with magnetic disturbances remains one of the key hurdles of current technologies for flexible magnetoelectronics.

ADVANCED SCIENCE NEWS
www.advancedsciencenews.com

ADVANCED FUNCTIONAL MATERIALS
www.afm-journal.de

We devise magnetosensitive smart skins with SV switches by attaching them to a pointing finger (**Figure 3**a). The device is connected in a 4-point configuration for the measurement of electrical resistance as it hovers over an interactive surface with magnetic stimuli. The surface contains two magnetic buttons indicated as "ON" and "OFF", which are represented by a permanent magnet with its South and North pole facing up, respectively (Figure 3b). These buttons can be used to switch on and off a virtual display showing a navigation route in a touchless way by approaching a finger with an on-skin
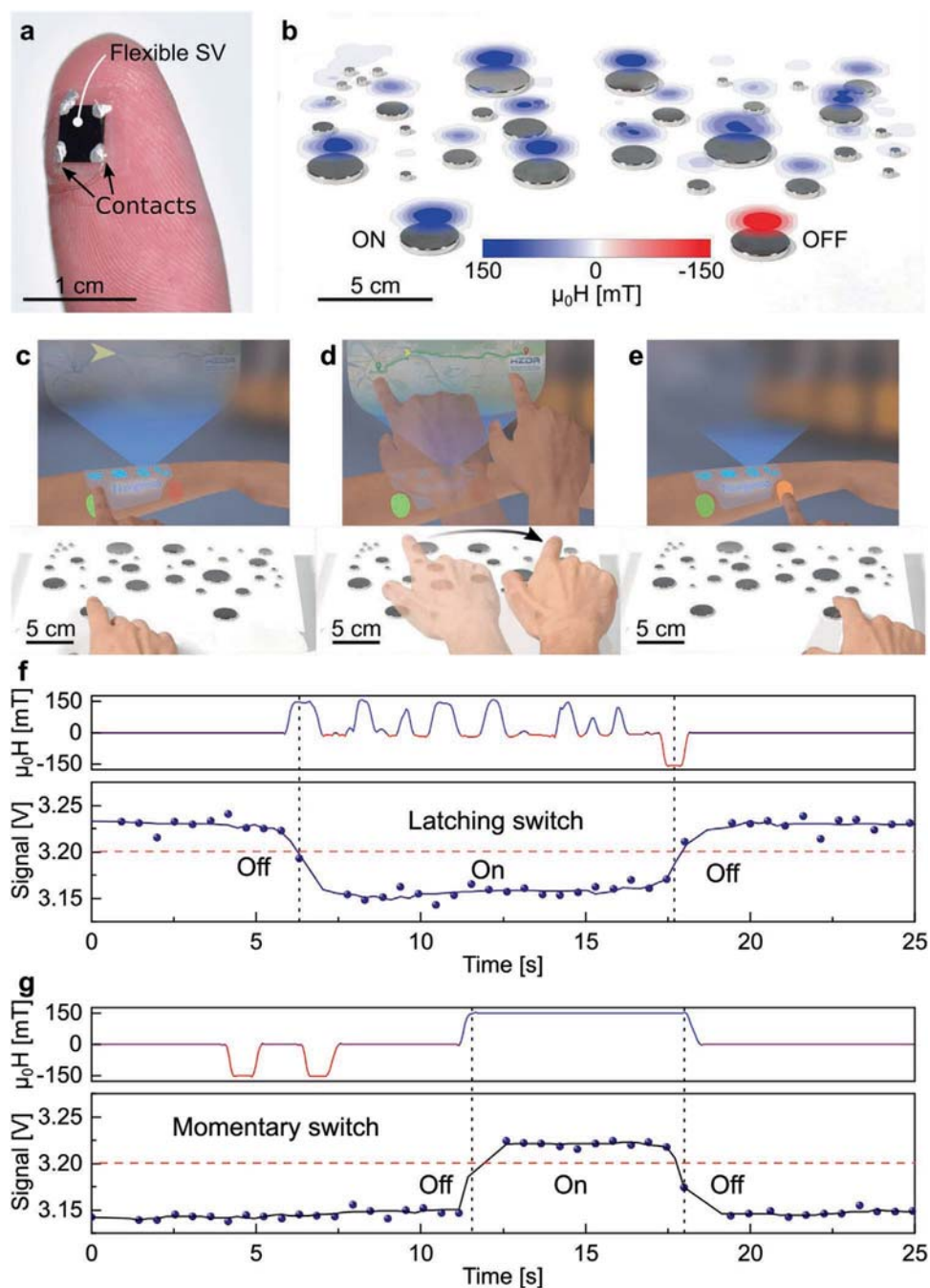
Figure 3. Momentary and latching switching capabilities. a) Flexible SV switch affixed on a pointing finger and contacted in a 4-point configuration. b) Array of magnets used in the demonstration. The color map represents the distribution of the out-of-plane component of the magnetic field measured 1 cm above the magnets surface. c–f) Latching switch performance of the SV with 3 nm thick Cu spacer. (c–e) Snapshots of the Movie S2, Supporting Information, showing the interactive process by switching ON and OFF the navigation software on a virtual display. f) Top panel represents the temporal variation of the magnetic field, which is experienced by the SV switch upon its motion above the array of magnets. Bottom panel shows the corresponding voltage readout. g) Momentary switching performance of the SV with 2 nm thick Cu spacer. Timeline of the magnetic field applied to the SV (top panel) and corresponding signal readout (bottom panel). The corresponding video sequence is shown in Movie S4, Supporting Information.

**ADVANCED
SCIENCE NEWS**
www.advancedsciencenews.com

**ADVANCED
FUNCTIONAL
MATERIALS**
www.afm-journal.de

magnetosensitive element. To mimic magnetic disturbances, we assembled an array of permanent magnets of different sizes and strength as shown in Figure 3b. The contour plot over each magnet represents the spatial profile of the magnetic stray field 1 cm above the surface of the magnets (Figure S11, Supporting Information).

We note that the use of any magnetic field sensor including regular GMR multilayers enables the possibility to switch on and off the display (Movie S1 and Figure S12, Supporting Information). However, without additional electronic logic to condition the sensor, proximity sensors fail to operate in the presence of magnetic disturbances. Thus, after switching on the display upon approaching the GMR multilayer sensor to the ON button, the process of moving the finger above the array of permanent magnets leads to intermittent on-off switching of the virtual display.

In stark contrast, when using latching switches prepared based on the SV with a Cu spacer thickness of 3 nm, the device reveals a stable performance and is not affected by magnetic disturbances (Figure 3c–f and Movies S2 and S3, Supporting Information). In this case, the magnetoreceptor can be used to permanently switch the virtual display on upon approaching the magnetic ON button. The switching between ON and OFF states is recognized by crossing a pre-defined threshold of 3.2 V. The signal remains constant even as the SV is removed from the magnetic ON button and moved above the array of magnets. Accordingly, the virtual display stays ON independent of magnetic disturbances. To switch off the navigation panel, the magnetic OFF button is approached with the SV switch, which returns the signal to its initial value. In this example, the discrimination of the signal level and rejection of magnetic noise is done without any additional electronic components, just by using a flexible SV switch operating in the latching mode.

Another appealing functionality is offered by the momentary switch. This device is realized using a SV switch with a 2 nm thick Cu spacer layer. We program the SV device to respond to the positive magnetic field (corresponding to the ON button). These devices can be used to temporarily switch the virtual display on by approaching to the ON button but elicit no response when nearing the OFF button (Figure 3g and Movie S4, Supporting Information). This is a major advantage compared to the regular GMR multilayers, which possess a symmetric response curve and would equally be activated by magnetic fields of any polarity. Momentary switches can help to save energy by switching on the display only during the time when the SV is in the proximity to the ON button. The display goes off as soon as the finger is displaced away from the ON button.

3. Conclusions

In this work, we demonstrate the first flexible magnetoresistive spin valve switch operating with out-of-plane magnetic fields. By tailoring the magnetic exchange coupling in the complex layer stack, we realize SVs operating as latching (or permanent) switches and momentary switches. In this case, the magnetoresistive functional elements can perform basic logic operations (permanent or temporary switches) using a single material science platform. The enabled out-of-plane magnetic

field sensitivity of our flexible SVs makes the decision process upon interaction with magnetic objects obvious and unambiguous. To achieve stable mechanical performance of our SV devices, we rely on all-metallic layer stack based on Co/Pd multilayers with out-of-plane easy axis of magnetization. Furthermore, to avoid using antiferromagnets due to their brittleness, we utilize high performance synthetic antiferromagnets fabricated on flexible polymeric foils. Our SV devices prepared on 125 µm thick PEN foils withstand bending to 3.5 mm as well as repetitive bending tests over more than 600 cycles without sacrificing their magnetoresistive performance.

This technology expands the functionality of magnetoreceptive e-skins beyond basic proximity and orientation sensing. By tailoring the strength of the exchange bias between the sensing and reference layers of the spin valve, we were able to embed momentary and latching operation modes, thus reducing the complexity of external logic circuits. Unambiguous interpretation of the out-of-plane magnetic field provides intuitive on-off logic states and simplifies the use of the device. This new kind of flexible magnetoreceptive functional elements shows great potential for use in human-machine interfaces or virtual- and augmented reality applications. We showcase the advantages of this technology for the realization of on-skin interactive magnetoelectronics, which are touchless, energy efficient (momentary switches) and insensitive to external magnetic disturbances (latching switches).

4. Experimental Section

Fabrication: Spin valve switches consist of $[Pd(0.9)/Co(0.4)]_4/Ru(0.4)/[Co(0.4)/Pd(0.9)]_3/Co(0.4)/Cu/[Co(0.4)/Pd(0.9)]_2$ stacks (in brackets, the thicknesses of individual layers is indicated in nanometers). The thickness of the Cu spacer layer was varied from 2 to 5 nm. The samples were deposited at room temperature by DC magnetron sputtering (BESTEC, Germany) on 125 µm thick polyethylene naphthalate (PEN) polymeric foils purchased from Teijin corporation (Teonex). The surface roughness of the PEN foils was <0.7 nm. In line with the findings on CoFeB/Pt-based SAFs,[47] a Ta(10 nm) / Pd(2.1 nm) seed layer was used to favor the growth of [Co/Pd] multilayers with [111] texture. The thickness of the individual layers and the number of repetitions in the [Co/Pd] stack were selected to ensure i) perpendicular magnetic anisotropy; ii) strong and compensated antiferromagnetic coupling in the SAF structure; and iii) two stable parallel/antiparallel magnetization configurations in the spin valve layer stack.[48] A capping layer of Pd (2.1 nm) was deposited to prevent the magnetic free layer from oxidation. All the layers were deposited under an Ar pressure of 3.5×10^{-3} mbar while the deposition rate was set to 0.067 nm s^{-1} (24 W) for Au, 0.03 nm s^{-1} (40 W) for Ta, 0.04 nm s^{-1} (26 W) for Pd, 0.025 nm s^{-1} (52 W) for Co, and 0.03 nm s^{-1} (48 W) for Ru. The magnetic and magnetoresistive performance of the samples are shown in Figures S3 and S4, Supporting Information. The observed change of the magnetic and magneto-resistive properties between the samples prepared on rigid and flexible support might be ascribed to a slightly higher average surface roughness of Teonex tapes ($\approx$0.7 nm accordingly to the data sheet) with respect to SiO$_x$/Si(100) rigid substrates (0.2–0.3 nm). The higher surface roughness could lead to surface inhomogeneity extending over the whole structure deposited on top, which might affect the PMA of the Co/Pd multilayers,[49] the individual layer reversal,[50] the interlayer exchange coupling in the synthetic antiferromagnetic reference layer,[51] and the magneto-resistive properties of the whole GMR spin-valve stack.[52] In particular, the increased interface roughness might explain the reduction of the GMR ratio as well as the changes of the MR curves for t_{Cu} = 2 nm, which could originate from an interlayer coupling between the free layer and the top

SAF layer induced by interlayer magnetostatic interactions (orange-peel Néel coupling) or a direct exchange coupling through the formation of pinholes in the Cu spacer layer.

GMR multilayers consist of [Co(1 nm)/Cu(2.2 nm)]$_{50}$ stacks coupled at the 2nd antiferromagnetic maximum. The layer stack was deposited on a polyester foil (Melinex ST505) with a thickness of 175 µm by DC magnetron sputtering at room temperature (Ar was used as a sputter gas; Ar pressure was 8×10^{-4} mbar; base pressure was 10^{-7} mbar; deposition rate was 0.2 nm s^{-1}). The magnetoresistive curve of the samples is shown in Figure S9, Supporting Information.

Transparency Measurements: Due to the difference in the thickness of the layer stack, the SV switches and GMR multilayers revealed a different level of transparency (Figure S2, Supporting Information). In these measurements, a reflective neutral density optical filter (Thorlabs, USA) was placed between an HXP 120 V (Zeiss, Germany) light source and the sample, to reduce the intensity of the source. The incoming light was transmitted through the sample, collected and analyzed with a USB 650 spectrometer (Ocean Insight, USA). Two segments of the optical fiber were placed before and after the sample to guide and gathered the incoming and transmitted light, respectively.

Electron Microscopy: TEM analysis was performed by means of a Philips CM200 microscope on cross sectioned films. TEM samples were prepared relying on a thinning procedure consisting of mechanical thinning by grinding papers, diamond pastes, and a dimple grinder. Final thinning was carried out with a precision ion polishing system (GATAN 691). SEM images were obtained using a Phenom XL Desktop Scanning Electron Microscope. For imaging of the samples in a bent state, the SV was fixed in a tensile tester sample holder and bent to the desired radius of curvature.

Integral Magnetic Properties: Magnetic hysteresis loops were investigated at room temperature by using a vibrating sample magnetometer (Model 10, MicroSense) equipped with a rotating electromagnet that could supply a maximum field of 2 T.

Magnetoresistive Responses: Magnetoresistive performance of the SVs in the bent state was investigated by applying an out-of-plane magnetic field with an electromagnet powered by bipolar power supply (Kepco, USA). A maximum field of 500 mT (150 mT) was applied for full (minor) loop measurements. The resistance of the SVs was monitored in a 4-wire configuration using a tensormeter setup (HZDR Innovation GmbH, Germany). Room temperature magneto-transport properties were measured on square-shaped samples employing the van der Pauw method in current-in-plane geometry. Currents in the order of 10 mA were injected using a Keithley 6221 current source, while voltages were measured by a Keithley 2182A nanovoltmeter. The magnetic field was provided by a dipole electromagnet (GMW Associates, USA).

Bending Performance: Static mechanical bending tests were performed using a custom built bending setup. SV switches were horizontally fixed using two clamps and bent to the desired curvature radius by gradual decrease of the distance between the clamps. The change of the bending radius along the sample was determined from the analysis of the optical photographs of the bent sample (Figure S7, Supporting Information). Magnetoresistive performance was measured in bent and flattened states. The characterization of the SV under dynamic bending conditions was performed using a Tensile Sample Holder of the Phenom XL SEM. The SV was mounted in the same manner as for static bending experiments. The sample holder was programmed to repeatedly bend the SV between 28 and 14 mm bending radii. A 4-wire resistance of the SV was continuously monitored using a digital multimeter (Keysight 34461A; Keysight Technologies, USA).

Interactive Magnetoreceptor Demonstrators: A flexible SV switch with a lateral dimension of 4×4 mm^2 was fixed on a pointing finger and electrically connected in a four-point configuration using 50 µm thick copper wires with a conductive silver paste. To mimic spatially varying magnetic disturbances, an array of NdFeB magnets of different dimensions was assembled (HKCM Engineering e.K., Germany). All magnets in the array were oriented with their South pole facing up. Two magnets (indicated in Figure 3 with "On"/"Off") represent interactive magnetic buttons to start/stop a navigation software. These

two magnets were oriented in the following way: "On" magnet with its south pole facing up and "Off" magnet with its north pole facing up.

For the measurement of the sensor response, the current to the SV was supplied by a Source/Measure unit (B2902A, Keysight Technologies, USA) and the voltage was first pre-amplified and then readout by a DAQ (National Instruments, USB-6009, USA). The sensor response was analyzed by a NI LabVIEW (2019 SP1 version) script, which was controlling the frames of the representative animation. Crossing the pre-defined voltage threshold of 3.2 V was recognized as either an "On" or "Off" command. Prior to the demonstration both of the switches were programmed to respond to positive magnetic field by subjecting them to −450 mT using a permanent magnet.

Mapping the Magnetic Stray Fields: The magnetic stray field produced by the array of magnets in Figure 3 (see also Figure S10, Supporting Information) was measured with a Gaussmeter (HGM09s, MAGSYS, Germany) mounted on a micromanipulator. The Hall probe of the Gaussmeter was swept in the plane parallel to the plane of the magnets at a distance of 1 cm. In this measurement, only the out-of-plane component of the magnetic stray field was detected.

Strain Calculation: The strain distribution along the SV upon bending was estimated using the following equation:[53]

$$\varepsilon = \frac{(d_\mathrm{f}+d_\mathrm{s})}{2R}\frac{(1+2\eta+\chi\eta^2)}{(1+\eta)(1+\chi\eta)} \tag{1}$$

where $\eta = d_\mathrm{SV}/d_\mathrm{s}$ and $\chi = Y_\mathrm{SV}/Y_\mathrm{s}$. d_SV is the total thickness of the spin valve metal stack and d_s is the substrate thickness (125-µm-thick PEN). The Young's modulus of the metallic film (Y_SV) was calculated to be 180 GPa, assuming a composite structure of the stack and taking into account the mechanical properties of the corresponding bulk metals (177 GPa for Pd, 211 GPa for Co, 414 GPa for Ru, 110 GPa for Cu, and 186 GPa for Ta). The Young's modulus of the PEN substrate (Y_s) was taken as 2.2 GPa. ε is the surface strain in metal layers when the structure is bent to a radius R.

Use of On-Skin Electronics: The measurements using on-skin electronics were performed with the consent of all volunteers who participated in the study.

Supporting Information

Supporting Information is available from the Wiley Online Library or from the author.

Acknowledgements

Conflict of Interest

The authors declare no conflict of interest.

Data Availability Statement

The data that support the findings of this study are available from the corresponding author upon reasonable request.

**ADVANCED
SCIENCE NEWS**

www.advancedsciencenews.com

**ADVANCED
FUNCTIONAL
MATERIALS**

www.afm-journal.de

Keywords

[1] Y. Liu, S. Mo, S. Shang, P. Wang, W. Zhao, L. Li, *J. Sci.: Adv. Mater. Devices* **2020**, *5*, 451.

[2] W. Gao, H. Ota, D. Kiriya, K. Takei, A. Javey, *Acc. Chem. Res.* **2019**, *52*, 523.

[3] J. A. Rogers, T. Someya, Y. Huang, *Science* **2010**, *327*, 1603.

[4] Q. Hua, J. Sun, H. Liu, R. Bao, R. Yu, J. Zhai, C. Pan, Z. L. Wang, *Nat. Commun.* **2018**, *9*, 244.

[5] M. Kaltenbrunner, T. Sekitani, J. Reeder, T. Yokota, K. Kuribara, T. Tokuhara, M. Drack, R. Schwödiauer, I. Graz, S. Bauer-Gogonea, S. Bauer, T. Someya, *Nature* **2013**, *499*, 458.

[6] Y. Wan, Y. Wang, C. F. Guo, *Mater. Today Phys.* **2017**, *1*, 61.

[7] J. Zhao, H. Guo, Y. K. Pang, F. Xi, Z. W. Yang, G. Liu, T. Guo, G. Dong, C. Zhang, Z. L. Wang, *ACS Nano* **2017**, *11*, 11566.

[8] Z. Wang, T. Wang, M. Zhuang, H. S. Xu, *ACS Appl. Mater. Interfaces* **2019**, *11*, 45301.

[9] J.-H. Seo, E. Swinnich, Y.-Y. Zhang, M. Kim, *Mater. Res. Lett.* **2020**, *8*, 123.

[10] B. Zhang, Z. Xiang, S. Zhu, Q. Hu, Y. Cao, J. Zhong, Q. Zhong, B. Wang, Y. Fang, B. Hu, J. Zhou, Z. Wang, *Nano Res.* **2014**, *7*, 1488.

[11] M. S. Sarwar, Y. Dobashi, C. Preston, J. K. M. Wyss, S. Mirabbasi, J. D. W. Madden, *Sci. Adv.* **2017**, *3*, e1602200.

[12] J. Ge, L. Sun, F.-R. Zhang, Y. Zhang, L.-A. Shi, H.-Y. Zhao, H.-W. Zhu, H.-L. Jiang, S.-H. Yu, *Adv. Mater.* **2015**, *28*, 722.

[13] M. Melzer, M. Kaltenbrunner, D. Makarov, D. Karnaushenko, D. Karnaushenko, T. Sekitani, T. Someya, O. G. Schmidt, *Nat. Commun.* **2015**, *6*, 6080.

[14] D. Makarov, M. Melzer, D. Karnaushenko, O. G. Schmidt, *Appl. Phys. Rev.* **2016**, *3*, 11101.

[15] G. S. C. Bermúdez, D. D. Karnaushenko, D. Karnaushenko, A. Lebanov, L. Bischoff, M. Kaltenbrunner, J. Fassbender, O. G. Schmidt, D. Makarov, *Sci. Adv.* **2018**, *4*, eaao2623.

[16] M. Kondo, M. Melzer, D. Karnaushenko, T. Uemura, S. Yoshimoto, M. Akiyama, Y. Noda, T. Araki, O. G. Schmidt, T. Sekitani, *Sci. Adv.* **2020**, *6*, eaay6094.

[17] G. S. C. Bermúdez, H. Fuchs, L. Bischoff, J. Fassbender, D. Makarov, *Nat. Electron.* **2018**, *1*, 589.

[18] J. Ge, X. Wang, M. Drack, O. Volkov, M. Liang, G. S. C. Bermúdez, R. Illing, C. Wang, S. Zhou, J. Fassbender, M. Kaltenbrunner, D. Makarov, *Nat. Commun.* **2019**, *10*, 4405.

[19] Z. Wang, X. Wang, M. Li, Y. Gao, Z. Hu, T. Nan, X. Liang, H. Chen, J. Yang, S. Cash, N.-X. Sun, *Adv. Mater.* **2016**, *28*, 9370.

[20] N. Pérez, M. Melzer, D. Makarov, O. Ueberschär, R. Ecke, S. E. Schulz, O. G. Schmidt, *Appl. Phys. Lett.* **2015**, *106*, 153501.

[21] S. Ota, M. Ono, H. Matsumoto, A. Ando, T. Sekitani, R. Kohno, S. Iguchi, T. Koyama, D. Chiba, *Appl. Phys. Express* **2019**, *12*, 053001.

[22] G. V. Kurlyandskaya, E. Fernández, A. Svalov, A. B. Beitia, A. García-Arribas, A. Larrañaga, *J. Magn. Magn. Mater.* **2016**, *415*, 91.

[23] S. S. P. Parkin, K. P. Roche, T. Suzuki, *Jpn. J. Appl. Phys.* **1992**, *31*, L1246.

[24] F. Yan, G. Xue, F. Wan, *J. Mater. Chem.* **2002**, *12*, 2606.

[25] T. Uhrmann, L. Bär, T. Dimopoulos, N. Wiese, M. Rührig, A. Lechner, *J. Magn. Magn. Mater.* **2006**, *307*, 209.

[26] Y.-f. Chen, Y. Mei, R. Kaltofen, J. I. Mönch, J. Schumann, J. Freudenberger, H.-J. Klauß, O. G. Schmidt, *Adv. Mater.* **2008**, *20*, 3224.

[27] B. Özkaya, S. R. Saranu, S. Mohanan, U. Herr, *Phys. Status Solidi (a)* **2008**, *205*, 1876.

[28] C. Barraud, C. Deranlot, P. Seneor, R. Mattana, B. Dlubak, S. Fusil, K. Bouzehouane, D. Deneuve, F. Petroff, A. Fert, *Appl. Phys. Lett.* **2010**, *96*, 072502.

[29] a) A. Bedoya-Pinto, M. Donolato, M. Gobbi, L. E. Hueso, P. Vavassori, *Appl. Phys. Lett.* **2014**, *104*, 062412; b) A. Bedoya-Pinto, M. Donolato, M. Gobbi, L. E. Hueso, P. Vavassori, *Appl. Phys. Lett.* **2014**, *104*, 119902.

[30] T. Griesbach, M. C. Wurz, L. Rissing, *IEEE Trans. Magn.* **2012**, *48*, 3843.

[31] A. Alfadhel, J. Kosel, *Adv. Mater.* **2015**, *27*, 7888.

[32] B. Li, M. N. Kavaldzhiev, J. Kosel, *J. Magn. Magn. Mater.* **2015**, *378*, 499.

[33] H. Li, Q. Zhan, Y. Liu, L. Liu, H. Yang, Z. Zuo, T. Shang, B. Wang, R.-W. Li, *ACS Nano* **2016**, *10*, 4403.

[34] M. Melzer, D. Makarov, O. G. Schmidt, *J. Phys. D: Appl. Phys.* **2019**, *53*, 083002.

[35] P. N. Granell, G. Wang, G. S. C. Bermudez, T. Kosub, F. Golmar, L. Steren, J. Fassbender, D. Makarov, *npj Flexible Electron.* **2019**, *3*, 3.

[36] M. Melzer, J. I. Mönch, D. Makarov, Y. Zabila, G. S. C. Bermúdez, D. Karnaushenko, S. Baunack, F. Bahr, C. Yan, M. Kaltenbrunner, O. G. Schmidt, *Adv. Mater.* **2014**, *27*, 1274.

[37] Z. Wang, M. Shaygan, M. Otto, D. Schall, D. Neumaier, *Nanoscale* **2016**, *8*, 7683.

[38] H. Heidari, E. Bonizzoni, U. Gatti, F. Maloberti, R. Dahiya, *IEEE Sens. J.* **2016**, *16*, 8736.

[39] I. J. Monch, F. Bahr, M. Melzer, D. Karnaushenko, D. Makarov, W. Hofmann, O. G. Schmidt, *IEEE Trans. Magn.* **2015**, *51*, 1.

[40] G. A. Salvatore, N. Münzenrieder, T. Kinkeldei, L. Petti, C. Zysset, I. Strebel, L. Büthe, G. Tröster, *Nat. Commun.* **2014**, *5*, 2982.

[41] L. Petti, N. Münzenrieder, C. Vogt, H. Faber, L. Büthe, G. Cantarella, F. Bottacchi, T. D. Anthopoulos, G. Tröster, *Appl. Phys. Rev.* **2016**, *3*, 021303.

[42] G. Varvaro, *Ultrahigh-Density Magnetic Recording : Storage Materials and Media Designs*, Pan Stanford Publishing CRC Press, Taylor & Francis Group, London **2016**.

[43] S. S. P. Parkin, *Appl. Phys. Lett.* **1996**, *69*, 3092.

[44] M. Melzer, G. Lin, D. Makarov, O. G. Schmidt, *Adv. Mater.* **2012**, *24*, 6468.

[45] W. Cheng, Z. Zhou, M. Pan, H. Yang, Y. Xie, B. Wang, Q. Zhan, R.-W. Li, *J. Phys. D: Appl. Phys.* **2018**, *52*, 095003.

[46] H. Ehrenreich, *Solid State Physics : Advances in Research and Applications*, Academic Press, London **2001**.

[47] T. Vemulkar, R. Mansell, A. Fernández-Pacheco, R. P. Cowburn, *Adv. Funct. Mater.* **2016**, *26*, 4704.

[48] G. Varvaro, S. Laureti, D. Peddis, M. Hassan, G. Barucca, P. Mengucci, A. Gerardino, E. Giovine, O. Lik, D. Nissen, M. Albrecht, *Nanoscale* **2019**, *11*, 21891.

[49] J. Qiu, Z. Meng, Y. Yang, J. F. Ying, Q. J. Yap, G. Han, *AIP Adv.* **2016**, *6*, 056123.

[50] S. Nakagawa, H. Yoshikawa, *J. Magn. Magn. Mater.* **2005**, *287*, 193.

[51] M. Desai, A. Misra, W. D. Doyle, *IEEE Trans. Magn.* **2005**, *41*, 3151.

[52] E. Y. Tsymbal, D. G. Pettifor, *Solid State Phys.* **2001**, *56*, 113.

[53] Z. Suo, E. Y. Ma, H. Gleskova, S. Wagner, *Appl. Phys. Lett.* **1999**, *74*, 1177.

Time Refraction of Spin Waves

K. Schultheiss,[1,*] N. Sato,[1] P. Matthies,[1,2] L. Körber,[1,2] K. Wagner,[1] T. Hula,[1] O. Gladii,[1] J. E. Pearson,[3]
A. Hoffmann,[3,†] M. Helm,[1,2] J. Fassbender,[1,2] and H. Schultheiss[1,2]

[1]*Helmholtz-Zentrum Dresden - Rossendorf, Institute of Ion Beam Physics and Materials Research, 01328 Dresden, Germany*
[2]*Fakultät Physik, Technische Universität Dresden, 01062 Dresden, Germany*
[3]*Materials Science Division, Argonne National Laboratory, Argonne, Illinois 60439, USA*

We present an experimental study of time refraction of spin waves (SWs) propagating in microscopic waveguides under the influence of time-varying magnetic fields. Using space- and time-resolved Brillouin light scattering microscopy, we demonstrate that the broken translational symmetry along the time coordinate results in a loss of energy conservation for SWs and thus allows for a broadband and controllable shift of the SW frequency. With an integrated design of SW waveguide and microscopic current line for the generation of strong, nanosecond-long, magnetic field pulses, a conversion efficiency up to 39% of the carrier SW frequency is achieved, significantly larger compared to photonic systems. Given the strength of the magnetic field pulses and its strong impact on the SW dispersion relation, the effect of time refraction can be quantified on a length scale comparable to the SW wavelength. Furthermore, we utilize time refraction to excite SW bursts with pulse durations in the nanosecond range and a frequency shift depending on the pulse polarity.

The manipulation of waves can be achieved by modulating the properties of the medium in which the wave propagates either in space or in time. Changes along the space coordinates affect the momentum of the wave due to the lost translational invariance of space but conserve the energy of the wave. Well-known examples are the diffraction of waves at opaque obstacles or the refraction of light according to Snell's law. While these phenomena are classified by the term "space refraction," its counterpart is known as "time refraction," which conserves the momentum of the wave but changes its energy due to the lost translational invariance of time [1]. A key requirement for time refraction is to temporarily change the medium parameters, which affect the dispersion relation of the wave, in an adiabatic manner, i.e., slower than the oscillation period of the wave but faster than its lifetime. Recently, Zhou *et al.* reported on the experimental observation of time refraction of photons using a subwavelength-thick indium tin oxide film in its epsilon-near-zero (ENZ) spectral range [2]. Making use of the strong nonlinear light-matter interactions in the ENZ state, the authors were able to reach frequency conversion efficiencies up to 6% of the carrier frequency, clearly exceeding previous works reporting efficiencies around 0.145% [3]. At the same time, Zhou *et al.* kept the interaction length of photons and refractive medium smaller than the photon wavelength, which is especially challenging in photonic systems. In ferromagnets, however, which host spin waves (SWs) as collective excitations of the spin system, the strong coupling of SWs to the magnetic field and their rather small phase velocity

compared to the speed of light allows for even higher relative frequency shifts and a full spatiotemporal study of time refraction.

The dispersion relation of SWs depends strongly on the effective magnetic field, the magnitude and direction of the magnetization, and the thickness and lateral dimensions of the SW waveguide [4]. Typically, SWs have frequencies in the gigahertz range and their phase and group velocities are comparable to the speed of sound in solids. Space refraction of SWs was already demonstrated in the last two decades for spatially inhomogeneous magnetic fields [5], changes of the waveguide width [6], spatial variations of the magnetization generated by heat gradients [7], directional changes of the magnetization [8,9], and thickness variations along the SW propagation path [10,11]. In all these studies, changes of the SW momenta were reported under conservation of the SW energy. However, there are only few reports on time refraction of SWs in macroscopic yttrium-iron-garnet waveguides dating back up to 50 years [12–14]. Given the lack of spatially resolved methods for mapping SW propagation at that time, these studies could only analyze the change of the SW energy after propagation of 1 cm. These experiments demonstrated frequency shifts without significant distortions of the SW pulse up to 90 MHz for a carrier frequency of 1.2 GHz, yielding a conversion efficiency of 7.5%.

In this Letter, we report on micron sized SW waveguides with integrated current lines for generating large and rapidly changing magnetic fields using current pulses. For the first time, we present a full spatiotemporal

quantification of time refraction of SWs using time-resolved Brillouin light scattering (TR-μBLS) microscopy [15]. We demonstrate relative changes of the SW frequency up to 39% over propagation distances comparable to the SW wavelength. Depending on the polarity of the dc pulses, the SW energy can be increased or decreased within a few nanoseconds.

The experimental layout is shown in Fig. 1. We pattern a ferromagnetic $Ni_{81}Fe_{19}$ waveguide (width $w = 2$ μm, thickness $t = 30$ nm) on top of a Cr(10 nm)/Au(25 nm) conduction line ($w = 3.2$ μm), as can be seen in the scanning electron micrograph in Fig. 1. A current pulse flowing in the conduction line generates a pulsed Oersted field H_{Oe}, which is aligned either parallel or antiparallel to the direction of an external magnetic field H_{ext}, depending on the polarity of the current pulse. This allows for a rapid change of the total magnetic field inside the $Ni_{81}Fe_{19}$ waveguide. Note that the broadening of the Au conduction line in y direction is not relevant for this study since all measurements were performed in the 6.4 μm-long part before the broadening begins.

A microwave current flowing through a CPW (see Fig. 1) excites SWs with a fixed frequency $f_{rf} = 3.65$ GHz and a preferential wave vector $k_{max} = 1.04$ rad/μm. The shaded area in Fig. 2 plots the normalized excitation efficiency of the CPW on a linear scale to illustrate its wave vector dependence. It is calculated via a fast Fourier transform of the Oersted field generated by the currents flowing in the CPW. To determine the resonance field for these specific excitation conditions, we use BLS microscopy to measure the SW intensity in 1 μm distance to the CPW as a function of the external magnetic field H_{ext}, without applying any dc current pulses. As can be seen from the results in Fig. 2(a), SWs are excited most efficiently at the resonance field $\mu_0 H_{res} = 22.4$ mT.

In order to compare this to the dispersion relation, we need to take into account the strong influence of the demagnetizing field and the quantization of the SW wave vector across the waveguide width. Therefore, we simulate the static magnetization inside the waveguide for external fields between 10 and 50 mT using MuMax^3[16,17]. Black squares in Fig. 2(b) show the effective field B_{eff}, which is determined in the center of the waveguide. The effective quantization width w_{eff} is given by red triangles in Fig. 2(b) and is derived from the positions at which the y component of the magnetization reaches 99% of the saturation magnetization $m_y = 0.99 M_S$. For $H_{ext} \leq H_{crit} = 14$ mT, the external field is too weak to compensate the demagnetizing fields so that the magnetization is aligned predominantly along the waveguide.

Based on the results for B_{eff} and w_{eff}, we plot dispersion relations for various magnetic fields $16 \leq \mu_0 H_{tot} \leq 50$ mT in Fig. 2(c). The calculations follow the formalism of Kalinikos and Slavin [4], taking into account the quantization of the wave vector across the waveguide width

$k_y = \pi/w_{eff}$ and using the same material parameters as in the micromagnetic simulations [17]. The excitation conditions for SWs in our system ($f_{rf} = 3.65$ GHz, $k_{max} = 1.04$ rad/μm) match the dispersion calculated for $\mu_0 H_{ext} = 22$ mT [thicker green line in Fig. 2(c)], which is in good agreement with the measured resonance field $\mu_0 H_{res} = 22.4$ mT.

First, we demonstrate the influence of the pulsed Oersted fields in TR-μBLS measurements of the thermal SW signal. Figure 2(d) shows the temporal evolution of the thermal SW spectrum for $\mu_0 H_{ext} = 22.4$ mT with the BLS intensity color coded. Up to $t = 0$ ns, only the external field determines the SW frequencies with a minimum at 3.0 GHz. At $t = 0$ ns, a current pulse is applied with 20 ns duration, 3 ns rise and fall time, and amplitude $I_{dc} = 64.2$ mA. Inside the $Ni_{81}Fe_{19}$ waveguide, this generates an Oersted field $\mu_0 H_{Oe} = 12.2$ mT, which is aligned parallel to the external field and thus increases the overall magnetic field. Hence, in this 20 ns window, the SW spectrum is shifted to higher frequencies rising at around 4.6 GHz. To better visualize this shift, we integrate the BLS intensity inside (dc on) and outside (dc off) the 20 ns window and plot both spectra in Fig. 2(e). The frequencies of the rising flanks of the spectra measured without (3.0 GHz) and with (4.6 GHz) additional dc pulse are in excellent agreement with the onsets of the dispersion relation at $\mu_0 H_{tot} = 22.4$ and 34.6 mT, respectively.

In a next step, we study how SWs adapt to temporal changes of the magnetic field if a continuous microwave signal is applied to the CPW at $f_{rf} = 3.65$ GHz. Therefore, we distinguish different sequences of time-varying magnetic fields: the external magnetic field matches the resonance condition so that any additional dc pulse shifts SWs out of resonance [see arrows A and B in Fig. 2(a)] or the initial external magnetic field is larger than the
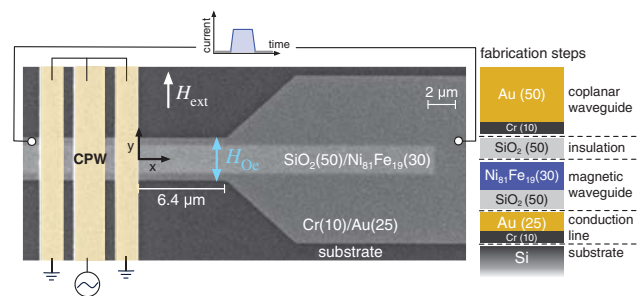
FIG. 1. Scanning electron microscopy (SEM) image of the investigated structure. A $Ni_{81}Fe_{19}$ waveguide (width $w = 2$ μm, thickness $t = 30$ nm) is fabricated on top of a Cr(10 nm)/Au(25 nm) conduction line ($w = 3.2$ μm), insulated by 50 nm SiO_2. SWs are excited by a coplanar waveguide (CPW) and propagate along the $+x$ direction, with $x = 0$ μm defined by the right edge of the CPW. An external magnetic field H_{ext} is applied along the $+y$ direction. Fabrication steps on the right highlight the insulation layers, which are not visible in the SEM image.
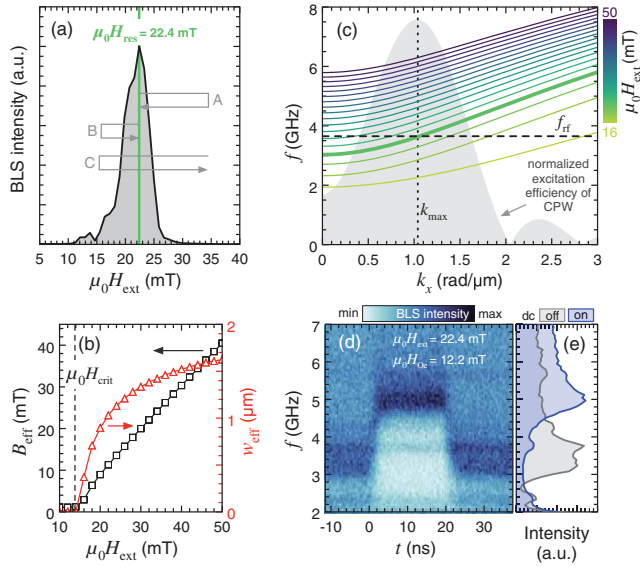
FIG. 2. (a) BLS intensity measured for SWs excited at $f_{rf} = 3.65$ GHz as a function of the externally applied field. The arrows A–C depict different sequences of the time-varying magnetic fields. (b) Effective field B_{eff} and effective localization width w_{eff} determined from micromagnetic simulations for different external magnetic fields. (c) Dispersion relations calculated considering the resulting B_{eff} and w_{eff} as in (b). The dotted vertical line indicates the wave vector k_{max}, which is excited most efficiently by the CPW. The horizontal dashed line indicates the excitation frequency f_{rf}, fixed in all measurements at 3.65 GHz. (d) BLS measurement of the thermal SW intensity as a function of frequency and time with the BLS intensity color coded. (e) Frequency spectra integrated in time windows when the dc pulse is on and off, respectively.

resonance field, and the dc pulse is injected so that the associated Oersted field reduces the total magnetic field to cross the resonance condition [see arrow C in Fig. 2(a)].

We start with the case when the external field is set to the resonance field $\mu_0 H_{ext} = \mu_0 H_{res} = 22.4$ mT and the dc pulse generates an Oersted field $\mu_0 H_{Oe} = 12.2$ mT parallel to the external field [arrow A in Fig. 2(a)]. The pulse duration is 20 ns with 3 ns rise and fall time. Figure 3(a) shows the corresponding intensity plot of the μBLS signal, which was measured in $x = 4$ μm distance from the edge of the CPW. Up to $t = 0$ ns, i.e., before injecting the dc pulse, a strong BLS signal is detected at 3.65 GHz, as expected for resonant excitation.

During the 3 ns rise time of the dc pulse, we detect a rapid increase of the SW frequency. This frequency shift is due to the parallel alignment of external field and Oersted field $H_{Oe} \uparrow\uparrow H_{ext}$, which causes an increase of the total magnetic field H_{tot} and shifts the dispersion to higher frequencies. However, unlike in the case of thermal SWs, the SW signal vanishes shortly after the dc pulse sets in. Only as long as $\mu_0 H_{tot} = \mu_0 H_{res} = 22.4$ mT (i.e., $t < 0$ ns), SWs are resonantly excited by the CPW. With the additional Oersted field, $H_{tot} > H_{res}$ and no more SWs
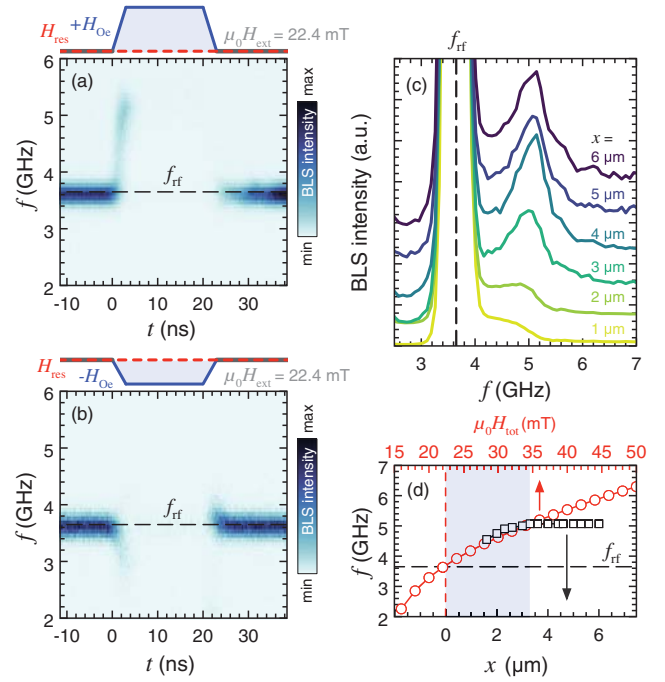
FIG. 3. TR-BLS signal measured at $x = 4$ μm for (a) $H_{Oe} \uparrow\uparrow H_{ext}$ with $\mu_0 H_{Oe} = 12.2$ mT and (b) $H_{Oe} \uparrow\downarrow H_{ext}$ with $\mu_0 H_{Oe} = 6.8$ mT. The excitation was fixed at $f_{rf} = 3.65$ GHz (horizontal dashed lines). (c) SW intensities integrated over all times and measured at different distances x to the edge of the CPW. Plots for different x are drawn with different intensity offsets to separate the plots vertically and thus increase readability. (d) Frequencies measured for the shifted SW peak as function of x (black squares) compared to frequencies calculated from the dispersion relation for the wave vector $k_{max} = 1.04$ rad/μm as function of the total magnetic field (red circles). The light blue area highlights the field range covered by the dc pulse.

can be excited at $f_{rf} = 3.65$ GHz. Only those SWs that were excited before the dc pulse sets in and are still propagating along the waveguide experience the changing magnetic field and adjust their frequency due to time refraction. Naturally, after the dc pulse is switched off, the total magnetic field matches the resonance condition and SWs can be excited again.

If we keep the external field to match the resonance condition $\mu_0 H_{ext} = \mu_0 H_{res} = 22.4$ mT but reverse the direction of the Oersted field [arrow B in Fig. 2(a)] with reduced amplitude $\mu_0 H_{Oe} = 6.8$ mT, the result is similar. Now, $H_{Oe} \uparrow\downarrow H_{ext}$ so that the total field is reduced during the dc pulse and the SW frequency shifts to lower values during the rise time of the pulse, as can be seen in Fig. 3(b). Note that this results in $H_{tot} < H_{crit}$ [see Fig. 2(b)], which does not suffice to saturate even parts of the waveguide along its short axis. Hence, SW propagation is less efficient and the shifted signal in Fig. 3(b) is much weaker compared to Fig. 3(a).

So far, we detected SWs only in one fixed position. Now, we analyze the amplitude of the frequency shift as a

function of the propagation distance x. In Fig. 3(c), we plot the μBLS intensity integrated over time that was measured at different positions x for $\boldsymbol{H}_{\mathrm{Oe}} \uparrow\uparrow \boldsymbol{H}_{\mathrm{ext}}$ with $\mu_0 H_{\mathrm{ext}} = 22.4$ and $\mu_0 H_{\mathrm{Oe}} = 12.2$ mT. Each plot shows two peaks: one peak at 3.65 GHz, which is associated with resonant excitation when the dc pulse is still off and is cut off in the plot due to its very high intensity, and a second peak with much lower intensities at higher frequencies showing SWs that are shifted due to time refraction. Since we are interested only in the frequencies of the shifted peaks, we focus our plot on the lower intensity range and chose different intensity offsets for different x to separate the plots vertically and increase readability. As can be seen, the frequency shift increases gradually and does not change for $x \geq 4$ μm.

In Fig. 3(d), black squares plot the shifted frequencies as a function of x. To compare our data to the dispersion relation, red circles show the frequencies that were calculated for $k_{\max} = 1.04$ rad/μm from the dispersion relation in Fig. 2(c). To match the different x axes for both sets of data, we have to consider that only propagating SWs adjust to the changing field and propagation from the antenna to position x needs a certain amount of time. This means, at $x = 0$ μm, SWs are detected directly where they are excited and cannot be affected by any changes of the magnetic field. Hence, the field still matches the externally applied field $\mu_0 H_{\mathrm{ext}} = 22.4$ mT. When measuring at $x > 0$ μm, SWs propagate in the changing field for a few nanoseconds and adjust their frequency before they are detected. As soon as SWs propagate longer than 3 ns, which equals the rise time of the dc pulse, the frequency shift does not increase any more because the maximum Oersted field is reached already. In our experiment, this is the case for $x \geq 3.3$ μm where the detected frequency shift reaches its maximum value of 1.42 GHz. This corresponds to 39% relative frequency shift due to time refraction. Up to the point where the measured data reach the plateau, measured and calculated frequencies are in excellent agreement.

Now we consider the case when the initial external magnetic field is larger than the resonance field and the dc pulse is injected to generate an Oersted field that reduces the effective field to cross the resonance condition [arrow C in Fig. 2(a)]. Figure 4(a) shows the BLS intensity for $\boldsymbol{H}_{\mathrm{Oe}} \uparrow\downarrow \boldsymbol{H}_{\mathrm{ext}}$ with $\mu_0 H_{\mathrm{ext}} = 34.5$ and $\mu_0 H_{\mathrm{Oe}} = 19.0$ mT. Only for two short moments in time, during the rise and fall time of the dc pulse, SW bursts are detected. Only at these times, the total field matches the resonance field $\mu_0 H_{\mathrm{tot}} = \mu_0 H_{\mathrm{res}} = 22.4$ mT and allows for the excitation of SW bursts with $f_{\mathrm{rf}} = 3.65$ GHz. However, the SW bursts are not detected at 3.65 GHz but at lower (higher) values at the rising (falling) edge of the dc pulse, respectively. This is related to the still changing total magnetic field while the SW bursts propagate. At the rising edge of the dc pulse, the total field continues to reduce, leading to a downshift of the burst frequency. At the falling edge, the
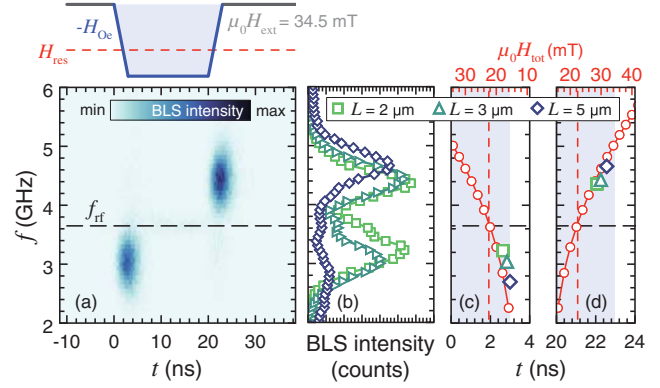
FIG. 4. (a) Time-resolved BLS signal measured at $x = 3$ μm for $\boldsymbol{H}_{\mathrm{Oe}} \uparrow\downarrow \boldsymbol{H}_{\mathrm{ext}}$ with $\mu_0 H_{\mathrm{ext}} = 34.5$ and $\mu_0 H_{\mathrm{Oe}} = 19.0$ mT. The excitation frequency was fixed to $f_{\mathrm{rf}} = 3.65$ GHz (horizontal dashed line). (b) BLS spectra integrated over time for different x with the same field configuration as in (a). (c),(d) Frequencies and detection times of the SW bursts measured at different x for (c) the rising edge of the dc pulse and (d) the falling edge. The 3 ns rise and fall time are highlighted in light blue.

total field still increases, resulting in a higher average frequency of the SW burst.

Figure 4(b) shows the BLS intensity integrated over time and measured at different distances x to the antenna. Moving away from the antenna, the frequency shifts of the SW bursts increase, similar to our observations for resonant excitation discussed above. The larger the propagation distance, the longer the bursts propagate in the time-varying field and hence the more their frequencies are shifted.

To compare this with calculations of the dispersion, the frequencies of the SW bursts are plotted as a function of time in Fig. 4(c) for the rising edge of the dc pulse and in Fig. 4(d) for the falling edge. Red circles show the frequencies that were calculated from the dispersion for $k_{\max} = 1.04$ rad/μm as a function of the total magnetic field (upper x axis). To match both x axes, we have to consider that, for the rising edge of the dc pulse, the total field at $t = 0$ ns still matches the externally applied field: $\mu_0 H_{\mathrm{tot,0 \ ns}} = 34.5$ mT. After 3 ns rise time, the pulse amplitude reaches its maximum, which yields $\mu_0 H_{\mathrm{Oe}} = 19.0$ and $\mu_0 H_{\mathrm{tot,3 \ ns}} = 15.5$ mT. As can be seen in Fig. 4(c), the measured frequencies of the SW bursts nicely coincide with what is expected from theory. For the falling edge of the dc pulse [Fig. 4(d)], the axis of the total magnetic field is simply reversed, i.e., $\mu_0 H_{\mathrm{tot,20 \ ns}} = 15.5$ mT and $\mu_0 H_{\mathrm{tot,23 \ ns}} = 34.5$ mT. Experimental data and theoretical calculations match well.

In conclusion, we have experimentally quantified time refraction of SWs in combined space- and time-resolved studies of SW propagation in rapidly changing magnetic fields. We demonstrated the acceleration and deceleration of SWs with frequencies in the gigahertz range on length scales comparable to the SW wavelength. The prospect of

manipulating SW frequencies on such short time and length scales is of fundamental importance for hybrid quantum systems in which magnons, the quanta of SWs, are considered as strongly localized and tunable microwave sources to pump and control solid-state qubits [18,19].

---

[*]k.schultheiss@hzdr.de

[†]Permanent address: Department of Materials Science and Engineering, University of Illinois at Urbana-Champaign, Urbana, Illinois 61801, USA.

[1] J. T. Mendonça, A. Guerreiro, and A. M. Martins, Phys. Rev. A **62**, 033805 (2000).

[2] Y. Zhou, M. Z. lam, M. Karimi, J. Upham, O. Reshef, C. Liu, A. E. Willner, and R. W. Boyd, Nat. Commun. **11**, 2180 (2020).

[3] S. F. Preble, Q. Xu, and M. Lipson, Nat. Photonics **1**, 293 (2007).

[4] B. A. Kalinikos and A. N. Slavin, J. Phys. C **19**, 7013 (1986).

[5] A. V. Chumak, T. Neumann, A. A. Serga, B. Hillebrands, and M. P. Kostylev, J. Phys. D **42**, 205005 (2009).

[6] V. E. Demidov, M. P. Kostylev, K. Rott, J. Münchenberger, G. Reiss, and S. O. Demokritov, Appl. Phys. Lett. **99**, 082507 (2011).

[7] B. Obry, V. I. Vasyuchka, A. V. Chumak, A. A. Serga, and B. Hillebrands, Appl. Phys. Lett. **101**, 192406 (2012).

[8] K. Vogt, F. Y. Fradin, J. E. Pearson, T. Sebastian, S. D. Bader, B. Hillebrands, A. Hoffmann, and H. Schultheiss, Nat. Commun. **5**, 3727 (2014).

[9] S.-K. Kim, S. Choi, K.-S. Lee, D.-S. Han, D.-E. Jung, and Y.-S. Choi, Appl. Phys. Lett. **92**, 212501 (2008).

[10] J. Stigloher, M. Decker, H. S. Körner, K. Tanabe, T. Moriyama, T. Taniguchi, H. Hata, M. Madami, G. Gubbiotti, K. Kobayashi, T. Ono, and C. H. Back, Phys. Rev. Lett. **117**, 037204 (2016).

[11] J. N. Toedt, S. Mansfeld, D. Mellem, W. Hansen, D. Heitmann, and S. Mendach, Phys. Rev. B **93**, 184416 (2016).

[12] S. M. Rezende and F. R. Morgenthaler, Appl. Phys. Lett. **10**, 184 (1967).

[13] B. A. Auld, J. H. Collins, and H. R. Zapp, Appl. Phys. Lett. **10**, 186 (1967).

[14] V. L. Preobrazhenskii and Y. K. Fetisov, Sov. Phys. J. **31**, 898 (1988).

[15] T. Sebastian, K. Schultheiss, B. Obry, B. Hillebrands, and H. Schultheiss, Front. Phys. **3**, 35 (2015).

[16] A. Vansteenkiste, J. Leliaert, M. Dvornik, M. Helsen, F. Garcia-Sanchez, and B. Van Waeyenberge, AIP Adv. **4**, 107133 (2014).

[17] The dispersion relation and micromagnetic simulations were performed using the following material parameters: saturation magnetization $M_s = 830$ kA/m, reduced gyromagnetic ratio $\gamma/2\pi = 28$ GHz/T, exchange constant $A = 13$ pJ/m.

[18] P. Andrich, C. F. de las Casas, X. Liu, H. L. Bretscher, J. R. Berman, F. J. Heremans, P. F. Nealey, and D. D. Awschalom, npj Quantum Inf. **3**, 28 (2017).

[19] Y. Li, W. Zhang, V. Tyberkevych, W.-K. Kwok, A. Hoffmann, and V. Novosad, J. Appl. Phys. **128**, 130902 (2020).

RESEARCH

NUCLEAR ASTROPHYSICS

^{60}Fe and ^{244}Pu deposited on Earth constrain the r-process yields of recent nearby supernovae

A. Wallner[1,2]*, M. B. Froehlich[1], M. A. C. Hotchkis[3], N. Kinoshita[4], M. Paul[5], M. Martschini[1]†,
S. Pavetich[1], S. G. Tims[1], N. Kivel[6], D. Schumann[6], M. Honda[7]‡, H. Matsuzaki[8], T. Yamagata[8]

Half of the chemical elements heavier than iron are produced by the rapid neutron capture process (r-process). The sites and yields of this process are disputed, with candidates including some types of supernovae (SNe) and mergers of neutron stars. We search for two isotopic signatures in a sample of Pacific Ocean crust—iron-60 (^{60}Fe) (half-life, 2.6 million years), which is predominantly produced in massive stars and ejected in supernova explosions, and plutonium-244 (^{244}Pu) (half-life, 80.6 million years), which is produced solely in r-process events. We detect two distinct influxes of ^{60}Fe to Earth in the last 10 million years and accompanying lower quantities of ^{244}Pu. The ^{244}Pu/^{60}Fe influx ratios are similar for both events. The ^{244}Pu influx is lower than expected if SNe dominate r-process nucleosynthesis, which implies some contribution from other sources.

All naturally occurring nuclides heavier than iron are produced in stellar environments, almost exclusively by nuclear processes involving the successive captures of neutrons to build up heavier masses. About half of these nuclides are synthesized slowly as a by-product of steady stellar fusion. The other half, including all actinide elements, require a very short but intense flux of neutrons, resulting in a rapid neutron capture process (r-process). The sites and yields of the r-process remain a topic of debate (1–6). It is expected to occur in explosive stellar environments such as certain types of supernovae (SNe) or neutron-star mergers (NSMs), the latter of which has been supported by observations of the gravitational-wave event GW170817 (7). The abundance patterns of r-process nuclides can be used to constrain the production site. Radioactive isotopes (radionuclides) provide additional time information resulting from their decay over time following their synthesis. Such radionuclides should be scattered through the interstellar medium (ISM) and could be deposited on Earth.

The Solar System (SS) is located inside a large ISM structure [the Local Superbubble (LB)] that was shaped by supernova (SN) explosions during the last ~12 million years (Myr) (8). Earth has therefore been exposed to both ejecta from the SNe and swept-up interstellar material that traversed the SS during this time period (9, 10). Dust particles from the ISM pass through the SS (11) and contain nucleosynthetic products of stellar events (e.g., stellar winds and SNe) (10, 12, 13). Earth's initial abundance of the ^{60}Fe radionuclide [half-life ($t_{1/2}$) = 2.6 Myr (14, 15)] has decayed to extinction over the 4.6 billion years (Gyr) since the SS's formation. ^{60}Fe, however, is produced in massive stars and ejected in SN explosions. Evidence for the deposition of extraterrestrial ^{60}Fe on Earth has been found in deep-sea geological archives dated to between 1.7 and 3.2 million years ago (Ma) (16–20), at recent times (21, 22), and possibly also around 7 Ma (19). ^{60}Fe has also been detected in lunar samples (23), in astronomical observations of gamma rays associated with its radioactive decay (24), and in galactic cosmic rays (25). SN activity in the last ~2 Myr is suggested by an excess in the local cosmic-ray spectrum (26). Other radionuclides are also produced and ejected in such explosions (9, 27–30). If substantial r-process nuclei are produced in SNe this would also have enriched the local ISM with actinides, such as ^{244}Pu. With a half-life of 80.6 Myr, ^{244}Pu is much longer lived than ^{60}Fe, so it can be contributed by older r-process events, not limited to those that formed the LB. Either as part of the SN direct

[1]Department of Nuclear Physics, Research School of Physics, Australian National University, Canberra, ACT 2601, Australia. [2]Helmholtz-Zentrum Dresden-Rossendorf, Institute of Ion Beam Physics and Materials Research, 01328 Dresden, Germany. [3]Australian Nuclear Science and Technology Organisation, Lucas Heights, NSW 2234, Australia. [4]Institute of Technology, Shimizu Corporation, Tokyo 135-8530, Japan. [5]Racah Institute of Physics, The Hebrew University of Jerusalem, Jerusalem 91904, Israel. [6]Laboratory of Radiochemistry, Department for Nuclear Energy and Safety, Paul Scherrer Institute, 5232 Villigen, Switzerland. [7]Graduate School of Pure and Applied Sciences, University of Tsukuba, Ibaraki 305-8577, Japan. [8]Micro Analysis Laboratory, Tandem Accelerator, The University Museum, The University of Tokyo, Tokyo 113-0032, Japan.
*Corresponding author. Email: anton.wallner@hzdr.de or anton. wallner@anu.edu.au
†Present address: Vienna Environmental Research Accelerator Laboratory, Faculty of Physics, University of Vienna, Vienna 1090, Austria.
‡Present address: Nuclear Science Research Institute, Japan Atomic Energy Agency, Ibaraki 319-1195, Japan.

Fig. 1. Influx of interstellar ^{60}Fe and ^{244}Pu. (**A**) ^{60}Fe incorporation rates for Crust-3. The data (red points) have been decay corrected, and each layer is equivalent to 400 thousand years. The absolute ages have an uncertainty of ~0.3 to 0.5 Myr (27). (**B**) ^{244}Pu incorporation rates for the three layers after subtraction of the anthropogenic ^{244}Pu fraction (27). (**C**) ^{244}Pu$_{ISM}$/^{60}Fe number ratio in the crust sample with layers 1 and 2 combined (horizontal solid lines with shaded error bars). All error bars show 1σ Poisson statistics.

Fig. 2. Measured Pu isotope ratios and comparison with global fallout values. (**A** and **B**) Variations of the measured ^{240}Pu/^{239}Pu ratio (A) and the ^{244}Pu/^{239}Pu ratio (B) across the three layers (solid red lines). The dashed red lines and gray shading indicate 1σ uncertainties. The blue shaded area and solid line represent the expected ratios for Pu from nuclear weapons fallout (27). ^{240}Pu/^{239}Pu remains constant across the three layers, whereas ^{244}Pu/^{239}Pu is enhanced in the deeper (older) layers. We attribute the excess above anthropogenic (anthr) levels to extraterrestrial ^{244}Pu. Equivalent data for ^{241}Pu/^{239}Pu are shown in fig. S4.

Table 1. ^{60}Fe/Fe ratios from AMS measurements of layered samples of Crust-3. Twenty-four individual samples, distributed equally across 10 Myr, were analyzed and combined into four sections (individual data are listed in table S1). The stable Fe content was measured separately through inductively coupled plasma mass spectrometry (ICP-MS) (table S4). Ages are derived from ^{10}Be measurements (table S5) and have an uncertainty of ±0.3 Myr (27).The number of ^{60}Fe background events expected was calculated by scaling (in measurement time and beam intensity) measurements of terrestrial Fe blank samples. ^{60}Fe/Fe$_{d.c.}$ denotes background- and decay-corrected data (27). Dashes in otherwise empty cells indicate not applicable.

Section	Depth (mm)	Time period (Ma)	^{60}Fe detector events	^{60}Fe background events expected	^{60}Fe/Fe (10^{-15})	^{60}Fe/Fe$_{d.c.}$ (10^{-15})	^{60}Fe incorporation (10^6 atoms cm^{-2} per section)	^{60}Fe incorporation rate (atoms cm^{-2} yr^{-1})
I	0 – 9.2	0 – 4.2	379	10	1.10 ± 0.06	1.87 ± 0.12	6.10 ± 0.31	1.46 ± 0.07
II	9.2 – 12	4.2 – 5.5	3	2	0.05 ± 0.03	$0.06^{+0.14}_{-0.06}$	$0.09^{+0.23}_{-0.09}$	$0.07^{+0.16}_{-0.07}$
III	12 – 15	5.5 – 7.0	49	3	0.40 ± 0.06	1.96 ± 0.31	1.77 ± 0.25	1.12 ± 0.16
IV	15 – 24	7.0 – 10.0	4	5	0.02 ± 0.01	<0.05	<0.2	<0.07
Total	0 – 24	0 – 10	435	20	0.56 ± 0.03	0.56 ± 0.03	7.96 ± 0.38	0.79 ± 0.04
Blank	terrestrial Fe	–		2	–	0.03 ± 0.02	–	–	–

ejecta or as continuous ISM influx, we expect dust particles containing ^{244}Pu to enter the SS, similarly to ^{60}Fe, but probing different nucleosynthetic processes. Previous measurements in terrestrial or lunar archives have provided only upper limits on actinide influx (12, 31–33).

We searched for extraterrestrial ^{60}Fe and ^{244}Pu incorporated into a deep-sea sample on Earth—a ferromanganese crust (which we refer to as Crust-3) that spans the last 10 Myr, sampled at ~1500 m below sea level in the Pacific Ocean, with 115-cm^2 cross-sectional area and ~25-mm thickness (27). The radionuclides were identified and counted using accelerator mass spectrometry (AMS) (27). For ^{60}Fe, a time-resolved depth profile of ~1-cm^2 area was analyzed, subdivided into 24 layers, each ~1-mm thick, corresponding to a time resolution of ~0.4 Myr per layer [crust growth-rate of ~2.4 mm Myr^{-1}, dated with terrestrial ^{10}Be (27)]. The remaining part of Crust-3 (114-cm^2 area), after separating the aliquots used for ^{60}Fe analysis, was split into three thick, horizontal layers designated 3/A (extending from 0 to 3 mm, equivalent to 0 to 1.3 Ma, with a mass of ~20 g), 3/B (3 to 10 mm, 1.3 to 4.6 Ma, 179 g), and 3/C (10 to 20 mm, 4.6 to 9.0 Ma, 208 g), given the anticipated low abundance of ^{244}Pu. We expected the top layer to contain anthropogenic Pu from atmospheric nuclear weapons tests performed during the 20th century.

The ^{60}Fe content was measured as the isotope ratio ^{60}Fe/Fe, where single ^{60}Fe atoms were counted in a particle detector and normalized to the stable Fe content in the sample (15, 19, 27). We obtained a measurement background of ^{60}Fe/Fe = $(3 \pm 1) \times 10^{-17}$, equivalent to one identified background event over ~1 day of measurement (fig. S1). A total of 435 ^{60}Fe detector events were registered over the 24 samples of the crust (Table 1). Two distinctly separated ^{60}Fe signals are observed, with maxima at 2.5 and 6.3 Ma (Fig. 1). No ^{60}Fe above the background was observed between 4.2 and

5.5 Ma and for samples older than 7 Ma. The absolute ^{60}Fe flux and its time profile confirm previous results in sediment, crust, and nodule samples (fig. S2). The ^{60}Fe incorporation was $(6.10 \pm 0.31) \times 10^6$ atoms cm^{-2} and $(1.77 \pm 0.25) \times 10^6$ atoms cm^{-2} for the younger and older signals, respectively, consistent with previous reports [$(5.9 \pm 0.8) \times 10^6$ and $(3.5 \pm 1.4) \times 10^6$ atoms cm^{-2}, respectively] (19) (all uncertainties are given as 1σ values). Unlike sediments, crusts have incorporation efficiencies for Fe and Pu of <100% (see supplementary text). By comparing with sediment data (19), we deduce an incorporation efficiency for ^{60}Fe into Crust-3 of 17% [previously measured crusts had efficiencies of 17 and 6% (17, 19)]. We found a similar efficiency for ^{244}Pu incorporation (27).

The three larger aliquots for ^{244}Pu analysis were completely dissolved and spiked with a known amount of ^{242}Pu to monitor the chemical yield of Pu (27). Pu abundances were measured using an AMS system that was specifically optimized for Pu measurements (34).

We observed an anthropogenic Pu signal in the top layer of Crust-3, which has ^{240}Pu/^{239}Pu and ^{241}Pu/^{239}Pu isotope ratios that are consistent with the expected values for nuclear weapons fallout (supplementary text). ^{239}Pu, ^{240}Pu, and ^{244}Pu events were observed in all three crust layers, and ^{241}Pu was observed in the first two layers. The ^{240}Pu/^{239}Pu and ^{241}Pu/^{239}Pu ratios are constant over these layers. The ^{244}Pu/^{239}Pu ratio shows an excess over anthropogenic levels in the two deeper layers (Fig. 2 and fig. S4). Assuming that the ^{244}Pu abundance is dominated by the anthropogenic contribution in the top layer, we correct the deeper layers for this contribution and attribute the additional ^{244}Pu to extraterrestrial deposition. The amount of short-lived anthropogenic Pu in the deeper layers indicates some anthropogenic Pu penetrated below the top layer (with concentrations relative to the top layer A of 1.5 and 0.1% in layers B and C, respectively), possibly as a result of pore water–

induced redistribution into the deeper layers (27). If ^{60}Fe also migrates in crusts, our observed time profile (Fig. 1A) could have been slightly broadened by this effect.

We attribute 181 detector events to extraterrestrial ^{244}Pu in the three layers of Crust-3, compared with about one ^{244}Pu event for blank samples (27). The averaged extraterrestrial ^{244}Pu incorporation rate was (71 ± 8) and $\left(11.5^{+7.8}_{-5.8}\right)$ atoms cm^{-2} Myr^{-1} for 0 to 4.6 Ma and 4.6 to 9 Ma, respectively. These results are consistent with previous 2σ limits of <188 (0.5 to 5 Ma) and <66 atoms cm^{-2} Myr^{-1} (5 to 12 Ma) based on zero and one ^{244}Pu event, respectively (12) (fig. S8). Combining the decay-corrected ^{244}Pu and ^{60}Fe concentrations in Crust-3, we find an atom ratio of ^{244}Pu/^{60}Fe = $(5.3 \pm 0.7) \times 10^{-5}$, averaged over the last ~4.6 Myr, and $\left(2.8^{+1.9}_{-1.4}\right) \times 10^{-5}$ for 4.6 to 9 Ma, consistent with each other within the uncertainties (Table 2).

We attribute the two peaks in the ^{60}Fe deposition profile (Fig. 1A) to multiple nearby SN explosions during the last 10 Myr. Earth may have been exposed to separate waves of SN ejecta, or alternatively, the SS may have traversed clouds of ^{60}Fe-enriched dust. There are several potential explanations for the 3 to 4× higher ^{60}Fe influx for the younger time period: a SN at about half the distance of the older event, a more massive star that produced substantially more ^{60}Fe, more than one SN explosion (compatible with the broader peak), or different ISM conditions affecting dust survival and penetration into the SS.

After decay correction (27), our measured ^{60}Fe fluence is equivalent to a 10-Myr-averaged ^{60}Fe local concentration of $(0.3 \text{ to } 0.6) \times 10^{-12}$ ^{60}Fe atoms cm^{-3} at Earth's orbit [with an incorporation efficiency of 17% (see above) and assuming a relative velocity of the SS in the ISM between 10 and 20 km s^{-1} (supplementary text)]. Two SNe, with a ^{60}Fe-yield of 2×10^{-5} solar masses ($M_\odot$) each (19, 35), would enrich the ISM within a volume of 75-parsecs

Table 2. ^{60}Fe and ^{244}Pu data for three time periods during the last 10 Myr from three crust layers. Crust-3 data are from this work, and Crust-0 data are from (12, 19). For details on the ISM (extraterrestrial) flux and fluence calculations, see (27). The FeMn-crust sample was split into three layers A, B, and C for ^{244}Pu (18, 179, and 208 g, respectively). The individual ^{60}Fe data (background-corrected) from table S1 were combined to cover the same time periods as ^{244}Pu. All uncertainties are 1σ [we converted the 2σ values for Crust-0 (12) to 1σ]. The bolded lines (Crust-3$_{0\text{-}4.6}$ and Crust-0$_{0.5\text{-}5.0}$) cover the time periods of the younger ^{60}Fe influx (0 to 4.6 Ma and 0.5 to 5.0 Ma, respectively). The italicized lines (Crust-3$_{0\text{-}9.0}$ and Crust-0$_{0.5\text{-}12}$) represent the time integral over the 9 Myr covered by Crust-3 as well as the similar time span of 0.5 to 12 Ma investigated for Crust-0 (12). Dashes in otherwise empty cells indicate not applicable.

Layer	Depth (mm)	Time period (Myr)	^{60}Fe$_{ISM}$ atoms detected	^{60}Fe rate (atom cm^{-2} yr^{-1})	^{60}Fe layer incorporation (10^6 atoms cm^{-2})
Crust-3/A	0 – 3	0 – 1.34	88 ± 9	0.72 ± 0.08	0.97 ± 0.10
Crust-3/B	3 – 10	1.34 – 4.57	282 ± 17	1.61 ± 0.09	5.19 ± 0.31
Crust-3/C	10 – 20	4.57 – 9.0	46 ± 7	0.42 ± 0.04	1.82 ± 0.26
Crust-3$_{0\text{-}4.6}$	**0 – 10**	**0 – 4.57**	**370 ± 19**	**1.35 ± 0.07**	**6.14 ± 0.31**
Crust-3$_{0\text{-}9.0}$	*0 – 20*	*0 – 9.0*	*415 ± 20*	*0.89 ± 0.04*	*7.96 ± 0.38*
blank	–	–	2	–	–

Layer	Time period (Myr)	^{244}Pu$_{ISM}$ atoms detected	^{244}Pu rate (atoms cm^{-2} Myr^{-1})	^{244}Pu layer incorporation (atoms cm^{-2})	^{244}Pu$_{ISM}$ flux at Earth orbit (10^3 atoms cm^{-2} Myr^{-1})	^{244}Pu$_{ISM}$ fluence at Earth orbit 10^3 atoms cm^{-2}	^{244}Pu/^{60}Fe (10^{-6} at/at)
Crust-3/A	0 – 1.34	34 ± 17	38 ± 19	51 ± 26	0.90 ± 0.48	1.2 ± 0.6	52 ± 26
Crust-3/B	1.34 – 4.57	141 ± 19	85 ± 11	274 ± 37	1.99 ± 0.44	6.4 ± 1.4	53 ± 7
Crust-3/C	4.57 – 9.0	6.3$^{+4.3}_{-3.2}$	11.5$^{+7.8}_{-5.8}$	51$^{+35}_{-26}$	0.27$^{+0.18}_{-0.14}$	1.2$^{+0.8}_{-0.6}$	28$^{+19}_{-14}$
Crust-3$_{0\text{-}4.6}$	**0 – 4.57**	**175 ± 19**	**71 ± 8**	**325 ± 40**	**1.67 ± 0.35**	**7.7 ± 1.6**	**53 ± 6**
Crust-3$_{0\text{-}9.0}$	*0 – 9.0*	*181 ± 19*	*42 ± 4*	*376 ± 40*	*0.98 ± 0.18*	*8.9 ± 1.8*	*47 ± 5*
Blank	–	1	–	–	–	–	–
Crust-0$_{0.5\text{-}5.0}$	**0.3 – 5.0**	**0**	**<100**	**<420**	**<2.2**	**<10.0**	**<170**
Crust-0$_{0.5\text{-}12}$	*0.3 – 12*	*1*	*<40*	*<440*	*<1*	*<10.0*	*–*
Crust-0$_{0.5\text{-}25}$	0.3 – 25	2	<30	<700	<0.6	<15.0	–

(pc) radius to ≲10^{-11} ^{60}Fe atoms cm^{-3}, if distributed homogeneously and taking into account radioactive decay. The Galaxy-averaged concentration of ^{60}Fe is ~4 × 10^{-12} atoms cm^{-3}, deduced from the average SN rate for the Milky Way and gamma-ray astronomical observations (22) (supplementary text). Assuming that ^{60}Fe only reaches Earth when adsorbed on dust grains, comparison of the measured local ^{60}Fe concentration and typical SN yields lead to a probability of dust formation and SS penetration for SN-produced ^{60}Fe of ~3 to 6% in mass, close to the measured fraction of interstellar dust grains reaching the inner SS at present times of ~(6 ± 3)% (11, 12). This 3 to 6% (in mass) probability of dust reaching Earth reflects the selective filtering of interstellar dust particles that favors larger dust grains (supplementary text). We conclude that the ^{60}Fe fluence reaching Earth ~2.5 and 6.5 Ma is compatible with two to four SN events at distances of 50 to 100 pc.

The extraterrestrial ^{244}Pu, deposited concomitantly with SN-produced ^{60}Fe, shows an approximately constant ^{244}Pu/^{60}Fe ratio of (3 to 5) × 10^{-5} (Fig. 1). Assuming no fractionation between ^{244}Pu and ^{60}Fe, these values represent their atom ratio in the ISM. If ^{244}Pu and ^{60}Fe originate from the same SN events, this ratio can be used to deduce ^{244}Pu SN yields (36) (supplementary text), though the absolute yield estimates in those models have large uncertainties for ^{60}Fe and ^{244}Pu. Unusual types of SNe are improbable if there were two consecutive local SN events. If the ^{244}Pu was already present in the ISM from older r-process events, any actinide yields from the recent SN explosions would be accordingly lower.

We next consider alternative scenarios for the origin of extraterrestrial ^{244}Pu. The 30× longer half-life of ^{244}Pu compared with that of ^{60}Fe means that it could have been produced in older events than the SNe that produced the ^{60}Fe. The ^{244}Pu influx during the past 9 Myr could be a remainder of an older r-process event if it was incorporated into dust that survived the LB formation (>10 to 15 Ma) and was swept up by the more recent SN ejecta, together with freshly produced ^{60}Fe. Depending on the rate of actinide production, older ^{244}Pu (and other actinides) could be present in the ISM in (i) a steady-state concentration, if produced with high frequency compared with its lifetime (e.g., in SNe), or (ii) as the remaining fraction of an earlier rare event [such as NSMs, collapsars, or magneto-rotational SNe (3–5)], after radioactive decay has lowered an initially high actinide nucleosynthesis yield. Alternatively, the SS could have moved through two separate dust clouds containing SN-produced ^{60}Fe and older ^{244}Pu.

We calculate whether our data are compatible with ^{244}Pu having a steady-state concentration in the local ISM, assuming ^{244}Pu and ^{60}Fe are similarly adsorbed onto dust particles. Combining the Galaxy-averaged concentration of ^{60}Fe, 4 × 10^{-12} atoms cm^{-3} (24) (supplementary text), with the measured ^{244}Pu/^{60}Fe ratio leads to a concentration (c) of ^{244}Pu in the local ISM $c_{^{244}\text{Pu,ISM}} = (1.2 \text{ to } 2.0) \times 10^{-16}$ atoms cm^{-3}. Assuming that $c_{^{244}\text{Pu,ISM}}$ is associated with ISM dust particles of a composition similar to that of the early SS, we calculate (supplementary text) that steady-state conditions lead to an expected dust mass concentration of ~(1 to 2) × 10^{-28} g cm^{-3}. This value is one-hundredth the size of—and is inconsistent with—the measured local (within a few parsecs) dust mass density at the present time, which is ~1.5 × 10^{-26} g cm^{-3} (37) (supplementary text). However, it is consistent with the recent SNe exploding inside the LB, a region of very low-density ISM. Earlier SN ejecta could have reached Earth prior to the more recent SNe; if so, they would have swept up older ISM material and erased any existing steady-state ^{244}Pu inside the newly forming LB.

Our measurements of extraterrestrial ^{244}Pu and ^{60}Fe confirm an influx of interstellar material into the inner SS through two or more local and transient SN events over the last ~10 Myr, and they are compatible with some production of actinides in core-collapse SNe, possibly of common type. Combining these data with previous results of ^{244}Pu influx over the past 25 Myr (12) (extending prior to the

formation of the LB) indicates that SN actinide yields seem insufficient to account for the overall abundance of r-process nuclides in the Galaxy (fig. S8). These yields can be compared with the total r-process inventory calculated by SN actinide nucleosynthesis simulations, which, however, is limited by model uncertainties. The present data are compatible with the LB being a local disturbance of a large-scale Galactic steady-state (from SN enrichment of the ISM occurring more frequently than the radioactive half-life), with less-frequent injections from rarer r-process sources that nevertheless dominate the production of r-process elements, such as NSMs. The data are also consistent with the hypothesis of a nearby rare event before the time of SS formation that supplied the majority of the SS known inventory of the primordial actinides Th, U, and Pu (12, 38) (fig. S9 and supplementary text).

REFERENCES AND NOTES

1. Y.-Z. Qian, *Prog. Part. Nucl. Phys.* **50**, 153–199 (2003).
2. M. Arnould, S. Goriely, K. Takahashi, *Phys. Rep.* **450**, 97–213 (2007).
3. F. K. Thielemann *et al.*, *Prog. Part. Nucl. Phys.* **66**, 346–353 (2011).
4. J. J. Cowan *et al.*, *Rev. Mod. Phys.* **93**, 015002 (2021).
5. J. M. Lattimer, D. N. Schramm, *Astrophys. J.* **210**, 549–567 (1976).
6. A. P. Ji, A. Frebel, A. Chiti, J. D. Simon, *Nature* **531**, 610–613 (2016).
7. D. Kasen, B. Metzger, J. Barnes, E. Quataert, E. Ramirez-Ruiz, *Nature* **551**, 80–84 (2017).
8. D. Breitschwerdt *et al.*, *Nature* **532**, 73–76 (2016).
9. J. Ellis, B. D. Fields, D. N. Schramm, *Astrophys. J.* **470**, 1227 (1996).
10. B. J. Fry, B. D. Fields, J. R. Ellis, *Astrophys. J.* **827**, 48 (2016).
11. N. Altobelli *et al.*, *J. Geophys.* **110**, A07102 (2005).
12. A. Wallner *et al.*, *Nat. Commun.* **6**, 5956 (2015).
13. G. Korschinek, T. Faestermann, K. Knie, C. Schmidt, *Radiocarbon* **38**, 68 (1996).
14. G. Rugel *et al.*, *Phys. Rev. Lett.* **103**, 072502 (2009).
15. A. Wallner *et al.*, *Phys. Rev. Lett.* **114**, 041101 (2015).
16. K. Knie *et al.*, *Phys. Rev. Lett.* **83**, 18–21 (1999).
17. K. Knie *et al.*, *Phys. Rev. Lett.* **93**, 171103 (2004).
18. C. Fitoussi *et al.*, *Phys. Rev. Lett.* **101**, 121101 (2008).
19. A. Wallner *et al.*, *Nature* **532**, 69–72 (2016).
20. P. Ludwig *et al.*, *Proc. Natl. Acad. Sci. U.S.A.* **113**, 9232–9237 (2016).
21. A. Wallner *et al.*, *Proc. Natl. Acad. Sci. U.S.A.* **117**, 21873–21879 (2020).
22. D. Koll *et al.*, *Phys. Rev. Lett.* **123**, 072701 (2019).
23. L. Fimiani *et al.*, *Phys. Rev. Lett.* **116**, 151104 (2016).
24. R. Diehl, *Rep. Prog. Phys.* **76**, 026301 (2013).
25. W. R. Binns *et al.*, *Science* **352**, 677–680 (2016).
26. M. Kachelrieß, A. Neronov, D. V. Semikoz, *Phys. Rev. Lett.* **115**, 181103 (2015).
27. Materials and methods are available as supplementary materials.
28. J. Feige *et al.*, *Phys. Rev. Lett.* **121**, 221103 (2018).
29. G. Korschinek *et al.*, *Phys. Rev. Lett.* **125**, 031101 (2020).
30. B. J. Fry, B. D. Fields, J. R. Ellis, *Astrophys. J.* **800**, 71 (2015).
31. C. Wallner *et al.*, *New Astron. Rev.* **48**, 145–150 (2004).
32. M. Paul *et al.*, *Astrophys. J.* **558**, L133–L135 (2001).
33. P. R. Fields *et al.*, *Science* **167**, 499–501 (1970).
34. M. A. C. Hotchkis *et al.*, *Nucl. Instrum. Methods Phys. Res. B* **438**, 70–76 (2019).
35. M. Limongi, A. Chieffi, *Astrophys. J.* **647**, 483–500 (2006).
36. S. Goriely, H.-Th. Janka, *Mon. Not. R. Astron. Soc.* **459**, 4174–4182 (2016).
37. A. Li, *J. Phys. Conf. Ser.* **6**, 229–248 (2005).
38. K. Hotokezaka, T. Piran, M. Paul, *Nat. Phys.* **11**, 1042 (2015).

Statistics

User facilities and services

Ion Beam Center (IBC)

The Ion Beam Center (IBC) at HZDR combines various machines (electrostatic accelerators, ion implanters, low-energy and focused ion beam systems) into a unique facility used for ion beam modification and ion beam analysis of materials. The available energy range spans from a few eV to 60 MeV with a respective interaction depth in solids between 0.1 nm to 10 µm. In addition to standard broad beams also focused (down to 1 nm) and highly-charged ion beams are available with charge states up to 45+. In combination with an allocated ion beam experiment, users can also profit from structural analysis (electron microscopy and spectroscopy, X-ray scattering techniques) and sample or device processing under clean-room conditions. At the 6-MV tandem accelerator, the DREAMS (DREsden AMS = accelerator mass spectrometry) facility is used for the determination of long-lived radionuclides, like ^{7,10}Be, ^{26}Al, ^{36}Cl, ^{41}Ca, ^{55}Fe, ^{129}I, and others. A schematic overview of the IBC including the description of the main beam lines and experimental stations is given on page 61 of this Annual Report. In 2021, about 14,400 beam time hours were delivered for about 151 proposals from 120 users of 17 countries worldwide performing experiments at IBC or using the capabilities for ion beam services.
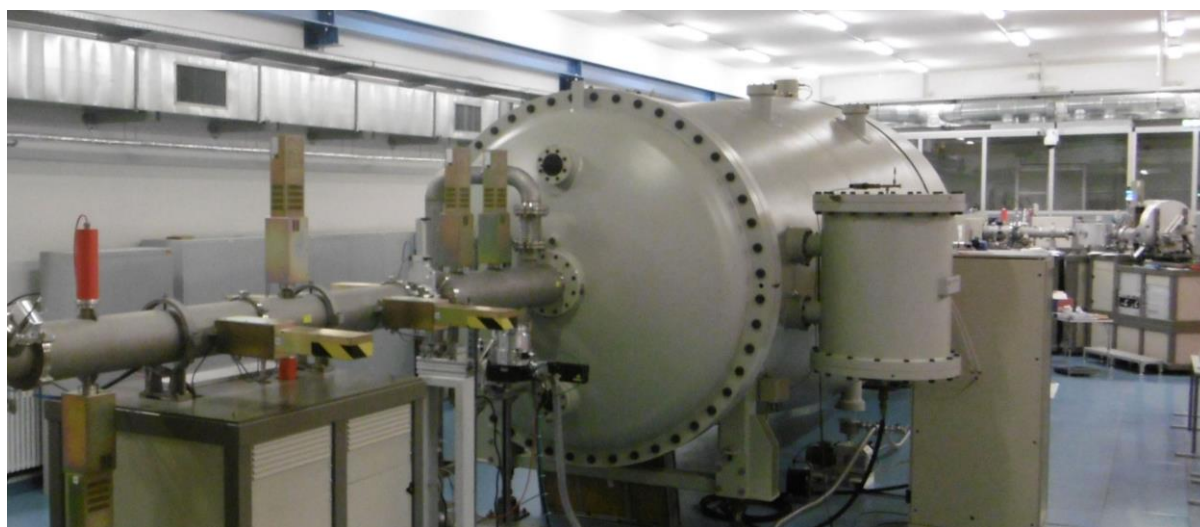
The IBC has provided ion beam technology as a user and competence center for ion beam applications for more than 30 years. With respect to user beam time hours, the IBC is internationally leading, and has been supported by numerous national and European grants, and by industry.

The research activities cover both ion beam modification and ion beam analysis (IBA), as well as rare isotope detection capabilities (AMS).

The operation of IBC is accompanied by a strong in-house research at the affiliated host "Institute of Ion Beam Physics and Materials Research", both in experiment and theory. Furthermore, the IBC strongly supports the commercial exploitation of ion beam technologies of partners from industry, which is essential for materials science applications. For ion beam services, the HZDR Innovation GmbH (spin-off of the HZDR) – www.hzdr-innovation.de – provides a direct and fast access to the IBC facilities based on individual contracts.

Quite recently, new ion beam tools and end stations have been commissioned which will attract new users by state-of-the-art experimental instrumentation. In a new end station for Rutherford-backscattering spectrometry (RBS), solid-liquid interfaces can now be investigated in-situ in an electro-

chemical cell. An ion microscope *ORION NanoFab* (He/Ne ions, 5 – 35 keV) provides unique possibilities for surface imaging, nano-fabrication, and for the first time, elemental analysis based on ion beam techniques. The cluster tool at the 6-MV accelerator allows *in-situ* deposition and analysis investigations at temperatures of up to 800 °C. Medium-energy ion scattering (MEIS) is now available for investigation of elemental compositions and depth profiles of ultra-thin layers at the new 100-kV accelerator.

IBC activities are efficiently integrated into various Helmholtz programmes within the research field "Matter", but also in the Helmholtz cross-programme activities "Mineral Resources", "Materials Research for Energy Technologies", and "Helmholtz Energy Materials Foundry". Since 2013, the IBC has been recognized as a large-scale facility within the "BMBF Verbundforschung" promoting long-term collaborations with universities. In addition, as of 2019 the IBC is coordinating the EU Integrated Infrastructure Initiative (I3) project RADIATE, which provides trans-national access to the largest ion beam centers in Europe (www.ionbeamcenters.eu).

Following the rules of a European and national user facility, access for scientific experiments to IBC is provided on the basis of a proposal procedure (www.hzdr.de/IBC) via the common HZDR user facility portal **HZDR-GATE** (gate.hzdr.de), and for RADIATE via www.ionbeamcenters.eu. IBC users from EU countries are eligible to receive support through the RADIATE initiative. Due to the availability of multiple machines and versatile instrumentation, IBC proposals can be submitted continuously. The scientific quality of the proposals is evaluated and ranked by an external international User Selection Panel. For successfully evaluated proposals, users get free access to IBC facilities for their experiments. The use of the IBC facilities includes the scientific and technical support during planning, execution, and evaluation of the experiments. For AMS samples preparation, two chemistry laboratories are available.

For more detailed information, please contact Dr. Stefan Facsko (s.facsko@hzdr.de), or Dr. René Heller (r.heller@hzdr.de), for AMS enquiries Prof. Anton Wallner (a.wallner@hzdr.de), and visit the IBC webpage: www.hzdr.de/IBC.

Free Electron Laser FELBE

FELBE is an acronym for the free-electron laser (FEL) at the Electron Linear accelerator with high Brilliance and low Emittance (ELBE) located at the Helmholtz-Zentrum Dresden-Rossendorf. The heart of ELBE is a superconducting linear accelerator operating in continuous-wave (cw) mode with a pulse repetition rate of 13 MHz. The electron beam (40 MeV, 1 mA max.) is guided to several laboratories where secondary beams (particle and electromagnetic) are generated. Two free-electron lasers (U37-FEL and U100-FEL) produce intense, coherent electromagnetic radiation in the mid and far infrared,

which is tunable over a wide wavelength range (5 –250 µm) by changing the electron energy or the undulator magnetic field. Main parameters of the infrared radiation produced by FELBE are as follows:

Wavelength λ	5 – 40 µm	FEL with undulator U37
	18 – 250 µm	FEL with undulator U100
Pulse energy	0.1 – 2 µJ	depends on wavelength
Pulse length	1 – 25 ps	depends on wavelength
Repetition rate	13 MHz	3 modes: • cw
		• macropulsed (> 100 µs, < 25 Hz)
		• single pulsed (Hz … kHz)

In addition, there is the THz beamline TELBE that is run by the Institute of Radiation Physics. TELBE delivers high-power pulses (up to 10 µJ) in the low THz range (0.1 to 2.5 THz) at a repetition rate of 100 kHz. ELBE is a user facility and applications for beam time can be submitted twice a year, typically by April 15 and October 15. FELBE and TELBE users from EU countries were eligible to receive support through the HORIZON 2020 Integrated Infrastructure Initiative (I3) CALIPSOplus (**C**onvenient **A**ccess to **Li**ght Sources **Op**en to Innovation, **S**cience and to the W**o**rld) from May 2017 to October 2021.

Typical applications are picosecond pump-probe spectroscopy (also in combination with several other femtosecond lasers, which are synchronized to the FEL), near-field microscopy, and nonlinear optics. The FELBE facility also serves as a far-infrared source for experiments at the Dresden High Magnetic Field Laboratory (HLD) involving pulsed magnetic fields up to 70 T.

Beamtime Distribution at ELBE 2021

NUC: Nuclear Physics   RAD: RadiationPhysics
NEU: Neutron Physics   FEL: Free Electron Laser
POS: Positron Physics   IP: Instrument Proposal
THZ: Terahertz   MD: Machine Development

The statistics shows that the FEL used about 700 hours beam time of the ELBE accelerator. This corresponds to 14 % of total beam time, which is again distributed among internal and external users.

For further information, please contact Prof. Manfred Helm (m.helm@hzdr.de) or visit the FELBE webpage www.hzdr.de/FELBE.

Experimental equipment

Accelerators, ion implanters, and other ion processing tools

Van de Graaff Accelerator (VdG)	2 MV	*TuR Dresden, DE*
Tandetron Accelerator (T1)	3 MV	*HVEE, NL*
Tandetron Accelerator (T2)	6 MV	*HVEE, NL*
Low-Energy Ion Implanter	0.1 – 40 kV	*Danfysik, DK*
Low-Energy Ion Platform	20 – 130 kV	*HVEE, NL*
High-Energy Ion Implanter	20 – 500 kV	*HVEE, NL*
Mass-Separated Focused Ion Beam (FIB) (15 nm, variable ions, Laser stage)	10 – 30 keV >10 A/cm^2	*Orsay Physics, FR*
Mass-Separated Focused Ion Beam (FIB) (variable ions, UHV, Lithography)	10 – 30 keV >10 A/cm^2	*Orsay Physics, FR*
ORION NanoFab HIM (including GIS, Nanopatterning, TOF-SIMS, µ-manipulators and heater)	He, Ne ions, 10 – 35 kV, Resolution ~ 0.5/1.8 nm	*Carl Zeiss Microscopy, DE*
ORION PLUS HIM modified for STIM	He ions, 10 – 35 kV, Resolution 0.35 nm	*Carl Zeiss Microscopy, DE*
Highly-Charged Ion Facility	25 eV – 6 keV $\times$ Q Q = 1 … 45 (Xe)	*DREEBIT, DE; PREVAC, PL*
Surface Modifications by Low-Energy Ion Irradiation	200 – 1200 eV	*Home-built*
UHV Ion Irradiation (Ar, He, etc.)	0 – 5 kV Scan 10 $\times$ 10 mm^2	*Cremer, DE; VG, USA*

Ion beam analysis (IBA)

A wide variety of advanced IBA techniques are available at the MV accelerators (see figure).

RBS	Rutherford Backscattering Spectrometry	(A1), (A2), (5), (9), (11), (14)	*VdG, T1, T2, HIM*
RBS/C	RBS – Channeling	(A1)	*VdG*
Liquid-RBS	Liquid Rutherford Backscattering Spectrometry	(A2)	*VdG*
MEIS	Medium Energy Ion Scattering	MEIS	
ERDA	Elastic Recoil Detection Analysis	(2), (9)	*T2*
PIXE	Particle-Induced X-ray Emission	(A1), (A2), (5), (14)	*VdG, T1, T2*
PIGE	Particle-Induced gamma Emission	(5), (14)	*T1, T2*
NRA	Nuclear Reaction Analysis	(1), (14)	*T1, T2*
NMP	Nuclear Microprobe	(14)	*T1*

Some stations are equipped with additional process facilities enabling *in-situ* IBA investigations during ion irradiation, sputtering, deposition, annealing, investigations at solid-liquid interfaces, etc.
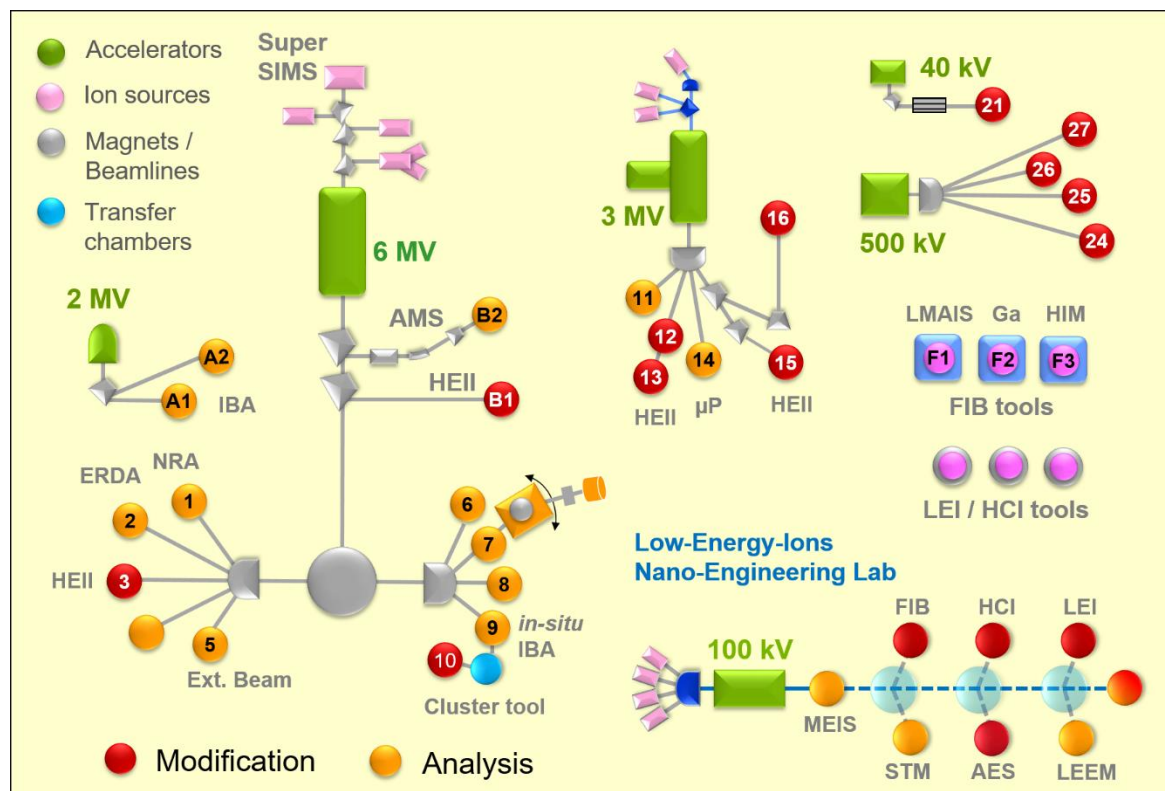
Schematic overview of the HZDR Ion Beam Center

Accelerator Mass Spectrometry (AMS)

AMS	Accelerator Mass Spectrometry	(B2)	*T2*

(focused to long-lived radionuclides: ^{7}Be, ^{10}Be, ^{26}Al, ^{36}Cl, ^{41}Ca, ^{129}I)

Other particle-based analytical techniques

SEM	Scanning Electron Microscope (S4800 II)	1 – 30 keV + EDX	*Hitachi, JP*
TEM	Transmission Electron Microscope (Titan 80-300 with Image Corrector)	80 – 300 keV + EDX, EELS	*FEI, NL*
TEM	Transmission Electron Microscope (Talos F200X)	20 – 200 keV + SuperX EDX	*FEI, NL*
FIB/SEM	Focused Ion/Electron Cross Beam (NVision 40)	1 – 30 keV + EDX, EBSD	*Carl Zeiss Microscopy, DE*
FIB/SEM	Focused Ion/Electron Instrument (Helios 5 CX DualBeam)	0.5 – 30 keV	*Thermo Fisher Sci. - FEI, US*
AES	Auger Electron Spectroscopy	+ SAM, SEM, XPS, EDX, CL	*Scienta Omicron, DE*
LEEM	Low-Energy Electron Microscope (Spec-LEEM-III)	0 eV – 4.5 keV Resolution < 6 nm + AES	*Elmitec, DE*
SIMS	Secondary Ion Mass Spectrometer (IMS7f-auto)	3 – 15 keV Ce and O beam	*CAMECA, FR*

Photon-based analytical techniques

XRD/XRR	X-Ray Diffractometers	Cu-Kα	
	θ-θ Powder D8 Advance		*Bruker, DE*
	θ-θ 4-Circle Empyrean		*PANalytical, NL*
	θ-θ 4-Circle SmartLab 3kW		*Rigaku, JP*
SE	Angle Dependent Spectroscopic Ellipsometry	250 – 1700 nm	*Woollam, US*
UV-Vis	Solid Spec 3700 DUV	190 – 3300 nm	*Shimadzu, JP*
FTIR	Fourier-Transform Infrared Spectrometer	50 – 15000 cm^{-1}	*Bruker, DE*
	Ti:Sapphire Femtosecond Laser	78 MHz	*Spectra Physics, US*
	Femtosecond Optical Parametric Osci.		*APE, DE*
	Ti:Sapphire Femtosecond Amplifier	1 kHz, 250 kHz	*Coherent, US*
	Femtosecond Optical Parametric Amplifier		*Light Conversion, LT*
THz-TDS	Terahertz Time-Domain Spectroscopy	0.1 – 4 THz	*Home-built*
Raman	Raman Spectroscopy	> 10 cm^{-1}	*Jobin-Yvon-Horiba, FR*
	In-situ Raman Spectroscopy	> 100 cm^{-1}	*Jobin-Yvon-Horiba, FR*
PL	Photoluminescence (10 – 300 K)	405 – 1550 nm	*Jobin-Yvon-Horiba, FR*
	Micro-Photoluminescence	< 0.5 µm	*Jobin-Yvon-Horiba, FR*
TRPL	Time-Resolved Photoluminescence	τ = 3 ps – 2 ns τ > 5 ns	*Hamamatsu Phot., JP* *Stanford Res., US*
EL	Electroluminescence	300 – 1600 nm	*Jobin-Yvon-Horiba, FR*
	Optical Split-Coil Supercond. Magnet	7 T	*Oxford Instr., UK*
PR	Photomodulated Reflectivity	300 – 1600 nm	*Jobin-Yvon-Horiba, FR*
PLE	Photoluminescence Excitation	300 – 1600 nm	*Jobin-Yvon-Horiba, FR*
OES	Optical Emission Spectroscopy	250 – 800 nm	*Jobin-Yvon-Horiba, FR*
Confocal	Confocal scanning photoluminescence microscope	~1 µm resol. 5 – 300 K	*Attocube, DE*
SSPD	Superconducting single photon detectors	800 – 1500 nm	*Single Quantum, NL*

Magnetic thin film analysis

MFM	Magnetic Force Microscope	~ 50 nm resol.	*VEECO; DI, US*
AFM/MFM	Magnetic Force Microscope	~ 50 nm resol.	*BRUKER ICON tool, US*
SQUID VSM	Vibrating Sample Magnetometer	$\pm$ 7 T	*Quantum Design, US*
Vector-VSM	Vibrating Sample Magnetometer	$\pm$ 2 T	*Microsense, US*
MOKE	Magneto-Optic Kerr Effect (in-plane)	$\pm$ 0.35 T	*Home-built*
MOKE	Magneto-Optic Kerr Effect (perpend.)	$\pm$ 2 T	*Home-built*
FR-MOKE	Frequency-Resolved Magneto-Optic KE	$\pm$ 1.1 T	*Home-built*
SKM	Scanning Kerr Microscope		*Home-built*
	Kerr Microscope		*Evico Magnetics, DE*
VNA-FMR	Vector Network Analyzer Ferromagnetic Resonance	50 GHz	*Agilent, DE; Home-built*
Cryo-FMR	Variable-Temperature Ferromagnetic Resonance	3 – 300 K	*Attocube, DE; Home-built*
ME	Magnetoellipsometer		*LOT, DE; AMAC, US*
µBLS	Brillouin Light Scattering Microscope	$\pm$ 0.8 T, 491 & 532 nm	*Home-built*
SKM	Scanning Kerr Microscope with RF Detection (Spectrum Analyzer)	$\pm$ 0.5 T, 40 GHz	*Home-built*
MT-50G	High Frequency Magneto-Transport Setup	$\pm$ 1.5 T, 50 GHz 250 ps	*Home-built*

Other analytical and measuring techniques

STM/AFM	UHV Scanning Probe Microscope (variable T)		*Omicron, DE*
AFM	Atomic Force Microscope (Contact, Tapping, Spreading)		*Bruker, US*
AFM	Atomic Force Microscope (with c-AFM, SCM-Module)		*Bruker, US*
	Dektak Surface Profilometer		*Bruker, US*
	Micro Indenter/Scratch Tester		*Shimatsu, JP*
MPMS	Mechanical Properties Measurement System – Stretcher		*Home-built*
MS	Mass Spectrometers (EQP-300, HPR-30)		*HIDEN, UK*
	Wear Tester (pin-on disc)		*Home-built*
LP	Automated Langmuir Probe		*Impedans, IE*
HMS	Hall Measurement System	2 – 400 K, $\leq$ 9 T	*LakeShore, US*
	Van-der-Pauw HMS Ecopia	LNT & 300 K, 0.5 T	*Bridge Technol., US*
MTD	Magneto-Transport Device	300 K, $\leq$ 3 T	*Home-built*
RS	Sheet-Rho-Scanner		*AIT, KR*
Redmag	Redmag Tensormeter System	280 – 350 K, 2.5 T	*Home-built*
Greymag	Greymag Tensormeter System	300 K, 0.7 T (360°)	*Home-built*

Greenmag	Tensormeter System (TMCS)	30 – 320 K, 1.3 T (360°)	Tensor Instruments (HZDR Inno), DE
SEM	Scanning Electron Microscope (Phenom XL)	5 – 15 keV + EDS	Thermo Fisher Sci., US
IV / CV	I-V and C-V Semi-Automatic Prober	-60 – 300 °C	Süss, DE; Keithley, US
IV / CV	I-V and C-V Analyzer		Keithley, US
BCS	Battery test system, 8 channels		Bio-Logic Science, DE
GC	Gas Chromatography (GC-2010)		Shimadzu, JP
ECW	Electrochemical workstation (CHI 760e)		CH instruments, US
FDA	Forcedisplacement analysis machine		Sauter, DE
IV / VNA	I-V and VNA Prober for VHF, LCR and frequency analysis measurements	20 – 120 MHz	Süss, DE; Cascade, US; Keysight, US
OSCI	4-channel real time oscilloscope	1.5 GHz (BW), 5 GSa/s	Keysight, US
IR-Cam	TrueIR Thermal Imager	-20 – 350 °C	Keysight, US
CM	Confocal Microscope (Smartproof 5)	405 nm LED, z drive res. ~ 1 nm	Carl Zeiss, DE
FAS	Fluidic Analytic Setup – microscope, high speed camera, and fluidic pumps	2 GB 120 kfps, 5 modules	Zeiss, DE; Photron, US; Cetoni, DE

Deposition and processing techniques

Physical Deposition	2x DC / 2x RF Magnetron Sputter System, up to 4x 6" substrates	Nordiko, UK
	Thermal (2 sources) / Electron Beam (12 pockets) Evaporation System	CREAVAC, DE
	Thermal Evaporation	Bal-Tec, LI
	Thermal (1 source) / Electron Beam (7 pockets) Evaporation System	BESTEC, DE
	DC/RF Magnetron Sputter System, 4x 3" + 4x 2" magnetrons, substrate heating: RT – 950 °C, up to 4" wafers	BESTEC, DE
	DC/RF Magnetron Sputter System, 6x 2" confocal magnetrons, substrate heating: RT – 650 °C, up to 3" wafers	AJA International, US
	Dual Ion Beam Sputtering (IBAD), 6" targets, RT – 500 °C	Home-built
	High Power Impulse Magnetron Sputtering	Melec, DE
	Magnetron Sputter System (2 targets)	Home-built
PLD	Pulsed Laser Deposition	SURFACE, DE
Molecular Beam Epitaxy	III-V Semiconductors	Riber, FR
	Metals	CreaTec Fischer, DE
Chemical Vapor Deposition	Plasma Enhanced CVD: a-Si, a-Ge, SiO_2, SiON, Si_3N_4	Oxford Instr., UK
Atomic Layer Deposition	Al_2O_3, HfO_2, SiO_2, ZnO	Ultratech, US
Dry Etching	ICP-RIE, $\varnothing$ 6": CF_4, SF_6, C_4F_8 with interferometric etch-stop monitor	Sentech, DE

	RIBE, $\varnothing$ 6": Ar, CF$_4$ with SIMS etch-stop monitor	*Roth & Rau, DE*
	Barrel reactor, $\varnothing$ 4": O$_2$, Ar	*Diener electronic, DE*
Etching/Cleaning	incl. Anisotropic Selective KOH Etching, Metal-Assisted Chemical Etching, Photoelectrochemical Etching	
Photolithography	Mask-Aligner MA6, $\varnothing$ 6", < 2 µm accuracy; with two-side alignment	*Süss, DE*
	Direct Laser Writer DWL 66FS, $\varnothing$ 8"x8", 2 µm accuracy	*Heidelberg Instr., DE*
	Laser Micro Writer ML, 10 µm accuracy	*Durham Magneto Optics, UK*
Electron Beam Lithography	Raith 150-TWO: $\varnothing$ 6", 10 nm resolution	*Raith, DE*
	e-Line Plus: $\varnothing$ 4", 10 nm resolution	*Raith, DE*
Thermal Treatment	Room Temperature – 2000 °C	
Oxidation and annealing furnace		*INNOTHERM, DE*
Rapid Thermal Annealing JETFIRST 100		*JIPELEC, FR*
Rapid Thermal Annealing AW 610		*Allwin21, USA*
Flash-Lamp Units (0.5 – 20 ms)		*Home-built; FHR/DTF, DE*
Combined Flash Lamp Sputter Tool (Magnetron sputtering plus flash lamp annealing 0.3 – 3 ms, up to 10 Hz)		*ROVAK GmbH, DE*
RF Heating (Vacuum)		*JIPELEC, FR*
Laser Annealing (CW, 808 nm, 450 W)		*LIMO, DE*
Laser Annealing (30 ns pulse,10 Hz, 308 nm, 500 mJ)		*COHERENT, USA*
CVD Tube furnace (RT – 1200 °C, three channel gas)		*NBD, CN*
Vacuum oven (RT – 250 °C, Vacuum < 133 Pa)		*LAB-KITS, CN*
Vacuum oven (RT – 800 °C, Vacuum < 10^{-7} mbar)		*Home-built*
Bonding Techniques	Ultrasonic Wire Bonding	*Kulicke & Soffa, US*
	Semi-automatic Wire-bonder: Gold-ball and wedge-wedge bonding Ultrasonic generator: 60 kHz, 140 kHz Wire deformation control software	*F & S Bondtec, AT*
Cutting, Grinding, Polishing		*Bühler, DE*
TEM Sample Preparation	Plan View and Cross Section incl. Ion Milling Equipment	*Gatan, US*
SEM / HIM Sample Preparation	Mechanical milling, sawing, grinding, polishing	*Leica, AUT*
	Argon cross-section milling, surface polishing	*Hitachi, JP*
Disperse and mixer	Mixer for pastes and emulsions	*IKA, DE*
Centrifuge	Max. 17850 rpm, -10 – 40 °C	*Thermo Scientific, US*

Doctoral training programme

International Helmholtz Research School NANONET

The Institute of Ion Beam Physics and Materials Research was coordinating the International Helmholtz Research School for Nanoelectronic Networks (IHRS NANONET) supported by the Initiative and Networking Fund of the Helmholtz Association between October 2012 and December 2020 with a total funding of 1.2 Mio. €. At the moment, the non-scientific education programme is continued by institute's funds.

The IHRS NANONET was an international, interdisciplinary and thematically focused doctoral programme in the field of molecular electronics. The research school aimed at attracting and promoting excellence by educating promising doctoral candidates with backgrounds in physics, chemistry, materials science and electrical engineering. During a period of three to four years, doctoral researchers benefit from well-structured, comprehensive training curricula and multiple mentorship, while performing cutting edge research projects within one of the NANONET research groups.
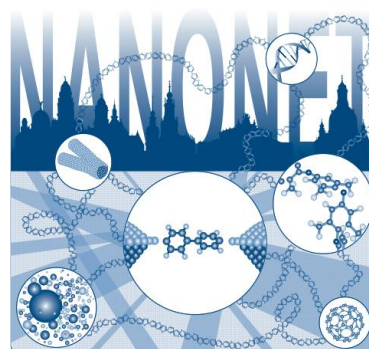
The IHRS NANONET fosters not only professional qualification but also personal development by equipping young graduates with competencies for successful careers in a wide variety of positions in academia and industry. The NANONET+ Annual Workshop 2021 was held in Klingenberg just before the fourth Corona wave and was attended by 34 participants of 12 nationalities.

Three senior students concluded their PhD degrees in 2021: Congratulations to Dr. Bilal Khan (TU Dresden), Dr. Filip Kilibarda (Univ Konstanz), and Dr. Florian Fuchs (TU Chemnitz).

The consortium
- Helmholtz-Zentrum Dresden-Rossendorf (HZDR)
- Technische Universität (TU) Dresden
- Leibniz Institute of Polymer Research (IPF) Dresden
- Fraunhofer Institute for Ceramic Technologies and Systems (IKTS) Dresden
- Nanoelectronic Materials Laboratory (NaMLab) gGmbH Dresden

For further information, please contact the NANONET coordinator, Dr. Peter Zahn (nanonet@hzdr.de), or visit the IHRS NANONET website: www.hzdr.de/NanoNet.

Publications and patents

Books and chapters

1. Escobar Galindo, R.; Krause, M.; Niranjan, K.; Barshilia, H.
    Solar selective coatings and materials for high-temperature solar thermal applications
    in: Sustainable Material Solutions for Solar Energy Technologies - Processing Techniques and Applications, Amsterdam: Elsevier, 2021, 978-0-12-821592-0, 383-427

2. Machalett, F.; Ying, B.; Wustelt, P.; Huth, V.; Bischoff, L.; Klingner, N.; Kübel, M.; Sayler, A.M.; Stöhlker, T.; Paulus, G.G.
    High brightness ion sources for laser-induced ionization of metal and metalloid ions
    in: Jahresbericht 2020 des Helmholtz-Instituts Jena, Jena: Helmholtz-Institut Jena, 2021

3. Posselt, M.
    "Materials" - Special Issue "First-Principle and Atomistic Modelling in Materials Science"
    Basel, Switzerland: MDPI, 2021

Publications in journals

1. Alencar, I.; Hatori, M.; Marmitt, G.G.; Trombini, H.; Grande, P.L.; Dias, J.F.; Papaléo, R.M.; Mücklich, A.; Assmann, W.; Toulemonde, M.; Trautmann, C.
    Nanoparticle emission by electronic sputtering of CaF_2 single crystals
    Applied Surface Science **537**, 147821 (2021)

2. Almeida, M.; Sharma, A.; Matthes, P.; Köhler, N.; Busse, S.; Müller, M.; Hellwig, O.; Horn, A.; Zahn, D.R.T.; Salvan, G.; Schulz, S.E.
    Laser induced crystallization of Co–Fe–B films
    Scientific Reports **11**, 14104 (2021)

3. Alsaadawi, Y.; Eichler-Volf, A.; Heigl, M.; Zahn, P.; Albrecht, M.; Erbe, A.
    Control Over Self-Assembled Janus Clusters by the Strength of Magnetic Field in H_2O_2
    European Physical Journal E **44**, 23 (2021)

4. Andreeva, M.; Smekhova, A.; Baulin, R.; Repchenko, Y.; Bali, R.; Schmitz-Antoniak, C.; Wende, H.; Sergueev, I.; Schlage, K.; Wille, H.C.
    Evolution of the magnetic hyperfine field profiles in ion-irradiated $Fe_{60}Al_{40}$ film measured by nuclear resonant reflectivity
    Journal of Synchrotron Radiation **28**, 1535 (2021)

5. Arekapudi, S.S.P.K.; Böhm, B.; Ramasubramanian, L.; Ganss, F.; Heinig, P.; Stienen, S.; Fowley, C.; Lenz, K.; Deac, A.M.; Albrecht, M.; Hellwig, O.
    Direct Imaging of Distorted Vortex Structure and Vortex-Antivortex Mediated Vortex Annihilation In Exchange Coupled Ferromagnetic/Antiferromagnetic Disk Structures
    Physical Review B **103**, 014405 (2021)

6. Babin, C.; Stöhr, R.; Morioka, N.; Linkewitz, T.; Steidl, T.; Wörnle, R.; Liu, D.; Hesselmeier, E.; Vorobyov, V.; Denisenko, A.; Hentschel, M.; Gobert, C.; Berwian, P.; Astakhov, G.; Knolle, W.; Majety, S.; Saha, P.; Radulaski, M.; Tien Son, N.; Ul-Hassan, J.; Kaiser, F.; Wrachtrup, J.
    Fabrication and nanophotonic waveguide integration of silicon carbide colour centres with preserved spin-optical coherence
    Nature Materials **21**, 67 (2022)

7. Bahmani, M.; Ghorbani Asl, M.; Frauenheim, T.
Effect of Interfacial Defects on the Electronic Properties of MoS$_2$ Based Lateral T–H Heterophase Junctions
RSC Advances **11**, 37995 (2021)

8. Balaghi, L.; Shan, S.; Fotev, I.; Moebus, F.; Rana, R.; Venanzi, T.; Hübner, R.; Mikolajick, T.; Schneider, H.; Helm, M.; Pashkin, O.; Dimakis, E.
High electron mobility in strained GaAs nanowires
Nature Communications **12**, 6642 (2021)

9. Barman, A.; Gubbiotti, G.; Ladak, S.; Adeyeye, A.O.; Krawczyk, M.; Gräfe, J.; Chumak, A.V.; Khitun, A.; Nikonov, D.; Young, I.A.; Vasyuchka, V.I.; Hillebrands, B.; Nikitov, S.A.; Yu, H.; Grundler, D.; Sadovnikov, A.V.; Grachev, A.A.; Sheshukova, S.E.; Duquesne, J.-Y.; Marangolo, M.; Csaba, G.; Porod, W.; Demidov, V.E.; Urazhdin, S.; Demokritov, S.O.; Albisetti, E.; Petti, D.; Bertacco, R.; Schultheiß, H.; Kruglyak, V.V.; Poimanov, V.D.; Sahoo, S.; Sinha, J.; Moriyama, T.; Mizukami, S.; Yang, H.; Münzenburg, M.; Landeros, P.; Gallardo, R.A.; Carlotti, G.; Kim, J.-V.; Stamps, R.L.; Camley, R.E.; Rana, B.; Otani, Y.; Yu, W.; Yu, T.; Bauer, G.E.W.; Back, C.; Uhrig, G.S.; Dobrovolskiy, O.V.; van Dijken, S.; Budinska, B.; Qin, H.; Adelmann, C.; Cotofana, S.; Naeemi, A.; Zingsem, B.W.; Winklhofer, M.
The 2021 Magnonics Roadmap
Journal of Physics: Condensed Matter **33**, 413001 (2021)

10. Barnett, J.; Wehmeier, L.; Heßler, A.; Lewin, M.; Pries, J.; Wuttig, M.; Klopf, J.M.; Kehr, S.C.; Eng, L.M.; Taubner, T.
Far-infrared Near-field Optical Imaging and Kelvin Probe Force Microscopy of Laser-crystallized and amorphized Phase Change Material Ge$_3$Sb$_2$Te$_6$
Nano Letters **21**, 9012 (2021)

11. Bayrak, T.; Martinez-Reyes, A.; Ruiz-Arce, D.D.; Kelling, J.; Samano, E.C.; Erbe, A.
Fabrication and temperature-dependent electrical characterization of a C-shape nanowire patterned by a DNA origami
Scientific Reports **11**, 1922 (2021)

12. Bejarano, M.; Trindade Goncalves, F.J.; Hollenbach, M.; Hache, T.; Hula, T.; Berencen, Y.; Faßbender, J.; Helm, M.; Astakhov, G.; Schultheiß, H.
Mapping the stray fields of a micromagnet using spin centers in SiC
IEEE Magnetics Letters **12**, 9380379 (2021)

13. Berkmann, F.; Ayasse, M.; Schlipf, J.; Mörz, F.; Weißhaupt, D.; Oehme, M.; Prucnal, S.; Kawaguchi, Y.; Schwarz, D.; Fischer, I.A.; Schulze, J.
Plasmonic gratings from highly doped Ge$_{1-y}$Sn$_y$ films on Si
Journal of Physics D: Applied Physics **54**, 445109 (2021)

14. Bittrich, E.; Domke, J.; Levichkova, M.; Jehnichen, D.; Bittrich, L.; Janke, A.; Formanek, P.; Hübner, R.; Uhlmann, P.; Eichhorn, K.-J.; Forker, R.; Gruenewald, M.; Al-Hussein, M.; Fritz, T.; Walzer, K.
Structural Templating of an Organic Solar Cell Absorber by Ellagic Acid To Tune Its Aggregation, Molecular Orientation, and Optical Properties
ACS Applied Energy Materials **4**, 14273 (2021)

15. Blaschke, D.; Pahlow, S.; Fremberg, T.; Weber, K.; Müller, A.D.; Kurz, S.; Spohn, J.; Dhandapani, V.; Rebohle, L.; Skorupa, I.; Schmidt, H.
Functionalized silicon substrates with stripe-patterned surface-near electrostatic forces for the self-organized, stable immobilization of biomolecules
Applied Surface Science **545**, 148729 (2021)

16. Boelens, P.; Lei, Z.; Drobot, B.; Rudolph, M.; Li, Z.; Franzreb, M.; Eckert, K.; Lederer, F.
     **High-Gradient Magnetic Separation of Compact Fluorescent Lamp Phosphors: Elucidation
     of the Removal Dynamics in a Rotary Permanent Magnet Separator**
     Minerals **11**, 1116 (2021)

17. Böhm, B.; Fallarino, L.; Pohl, D.; Rellinghaus, B.; Hellwig, O.
     **Noncollinear Remanent Textures Induced by Surface Spin Flop in Synthetic
     Antiferromagnets with Perpendicular Anisotropy**
     Physical Review Applied **16**, 014028 (2021)

18. Borisov, K.; Ehrler, J.; Fowley, C.; Eggert, B.; Wende, H.; Cornelius, S.; Potzger, K.; Lindner, J.;
     Faßbender, J.; Bali, R.; Stamenov, P.
     **Spin polarization and magnetotransport properties of systematically disordered $Fe_{60}Al_{40}$
     thin films**
     Physical Review B **104**, 134417 (2021)

19. Breev, I.D.; Likhachev, K.V.; Yakovleva, V.V.; Hübner, R.; Astakhov, G.; Mokhov, E.N.; Baranov,
     P.G.; Anisimov, A.N.
     Stress distribution at the AlN/SiC heterointerface probed by Raman spectroscopy
     Journal of Applied Physics **129**, 055304 (2021)

20. Breev, I.D.; Likhachev, K.V.; Yakovleva, V.V.; Veishtort, I.P.; Skomorokhov, A.M.; Nagalyuk,
     S.S.; Mokhov, E.N.; Astakhov, G.; Baranov, P.G.; Anisimov, A.N.
     Effect of Mechanical Stress on the Splitting of Spin Sublevels in 4H-SiC
     JETP Letters **114**, 274 (2021)

21. Breev, I.D.; Poshakinskiy, A.V.; Yakovleva, V.V.; Nagalyuk, S.S.; Mokhov, E.N.; Hübner, R.;
     Astakhov, G.; Baranov, P.G.; Anisimov, A.N.
     Stress-controlled zero-field spin splitting in silicon carbide
     Applied Physics Letters **118**, 084003 (2021)

22. Brorsson, J.; Hashemi, A.; Fan, Z.; Fransson, E.; Eriksson, F.; Ala-Nissila, T.; Krasheninnikov,
     A.; Komsa, H.-P.; Erhart, P.
     **Effcient Calculation of the Lattice Thermal Conductivity by Atomistic Simulations with Ab
     Initio Accuracy**
     Advanced Theory and Simulations, 2100217 (2021)

23. Canon Bermudez, G.S.; Makarov, D.
     Magnetosensitive E-Skins for Interactive Devices
     Advanced Functional Materials **31**, 2007788 (2021)

24. Cansever, H.; Lindner, J.
     **Microresonators and Microantennas—Tools to Explore Magnetization Dynamics in Single
     Nanostructures**
     Magnetochemistry **7**, 28 (2021)

25. Cao, L.; Herklotz, A.; Rata, D.; Yin, C.; Petracic, O.; Kentsch, U.; Helm, M.; Zhou, S.
     Metal–Insulator Transition via Ion Irradiation in Epitaxial $La_{0.7}Sr_{0.3}MnO_{3-\delta}$ Thin Films
     Physica Status Solidi (RRL) **15**, 2100278 (2021)

26. Cao, L.; Petracic, O.; Wei, X.-K.; Zhang, H.; Duchoň, T.; Gunkel, F.; Koutsioubas, A.;
     Zhernenkov, K.; Rushchanskii, K.Z.; Hartmann, H.; Wilhelm, M.; Li, Z.; Xie, Y.; He, S.; Weber,
     M.L.; Veltruská, K.; Stellhorn, A.; Mayer, J.; Zhou, S.; Brückel, T.
     **Migration kinetics of surface ions in oxygen-deficient perovskite during topotactic
     transitions**
     Small **17**, 2104356 (2021)

27. Chae, S.; Jin Choi, W.; Fotev, I.; Bittrich, E.; Uhlmann, P.; Schubert, M.; Makarov, D.; Wagner, J.; Pashkin, O.; Fery, A.
Stretchable Thin Film Mechanical Strain Gated Switches and Logic Gate Functions Based on a Soft Tunneling Barrier
Advanced Materials **33**, 2104769 (2021)

28. Chen, J.; Wang, H.; Hula, T.; Liu, C.; Liu, S.; Liu, T.; Jia, H.; Song, Q.; Guo, C.; Zhang, Y.; Zhang, J.; Han, X.; Yu, D.; Wu, M.; Schultheiß, H.; Yu, H.
Reconfigurable Spin-Wave Interferometer at the Nanoscale
Nano Letters **21**, 6237 (2021)

29. Chen, Z.; Du, N.; Kiani, M.; Zhao, X.; Skorupa, I.; Schulz, S.; Bürger, D.; Di Ventra, M.; Polian, I.; Schmidt, H.
Second harmonic generation exploiting ultra-stable resistive switching devices for secure hardware systems
IEEE Transactions on Nanotechnology **21**, 71 (2022)

30. Chin, M.L.; Matschy, S.; Stawitzki, F.; Poojali, J.; Hafez, H.A.; Turchinovich, D.; Winnerl, S.; Kumar, G.; Myers-Ward, R.L.; Dejarld, M.T.; Daniels, K.M.; Drew, H.D.; Murphy, T.E.; Mittendorff, M.
Observation of strong magneto plasmonic nonlinearity in bilayer graphene discs
Journal of Physics: Photonics **3**, 01LT01 (2021)

31. Choupanian, S.; Nagel, A.; Möller, W.; Pacholski, C.; Ronning, C.
The disappearance and return of nanoparticles upon low energy ion irradiation
Nanotechnology **33**, 035703 (2022)

32. Ciani, G.F.; Csedreki, L.; Balibrea-Correa, J.; Best, A.; Aliotta, M.; Barile, F.; Bemmerer, D.; Boeltzig, A.; Broggini, C.; Bruno, C.G.; Caciolli, A.; Cavanna, F.; Chillery, T.; Colombetti, P.; Corvisiero, P.; Davinson, T.; Depalo, R.; Di Leva, A.; Di Paolo, L.; Elekes, Z.; Ferraro, F.; Fiore, E.M.; Formicola, A.; Fülöp, Z.; Gervino, G.; Guglielmetti, A.; Gustavino, C.; Gyürky, G.; Imbriani, G.; Junker, M.; Kochanek, I.; Lugaro, M.; Marigo, P.; Masha, E.; Menegazzo, R.; Mossa, V.; Pantaleo, F.R.; Paticchio, V.; Perrino, R.; Piatti, D.; Prati, P.; Schiavulli, L.; Stöckel, K.; Straniero, O.; Szücs, T.; Takács, M.P.; Terrasi, F.; Trezzi, D.; Zavatarelli, S.
A new approach to monitor ^{13}C-targets degradation in situ for $^{13}C(\alpha,n)^{16}O$ cross-section measurements at LUNA
European Physical Journal A **56**, 75 (2021)

33. Creutzburg, S.; Mergl, M.; Hübner, R.; Jirka, I.; Erb, D.; Heller, R.; Niggas, A.; Grande, P.L.; Aumayr, F.; Wilhelm, R.A.; Kalbac, M.; Facsko, S.
Fluorination of graphene leads to susceptibility for nanopore formation by highly charged ion impact
Physical Review Materials **5**, 074007 (2021)

34. Cupak, C.; Szabo, P.S.; Biber, H.; Stadlmayr, R.; Grave, C.; Fellinger, M.; Brötzner, J.; Wilhelm, R.A.; Möller, W.; Mutzke, A.; Moro, M.V.; Aumayr, F.
Sputter yields of rough surfaces: Importance of the mean surface inclination angle from nano- to microscopic rough regimes
Applied Surface Science **570**, 151204 (2021)

35. Das, D.; Barman, A.; Sarkar, P.K.; Rajput, P.; Jha, S.N.; Hübner, R.; Kanjilal, D.; Johari, P.; Kanjilal, A.
Metal-induced progressive alteration of conducting states in memristors for implementing an efficient analog memory: a DFT-supported experimental approach
Journal of Materials Chemistry C **9**, 3136 (2021)

36. Das, P.; Möller, W.; Elliman, R.G.; Chatterjee, S.
Ion beam joining of ceramic and carbon-based nanostructures
Applied Surface Science **554**, 149616 (2021)

37. de Castro, O.; Biesemeier, A.; Serralta Hurtado De Menezes, E.; Bouton, O.; Barrahma, R.;
Hung Hoang, Q.; Cambier, S.; Taubitz, T.; Klingner, N.; Hlawacek, G.
**The npSCOPE: a new multimodal instrument for in-situ correlative analysis of
nanoparticles**
Analytical Chemistry **93**, 14417 (2021)

38. Diehl, R.; Lugaro, M.; Heger, A.; Sieverding, A.; Tang, X.; Li, K.A.; Li, E.T.; Doherty, C.L.;
Krause, M.G.H.; Wallner, A.; Prantzos, N.; Brinkman, H.E.; Den, H.J.W.; Wehmeyer, B.; Yagüe
López, A.; Pleintinger, M.M.M.; Banerjee, P.; Wang, W.
The radioactive nuclei ^{26}Al and ^{60}Fe in the Cosmos and in the solar system
Publications of the Astronomical Society of Australia (PASA) **38**, e062 (2021)

39. Ding, J.; Wu, D.; Zhu, J.; Rodríguez-Hernández, F.; Chen, Y.; Lu, C.; Zhou, S.; Zhang, J.;
Tranca, D.; Zhuang, X.
**High-entropy carbons: From high-entropy aromatic species to single-atom catalysts for
electrocatalysis**
Chemical Engineering Journal **426**, 131320 (2021)

40. Dixit, R.; Gupta, A.; Jordan, N.; Zhou, S.; Schild, D.; Weiß, S.; Guillon, E.; Jain, R.; Lens, P.
Magnetic properties of biogenic selenium nanomaterials
Environmental Science and Pollution Research **28**, 40264 (2021)

41. Du, R.; Jin, W.; Wu, H.; Hübner, R.; Zhou, L.; Xue, G.; Hu, Y.; Eychmüller, A.
**Rapid synthesis of gold-palladium core-shell aerogels for selective and robust
electrochemical CO_2 reduction**
Journal of Materials Chemistry A **9**, 17189 (2021)

42. Duan, J.; Chava, P.; Ghorbani Asl, M.; Krasheninnikov, A.; Erb, D.; Hu, L.; Schneider, H.;
Rebohle, L.; Erbe, A.; Helm, M.; Zeng, Y.-J.; Zhou, S.; Prucnal, S.
**Enhanced trion emission in monolayer $MoSe_2$ by constructing a type-I van der Waals
heterostructure**
Advanced Functional Materials **31**, 2104960 (2021)

43. Duan, J.; Wang, C.; Vines, L.; Rebohle, L.; Helm, M.; Zeng, Y.-J.; Zhou, S.; Prucnal, S.
Increased dephasing length in heavily doped GaAs
New Journal of Physics **23**, 083034 (2021)

44. Echresh, A.; Arora, H.; Fuchs, F.; Li, Z.; Hübner, R.; Prucnal, S.; Schuster, J.; Zahn, P.; Helm,
M.; Zhou, S.; Erbe, A.; Rebohle, L.; Georgiev, Y.
**Electrical Characterization of Germanium Nanowires Using a Symmetric Hall Bar
Configuration: Size and Shape Dependence**
Nanomaterials **11**, 2917 (2021)

45. Eichhorn, J.; Lechner, S.P.; Jiang, C.-M.; Folchi, G.; Munnik, F.; Sharp, I.D.
**Indirect bandgap, optoelectronic properties, and photoelectrochemical characteristics of
high-purity Ta_3N_5 photoelectrodes**
Journal of Materials Chemistry A **9**, 20653 (2021)

46. Eichler-Volf, A.; Alsaadawi, Y.; Vazquez Luna, F.; Khan, Q.A.; Stierle, S.; Xu, C.; Heigl, M.; Fekri,
Z.; Zhou, S.; Zahn, P.; Albrecht, M.; Steinhart, M.; Erbe, A.
Sensitivity of PS/CoPd Janus particles to an external magnetic field
RSC Advances **11**, 17051 (2021)

47. Erb, D.; Myint, P.; Evans-Lutterodt, K.; Ludwig, K.; Facsko, S.
In-situ GISAXS observation of ion-induced nanoscale pattern formation on crystalline Ge(001) in the reverse epitaxy regime
Physical Review B **104**, 235434 (2021)

48. Escobar Galindo, R.; Heras, I.; Guillén, E.; Munnik, F.; Azkona, I.; Krause, M.
Comprehensive microstructural and optical characterization of the thermal stability of aluminum-titanium oxynitride thin films after high temperature annealing in air
Emergent Materials **4**, 1559 (2021)

49. Fei, Y.; Fu, Y.; Bai, X.; Du, L.; Li, Z.; Komber, H.; Low, K.-H.; Zhou, S.; Lee Phillips, D.; Feng, X.; Liu, J.
Defective Nanographenes Containing Seven-Five-Seven (7–5–7)-Membered Rings
Journal of the American Chemical Society **143**, 2353 (2021)

50. Fischer, M.; Caridad, J.M.; Sajid, A.; Ghaderzadeh, S.; Ghorbani Asl, M.; Gammelgaard, L.; Bøggild, P.; Thygesen, K.S.; Krasheninnikov, A.; Xiao, S.; Wubs, M.; Stenger, N.
Controlled Generation of Luminescent Centers in Hexagonal Boron Nitride by Irradiation Engineering
Science Advances **7**, eabe7138 (2021)

51. Fischer, S.; Jain, R.; Krause, T.; Jain, P.; Tsushima, S.; Shevchenko, A.; Hübner, R.; Jordan, N.
Impact of the microbial origin and active microenvironment on the shape of biogenic elemental selenium nanomaterials
Environmental Science & Technology **55**, 9161 (2021)

52. Flacke, L.; Ahrens, V.; Mendisch, S.; Körber, L.; Böttcher, T.; Meidinger, E.; Yaqoob, M.; Müller, M.; Liensberger, L.; Kakay, A.; Becherer, M.; Pirro, P.; Althammer, M.; Geprägs, S.; Huebl, H.; Gross, R.; Weiler, M.
Robust formation of nanoscale magnetic skyrmions in easy-plane anisotropy thin film multilayers with low damping
Physical Review B **104**, L100417 (2021)

53. Friedrich, R.; Esters, M.; Oses, C.; Ki, S.; Brenner, M.J.; Hicks, D.; Mehl, M.J.; Toher, C.; Curtarolo, S.
Automated coordination corrected enthalpies with AFLOW-CCE
Physical Review Materials **5**, 043803 (2021)

54. Gallardo, R.A.; Alvarado-Seguel, P.; Kákay, A.; Lindner, J.; Landeros, P.
Spin-wave focusing induced by dipole-dipole interaction in synthetic antiferromagnets
Physical Review B **104**, 174417 (2021)

55. Galle, T.; Spittel, D.; Weiß, N.; Shamraienko, V.; Decker, H.; Georgi, M.; Hübner, R.; Metzkow, N.; Steinbach, C.; Schwarz, D.; Lesnyak, V.; Eychmüller, A.
Simultaneous Ligand and Cation Exchange of Colloidal CdSe Nanoplatelets toward PbSe Nanoplatelets for Application in Photodetectors
The Journal of Physical Chemistry Letters **12**, 5214 (2021)

56. Gentillon, A.; Richards, C.; Ortiz-Flores, L.A.; Metzner, J.; Montealegre, D.; Healey, M.; Cardon, K.; Westover, A.; Hellwig, O.; Chesnel, K.
Robustness of the remanent magnetic domain pattern formation and associated stripe-bubble transitions in Co/Pt multilayers against field sequencing
AIP Advances **11**, 015339 (2021)

57. Ghaderzadeh, S.; Kretschmer, S.; Ghorbani Asl, M.; Hlawacek, G.; Krasheninnikov, A.
Atomistic Simulations of Defect Production in Monolayer and Bulk Hexagonal Boron Nitride under Low- and High-Fluence Ion Irradiation
Nanomaterials **11**, 1214 (2021)

58. Gospodarič, P.; Młyńczak, E.; Soldatov, I.; Kakay, A.; Bürgler, D.E.; Plucinski, L.; Schäfer, R.; Faßbender, J.; Schneider, C.M.
Multistate current-induced magnetization switching in Au/Fe/MgO(001) epitaxial heterostructures
Physical Review Research **3**, 023089 (2021)

59. Guillén, E.; Krause, M.; Heras, I.; Rincón-Llorente, G.; Escobar-Galindo, R.
Tailoring crystalline structure of titanium oxide films for optical applications using non-biased filtered cathodic vacuum arc deposition at room temperature
Coatings **11**, 233 (2021)

60. Guo, E.; Xing, S.; Dollinger, F.; Hübner, R.; Wang, S.-J.; Wu, Z.; Leo, K.; Kleemann, H.
Integrated complementary inverters and ring oscillators based on vertical-channel dual-base organic thin-film transistors
Nature Electronics **4**, 588 (2021)

61. Ha, M.; Canon Bermudez, G.S.; Kosub, T.; Mönch, J.I.; Zabila, Y.; Oliveros Mata, E.S.; Illing, R.; Wang, Y.; Faßbender, J.; Makarov, D.
Printable and Stretchable Giant Magnetoresistive Sensors for Highly Compliant and Skin-Conformal Electronics
Advanced Materials **33**, 2005521 (2021)

62. Ha, M.; Canon Bermudez, G.S.; Liu, J.A.-C.; Oliveros Mata, E.S.; Evans, B.A.; Tracy, J.B.; Makarov, D.
Reconfigurable magnetic origami actuators with on-board sensing for guided assembly
Advanced Materials **33**, 2008751 (2021)

63. Han, J.; Chin, M.L.; Matschy, S.; Poojali, J.; Seidl, A.; Winnerl, S.; Hafez, H.A.; Turchinovich, D.; Kumar, G.; Myers-Ward, R.L.; Dejarld, M.T.; Daniels, K.M.; Drew, H.D.; Murphy, T.E.; Mittendorff, M.
Plasmonic terahertz nonlinearity in graphene disks
Advanced Photonics Research **3**, 2100218 (2021)

64. Hartley, N.; Grenzer, J.; Huang, L.; Inubushi, Y.; Kamimura, N.; Katagiri, K.; Kodama, R.; Kon, A.; Lu, W.; Makita, M.; Matsuoka, T.; Nakajima, S.; Ozaki, N.; Pikuz, T.; Rode, A.V.; Sagae, D.; Schuster, A.; Tono, K.; Voigt, K.; Vorberger, J.; Yabuuchi, T.; McBride, E.E.; Kraus, D.
Using Diffuse Scattering to Observe X-Ray-Driven Nonthermal Melting
Physical Review Letters **126**, 015703 (2021)

65. Hashemi, A.; Linderälv, C.; Krasheninnikov, A.; Ala-Nissilä, T.; Erhart, P.; Komsa, H.-P.
Photoluminescence Lineshapes for Defect Centers in Silicon Carbide from First-Principles Calculations
Physical Review B **103**, 125203 (2021)

66. Hassani, N.; Ghorbani Asl, M.; Radha, B.; Drndic, M.; Krasheninnikov, A.; Neek-Amal, M.
Gas permeability and selectivity of a porous WS_2 monolayer
Journal of Physical Chemistry C **125**, 25055 (2021)

67. Hedrich, N.; Wagner, K.; Pylypovskyi, O.; Shields, B.J.; Kosub, T.; Sheka, D.; Makarov, D.; Maletinsky, P.
Nanoscale mechanics of antiferromagnetic domain walls
Nature Physics **17**, 574 (2021)

68. Hernandez-Minguez, A.; Poshakinskiy, A.V.; Hollenbach, M.; Santos, P.V.; Astakhov, G.
Acoustically induced coherent spin trapping
Science Advances **7**, eabj5030 (2021)

69. Hu, L.; Cao, L.; Li, L.; Duan, J.; Liao, X.; Long, F.; Zhou, J.; Xiao, Y.; Zeng, Y.-J.; Zhou, S.
Two-dimensional magneto-photoconductivity in non-van der Waals manganese selenide
Materials Horizons **8**, 1286 (2021)

70. Huang, L.; Li, L.; Shang, Z.; Wang, M.; Kang, J.; Luo, W.; Liang, Z.; Prucnal, S.; Kentsch, U.; Ji, Y.; Zhang, F.; Wang, Q.; Yuan, Y.; Sun, Q.; Zhou, S.; Wang, X.
Structure and luminescence of a-plane GaN on r-plane sapphire substrate modified by Si implantation
Chinese Physics B **30**, 056104 (2021)

71. Iurchuk, V.; Körber, L.; Deac, A.M.; Faßbender, J.; Lindner, J.; Kakay, A.
Stress-induced modification of gyration dynamics in stacked double-vortex structures studied by micromagnetic simulations
Journal of Physics D: Applied Physics **54**, 475002 (2021)

72. Jager, N.; Meindlhumer, M.; Zitek, M.; Spor, S.; Hruby, H.; Nahif, F.; Julin, J.; Keckes, J.; Mitterer, C.; Daniel, R.
Impact of Si on the high-temperature oxidation of AlCr(Si)N coatings
Journal of Materials Science and Technology **100**, 91 (2022)

73. Jakob, A.M.; Robson, S.G.; Schmitt, V.; Mourik, V.; Posselt, M.; Spemann, D.; Johnson, B.C.; Firgau, H.R.; Mayes, E.; McCallum, J.C.; Morello, A.; Jamieson, D.N.
Deterministic Shallow Dopant Implantation in Silicon with Detection Confidence Upper-Bound to 99.85% by Ion–Solid Interactions
Advanced Materials **34**, 2103235 (2022)

74. Jia, Z.; Wang, W.; Li, Z.; Sun, R.; Zhou, S.; Leonard Deepak, F.; Su, C.; Li, Y.; Wang, Z.
Morphology-Tunable Synthesis of Intrinsic Room-Temperature Ferromagnetic γ-Fe$_2$O$_3$ Nanoflakes
ACS Applied Materials and Interfaces **13**, 24051 (2021)

75. Jiang, G.; Erdem, O.; Hübner, R.; Georgi, M.; Wei, W.; Fan, X.; Wang, J.; Demir, H.V.; Gaponik, N.
Mechanosynthesis of polymer-stabilized lead bromide perovskites: insight into the formation and phase conversion of nanoparticles
Nano Research **14**, 1078 (2021)

76. Jiang, X.; Du, R.; Hübner, R.; Hu, Y.; Eychmüller, A.
A Roadmap for 3D Metal Aerogels: Materials Design and Application Attempts
Matter **4**, 54 (2021)

77. Joseph, T.; Ghorbani Asl, M.; Batzill, M.; Krasheninnikov, A.
Water dissociation and association on mirror twin boundaries in two-dimensional MoSe$_2$: insights from density functional theory calculations
Nanoscale Advances **3**, 6992 (2021)

78. Jóźwik, I.; Jagielski, J.; Caban, P.; Kamiński, M.; Kentsch, U.
Direct visualization of highly resistive areas in GaN by means of low-voltage scanning electron microscopy
Materials Science in Semiconductor Processing **138**, 106293 (2022)

79. Jozwik, I.; Jagielski, J.; Dumiszewska, E.; Kaminski, M.; Kentsch, U.
Resistivity contrast imaging in semiconductor structures using ultra-low energy scanning electron microscopy
Ultramicroscopy **228**, 113333 (2021)

80. Khan, M.B.; Prucnal, S.; Ghosh, S.; Deb, D.; Hübner, R.; Pohl, D.; Rebohle, L.; Mikolajick, T.; Erbe, A.; Georgiev, Y.
Controlled Silicidation of Silicon Nanowires using Flash Lamp Annealing
Langmuir **37**, 14284 (2021)

81. Kilibarda, F.; Strobel, A.; Sendler, T.; Wieser, M.; Mortensen, M.; Brender Trads, J.; Helm, M.; Kerbusch, J.; Scheer, E.; Gemming, S.; Gothelf, K.V.; Erbe, A.
Single Molecule Doping: Conductance Changed by Transition Metal Centers in Salen Molecules
Advanced Electronic Materials **7**, 2100252 (2021)

82. Kondinski, A.; Ghorbani Asl, M.
Polyoxoplatinates as Covalently Dynamic Electron Sponges and Molecular Electronics Materials
Nanoscale Advances **3**, 5663 (2021)

83. Körber, L.; Kakay, A.
Numerical reverse engineering of general spin-wave dispersions: Bridge between numerics and analytics using a dynamic-matrix approach
Physical Review B **104**, 174414 (2021)

84. Körber, L.; Quasebarth, G.; Otto, A.; Kakay, A.
Finite-element dynamic-matrix approach for spin-wave dispersions in magnonic waveguides with arbitrary cross section
AIP Advances **11**, 095006 (2021)

85. Körber, L.; Zimmermann, M.; Wintz, S.; Finizio, S.; Kronseder, M.; Bougeard, D.; Dirnberger, F.; Weigand, M.; Raabe, J.; Otálora, J.A.; Schultheiß, H.; Josten, E.; Lindner, J.; Kézsmárki, I.; Back, C.H.; Kakay, A.
Symmetry and curvature effects on spin waves in vortex-state hexagonal nanotubes
Physical Review B **104**, 184429 (2021)

86. Köster, J.; Ghorbani Asl, M.; Lehnert, T.; Komsa, H.-P.; Kretschmer, S.; Krasheninnikov, A.; Kaiser, U.
Defect Agglomeration and Electron Beam-Induced Local Phase Transformations in Single-Layer MoTe$_2$
Journal of Physical Chemistry C **125**, 13601 (2021)

87. Krause, M.; Sonnenberg, J.; Munnik, F.; Grenzer, J.; Hübner, R.; Garcia Valenzuela, A.; Gemming, S.
Formation, structure, and optical properties of copper chromite thin films for high-temperature solar absorbers
Materialia **18**, 101156 (2021)

88. Lachner, J.; Martschini, M.; Kalb, A.; Kern, M.; Marchhart, O.; Plasser, F.; Priller, A.; Steier, P.; Wieser, A.; Golser, R.
Highly sensitive ^{26}Al measurements by Ion-Laser-InterAction Mass Spectrometry
International Journal of Mass Spectrometry **465**, 116576 (2021)

89. Lehnert, T.; Kretschmer, S.; Bräuer, F.; Krasheninnikov, A.; Kaiser, U.
Quasi-two-dimensional NaCl crystals encapsulated between graphene sheets and their decomposition under an electron beam
Nanoscale **13**, 19626 (2021)

90. Li, J.; Kolekar, S.; Ghorbani Asl, M.; Lehnert, T.; Biskupek, J.; Kaiser, U.; Krasheninnikov, A.; Batzill, M.
Layer-Dependent Band Gaps of Platinum-Dichalcogenides
ACS Nano **15**, 13249 (2021)

91. Li, J.; Rana, R.; Zhu, L.; Liu, C.; Schneider, H.; Pashkin, O.
Limitation of THz conversion efficiency in DSTMS pumped by intense femtosecond pulses
Optics Express **29**, 22494 (2021)

92. Li, J.; Rana, R.; Zhu, L.; Liu, C.; Schneider, H.; Pashkin, O.
Optical Kerr nonlinearity and multi-photon absorption of DSTMS measured by Z-scan method
Journal of the Optical Society of America B **38**, 2511 (2021)

93. Li, S.; Cao, P.; Li, F.; Asghar, W.; Wu, Y.; Xiao, H.; Liu, Y.; Zhou, Y.; Yang, H.; Zhang, Y.; Shang, J.; Makarov, D.; Li, R.-W.
Self-powered Stretchable Strain Sensors for Motion Monitoring and Wireless Control
Nano Energy **92**, 106754 (2022)

94. Li, Y.; Jiang, K.; Yang, J.; Zheng, Y.; Hübner, R.; Ou, Z.; Dong, X.; He, L.; Wang, H.; Li, J.; Sun, Y.; Lu, X.; Zhuang, X.; Zheng, Z.; Liu, W.
Tungsten Oxide/Reduced Graphene Oxide Aerogel with Low-Content Platinum as High-Performance Electrocatalyst for Hydrogen Evolution Reaction
Small **17**, 2102159 (2021)

95. Li, Z.; Xie, Y.; Yuan, Y.; Ji, Y.; Begeza, V.; Cao, L.; Hübner, R.; Rebohle, L.; Helm, M.; Kornelius, N.; Prucnal, S.; Zhou, S.
Phase selection in Mn-Si alloys by fast solid-state reaction with enhanced skyrmion stability
Advanced Functional Materials **31**, 2009723 (2021)

96. Li, Z.; Xie, Y.; Yuan, Y.; Wang, M.; Xu, C.; Hübner, R.; Prucnal, S.; Zhou, S.
B20-type FeGe on Ge(100) prepared by pulsed laser melting
Journal of Magnetism and Magnetic Materials **532**, 167981 (2021)

97. Li, Z.; Yuan, Y.; Hübner, R.; Begeza, V.; Rebohle, L.; Helm, M.; Nielsch, K.; Prucnal, S.; Zhou, S.
B20-MnSi films grown on Si(100) substrates with magnetic skyrmion signature
Materials Today Physics **21**, 100541 (2021)

98. Lin, G.; Liu, Y.; Huang, G.; Chen, Y.; Makarov, D.; Lin, J.; Quan, Z.; Jin, D.
3D Rotation-Trackable and Differentiable Micromachines with Dimer-Type Structures for Dynamic Bioanalysis
Advanced Intelligent Systems **3**, 2000205 (2021)

99. Lin, Y.-C.; Motoyama, A.; Kretschmer, S.; Ghaderzadeh, S.; Ghorbani Asl, M.; Araki, Y.; Krasheninnikov, A.; Ago, H.; Suenaga, K.
Polymorphic Phases of Metal Chlorides in the Confined 2D Space of Bilayer Graphene
Advanced Materials **33**, 2105898 (2021)

100. Lin, Y.; Karthikeyan, J.; Chang, Y.; Li, S.; Kretschmer, S.; Komsa, H.; Chiu, P.; Krasheninnikov, A.; Suenaga, K.
Formation of Highly Doped Nanostripes in 2D Transition Metal Dichalcogenides via a Dislocation Climb Mechanism
Advanced Materials **33**, 2007819 (2021)

101. Liu, K.; Li, J.; Qi, H.; Hambsch, M.; Rawle, J.; Romaní Vázquez, A.; Shaygan Nia, A.; Pashkin, O.; Schneider, H.; Polozij, M.; Heine, T.; Helm, M.; Mannsfeld, S.C.B.; Kaiser, U.; Dong, R.; Feng, X.
A Two-Dimensional Polyimide-Graphene Heterostructure with Ultra-fast Interlayer Charge Transfer
Angewandte Chemie **60**, 13859 (2021)

102. Liu, L.; Hu, X.; Wang, Y.; Krasheninnikov, A.; Chen, Z.; Sun, L.
Tunable electronic properties and enhanced ferromagnetism in $Cr_2Ge_2Te_6$ monolayer by strain engineering
Nanotechnology **32**, 485408 (2021)

103. Lokamani, M.; Kelling, J.; Ohmann, R.; Meyer, J.; Kühne, T.; Cuniberti, G.; Wolf, J.; Huhn, T.; Zahn, P.; Moresco, F.; Gemming, S.
A combined experimental and theoretical study of 1,4-bis(phenylethynyl)-2,5-bis(ethoxy)benzene adsorption on Au(111)
Surface Science **712**, 121877 (2021)

104. Lu, N.; Chen, Z.; Zhang, W.; Yang, G.; Liu, Q.; Böttger, R.; Zhou, S.; Liu, Y.
Effect of silver ion implantation on antibacterial ability of polyethylene food packing films
Food Packaging and Shelf Life **28**, 100650 (2021)

105. Luo, C.-Q.; Zhu, S.-C.; Xu, C.; Zhou, S.; Lame, C.-H.; Ling, F.C.-C.
Room temperature ferromagnetism in Sb doped ZnO
Journal of Magnetism and Magnetic Materials **529**, 167908 (2021)

106. Makarov, D.; Volkov, O.; Kakay, A.; Pylypovskyi, O.; Budinska, B.; Dobrovolskiy, O.
New dimension in magnetism and superconductivity: 3D and curvilinear nano-architectures
Advanced Materials **34**, 2101758 (2022)

107. Makushko, P.; Oliveros Mata, E.S.; Canon Bermudez, G.S.; Hassan, M.; Laureti, S.; Rinaldi, C.; Fagiani, F.; Barucca, G.; Schmidt, N.; Zabila, Y.; Kosub, T.; Illing, R.; Volkov, O.; Vladymyrskyi, I.; Faßbender, J.; Albrecht, M.; Varvaro, G.; Makarov, D.
Flexible magnetoreceptor with tunable intrinsic logic for on-skin touchless human-machine interfaces
Advanced Functional Materials **31**, 2101089 (2021)

108. Mazalski, P.; Ohnoutek, L.; Sveklo, I.; Beran, L.; Kurant, Z.; Powroźnik, W.; Wawro, A.; Liedke, M.O.; Butterling, M.; Wagner, A.; Faßbender, J.; Hamrle, J.; Antoš, R.; Kletecka, V.; Veis, M.; Maziewski, A.
Ultrathin Co films with Pt and Au covers - magnetic and structural properties driven by Ga^+ ion irradiation
New Journal of Physics **23**, 023015 (2021)

109. Merchel, S.; Braucher, R.; Lachner, J.; Rugel, G.
Which is the best ^9Be carrier for $^{10}Be/^9Be$ accelerator mass spectrometry?
MethodsX **8**, 101486 (2021)

110. Merchel, S.; Rugel, G.; Lachner, J.; Wallner, A.; Walther, D.; Ziegenrücker, R.
Evaluation of a sensitive, reasonable, and fast detection method for ^{55}Fe in steel
Journal of Radioanalytical and Nuclear Chemistry **330**, 727 (2021)

111. Mitrofanov, A.; Prudnikau, A.; Di Stasio, F.; Weiß, N.; Hübner, R.; Dominic, A.M.; Borchert, K.B.L.; Lesnyak, V.; Eychmüller, A.
Near-Infrared-Emitting $Cd_xHg_{1-x}Se$-Based Core/Shell Nanoplatelets
Chemistry of Materials **33**, 7693 (2021)

112. Morán-Pedroso, M.; Gago, R.; Julin, J.A.; Salas-Colera, E.; Jimenez, I.; de Andrés, A.; Prieto, C.
Correlated effects of fluorine and hydrogen in fluorinated tin oxide (FTO) transparent electrodes deposited by sputtering at room temperature
Applied Surface Science **537**, 147906 (2021)

113. Moro, M.V.; Wolf, P.M.; Bruckner, B.; Munnik, F.; Heller, R.; Bauer, P.; Primetzhofer, D.
Experimental electronic stopping cross section of tungsten for light ions in a large energy interval
Nuclear Instruments and Methods in Physics Research B **498**, 1 (2021)

114. Muduli, P.; Schlitz, R.; Kosub, T.; Hübner, R.; Erbe, A.; Makarov, D.; Goennenwein, S.T.B.
Local and nonlocal spin Seebeck effect in lateral Pt-Cr_2O_3-Pt devices at low temperatures
APL Materials **9**, 021122 (2021)

115. Mujtaba, J.; Liu, J.; Dey, K.K.; Li, T.; Chakraborty, R.; Xu, K.; Makarov, D.; Barmin, R.; Gorin, D.A.; Tolstoy, V.; Huang, G.S.; Solovev, A.A.; Mei, Y.F.
Micro-Bio-Chemo-Mechanical-Systems: Micromotors, Microfluidics and Nanozymes for Biomedical Applications
Advanced Materials **33**, 2007465 (2021)

116. Murton, J.B.; Opel, T.; Toms, P.; Blinov, A.; Fuchs, M.; Wood, J.; Gärtner, A.; Merchel, S.; Rugel, G.; Savvinov, G.; Wetterich, S.
A multimethod dating study of ancient permafrost, Batagay megaslump, east Siberia
Quaternary Research **105**, 1 (2022)

117. Napoli, G.; Pylypovskyi, O.; Sheka, D.; Vergoli, L.
Nematic shells: new insights in topology- and curvature-induced effects
Soft Matter **17**, 10322 (2021)

118. Neugebauer, N.; Hache, T.; Elm, M.T.; Hofmann, D.M.; Heiliger, C.; Schultheiß, H.; Klar, P.J.
Frequency- and magnetic-field-dependent properties of ordered magnetic nanoparticle arrangements
Physical Review B **103**, 094438 (2021)

119. Niggas, A.; Creutzburg, S.; Schwestka, J.; Wöckinger, B.; Gupta, T.; Grande, P.L.; Eder, D.; Marques, J.P.; Bayer, B.C.; Aumayr, F.; Bennett, R.; Wilhelm, R.A.
Peeling graphite layer by layer reveals the charge exchange dynamics of ions inside a solid
Communications Physics **4**, 180 (2021)

120. Nörenberg, T.; Wehmeier, L.; Lang, D.; Kehr, S.C.; Eng, L.M.
Compensating for artifacts in scanning near-field optical microscopy due to electrostatics
APL Photonics **6**, 0361021 (2021)

121. Ódor, G.; Gastner, M.; Kelling, J.; Deco, G.
Modelling on the very large-scale connectome
Journal of Physics: Complexity **2**, 045002 (2021)

122. Ódor, G.; Kelling, J.; Deco, G.
The effect of noise on the synchronization dynamics of the Kuramoto model on a large human connectome graph
Neurocomputing **461**, 696 (2021)

123. Oliveros Mata, E.S.; Canon Bermudez, G.S.; Ha, M.; Kosub, T.; Zabila, Y.; Faßbender, J.; Makarov, D.
Printable anisotropic magnetoresistance sensors for highly compliant electronics
Applied Physics A **127**, 280 (2021)

124. Olivotos, S.; Niedermann, S.; Flügel, T.; Mouslopoulou, V.; Merchel, S.; Cotterill, F.; Bookhagen, B.; Gärtner, A.; Rugel, G.; Scharf, A.; Nadeau, M.-J.; Braucher, R.; Seiler, M.
Quaternary landscape evolution in a tectonically active rift basin (paleo-lake Mweru, south-central Africa)
Geomorphology **381**, 107669 (2021)

125. Ozen, M.; Yahyaoglu, M.; Candolfi, C.; Veremchuk, I.; Kaiser, F.; Burkhardt, U.; Snyder, G.J.; Grin, Y.; Aydemir, U.
Enhanced thermoelectric performance in $Mg_{3+x}Sb_{1.5}Bi_{0.49}Te_{0.01}$ via engineering microstructure through melt-centrifugation
Journal of Materials Chemistry A **9**, 1733 (2021)

126. Pang, C.; Li, R.; Li, Z.; Sun, X.; Dong, N.; Wang, J.; Zhou, S.; Chen, F.
Q-switched mode-locked laser generation by Au nanoparticles embedded in $LiTaO_3$ crystals
Optical Materials **122**, 111714 (2021)

127. Pelizzo, M.G.; Corso, A.J.; Santi, G.; Hübner, R.; Garoli, D.; Doyle, D.; Lubin, P.; Cohen, A.N.; Erlikhman, J.; Favaro, G.; Bazzan, M.; Drobny, J.; Curreli, D.; Umansky, M.
Dependence of the damage in optical metal/dielectric coatings on the energy of ions in irradiation experiments for space qualification
Scientific Reports **11**, 3429 (2021)

128. Podlipec, R.; Mur, J.; Petelin, J.; Štrancar, J.; Petkovšek, R.
Method for controlled tissue theranostics using a single tunable laser source
Biomedical Optics Express **12**, 5881 (2021)

129. Podlipec, R.; Punzón-Quijorna, E.; Pirker, L.; Kelemen, M.; Vavpetič, P.; Kavalar, R.; Hlawacek, G.; Štrancar, J.; Pelicon, P.; Fokter, S.K.
Revealing inflammatory indications induced by titanium alloy wear debris in periprosthetic tissue by label-free correlative high-resolution ion, electron and optical micro-spectroscopy
Materials **14**, 3048 (2021)

130. Pretze, M.; von Kiedrowski, V.; Runge, R.; Freudenberg, R.; Hübner, R.; Davarci, G.; Schirrmacher, R.; Wängler, C.; Wängler, B.
$\alpha_v\beta_3$-Specific Gold Nanoparticles for Fluorescence Imaging of Tumor Angiogenesis
Nanomaterials **11**, 138 (2021)

131. Prucnal, S.; Hashemi, A.; Ghorbani Asl, M.; Hübner, R.; Duan, J.; Wei, Y.; Sharma, D.; Zahn, D.R.T.; Ziegenrücker, R.; Kentsch, U.; Krasheninnikov, A.; Helm, M.; Zhou, S.
Chlorine doping of $MoSe_2$ flakes by ion implantation
Nanoscale **13**, 5834 (2021)

132. Pylypovskyi, O.; Borysenko, Y.A.; Faßbender, J.; Sheka, D.; Makarov, D.
Curvature-driven homogeneous Dzyaloshinskii-Moriya interaction and emergent weak ferromagnetism in anisotropic antiferromagnetic spin chains
Applied Physics Letters **118**, 182405 (2021)

133. Pylypovskyi, O.; Tomilo, A.; Sheka, D.; Faßbender, J.; Makarov, D.
Boundary conditions for the Neel order parameter in a chiral antiferromagnetic slab
Physical Review B **103**, 134413 (2021)

134. Rana, R.; Klopf, J.M.; Ciano, C.; Singh, A.; Winnerl, S.; Schneider, H.; Helm, M.; Pashkin, O.
Gold implanted germanium photoswitch for cavity dumping of a free-electron laser
Applied Physics Letters **118**, 011107 (2021)

135. Redondo-Cubero, A.; Palomares, F.J.; Lorenz, K.; Rubio-Zuazo, J.; Hübner, R.; Mompéan, F.J.; García-Hernández, M.; Castro, G.R.; Vázquez, L.
Role of the metal supply pathway on silicon patterning by oblique ion beam sputtering
Applied Surface Science **580**, 152267 (2022)

136. Saha, S.; Zhou, J.; Hofhuis, K.; Kakay, A.; Scagnoli, V.; Heyderman, L.J.; Gliga, S.
Spin-wave dynamics and symmetry breaking in an artificial spin ice
ACS Nano **21**, 2382 (2021)

137. Arekapudi, S.S.P.K.; Bülz, D.; Ganss, F.; Samad, F.; Radu, F.; Zahn, D.R.T.; Lenz, K.; Salvan, G.; Albrecht, M.; Hellwig, O.
Highly Tunable Magnetic and Magnetotransport Properties of Exchange Coupled Ferromagnet/Antiferromagnet-based Heterostructures
ACS Applied Materials and Interfaces **13**, 59497 (2021)

138. Salazar-Cardona, M.M.; Körber, L.; Schultheiß, H.; Lenz, K.; Thomas, A.; Nielsch, K.; Kakay, A.; Otálora, J.A.
Nonreciprocity of spin waves in magnetic nanotubes with helical equilibrium magnetization
Applied Physics Letters **118**, 262411 (2021)

139. Salikhov, R.; Samad, F.; Böhm, B.; Schneider, S.; Pohl, D.; Rellinghaus, B.; Ullrich, A.; Albrecht, M.; Lindner, J.; Kiselev, N.S.; Hellwig, O.
Control of Stripe-Domain-Wall Magnetization in Multilayers Featuring Perpendicular Magnetic Anisotropy
Physical Review Applied **16**, 034016 (2021)

140. Samad, F.; Hlawacek, G.; Arekapudi, S.S.P.K.; Xu, X.; Koch, L.; Lenz, M.; Hellwig, O.
Controlled and deterministic creation of synthetic antiferromagnetic domains by focused ion beam irradiation
Applied Physics Letters **119**, 022409 (2021)

141. Schaefer, S.; Steudtner, R.; Hübner, R.; Krawczyk-Bärsch, E.; Merroun, M.L.
Effect of temperature and cell viability on uranium biomineralization by the uranium mine isolate Penicillium simplicissimum
Frontiers in Microbiology **12**, 802926 (2021)

142. Schneider, T.; Hill, D.; Kakay, A.; Lenz, K.; Lindner, J.; Faßbender, J.; Upadhyaya, P.; Liu, Y.; Wang, K.; Tserkovnyak, Y.; Krivorotov, I.N.; Barsukov, I.
Self-stabilizing exchange-mediated spin transport
Physical Review B **103**, 144412 (2021)

143. Schultheiß, K.; Sato, N.; Matthies, P.; Körber, L.; Wagner, K.; Hula, T.; Gladii, O.; Pearson, J.E.; Hoffmann, A.; Helm, M.; Faßbender, J.; Schultheiß, H.
Time refraction of spin waves
Physical Review Letters **126**, 137201 (2021)

144. Schwarz, H.; Uhlig, T.; Rösch, N.; Lindner, T.; Ganss, F.; Hellwig, O.; Lampke, T.; Wagner, G.; Seyller, T.
CoCrFeNi High-Entropy Alloy Thin Films Synthesised by Magnetron Sputter Deposition from Spark Plasma Sintered Targets
Coatings **11**, 468 (2021)

145. Schymura, S.; Rybkin, I.; Uygan, S.S.S.; Drev, S.; Podlipec, R.; Rijavec, T.; Mansel, A.; Lapanje, A.; Franke, K.; Strok, M.
Dissolution-based uptake of CeO_2 nanoparticles by fresh water shrimp – A dual-radiolabelling study of the fate of anthropogenic cerium in water organisms
Environmental Science: Nano **8**, 1934 (2021)

146. Shahzadeh, M.; Andriyevska, O.; Salikhov, R.; Fallarino, L.; Hellwig, O.; Pisana, S.
Nondiffusive Transport and Anisotropic Thermal Conductivity in High-Density Pt/Co Superlattices
ACS Applied Electronic Materials **3**, 1931 (2021)

147. Shaikh, M.S.; Wang, M.; Hübner, R.; Liedke, M.O.; Butterling, M.; Solonenko, D.; Madeira, T.I.; Li, Z.; Xie, Y.; Hirschmann, E.; Wagner, A.; Zahn, D.R.T.; Helm, M.; Zhou, S.
Phase evolution of Te-hyperdoped Si upon furnace annealing
Applied Surface Science **567**, 150755 (2021)

148. Shamraienko, V.; Spittel, D.; Hübner, R.; Khoshkhoo, M.S.; Weiß, N.; Georgi, M.; Borchert, K.B.L.; Schwarz, D.; Lesnyak, V.; Eychmüller, A.
Cation exchange on colloidal copper selenide nanosheets: a route to two-dimensional metal selenide nanomaterials
Journal of Materials Chemistry C **9**, 16523 (2021)

149. Shang, J.; Tang, X.; Gu, Y.; Krasheninnikov, A.; Picozzi, S.; Chen, C.; Kou, L.
Robust Magnetoelectric Effect in Decorated Graphene/In$_2$Se$_3$ Heterostructure
ACS Applied Materials and Interfaces **13**, 3033 (2021)

150. Shang, Z.; Berencen, Y.; Hollenbach, M.; Zhou, S.; Kraus, H.; Ohshima, T.; Astakhov, G.
Microwave-assisted spectroscopy of vacancy-related spin centers in hexagonal SiC
Physical Review Applied **15**, 034059 (2021)

151. Shimamoto, Y.; Trindade Goncalves, F.J.; Sogo, T.; Kousaka, Y.; Togawa, Y.
Anisotropic microwave propagation in a reconfigurable chiral spin soliton lattice
Physical Review B **104**, 174420 (2021)

152. Singh, A.; Li, J.; Pashkin, O.; Rana, R.; Winnerl, S.; Helm, M.; Schneider, H.
High-field THz pulses from GaAs photoconductive emitter for non-linear THz studies
Optics Express **29**, 19920 (2021)

153. Singh, S.; Horechyy, A.; Yadav, S.; Formanek, P.; Hübner, R.; Srivastava, R.K.; Sapra, S.; Fery, A.; Nandan, B.
Nanoparticle-Stabilized Perforated Lamellar Morphology in Block Copolymer/Quantum Dot Hybrids
Macromolecules **54**, 1216 (2021)

154. Singh, S.; Raulo, A.; Singh, A.; Mittal, M.; Horechyy, A.; Hübner, R.; Formanek, P.; Srivastava, R.K.; Sapra, S.; Fery, A.; Nandan, B.
Enhanced Photoluminescence of Gold Nanoparticle-Quantum Dot Hybrids Confined in Hairy Polymer Nanofibers
ChemNanoMat **7**, 831 (2021)

155. Sojkova, M.; Dobročka, E.; Hutár, P.; Tašková, V.; Pribusová-Slušná, L.; Stoklas, R.; Píš, I.; Bondino, F.; Munnik, F.; Hulman, M.
High carrier mobility epitaxially aligned PtSe$_2$ films grown by one-zone selenization
Applied Surface Science **538**, 147936 (2021)

156. Spanková, M.; Sojková, M.; Dobrocka, E.; Hutár, P.; Bodík, M.; Munnik, F.; Hulman, M.; Chromik, S.
Influence of precursor thin-film quality on the structural properties of large-area MoS$_2$ films grown by sulfurization of MoO$_3$ on c-sapphire
Applied Surface Science **540**, 148240 (2021)

157. Stübner, K.; Bookhagen, B.; Merchel, S.; Lachner, J.; Gadoev, M.
Unravelling the Pleistocene glacial history of the Pamir Mountains, Central Asia
Quaternary Science Reviews **257**, 106857 (2021)

158. Szabo, G.L.; Lehner, M.; Bischoff, L.; Pilz, W.; Kentsch, U.; Aumayr, F.; Klingner, N.; Wilhelm, R.A.
Nano-hillock formation on CaF$_2$ due to individual slow Au-cluster impacts
Nanotechnology **32**, 355701 (2021)

159. Tabean, S.; Mousley, M.; Pauly, C.; de Castro, O.; Serralta Hurtado De Menezes, E.; Klingner, N.; Hlawacek, G.; Wirtz, T.; Eswara, S.
Quantitative nanoscale imaging using transmission He ion channelling contrast: Proof-of-concept and application to study isolated crystalline defects
Ultramicroscopy **233**, 113439 (2022)

160. Thormählen, L.; Seidler, D.; Schell, V.; Munnik, F.; McCord, J.; Meyners, D.
Sputter Deposited Magnetostrictive Layers for SAW Magnetic Field Sensors
Sensors **21**, 8386 (2021)

161. Trindade Goncalves, F.J.; Hache, T.; Bejarano, M.; Hula, T.; Hellwig, O.; Faßbender, J.; Schultheiß, H.
Agility of spin Hall nano-oscillators
Physical Review Applied **16**, 054050 (2021)

162. Turkat, S.; Hammer, S.; Masha, E.; Akhmadaliev, S.; Bemmerer, D.; Grieger, M.; Hensel, T.; Julin, J.; Koppitz, M.; Ludwig, F.; Möckel, C.; Reinicke, S.; Schwengner, R.; Stöckel, K.; Szücs, T.; Wagner, L.; Zuber, K.
Measurement of the $^2H(p, \gamma)^3He$ S-factor at 265–1094 keV
Physical Review C **103**, 045805 (2021)

163. Tyschenko, I.E.; Voelskow, M.; Si, Z.; Popov, V.P.
Diffusion of In Atoms in SiO_2 Films Implanted with As^+ Ions
Semiconductors **55**, 289 (2021)

164. Vasileiadis, I.G.; Lymperakis, L.; Adikimenakis, A.; Gkotinakos, A.; Devulapalli, V.; Liebscher, C.H.; Androulidaki, M.; Hübner, R.; Karakostas, T.; Georgakilas, A.; Komninou, P.; Dimakis, E.; Dimitrakopulos, G.P.
Substitutional synthesis of sub-nanometer InGaN/GaN quantum wells with high indium content
Scientific Reports **11**, 20606 (2021)

165. Venanzi, T.; Selig, M.; Winnerl, S.; Pashkin, A.; Knorr, A.; Helm, M.; Schneider, H.
Terahertz-Induced Energy Transfer from Hot Carriers to Trions in a $MoSe_2$ Monolayer
ACS Photonics **8**, 2931 (2021)

166. Verba, R.; Körber, L.; Schultheiß, K.; Schultheiß, H.; Tiberkevich, V.; Slavin, A.
Theory of three-magnon interaction in a vortex-state magnetic nanodot
Physical Review B **103**, 014413 (2021)

167. Vogel, K.; Chekhonin, P.; Kaden, C.; Hernández-Mayoral, M.; Akhmadaliev, S.; Bergner, F.
Depth distribution of irradiation-induced dislocation loops in an Fe-^9Cr model alloy irradiated with Fe ions: The effect of ion energy
Nuclear Materials and Energy **27**, 101007 (2021)

168. Volkov, O.; Kronast, F.; Abert, C.; Oliveros Mata, E.S.; Kosub, T.; Makushko, P.; Erb, D.; Pylypovskyi, O.; Mawass, M.-A.; Sheka, D.; Zhou, S.; Faßbender, J.; Makarov, D.
Domain wall damping in ultrathin nanostripes with Dzyaloshinskii-Moriya interaction
Physical Review Applied **15**, 034038 (2021)

169. Wagner, C.; Schwuchow, M.; Venanzi, T.; Schneider, H.; Winnerl, S.; Thränhardt, A.
Kinetic Monte-Carlo simulation of exciton hopping: Urbach-tails in gas-molecule decorated $MoSe_2$
Physica Status Solidi (B) **258**, 2100186 (2021)

170. Wagner, K.; Körber, L.; Stienen, S.; Lindner, J.; Farle, M.; Kakay, A.
Numerical ferromagnetic resonance experiments in nanosized elements
IEEE Magnetics Letters **12**, 6100205 (2021)

171. Wallner, A.; Froehlich, M.B.; Hotchkis, M.A.C.; Kinoshita, N.; Paul, M.; Martschini, M.; Pavetich, S.; Tims, S.G.; Kivel, N.; Schumann, D.; Honda, M.; Matsuzaki, H.; Yamagata, T.
^{60}Fe and ^{244}Pu deposited on Earth constrain the r-process yields of recent nearby supernovae
Science **372**, 742 (2021)

172. Wang, Z.; Walter, L.S.; Wang, M.; Petkov, P.S.; Liang, B.; Qi, H.; Ngan Nguyen, N.; Hambsch, M.; Zhong, H.; Wang, M.; Park, S.; Renn, L.; Watanabe, K.; Taniguchi, T.; Mannsfeld, S.C.B.; Heine, T.; Kaiser, U.; Zhou, S.; Weitz, T.R.; Feng, X.; Dong, R.
Interfacial Synthesis of Layer-Oriented 2D Conjugated Metal-Organic Framework Films toward Directional Charge Transport
Journal of the American Chemical Society **143**, 13624 (2021)

173. Weiss, C.; Hübner, R.; Saunders, M.; Semisalova, A.; Ehrler, J.; Schmidt, N.; Seyd, J.; Albrecht, M.; Anwar, S.; Lindner, J.; Potzger, K.; Kostylev, M.
Effects of hydrogen absorption on magnetism in $Ni_{80}Fe_{20}$/Y/Pd trilayers
Physical Review B **104**, 094429 (2021)

174. Welsch, M.; Singh, A.; Winnerl, S.; Pashkin, O.; Xu, M.; Li, M.; Helm, M.; Schneider, H.
High Bias Field Operation of GaAs Photoconductive Terahertz Emitter
Journal of Infrared, Millimeter and Terahertz Waves **42**, 537 (2021)

175. Werner, Z.; Barlak, M.; Ratajczak, R.; Akhmadaliev, S.; Heller, R.; Staszkiewicz, B.; Zagórski, J.
Post-implantation defects in heavy ion implanted monocrystalline ZnO
Radiation Effects and Defects in Solids **176**, 538 (2021)

176. Wollenberg, A.; Drobot, B.; Hübner, R.; Kretzschmar, J.; Freitag, L.; Lehmann, F.; Günther, A.; Stumpf, T.; Raff, J.
Uranium(VI) bioassociation by different fungi – a comparative study into molecular processes
Journal of Hazardous Materials **411**, 125068 (2021)

177. Wu, Z.; Liu, Y.; Guo, E.; Darbandy, G.; Wang, S.-J.; Hübner, R.; Kloes, A.; Kleemann, H.; Leo, K.
Efficient and low-voltage vertical organic permeable base light-emitting transistors
Nature Materials **20**, 1007 (2021)

178. Xie, Y.; Yuan, Y.; Birowska, M.; Zhang, C.; Cao, L.; Wang, M.; Grenzer, J.; Kriegner, D.; Doležal, P.; Zeng, Y.-J.; Zhang, X.; Helm, M.; Zhou, S.; Prucnal, S.
Strain-induced switching between noncollinear and collinear spin configuration in magnetic Mn_5Ge_3 films
Physical Review B **104**, 064416 (2021)

179. Xu, M.; Dong, H.; Liu, C.; Wang, Y.; Hu, L.; Lan, C.; Luo, W.; Schneider, H.
Investigation of an opposed-contact GaAs photoconductive semiconductor switch at 1-kHz excitation
IEEE Transactions on Electron Devices **68**, 2355 (2021)

180. Yang, J.; Hübner, R.; Zhang, J.; Wan, H.; Zheng, Y.; Wang, H.; Qi, H.; He, L.; Li, Y.; Aregahegn Dubale, A.; Sun, Y.; Liu, Y.; Peng, D.; Meng, Y.; Zheng, Z.; Rossmeisl, J.; Liu, W.
A Robust PtNi Nanoframe/N-Doped Graphene Aerogel Electrocatalyst with Both High Activity and Stability
Angewandte Chemie - International Edition **60**, 9590 (2021)

181. Yang, Q.; Hu, X.; Shen, X.; Krasheninnikov, A.; Chen, Z.; Sun, L.
Enhancing Ferromagnetism and Tuning Electronic Properties of CrI_3 Monolayers by Adsorption of Transition-Metal Atoms
ACS Applied Materials and Interfaces **13**, 21593 (2021)

182. Yang, Q.; Li, X.; Liu, H.; Zheng, D.; Akhmadaliev, S.; Zhou, S.; Wu, P.
Obvious phase transition status induced by He⁺-ions implantation in KTN crystal
Acta Materialia **221**, 117376 (2021)

183. Yang, Y.; Yu, M.; Böke, F.; Qin, Q.; Hübner, R.; Knust, S.; Schwiderek, S.; Grundmeier, G.;
Fischer, H.; Keller, A.
Effect of nanoscale surface topography on the adsorption of globular proteins
Applied Surface Science **535**, 147671 (2021)

184. Ye, J.; Aftenieva, O.; Bayrak, T.; Jain, A.R.; König, T.A.F.; Erbe, A.; Seidel, R.
Complex metal nanostructures with programmable shapes from simple DNA building blocks
Advanced Materials **33**, 2100381 (2021)

185. Yu, H.; Xiao, J.; Schultheiß, H.
Magnetic texture based magnonics
Physics Reports **905**, 1 (2021)

186. Yuan, Y.; Xie, Y.; Yuan, N.; Wang, M.; Heller, R.; Kentsch, U.; Zhai, T.; Wang, X.
The Al Doping Effect on Epitaxial (In,Mn)As Dilute Magnetic Semiconductors Prepared by Ion Implantation and Pulsed Laser Melting
Materials **14**, 4138 (2021)

187. Zhang, X.; Li, G.; Li, Q.; Shaikh, M.S.; Li, Z.
The pure paramagnetism in graphene oxide
Results in Physics **26**, 104407 (2021)

188. Zhao, X.; Illing, R.; Ruelens, P.; Bachmann, M.; Cuniberti, G.; de Visser, J.A.G.M.; Baraban, L.
Coexistence of fluorescent Escherichia coli strains in millifluidic droplet reactors
Lab on a chip **21**, 1492 (2021)

189. Zhong, H.; Wang, M.; Ghorbani Asl, M.; Zhang, J.; Hoang Ly, K.; Liao, Z.-Q.; Chen, G.; Wei, Y.;
Biswal, B.P.; Zschech, E.; Weidinger, I.M.; Krasheninnikov, A.; Dong, R.; Feng, X.
Boosting the Electrocatalytic Conversion of Nitrogen to Ammonia on Metal-Phthalocyanine-based Two-Dimensional Conjugated Covalent Organic Frameworks
Journal of the American Chemical Society **143**, 19992 (2021)

190. Zhou, L.; Peng, Y.; Zhang, N.; Du, R.; Hübner, R.; Wen, X.; Li, D.; Hu, Y.; Eychmüller, A.
Size-Tunable Gold Aerogels: A Durable and Misfocus-Tolerant 3D Substrate for Multiplex SERS Detection
Advanced Optical Materials **9**, 2100352 (2021)

Patents

1. Canon Bermudez, G.S.; Mönch, J.I.; Makarov, D.
    P1908 - Verfahren zum Herstellen eines gedruckten magnetischen Funktionselements und gedrucktes magnetisches Funktionselement
    DE102019211970 - Offenlegung 11.02.2021; Nachanmeldungen: WO

2. Rebohle, L.; Fischer, C.; Skorupa, I.; Schmidt, H.; Krüger, S.; Blaschke, D.
    P2001 - Vorrichtung zur gezielten Anordnung von in einem Analyten gelösten, elektrisch polarisierbaren Materialien, Verfahren zur Bestimmung eines isoelektrischen Punktes eines elektrisch isolierenden Materials, Verfahren zum gezielten Anordnen eines in einem Analyten gelösten elektrisch polarisierbaren Materials
    DE102020200470 - Erteilung 20.05.2021; Nachanmeldungen: WO

3. Samad, F.; Koch, L.; Arekapudi, S.S.P.K.; Hellwig, O.; Schultheiß, H.
    P1915 - Magnetische Streufeld-Struktur, magnonisches Bauelement und Verfahren zur Herstellung einer magnetischen Streufeldstruktur
    DE102019129203 - Offenlegung 29.04.2021

Concluded scientific degrees

PhD Theses

1. Awan, A. Wajid
   Controlled modification of charge transport in two-dimensional materials
   TU Dresden, 29.04.2021

2. Balaghi, Leila
   Wide tuning of electronic properties in strained III-V core/shell nanowires
   TU Dresden, 12.01.2021

3. Buchriegler, Josef
   Full-field PIXE imaging using a Colour X-ray Camera - Advantages and drawbacks in elemental mapping of large areas with a poly-capillary optics
   TU Dresden, 07.05.2021

4. Creutzburg, Sascha
   Neutralisation langsamer hochgeladener Ionen in zwei-dimensionalen Materialien
   TU Dresden, 15.03.2021

5. Ghaderzadeh, Sadegh
   Atomistic Simulations of Irradiation-Induced Phenomena in Low-Dimensional Materials
   TU Dresden, 17.03.2021

6. Hache, Toni
   Frequency control of auto-oscillations of the magnetization in spin Hall nano-oscillators
   TU Chemnitz, 12.03.2021

7. Janke, Daniel
   Mechanism and directionality of nickel-induced crystallization of amorphous carbon
   TU BA Freiberg, 15.07.2021

8. Khan, Bilal
   Towards Scalable Reconfigurable FETs: Fabrication and Characterization
   TU Dresden, 17.12.2021

9. Kilibarda, Filip
   Single level model in molecular electronics
   Universität Konstanz, 01.10.2021

10. Li, Zichao
    Skyrmion-hosting B20-type MnSi films on Si substrates grown by flash lamp annealing
    TU Dresden, 23.09.2021

11. Shang, Zhen
    Microwave-assisted spectroscopy of spin defect centers in silicon carbide
    TU Dresden, 30.09.2021

12. Sorokin, Serhii
    Magnetization dynamics and spin-pumping in synthetic antiferromagnets
    TU Dresden, 07.09.2021

13. Wang, Xu
     Ultra-fast magnetic soft-bodied robots and high-motility visible light-driven micro robots
     TU Dresden, 25.11.2021

14. Xie, Yufang
     Investigation on physical properties of epitaxial ferromagnetic film Mn_5Ge_3 for spintronics application
     TU Dresden, 11.10.2021

Bachelor/Master/Diploma Theses

1. Seidel, Tom
    Charakterisierung von thermoelektrischen Nanostrukturen auf Substraten mit ioneninduzierter Vorstrukturierung
    TU Dresden (Diplom), 16.07.2021

2. Sondhi, Harpreet
    Charge transport through C_{60} molecules using mechanically controllable break junctions
    TU Dresden (M.Sc.), 08.10.2021

3. Stierle, Simon
    Investigation of colloidal systems driven by optical tweezers
    TU Dresden (Diplom), 12.07.2021

Awards and honors

Awards and honors

1. **Duan, Juanmei**

   PhD student in the department "Semiconductor Materials" won the **Graduate Student Award** of the E-MRS Fall Meeting 2021 for her talk "Enhanced Trion Emission in Monolayer $MoSe_2$ by Constructing a Type-I Van der Waals Heterostructure" (on-line), Warsaw, Poland, Sept. 20 – 23, 2021.

2. **Hache, Toni**

   Former PhD student in the Emmy-Noether group "Magnonics" received the **HZDR PhD Award 2021** for his dissertation "Frequency control of auto-oscillations of the magnetization in spin Hall nano-oscillators".

3. **Krasheninnikov, Arkady**

   Head of the group "Atomistic Simulations of Irradiation-induced Phenomena" was once again announced as **Highly Cited Researcher 2021** by Clarivate Analytics (Web of Science), Philadelphia, PA, USA.

4. **Li, Rang**

   PostDoc in the department "Semiconductor Materials" obtained a scholarship of the Alexander von Humboldt Foundation.

5. **Pylypovskyi, Oleksandr**

   PostDoc in the department "Intelligent Materials and Systems" received the **Best Poster Prize** at the 736. WE-Heraeus-Seminar on Magnetism at the Nanoscale: Imaging - Fabrication – Physics, Bad Honnef, Germany, January 6 – 8, 2021.

6. **Schultheiß, Kathrin**

   PostDoc in the department "Magnetism" was awarded the **HZDR Research Award 2021** for her work in the field of "Nonlinear magnonics as basis for a spin based neuromorphic computing architecture".

Invited conference contributions

1. Balaghi, L.; Tauchnitz, T.; Hilliard, D.; Moebus, F.; Shan, S.; Fotev, I.; Pashkin, O.; Hübner, R.;
    Grenzer, J.; Ghorbani Asl, M.; Krasheninnikov, A.; Schneider, H.; Helm, M.; Dimakis, E.
    Bandgap tuning and electron mobility enhancement in strained III-V nanowires
    Compound Semiconductor Week 2021, 09.-13.05.2021, Stockholm, Sweden

2. Begeza, V.; Rebohle, L.; Schumann, T.
    Temperature determination during Flash Lamp Annealing
    CERC 2021, 09.-10.09.2021, Cork, Ireland

3. Dimakis, E.
    Heterostructures in self-catalyzed III-As nanowires: benefits and challenges
    Nanostructures for Photonics, 15.-17.11.2021, St. Petersburg, Russia

4. Friedrich, R.
    Thermodynamics of ionic materials (AFLOW-CCE)
    AFLOW School for Materials Discovery 2021, 06.-10.09.2021, Online

5. Friedrich, R.; Esters, M.; Oses, C.; Ki, S.; Brenner, M.J.; Hicks, D.; Mehl, M.J.; Ghorbani-Asl, M.;
    Krasheninnikov, A.; Toher, C.; Curtarolo, S.
    Enabling materials design of ionic systems
    CECAM workshop Virtual Materials Design 2021, 20.-21.07.2021, Online

6. Hain, K.; Golser, R.; Hou, X.; Lachner, J.; Lin, M.; Meszar, M.; Qiao, J.; Sakaguchi, A.; Steier, P.;
    Wagreich, M.; Wallner, G.; Wiederin, A.; Wolf, J.
    **From the U-233/U-236 fingerprint towards an environmental tracer: Tracking down the
    sources of anthropogenic U-233**
    15th International Conference on Accelerator Mass Spectrometry (AMS-15), 15.-19.11.2021,
    Sydney, Australia

7. Helm, M.; Fotev, I.; Balaghi, L.; Lang, D.; Rana, R.; Winnerl, S.; Schneider, H.; Dimakis, E.;
    Pashkin, A.
    Nonlinear IR and THz Spectroscopy of Semiconductor Nanowires
    EMRS Spring Meeting, 31.05.-04.06.2021, Strasbourg, France

8. Helm, M.; Singh, A.; Pashkin, O.; Winnerl, S.; Beckh, C.; Sulzer, P.; Leitenstorfer, A.; Schneider,
    H.
    Germanium as an ultrabroadband THz material
    RJUSE TeraTech 2021, 01.-04.11.2021, Sendai, Japan

9. Klingner, N.; Heinig, K.-H.; Tucholski, D.; Möller, W.; Hübner, R.; Hlawacek, G.; Facsko, S.
    Transformation of tin spheres into hollow cubes by He+ irradiation
    FIB SIG User Group Meeting, 24.-25.09.2021, St Lucia Qld, Australia

10. Krause, M.; Lungwitz, F.; Mendez, A.; Hoppe, M.; Sonnenberg, J.; Garcia Valenzuela, A.;
    Munnik, F.; Grenzer, J.; Hübner, R.; Escobar Galindo, R.
    **Solar-selective coatings for high-temperature solar applications based on a selective
    transmitter on top of a black body absorber**
    Virtual MRS Spring Meeting 2021, Symposium EN05: Materials Challenges and Opportunities in
    Concentrated Solar Power Technologies, 19.-23.04.2021, online, USA

11. Krause, M.; Lungwitz, F.; Mendez, A.; Hoppe, M.; Sonnenberg, J.; Garcia-Valenzuela, A.;
    Munnik, F.; Grenzer, J.; Hübner, R.; Escobar Galindo, R.
    **Transparent conductive oxides on top of a black body absorber as alternative concept for
    high-temperature-stable solar-selective coatings**
    2021 Iberian Vacuum Meeting - RIVA Online, 04.-06.10.2021, Online, Spanien/ Portugal

12. Lohmann, S.; Holeňák, R.; Grande, P.L.; Primetzhofer, D.
    Ion-electron dynamics studied in a 3D-transmission approach
    27th International Symposium on Ion-Atom Collisions (ISIAC), 14.-16.07.2021, Online

13. Lohmann, S.; Holeňák, R.; Primetzhofer, D.
     Trajectory-dependent electronic excitations at keV ion energies
     25th International Conference on Ion Beam Analysis & 17th International Conference on Particle
     Induce X-ray Emission & International Conference on Secondary Ion Mass Spectrometry, 11.-
     15.10.2021, Online, Online

14. Makarov, D.
     Mechanically shapeable magnetic field sensor technologies
     27. NDVaK - Sensorik auf polymeren Oberflächen, 17.03.2021, Dresden, Germany

15. Makarov, D.
     **Manipulation of antiferromagnetism with electric fields: from fundamentals to memory
     concepts**
     School in the frame of the COST Action MAGNETOFON – "Ultrafast opto-magneto-electronics
     for non-dissipative information technology" (https://magnetofon.science.ru.nl), 05.-08.10.2021,
     Samobor, Croatia

16. Makarov, D.
     **Highly compliant flexible and printable magnetoelectronics for human-machine interfaces
     and soft robotics**
     2021 IEEE International Flexible Electronics Conference (IFETC), 09.08.2021, Glenview, USA

17. Makarov, D.
     Curvilinear magnetism
     W2S Seminar (Webinar series on Spintronics), 25.03.2021, Khurda, India

18. Makarov, D.
     Compliant magnetic sensor technologies
     8th International Symposium on Sensor Science, 21.05.2021, Dresden, Germany

19. Makarov, D.
     **Curvilinear magnetism: From curvature induced magnetochirality to shapeable
     magnetoelectronics**
     736. WE-Heraeus-Seminar "Magnetism at the Nanoscale: Imaging - Fabrication – Physics",
     06.01.2021, Bad Honnef, Germany

20. Makarov, D.
     Curvilinear magnetism: geometrically curved ferro- and antiferromagnets
     MRS Spring Meeting, 21.04.2021, Seattle, USA

21. Makarov, D.
     **Designing chiral magnetic responses by tailoring geometry of thin films: curvilinear ferro-
     and antiferromagnets**
     IEEE Trends in Magnetism, 06.-10.09.2021, Palermo, Italy

22. Makarov, D.
     Mechanically flexible magnetoelectronics for human-machine interfaces and soft robotics
     International School on Programmable Smart Sensors based on Bio-compatible Nanocomposite
     Materials (NanoSens), 17.-24.06.2021, Chemnitz, Germany

23. Makarov, D.
     Nanomagnetism and spintronics of Cr2O3 magnetoelectric antiferromagnets
     2021 IEEE 11th International Conference on "Nanomaterials: Applications & Properties", 05.-
     11.09.2021, Odesa, Ukraine

24. Makarov, D.
     Micromagnetism of magnetoelectric collinear antiferromagnets
     PetaSpin: Virtual Workshops and Seminars 2021, 15.10.2021, Messina, Italy

25. Makarov, D.
     Flexible magnetic field sensor technologies
     SPIE Spintronics Symposium 2021: Nanoscience + Engineering, 02.08.2021, San Diego, USA

26. Makarov, D.
     **Skin-conformal flexible and printable magnetoelectronics for human-machine interfaces
     and soft robotics**
     Advanced Nanomaterials Congress, 24.-27.10.2021, Stockholm, Sweden

27. Makarov, D.
    Flexible Electronics: From Interactive Smart Skins to In vivo Applications
    The International Conference on Metallurgical Coatings and Thin Films, 26.04.2021, San Diego, USA

28. Makarov, D.
    Advances in compliant magnetic field sensorics
    IEEE Advances in Magnetics 2020, 14.06.2021, Moena, Italy

29. Makarov, D.
    Nanomagnetism and spintronics of Cr_2O_3 thin-film magnetoelectric antiferromagnets
    3rd International Conference on Advances in Functional Materials, 18.08.2021, Los Angeles, USA

30. Martschini, M.; Lachner, J.; Marchhart, O.; Merchel, S.; Priller, A.; Steier, P.; Wieser, A.; Golser, R.
    Ion Laser InterAction Mass Spectrometry – prospects for AMS without chemistry
    15th International Conference on Accelerator Mass Spectrometry (AMS-15), 15.-19.11.2021, Sydney, Australia

31. Pashkin, O.
    Nonlinear response of semiconductor systems under intense THz excitation
    The 10th International Symposium on Ultrafast Phenomena and Terahertz Waves (ISUPTW 2021), 16.-19.06.2021, Chengdu, China

32. Pylypovskyi, O.
    Geometrical symmetry breaking in nanomagnets
    META 2021 The 11th International Conference on Metamaterials, Photonic Crystals and Plasmonics, 20.-23.07.2021, Warsaw (Online event), Poland

33. Pylypovskyi, O.
    Curvilinear Antiferromagnetism: Current State and Perspectives
    IEEE International Magnetic Virtual Conference INTERMAG21, 26.-30.04.2021, Online

34. Schneider, H.
    How to study nonlinear dynamics in semiconductors by terahertz wave free electron laser
    International Symposium on Ultrafast Phenomena and Terahertz Waves (ISUPT2021), 16.-19.06.2021, Chengdu, China

35. Schultheiß, K.; Schultheiß, H.
    Brillouin Light Scattering Revisited
    INTERMAG 2021, 26.-30.04.2021, online (planned: Lyon, France)

36. Wagner, A.; Butterling, M.; Elsherif, A.G.A.; Hirschmann, E.; Liedke, M.O.; Krause-Rehberg, R.
    Intense Positron Sources driven by a Superconducting Electron LINAC
    Positron Studies of Defects, 01.-05.03.2021, Mumbai, India

37. Zahn, P.
    Universal Limits of Thermopower and Figure of Merit from Transport Energy Statistics
    Understanding Transport Processes on the Nanoscale for Energy Harvesting Devices - 719. WE-Heraeus-Seminar, 08.-09.03.2021, online (planned: Bad Honnef, Deutschland)

38. Zhou, S.
    Tailoring oxide thin films by ion beam
    2nd International Workshop on Advanced Magnetic Oxides, 24.-26.11.2021, Aveiro, Portugal

39. Zhou, S.
    Tailoring oxide thin films by ion beam
    10th Vacuum and Surface Sciences Conference of Asia and Australia, 11.-14.10.2021, Shanghai, China

Conferences, workshops, colloquia and seminars

Organization of conferences and workshops

1. Astakhov, G. (member of organizational committee)
   Helmholtz Quantum Workshop
   12.02.2021, virtual event

2. Makarov, D.; Sheka, D.
   717. WE-Heraeus-Seminar: Curvilinear Condensed Matter: Fundamentals and Applications
   24. – 26.06.2021, virtual event

3. A.V. Poshakinskiy and G. V. Astakhov
   Session "Quantum spintronics with atomic defects in solids" at the International Conference on Metamaterials and Nanophotonics (METANANO 2021)
   17.09.2021, virtual event

4. Erbe, A.; Zahn, P.
   NANONET Annual Workshop 2021
   21. – 23.09.2021, Klingenberg, Germany

5. Audoit, G.; Moll, P.; Altmann, F.; Bábor, P.; Hlawacek, G.; Reuteler, J.; Winkler, R.
   4th EuFN Workshop and Fit4Nano meeting
   27. – 29.09.2021, Vienna, Austria

6. Makarov, D.; Thomas, A.
   Interdivisional SKM symposium at the DPG spring meeting 2021: Curvilinear Condensed Matter
   27.09. – 01.10.2021, virtual event

7. Flacke, L.; Hula, T.; Bejarano, M.
   SKM PhD Focus Session at the DPG spring meeting 2021: Magnetism - A potential platform for Big Data?
   01.10.2021, virtual event

8. Makarov, D.
   Workshop "HZDR meets Organic Electronic Saxony e.V."
   11.11.2021

9. Wallner, A. (member of organizational committee)
   15th Int. Conference on Accelerator Mass Spectrometry (AMS-15)
   15. – 19.11.2021, Sydney, Australia, virtual event

Colloquia

1. Ajayan, P.
   Rice University, USA
   Materials Science with 2D Atomic Layers
   15.10.2021

2. Fähler, S.
   Leibniz-Institut für Festkörper- und Werkstoffforschung Dresden, Germany
   Ferroic Materials: Fundamentals, Applications and Connections to the Research at HZDR
   12.05.2021

3. Mewes, T.
   University of Alabama, USA
   Magnetization Dynamics and Damping
   22.09.2021

4. Pal, S.
School of Physical Sciences, NISER, India
Scrutinizing microscopy of terahertz nonlinearities: From ferroelectrics to quantum cascade structures
01.06.2021

5. Sofer, Zd.
Department of Inorganic Chemistry, University of Chemistry and Technology Prague, Czech Republic
Layered materials beyond graphene – new possibilities and applications
13.10.2021

Seminars

1. Ali, S.
Technical University of Denmark, Department of Physics, Lyngby, Denmark
Defects in Semiconductors for Quantum Applications
17.09.2021

2. Davies, F.
University of Exeter, United Kingdom
First-principles simulations of van der Waals Heterostructures
02.09.2021

3. Ganss, F.
TU Chemnitz, Germany
Structural and Magnetic Characterization of Fe-Cu-Pt Thin Films
22.06.2021

4. Henstridge, M.
Max Planck Institute for the Structure and Dynamics of Matter, Hamburg, Germany
Controlling Functionality with Nonlinearly-Driven Polaritons
07.05.2021

5. Kameník, J.
Department of Nuclear Spectroscopy, Nuclear Physics Institute of the Czech Academy of Sciences, Řež, Czech Republic
Towards dating of a Lower Palaeolithic settlement in Transcarpathia, Ukraine. Cross border collaboration of Germany, Czech Republic, and Ukraine
01.12.2021

6. Kelardeh, H. K.
Max Planck Institute for the Physics of Complex Systems, Dresden, Germany
Strong-field and ultrafast dynamics in two-dimensional materials
21.09.2021

7. Knoch, J.
RWTH Aachen University, Germany
Nanoelectronics Devices Beyond the Regular MOSFET
10.11.2021

8. Meng, F.
Goethe University Frankfurt, Germany
THz spectroscopy of solid state materials
07.05.2021

9. Mentink, J.
Radboud University, Nijmegen, The Netherlands
Magnonics at the Edge of the Brillouin Zone
06.08.2021

10. Reindl, J.
Universität der Bundeswehr München, Institute for Applied Physics and Measurement Technology - Section Biomedical Radiation Phyiscs; Germany
Radiobiological and biomedical applications of high-energy ions
08.09.2021

11. Schüler, A.
    École Polytechnique Fédérale de Lausanne, Switzerland
    Solar radiation management with innovative materials
    10.03.2021

12. Shakfa, K.
    King Abdullah University of Science and Technology, Thuwal, Kingdom of Saudi Arabia
    Localization effects in disordered semiconductor nanostructures
    05.05.2021

13. Uykur, E.
    University of Stuttgart
    Optical fingerprints of unconventional carriers in correlated systems
    05.05.2021

14. Van der Wijngaart, W.; Raja, Sh.
    KTH Stockholm, Sweden
    Biomolecules and nanostructures
    09.06.2021

Projects

The projects are listed by funding institution and project starting date. In addition, the institute has several bilateral service collaborations with industrial partners and research institutions. These activities are not included in the following overview.

European Projects

1   01/2017 – 09/2021   European Union   EU
    TRANSPIRE –Terahertz Radio Communication
    Dr. A. Deac   *Phone: 0351 260 3709*   *a.deac@hzdr.de*

2   01/2017 – 06/2021   European Union   EU
    npSCOPE – Nanoparticle Characterization
    Dr. G. Hlawacek   *Phone: 0351 260 3409*   *g.hlawacek@hzdr.de*

3   05/2017 – 10/2021   European Union   EU
    CALIPSOplus – Coordinated Access to Lightsources
    Prof. M. Helm   *Phone: 0351 260 2260*   *m.helm@hzdr.de*

4   01/2019 – 06/2023   European Union   EU
    RADIATE – Research And Development with Ion Beams - Advancing Technology in Europe
    Prof. J. Fassbender *Phone: 0351 260 3096*   *j.fassbender@hzdr.de*

5   10/2020 – 09/2023   European Union   EU
    BIONANOSENS – Deeping collaboration on novel biomolecular electronics based on "smart" nanomaterials
    Dr. D. Makarov   *Phone: 0351 260 3273*   *d.makarov@hzdr.de*

6   10/2020 – 09/2023   NATO   NATO
    natoMYP – Spintronic Devices for Microwave Detection and Energy Harvesting Applications
    Dr. D. Makarov   *Phone: 0351 260 3273*   *d.makarov@hzdr.de*

7   11/2020 – 10/2024   European Cooperation in Science and Technology   COST
    FIT4NANO – Focused Ion Technology for Nanomaterials
    Dr. G. Hlawacek   *Phone: 0351 260 3409*   *g.hlawacek@hzdr.de*

8   11/2020 – 10/2024   European Union   EU
    RADICAL – Fundamental Breakthrough in Detection of Atmospheric Free Radicals
    Dr. Y. Georgiev   *Phone: 0351 260 2321*   *y.georgiev@hzdr.de*

9   05/2021 – 04/2025   European Union   EU
    Chemical Elements as Tracers of the Evolution of the Cosmos - Infrastructures for Nuclear Astrophysics
    Prof. A. Wallner   *Phone: 0351 260 3274*   *a.wallner@hzdr.de*

Helmholtz Association Projects

1   10/2017 – 03/2021   Helmholtz-Gemeinschaft   HGF
Helmholtz Exzellenznetzwerk – cfaed 2 + 3
Dr. A. Erbe   *Phone: 0351 260 2366*   *a.erbe@hzdr.de*

2   01/2019 – 12/2023   Helmholtz-Gemeinschaft   HGF
CROSSING – Crossing borders and scales - an interdisciplinary approach
Dr. J. v. Borany   *Phone: 0351 260 3378*   *j.v.borany@hzdr.de*

3   12/2019 – 11/2024   Helmholtz-Gemeinschaft   HGF
Helmholtz Innovation Lab – FlexiSens
Dr. D. Makarov   *Phone: 0351 260 3273*   *d.makarov@hzdr.de*

4   02/2020 – 01/2025   Helmholtz-Gemeinschaft   HGF
Helmholtz Innovation Lab – UltraTherm
Dr. L. Rebohle   *Phone: 0351 260 3368*   *l.rebohle@hzdr.de*

German Science Foundation Projects

1   05/2014 – 11/2021   Deutsche Forschungsgemeinschaft   DFG
Emmy Noether Junior Research Group – Magnonics
Dr. H. Schultheiß   *Phone: 0351 260 3243*   *h.schultheiss@hzdr.de*

2   11/2017 – 09/2021   Deutsche Forschungsgemeinschaft   DFG
ULTRACRITICAL – High-temperature superconductors
Dr. A. Pashkin   *Phone: 0351 260 3287*   *o.pashkin@hzdr.de*

3   04/2018 – 06/2021   Deutsche Forschungsgemeinschaft   DFG
Confined Microswimmers
Dr. A. Erbe   *Phone: 0351 260 2366*   *a.erbe@hzdr.de*

4   04/2018 – 02/2022   Deutsche Forschungsgemeinschaft   DFG
IMASTE – Graphene encapsulated quasi-2D materials
Dr. A. Krasheninnikov *Phone: 0351 260 3148*   *a.krasheninnikov@hzdr.de*

5   10/2018 – 11/2021   Deutsche Forschungsgemeinschaft   DFG
Doping by ALD and FLA
Dr. L. Rebohle   *Phone: 0351 260 3368*   *l.rebohle@hzdr.de*

6   01/2019 – 07/2021   Deutsche Forschungsgemeinschaft   DFG
Quantum control of single spin centers in silicon carbide coupled to optical microcavities
Dr. G. Astakhov   *Phone: 0351 260 3894*   *g.astakhov@hzdr.de*

7   01/2019 – 03/2022   Deutsche Forschungsgemeinschaft   DFG
Printable giant magnetoresistive sensors with high sensitivity at small magnetic fields
Dr. D. Makarov   *Phone: 0351 260 3273*   *d.makarov@hzdr.de*

8   06/2019 – 06/2022   Deutsche Forschungsgemeinschaft   DFG
Interacting Magnonic Currents and Chiral Spin Textures for Energy Efficient Spintronics
Dr. H. Schultheiß   *Phone: 0351 260 3243*   *h.schultheiss@hzdr.de*

9   07/2019 – 06/2022   Deutsche Forschungsgemeinschaft   DFG
3D tailoring of all-oxide heterostructures by ion beams
Dr. S. Zhou   *Phone: 0351 260 2484*   *s.zhou@hzdr.de*

10 07/2019 – 06/2022   Deutsche Forschungsgemeinschaft   DFG
**Lab-on-chip Systems Carrying Artificial Motors for Multiplexed and Multiparametric
Biochemical Assays**
Dr. D. Makarov   *Phone: 0351 260 3273*   *d.makarov@hzdr.de*

11 10/2019 – 11/2022   Deutsche Forschungsgemeinschaft   DFG
3D transport of spin waves in curved nano-membranes
Dr. A. Kakay   *Phone: 0351 260 2689*   *a.kakay@hzdr.de*

12   11/2019 – 10/2022   Deutsche Forschungsgemeinschaft   DFG
Functionalization of Ultrathin MoS$_2$ by Defect Engineering
Dr. A. Krasheninnikov Phone: 0351 260 3148   a.krasheninnikov@hzdr.de

13   02/2020 – 01/2023   Deutsche Forschungsgemeinschaft   DFG
TRIGUS - Friction-induced interface and structure-changing processes in dry lubrication systems under defined atmospheres
Dr. M. Krause   Phone: 0351 260 3578   matthias.krause@hzdr.de

14   04/2020 – 08/2024   Deutsche Forschungsgemeinschaft   DFG
CurvMag – Non-Local Chiral Interactions In Corrugated Magnetic Nanoshells
Dr. D. Makarov   Phone: 0351 260 3273   d.makarov@hzdr.de

15   07/2020 – 06/2024   Deutsche Forschungsgemeinschaft   DFG
SFB 1415 – "Chemistry of Synthetic Two-Dimensional Materials"
Dr. A. Krasheninnikov Phone: 0351 260 3148   a.krasheninnikov@hzdr.de

16   08/2020 – 07/2023   Deutsche Forschungsgemeinschaft   DFG
AMSIGE – Topological order and its correlation to self-atom transport in amorphous materials:silicon and germanium as model systems
Dr. M. Posselt   Phone: 0351 260 3279   m.posselt@hzdr.de

17   09/2020 – 08/2023   Deutsche Forschungsgemeinschaft   DFG
3Dmag – Krümmungsinduzierte Effekte in magnetischen Nanostrukturen
Dr. D. Makarov   Phone: 0351 260 3273   d.makarov@hzdr.de

18   11/2020 – 10/2023   Deutsche Forschungsgemeinschaft   DFG
miracuSi – Room-temperature broadband MIR photodetector based on Si:Te for wafer-scale integration
Dr. M. Wang   Phone: 0351 260 2833   m.wang@hzdr.de

19   01/2021 – 12/2023   Deutsche Forschungsgemeinschaft   DFG
eSensus – Compliant and breathable magnetoelectronics: towards electronic proprioception
Dr. D. Makarov   Phone: 0351 260 3273   d.makarov@hzdr.de

20   08/2021 – 07/2024   Deutsche Forschungsgemeinschaft   DFG
TOPCURVE – Curvature-induced Effects in Magnetic Nanostructures
Dr. A. Kakay   Phone: +49 351 260 2689   a.kakay@hzdr.de

21   12/2020 – 11/2023   Deutsche Forschungsgemeinschaft   DFG
MUMAGI II – Microscopic understanding of disorder induced ferromagnetism in B2-alloy thin films II
Dr. R. Bali   Phone: 0351 260 2919   r.bali@hzdr.de

22   01/2021 – 12/2023   Deutsche Forschungsgemeinschaft   DFG
Search for magnetochiral responses in curvilinear geometries
Dr. O. Volkov   Phone: 0351 260 2186   o.volkov@hzdr.de

23   04/2021 – 03/2024   Deutsche Forschungsgemeinschaft   DFG
Hybrid nanomechanical systems including atom-scale defects based on silicon carbide
Dr. A. Erbe   Phone: 0351 260 2366   a.erbe@hzdr.de

24   06/2021 – 05/2024   Deutsche Forschungsgemeinschaft   DFG
Hybrid nanomechanical systems including atom-scale defects based on silicon carbide
Dr. G. Astakhov   Phone: 0351 260 3894   g.astakhov@hzdr.de

25   06/2021 – 05/2024   Deutsche Forschungsgemeinschaft   DFG
Transport and Magnetic Properties of Disordered Cr2AlC MAX Phases (TRANSMAX)
Dr. R. Bali   Phone: 0351 260 2919   r.bali@hzdr.de

26   10/2021 – 10/2023   Deutsche Forschungsgemeinschaft   DFG
Coupling Effects in Re-Programmable Micro-Matter
Dr. S. Fähler   Phone: 0351 260 2775   s.faehler@hzdr.de

Federally and Saxony State Funded Projects

1. 11/2018 – 03/2022   Bundesministerium für Bildung und Forschung   BMBF
   Metal-germanium interface: Schottky barrier and ohmic contacts
   Dr. S. Prucnal   Phone: 0351 260 2065   s.prucnal@hzdr.de

2. 03/2019 – 03/2021   Arbeitsgemeinschaft industrielle Forschung   AiF
   Improvement of the dynamic properties of GaAs power diodes by proton irradiation
   Dr. J. v. Borany   Phone: 0351 260 3378   j.v.borany@hzdr.de

3. 05/2019 – 02/2021   Bundesministerium für Wirtschaft und Klimaschutz   BMWK
   Magnetoelectrical detector
   Dr. D. Makarov   Phone: 0351 260 3273   d.makarov@hzdr.de

4. 07/2019 – 01/2022   Sächsische Aufbaubank   SAB
   Innovative product platform for space-based Global Navigation Satellite Systems (GNSS)
   Dr. J. v. Borany   Phone: 0351 260 3378   j.v.borany@hzdr.de

5. 10/2019 – 09/2023   Bundesministerium für Bildung und Forschung   BMBF
   SiGeSn - Group IV-heterostructures for most advanced nanoelectronics devices
   Dr. Y. Georgiev   Phone: 0351 260 2321   y.georgiev@hzdr.de
   Dr. S. Prucnal   Phone: 0351 260 2065   s.prucnal@hzdr.de

6. 10/2019 – 09/2023   Bundesministerium für Bildung und Forschung   BMBF
   SPES3 - Black phosphorus in sensitive, selective and stable sensors
   Dr. A. Erbe   Phone: 0351 260 2366   a.erbe@hzdr.de

7. 06/2020 – 05/2022   EFDS e. V.   EFDS
   **Novel Eddy current sensors based on flexible GMR sensor arrays for the analysis of
   components of complex shape**
   Dr. D. Makarov   Phone: 0351 260 3273   d.makarov@hzdr.de

8. 03/2020 – 02/2022   Arbeitsgemeinschaft industrielle Forschung   AiF
   Magnetic Nanostructures
   Dr. L. Bischoff   Phone: 0351 260 2866   l.bischoff@hzdr.de

9. 10/2020 – 09/2023   Bundesministerium für Wirtschaft und Klimaschutz   BMWK
   RoSiLIB – Nanoporous Si anodes of lithium ion batteries by microdroplet quenching
   Dr. K.-H. Heinig   Phone: 0351 260 3288   k.h.heinig@hzdr.de

10. 05/2021 – 05/2022   Sächsische Aufbaubank   SAB
    Contactless human-machine interface based on flexible magnetic field sensors
    Dr. D. Makarov   Phone: 0351 260 3273   d.makarov@hzdr.de

11. 05/2021 – 06/2021   Sächsische Aufbaubank   SAB
    **M-ERA-NET Call2021 - PreProposal: Processing of Si-Anode and LiTDI Electrolyte for the
    next generation fast-charging lithium-ion batteries**
    Dr. C. Cherkouk   Phone: 0351 260 2028   c.cherkouk@hzdr.de

12. 07/2021 – 06/2024   LeibnizX   LX
    **Defect-engineering in graphene via focused ion beam for tailored van der Waals epitaxy of
    h-BN**
    Dr. A. Krasheninnikov Phone: 0351 260 3148   a.krasheninnikov@hzdr.de
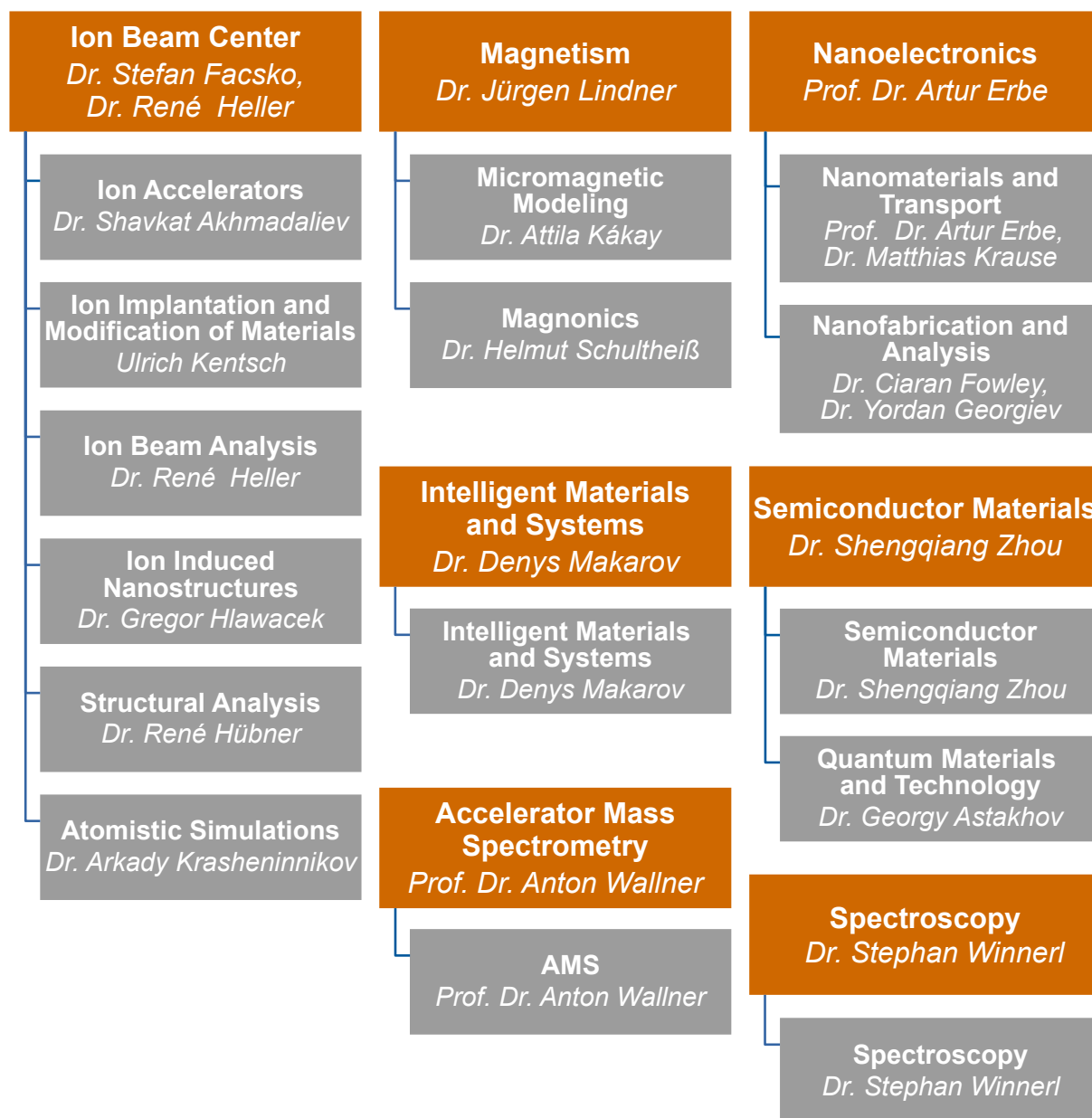
Personnel Exchange Projects and Society Chairs

1 05/2017 – 12/2023   Institute of Electrical and Electronics Engineers   IEEE
Magnetics Society German Chapter Chair
Dr. H. Schultheiß   Phone: 0351 260 3243   h.schultheiss@hzdr.de

2 07/2017 – 12/2021   Alexander-von-Humboldt-Stiftung   AvH
Humboldt fellowship Prof. Sheka
Dr. D. Makarov   Phone: 0351 260 3273   d.makarov@hzdr.de

3 10/2020 – 09/2021   Alexander-von-Humboldt-Stiftung   AvH
Feodor Lynen Return Grant for Dr. Rico Friedrich
Dr. A. Krasheninnikov Phone: 0351 260 3148   a.krasheninnikov@hzdr.de

4 03/2021 – 08/2021   Deutscher Akademischer Austauschdienst   DAAD
DAAD fellowship Chepkasov
Dr. A. Krasheninnikov Phone: 0351 260 3148   a.krasheninnikov@hzdr.de

5 03/2021 – 06/2024   Sino-German-Center   SGC
The magnetosensitive e-Skins for magnetic perception ability of human and soft robots
Dr. D. Makarov   Phone: 0351 260 3273   d.makarov@hzdr.de

6 03/2021 – 05/2021   Deutscher Akademischer Austauschdienst   DAAD
DAAD fellowship Pyeshkova
Dr. D. Makarov   Phone: 0351 260 3273   d.makarov@hzdr.de

7 04/2021 – 03/2022   Alexander-von-Humboldt-Stiftung   AvH
Alexander von Humboldt fellowship Dr. Li
Prof. M. Helm   Phone: 0351 260 2260   m.helm@hzdr.de

8 10/2021 – 10/2021   Deutscher Akademischer Austauschdienst   DAAD
DAAD fellowship Prof. Otalora
Dr. A. Kakay   Phone: 0351 260 2689   a.kakay@hzdr.de

Organization chart

Institute of Ion Beam Physics and Materials Research
Prof. Dr. Jürgen Faßbender   *Prof. Dr. Manfred Helm*

Ion Beam Center
Dr. Stefan Facsko,
Dr. René Heller

- **Ion Accelerators**
  Dr. Shavkat Akhmadaliev

- **Ion Implantation and Modification of Materials**
  Ulrich Kentsch

- **Ion Beam Analysis**
  Dr. René Heller

- **Ion Induced Nanostructures**
  Dr. Gregor Hlawacek

- **Structural Analysis**
  Dr. René Hübner

- **Atomistic Simulations**
  Dr. Arkady Krasheninnikov

Magnetism
Dr. Jürgen Lindner

- **Micromagnetic Modeling**
  Dr. Attila Kákay

- **Magnonics**
  Dr. Helmut Schultheiß

Intelligent Materials and Systems
Dr. Denys Makarov

- **Intelligent Materials and Systems**
  Dr. Denys Makarov

Accelerator Mass Spectrometry
Prof. Dr. Anton Wallner

- **AMS**
  Prof. Dr. Anton Wallner

Nanoelectronics
Prof. Dr. Artur Erbe

- **Nanomaterials and Transport**
  Prof. Dr. Artur Erbe,
  Dr. Matthias Krause

- **Nanofabrication and Analysis**
  Dr. Ciaran Fowley,
  Dr. Yordan Georgiev

Semiconductor Materials
Dr. Shengqiang Zhou

- **Semiconductor Materials**
  Dr. Shengqiang Zhou

- **Quantum Materials and Technology**
  Dr. Georgy Astakhov

Spectroscopy
Dr. Stephan Winnerl

- **Spectroscopy**
  Dr. Stephan Winnerl

International Helmholtz Research School for Nanoelectronic Networks (IHRS NanoNet)
Speaker: Prof. Dr. Artur Erbe | Teaching Director: Dr. Peter Zahn

List of personnel 2021

DIRECTORS	**OFFICE**
Prof. Dr. M. Helm, Prof. Dr. J. Faßbender	**S. Gebel, S. Kirch**

SCIENTIFIC STAFF

Permanent staff

Dr. C. Akhmadaliev
Dr. G. Astakhov
Dr. L. Bischoff
Dr. J. von Borany
Dr. E. Dimakis
Dr. A. Erbe
Dr. S. Facsko
Dr. S. Fähler
Dr. C. Fowley
Dr. Y. Georgiev
Dr. J. Grenzer
Dr. R. Heller
Dr. G. Hlawacek
Dr. R. Hübner
Dr. A. Kákay
Dr. A. Krasheninnikov
Dr. M. Krause
Dr. J. Lachner
Dr. K. Lenz
Dr. J. Lindner
Dr. D. Makarov
Dr. F. Munnik
Dr. A. Pashkin
Dr. K. Potzger
Dr. S. Prucnal
Dr. L. Rebohle
Dr. G. Rugel
Dr. H. Schneider
Prof. Dr. A. Wallner
Dr. S. Winnerl
Dr. P. Zahn
Dr. S. Zhou

Non-permanent staff

Dr. H. Arora
Dr. R. Bali
Dr. Y. Berencén
Dr. G. S. Canon Bermudez (P)
Dr. H. Cansever (P)
Dr. C. Cherkouk (P)
Dr. F. Davies (P)
Dr. H.-J. Engelmann (P)
Dr. D. Erb
Dr. S. Fichter
Dr. C. Folgner (P)
Dr. R. Friedrich (P)
Dr. A. Froideval (P)
Dr. F. Ganss
Dr. A. Garcia Valenzuela (P)
Dr. M. Ghorbani Asl
Dr. O. Gladii (P)
Dr. F. Goncalves (P)
Dr. M. Grobosch (P)
Dr. C. Habenicht (P)
Dr. T. Hache
Dr. K.-H. Heinig (P)
Prof. Dr. O. Hellwig
Dr. V. Iurchuk
R. Kaltofen (P)
Dr. M.B. Khan (P)
Dr. N. Klingner (P)
Dr. S. Kretschmer
Dr. C. Lei (P)
Dr. R. Li (P)

Dr. A. Lindner
Dr. S. Lohmann (P)
Prof. Dr. W. Möller (P)
Dr. I. Mönch (P)
Dr. J.P. Navarro
Dr. R. Podlipec (P)
Dr. M. Posselt (P)
Dr. O. Pylypovskyi
Dr. R. Rana
Dr. R. Salikhov (P)
Dr. H. Schultheiß
Dr. K. Schultheiß
Dr. J. Schütt (P)
Dr. A. Singh
Dr. W. Skorupa (P)
Dr. S. Sorokin (P)
Dr. S. Stienen
Dr. K. Stübner
Dr. X. Sun
Dr. I. Veremchuk
Dr. C. Vivo Vilches (P)
Dr. O. Volkov (P)
Dr. M. Wang
Dr. S. Winkler
Dr. R. Xu (P)
Dr. Y. Zabila (P)

TECHNICAL STAFF

Permanent staff

Rb. Aniol	H. Lange	T. Schönherr
Rm. Aniol	U. Lucchesi	J. Schulz
C. Bischoff	F. Ludewig	T. Schumann
E. Christalle	D. Medger	I. Skorupa
S. Eisenwinder	R. Mester	M. Steinert
H. Gude	Dr. R. Narkovic	T. Tarnow
J. Heinze	T. Naumann	T. Voitsekhivska
A. Henschke	C. Neisser	J. Wagner
H. Hilliges	F. Nierobisch	A. Weise
Dr. R. Illing	T. Putzke	A. Weißig
U. Kentsch	A. Reichel	J. Winkelmann
S. Klare	B. Scheumann	R. Ziegenrücker
J. Kreher	G. Schnabel	L. Zimmermann
A. Kunz	A. Schneider	J. Zscharschuch
K. Lang	A. Scholz	

Non-permanent staff

M. Baum
A. Berens (P)
T. Döring (P)
M. Görlich
K. Jarschel
R. Krause
S. Krüger (P)
A. Legrand
L. Ramasubramanian (P)
Dr. F. Ritschel (P)
C. Schmoldt (P)
C. Schubert (P)
A. Worbs

(P) Projects

PhD STUDENTS

Y. Alsaadawi	S. Ghosh	L. Körber	A. Seidl
V. Begeza	P. Heinig	Y. Li	E. Serralta Hurtado
M. Bejarano	C. Heins	Z. Li	M.S. Shaikh
P. Chava	D. Hilliard	A. Luferau	Z. Shang
S. Creutzburg	M. Hollenbach	P. Makushko	O. Steuer
J. Duan	T. Hula	E.S. Oliveros Mata	D. Tucholski
A. Echresh	N. Jagtap	K. Mavridou	Y. Xie
Z. Fekri	M. Jain	G. Patel	Z. Yu
I. Fotev	T. Joseph	J. Cabaco Salgado	N. Yuan
Y. Ge	M.M. Khan	F. Samad	Y. Zhou
S. Ghaderzadeh	D. Koll	T. Seidel	

STUDENTS (diploma / MSc / BSc)

M. Bhavsar	P. Singh	H. Sondhi	S. Stierle